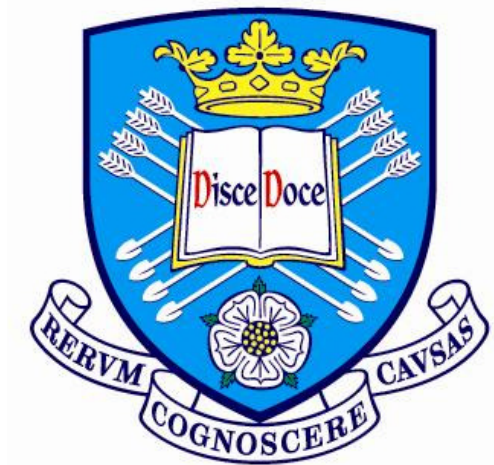


# Mechanical Response of Mesh Materials



A Thesis submitted to the University of Sheffield  
for the degree of Doctor of Philosophy in the Faculty of Engineering

by

Emiliano Ximenes

Department of Mechanical Engineering

University of Sheffield

September 2021



# Abstract

Viscous type damping from viscoelastics is one of the most largely adopted and studied forms of damping. However, there are some harsh environments such as outer space where viscoelastic materials are not favourable due to extreme conditions such as high and low temperatures, corrosive environments, exposure to vacuum and radiation from cosmic rays. In all of these cases, frictional (also called Coulomb or Coulombic) dampers pose as a valid alternative, thanks to the advantage of a higher resistance to temperature effects and a large applicability to different conditions, this being only limited by the properties of their constitutive materials. Because of these advantages, Coulomb dampers have been largely adopted in many applications and they are available in several different configurations.

This thesis focuses on a specific type of friction material that is referred to by the author as *plain-weave mesh material* (PWMM), which consists in a highly ordered structure composed of interwoven wires where the mutual frictional contact at the numerous intersections generates the energy dissipation responsible for damping. Their stiffness and damping behaviour is investigated through an in-depth finite element (FE) analysis and a set of analytical models is developed to predict the mechanical response to tension, in-plane shear and out-of-plane bending. These mathematical models are compared to the numerical results for validation and a general good agreement is observed between them for a wide range of displacement. A reduced finite element model is developed, based on these theoretical formulations which are exploited to calculate the effective properties of the material. This model can be implemented in a FE code for achieving

a consistent reduction in computational demand. With this purpose, based on the reduced model, a concept software is developed in a MATLAB-ANSYS integrated environment, aimed at providing a tool to assist in the design of friction mesh dampers and structures with complex geometries and load conditions. Finally, some conceptual mesh damping devices are proposed and discussed as potential industrial applications, considering different geometries, materials and loads, and their hysteretic response to cyclic loading is reported.

# Acknowledgements

Before all else, I would like to express my profound gratitude to my supervisors Dr. Charles Lord and Dr. Jem Rongong, for providing me their guidance and support throughout this research and sharing with me their valuable experience. They have provided me with constant encouragement and motivation and supported me not only from a professional but also from a human perspective. They created a joyful and friendly working environment that have made these years unforgettable for me. This priceless help, especially during these recent times of pandemic, has being fundamental for me to the successful completion of this project.

I would also like to express my appreciation to all the members of the Dynamics Research Group and the Department of Mechanical Engineering that have shared with me some joyful moments throughout these years. Among all, I would like to express my special thanks to Tianwei Zhang, Iason Iakovidis, Kartik Chandrasekhar, Sheng Ai, Ian Efremov, Jose Pérez Muñoz, Luke Jones, Suzhou Chen, Haichen Shi, Ning Tang, and Vimanyu Beedasy.

In conclusion, I would like to thank my family and my wife Violet for accompanying me with continuous support and patience throughout this journey. Without them, I would never have succeeded in completing this work.

# List of publications

## Journal papers:

[1] E. Ximenes, C. Lord, and J. Rongong. Mechanical response and energy dissipative modelling for plain-weave architected mesh materials. *Engineering Structures*. **In progress**.

[2] E. Ximenes, C. Lord, and J. Rongong. Reduced order model using beam-shell elements for frictional architected plain-weave mesh materials. *International Journal of Engineering Science*. **In progress**.

## Conferences:

[1] E. Ximenes, C. Lord, and J. Rongong. Modeling the mechanical response of ordered mesh architected materials. *Proceedings of EURO-DYN 2020 - XI International Conference on Structural Dynamics*, 23-26 November 2020, Athens, Greece.

# Contents

<b>Abstract</b>	<b>i</b>
<b>Acknowledgements</b>	<b>iii</b>
<b>List of publications</b>	<b>iv</b>
<b>List of symbols</b>	<b>xix</b>
<b>List of acronyms</b>	<b>xxiii</b>
<b>1 Introduction</b>	<b>1</b>
1.1 Mesh materials . . . . .	1
1.1.1 Non-ordered mesh materials . . . . .	1
1.1.2 Ordered mesh materials . . . . .	2
1.1.2.1 Woven and plain-weave mesh materials . . . . .	4
1.2 Aims and main contributions . . . . .	6
1.3 Thesis layout . . . . .	7
<b>2 Literature review</b>	<b>10</b>
2.1 Introduction . . . . .	10

---

2.2	Behaviour of mesh materials . . . . .	10
2.2.1	Ordered mesh materials . . . . .	10
2.2.2	Non-ordered mesh materials . . . . .	12
2.2.2.1	Experimental approaches . . . . .	14
2.2.2.2	Modelling . . . . .	15
2.3	Plain-weave pattern in textiles and composites . . . . .	17
2.3.1	Modelling of woven fabrics . . . . .	18
2.3.1.1	Geometry . . . . .	18
2.3.1.2	Tension . . . . .	19
2.3.1.3	Bending . . . . .	20
2.3.1.4	Shear . . . . .	20
2.3.2	Modelling of fibre-reinforced composites . . . . .	21
2.4	Conclusions . . . . .	25
<b>3</b>	<b>Material characterisation</b>	<b>27</b>
3.1	Introduction . . . . .	27
3.2	Metamaterials . . . . .	28
3.3	Geometry of plain-weave mesh materials . . . . .	29
3.3.1	Image analysis . . . . .	31
3.3.1.1	Analysis of longitudinal path of the wires . . . . .	31
3.3.1.2	Statistical investigation of mesh aperture . . . . .	33
3.4	Constituent materials . . . . .	36
3.4.1	Stainless steel . . . . .	36
3.4.2	Nitinol . . . . .	37
3.5	Conclusions . . . . .	39

---

<b>4</b>	<b>Analytical modelling</b>	<b>40</b>
4.1	Introduction . . . . .	40
4.2	Beam theories . . . . .	41
4.2.1	Euler-Bernoulli . . . . .	42
4.2.2	Timoshenko . . . . .	44
4.2.3	Model selection . . . . .	45
4.3	Energy-based methods in structural analysis . . . . .	47
4.3.1	Principle of virtual work . . . . .	48
4.3.1.1	Normal force . . . . .	49
4.3.1.2	Shear force . . . . .	50
4.3.1.3	Bending moment . . . . .	50
4.3.1.4	Total virtual internal energy . . . . .	51
4.3.2	Castigliano's theorem for elastic structures . . . . .	51
4.4	Contact mechanics . . . . .	53
4.4.1	Hertz theory . . . . .	54
4.4.1.1	Sphere-to-sphere contact . . . . .	55
4.4.1.2	Cylinder-to-cylinder contact: parallel and perpendicular axes . . . . .	56
4.4.1.3	General case and cylinder crossed with arbitrary angle . . . . .	57
4.4.2	Adhesive contact: JKR theory . . . . .	59
4.4.3	Contact model selection . . . . .	62
4.5	Frictional interaction of surfaces . . . . .	65
4.5.1	Micromechanics of dry friction . . . . .	66

---

4.5.2	Macro-scale modelling of friction . . . . .	70
4.5.2.1	Coulomb model . . . . .	70
4.5.2.2	Dahl model . . . . .	72
4.5.2.3	Lund-Grenoble (LuGre) model . . . . .	74
4.5.2.4	Friction model selection . . . . .	76
4.6	Tension-compression model . . . . .	77
4.6.1	Elastic stiffness of a single wire (decoupled) . . . . .	78
4.6.2	Warp/weft wire interaction . . . . .	82
4.6.2.1	Contact force . . . . .	83
4.6.2.2	Effective stiffness . . . . .	89
4.6.2.3	Effective Poisson's ratio . . . . .	91
4.6.2.4	Linearised mechanical properties . . . . .	94
4.6.2.5	Orthotropic effective properties . . . . .	98
4.7	Shear model . . . . .	99
4.7.1	Lubkin's theory . . . . .	100
4.7.2	Lubkin's function approximation . . . . .	102
4.7.3	Solution for elastic spheres in contact . . . . .	104
4.7.4	Solution for elastic cylinders in contact . . . . .	106
4.7.5	Torque-rotation hysteresis loop and damping loss factor . .	110
4.8	Out-of-plane bending model . . . . .	115
4.9	Conclusions . . . . .	119
<b>5</b>	<b>Numerical modelling</b>	<b>121</b>
5.1	Introduction . . . . .	121

---

5.2	ANSYS finite element package . . . . .	122
5.3	Element formulation . . . . .	124
5.3.1	Solid elements . . . . .	125
5.3.2	Contact elements . . . . .	127
5.4	Meshing . . . . .	129
5.5	Boundary conditions and loads . . . . .	132
5.6	Results . . . . .	133
5.6.1	Tension model . . . . .	133
5.6.2	Shear model . . . . .	139
5.6.2.1	Sphere-to-sphere torsional friction . . . . .	140
5.6.2.2	Cylinder-to-cylinder torsional friction . . . . .	141
5.6.2.3	Wire-to-wire torsional friction . . . . .	144
5.6.3	Out-of-plane bending model . . . . .	146
5.7	Conclusions . . . . .	149
<b>6</b>	<b>Reduced order finite element model</b>	<b>151</b>
6.1	Introduction . . . . .	151
6.2	Model order reduction techniques . . . . .	152
6.2.1	Homogenization method as a physical coordinate reduction	153
6.3	Reduced element formulation . . . . .	155
6.3.1	SHELL281 . . . . .	156
6.3.2	BEAM188 . . . . .	158
6.3.3	Coupling and role of different elements . . . . .	159
6.4	MATLAB-ANSYS algorithm . . . . .	162

---

6.4.1	Main script . . . . .	162
6.4.2	MATLAB post-processing . . . . .	163
6.4.2.1	Convergence criteria . . . . .	165
6.4.3	ANSYS APDL subroutines and restart solution . . . . .	166
6.5	Reduced model validation . . . . .	167
6.5.1	Single RUC . . . . .	167
6.5.1.1	Tension . . . . .	167
6.5.1.2	In-plane shear . . . . .	171
6.5.2	Mesh material plate . . . . .	174
6.5.3	Experimental validation from bias-extension test . . . . .	176
6.6	Conclusions . . . . .	180
<b>7</b>	<b>Application: design of a damping device</b>	<b>181</b>
7.1	Introduction . . . . .	181
7.2	Design concept of mesh friction dampers . . . . .	181
7.2.1	Cylindrical damper . . . . .	182
7.2.1.1	Torsional configuration . . . . .	182
7.2.1.2	Linear configuration . . . . .	185
7.2.2	Sinusoidal plate damper . . . . .	187
7.2.2.1	Squeeze damper . . . . .	189
7.2.2.2	Mesh material constrained layer damper . . . . .	190
7.3	Conclusions . . . . .	192
<b>8</b>	<b>Conclusions and future work</b>	<b>194</b>
8.1	Overall conclusions . . . . .	194
8.2	Main contributions from this work . . . . .	196
8.3	Suggestions for future further work . . . . .	198
	<b>Bibliography</b>	<b>213</b>
<b>A</b>	<b>MATLAB main script</b>	<b>214</b>

# List of Figures

1.1	Non-ordered mesh materials: example of tangled metal wire device.	2
1.2	Basic weaving patterns: (a) plain, (b) twill and (c) satin. . . . .	4
1.3	Woven materials: example of plain-weave mesh material. . . . .	5
3.1	Geometry of plain-weave mesh materials. . . . .	30
3.2	Longitudinal undulation of the wires: (a) original image acquisition, (b) Fourier series data fitting, and (c) comparison between three-harmonic Fourier series and sinusoidal curve (the z-axis is scaled twice). . . . .	32
3.3	Aperture detection method: (a) original image and (b) processed image. In (b) the detected plain-weave pattern is represented by the blue grid. . . . .	33
3.4	Frequency distribution of aperture and fitted normal distribution for <i>Sample 1</i> (a), <i>Sample 2</i> (b), and <i>Sample 3</i> (c). . . . .	35
4.1	Normalised difference in deflection between Timoshenko and Euler-Bernoulli beam theory for a tip-loaded cantilever beam at various slenderness ratios. . . . .	46
4.2	Normalised difference in contact area between JKR and Hertz theory for two crossed cylinders at various contact forces. . . . .	63
4.3	Ratio of Hertzian contact area to radius of curvature for two crossed cylinders at various contact forces. . . . .	64

4.4	Representation of the contact surface on a microscopic scale: the cross-section appears as a multitude of asperities that interlock each other only in a small portion of the surface (red circles). . . . .	67
4.5	Coulomb's micromechanical friction model: (a) contact surfaces defined by a periodic profile and (b) free-body-diagram for a single asperity. . . . .	68
4.6	Coulomb model combined with different other friction models: (a) pure Coulomb, (b) Coulomb + stiction, (c) Coulomb + Stribeck, (d) Coulomb + Stribeck + viscous . . . . .	71
4.7	Dahl friction model response: friction force as a function of displacement in non-dimensional coordinates at various $\alpha$ . . . . .	74
4.8	Lu-Gre friction model: representation of the contact surfaces as a series of bristles. For simplicity, the bristles on the lower body are represented as rigid. . . . .	75
4.9	Boundary conditions of a single wire: (a) pin-roller supported beam and (b) roller-roller supported beam. . . . .	78
4.10	Stiffness and strain of a single wire at various $\psi$ . . . . .	80
4.11	Schematisation of plain-weave RUC under biaxial tension. . . . .	82
4.12	Diagram of warp wire with loads and boundary conditions. . . . .	83
4.13	Kinematics of RUC under tensile load. . . . .	85
4.14	Contact force as a function of total tension force $P_{(x+y)}$ . . . . .	88
4.15	Effective stiffness of RUC. . . . .	90
4.16	Force-displacement curve for the RUC (solid line) and a decoupled wire (dashed line). . . . .	91
4.17	Effective Poisson's ratio of RUC. . . . .	94
4.18	Comparison between non-linear and linearised response to tension (non-linearity is emphasized for better clarity). . . . .	96

4.19	Linearised effective properties: (a) stiffness and (b) Poisson's ratio.	97
4.20	Sphere-to-sphere frictional torque: slipping and sticking zone of contact area. . . . .	100
4.21	Lubkin's function approximation. . . . .	103
4.22	Non-dimensional torsional moment. . . . .	105
4.23	Solution for two spheres. . . . .	105
4.24	Warp/weft intersection: in the proximity of the contact area (red circle) the surface of the wires can be approximated to a straight cylinder. . . . .	106
4.25	Elliptic contact area under frictional torsion. . . . .	108
4.26	Rotation of the wires around their common normal: starting from an initial position $\theta_i$ at rest, wire A is twisted by an angle $\beta$ with respect to wire B. . . . .	111
4.27	Torque-rotation hysteresis loop for a cylinder-to-cylinder contact in non-dimensional coordinates. . . . .	113
4.28	Calculation of the loss factor: (a) dissipated energy and (b) stored strain energy. . . . .	114
4.29	Schematisation of RUC as two crossed Timoshenko beams: 1-A-2 = warp wire, 3-B-4 = weft wire. . . . .	115
5.1	ANSYS SOLID187 element nodes: I through L represent the corner nodes, whereas M through R represent the mid-side nodes. . . . .	126
5.2	Local mesh refinement: in the circle a close-up image of the contact area, showing the high density of elements. . . . .	130
5.3	Contact mesh refinement demonstrating an asymptotic convergence for (a) the relative error and (b) the contact penetration. . . . .	130
5.4	Effect of contact stiffness factor on numerical results. . . . .	132

---

5.5	3-D FE model with boundary conditions used to represent the analytical tension model. . . . .	134
5.6	FEM and analytical results for S01: contact force versus total tension load for (a) steel against steel, (b) Nitinol against Nitinol and (c) Nitinol against steel. . . . .	136
5.7	FEM and analytical results for S02: stiffness and Poisson's ratio for (a)-(b) steel against steel, (c)-(d) Nitinol against Nitinol and (e)-(f) Nitinol against steel. . . . .	138
5.8	Load history for shear model validation. . . . .	139
5.9	Boundary conditions and loads for S03. . . . .	140
5.10	FEM and analytical results for S03. . . . .	141
5.11	FEM boundary conditions and loads for S04: initially perpendicular cylinders. . . . .	142
5.12	FEM and analytical results for S04: (a) steel against steel, (b) Nitinol against Nitinol and (c) Nitinol against steel. . . . .	143
5.13	FEM boundary conditions and loads for S05: initially perpendicular wires. . . . .	144
5.14	FEM and analytical torque-rotation response for S05. . . . .	145
5.15	3-D FE model and boundary conditions for the out-plane bending model. . . . .	146
5.16	FEM and analytical results for out-of-plane bending model: (a) steel against steel, (b) Nitinol against Nitinol and (c) Nitinol against steel. . . . .	148
6.1	Example of reduction technique adopted. . . . .	155
6.2	ANSYS SHELL281 element nodes: I through L are the corner nodes, whilst M through P are the mid-side nodes. . . . .	157

6.3	BEAM188: geometry and nodes. . . . .	159
6.4	Reduced beam-shell element: a shell surrounded by 8 beams along the perimeter. Shell nodes are in letters (I through P) and beam nodes are in numbers (1 through 12). . . . .	160
6.5	Logical scheme of the MATLAB-ANSYS algorithm for the i-th iteration. . . . .	164
6.6	Deformed reduced FEM: load and BCs for uniaxial tension of a single RUC. . . . .	168
6.7	Reduced FEM and analytical results: contact force of a single RUC for (a)-(b) steel against steel, (c)-(d) Nitinol against Nitinol and (e)-(f) Nitinol against steel. . . . .	169
6.8	Reduced FEM and analytical results: linearised effective properties of a single RUC for (a)-(b) steel against steel, (c)-(d) Nitinol against Nitinol and (e)-(f) Nitinol against steel. . . . .	170
6.9	Deformed reduced FEM of a single RUC for (a) pure shear and (b) $\pi/4$ transformed shear. . . . .	172
6.10	Reduced FEM validation: pure shear of a single RUC for (a) steel against steel, (b) Nitinol against Nitinol and (c) Nitinol against steel. . . . .	173
6.11	Reduced FEM results: load and BCs for uniaxial tension of a 10x10 mesh material plate. . . . .	174
6.12	Reduced FEM contact force results: 10x10 mesh material plate under uni-axial tension. The numbers in blue are computed with the reduced model, whereas the numbers in black are computed with the full model. . . . .	175
6.13	Contact force relative error between reduced and full model for a 10x10 mesh material plate. . . . .	176
6.14	3-D model of the bias-extension mesh material plate. . . . .	177

---

6.15	Comparison between numerical and experimental bias-extension test results for (a) 1mm, (b) 5mm, and (c) 10mm uniaxial displacement. . . . .	179
7.1	3-D model of the damper under deformation. (a) Step 1: axial pre-tensioning of the device. The numbers in black represent the contact forces for the elements of the corresponding row. The deformation is scaled 50 times to enhance the radial shrinkage of the weft wires due to the effective Poisson's ratio. (b) Step 2: the twisting of the shaft causes a uniform shear strain on the elements.	183
7.2	Torque-rotation hysteresis loop for the torsional damper with a pre-tension of 0.08mm. . . . .	184
7.3	3-D model of the cylindrical linear damper. (a) Underformed model. (b) Shape after deformation (results are scaled 10 times). . . . .	185
7.4	Hysteresis loop for the cylindrical linear damper. . . . .	186
7.5	Variation of maximum torque reaction and shear strain for a single element along the z-axis. . . . .	187
7.6	3-D model of the sine plate damper. . . . .	188
7.7	Boundary conditions and loads for the sine plate squeeze damper.	189
7.8	Force-displacement hysteresis loop for the sine plate squeeze damper.	190
7.9	Boundary conditions and loads for the mesh material constrained layer damper. . . . .	191
7.10	3-D model of the mesh material constrained layer damper after deformation. . . . .	192
7.11	Force-displacement hysteresis loop for the mesh material constrained layer damper. (a) Results for a pre-tensional contact force of 20N. (b) Comparison of hysteretic response for different level of pre-tension in normalised coordinates. . . . .	192
8.1	NASA spring tire. . . . .	200



# List of Tables

3.1	Geometry of different PWMM samples. . . . .	31
3.2	Mechanical properties of stainless steel. . . . .	37
3.3	Mechanical properties of Nitinol 60 (60NiTi). . . . .	38
4.1	Slenderness ratio for different PWMM samples. . . . .	45
4.2	Friction coefficient for the different material combinations. . . . .	77
4.3	Wire properties. . . . .	81
5.1	Ratio $a/h$ , number of elements and nodes, and solution time for various element sizes. . . . .	131
5.2	Normal load for the different material combinations. . . . .	142
6.1	Properties of mesh material employed in the experimental validation. . . . .	177
7.1	Loss factor and dissipated energy per unit area at various levels of pre-tension. . . . .	184
7.2	Material properties and geometrical dimensions of the sinusoidal plate damper. . . . .	188
7.3	Loss factor and dissipated energy per unit area at various levels of pre-tensional contact force. . . . .	191

# List of symbols

Symbol	Description	Unit
<i>Mesh material geometry</i>		
$w$	Aperture	mm
$d$	Diameter of wires	mm
$L$	Longitudinal semi-wavelength of wires	mm
$Z$	Amplitude of wires	mm
$A$	Cross-section area of wires	mm <sup>2</sup>
$I$	Second moment of area of wires	mm <sup>4</sup>
$\psi$	Waviness ratio	-
<i>Constitutive material properties</i>		
$E$	Young's modulus	GPa
$G$	Shear modulus	GPa
$\nu$	Poisson's ratio	-
$\rho$	Density	kg/m <sup>3</sup>
<i>Beam theories</i>		
$N$	Internal normal force	N
$V$	Internal shear force	N
$M$	Internal bending moment	N·mm
$q$	Transverse distributed load	N/mm

$P$	Transverse concentrated load	N
$\tilde{K}$	Timoshenko's shape coefficient	-
$w$	Transverse deflection	mm

### ***Energy based methods***

$W_e$	Real external work	J
$U_i$	Real strain energy	J
$W_{e,v}$	Virtual external work	J
$U_{i,v}$	Virtual strain energy	J
$N, V, M$	Real internal forces	N, N, N·mm
$N', V', M'$	Virtual internal forces	N, N, N·mm
$\{P\}$	Real external forces vector	N
$\{P'\}$	Virtual external forces vector	N
$\{\delta\}$	Real displacements vector	mm
$\{\sigma\}$	Real stresses vector	N/mm <sup>2</sup>
$\{\sigma'\}$	Virtual stresses vector	N/mm <sup>2</sup>
$\{\epsilon\}$	Real strains vector	-
$\{\epsilon'\}$	Virtual strains vector	-
$\chi$	Inverse of Timoshenko's coefficient	-

### ***Contact mechanics***

$R', R''$	Principal relative radii of curvature	mm
$\theta$	Angle between principal axes of contact surfaces	rad
$h$	Separation between contact surfaces	mm
$R$	Effective radius of curvature	mm
$E^*$	Effective elastic modulus	MPa
$P$	Contact compressive load	N
$a$	Radius/semi-major axis of contact area	mm
$b$	Semi-minor axis of contact area	mm
$\sigma\{r\}$	Contact normal pressure distribution	N/mm <sup>2</sup>
$e$	Eccentricity of contact area	-

$K(e), E(e)$	Complete elliptic integrals of first and second kind	-
$a_0, a_1$	Hertzian and actual contact radius in JKR theory	mm
$U_T$	Total energy	J
$U_E$	Stored elastic energy	J
$U_S$	Surface energy	J
$\gamma$	Adhesion energy	mJ/m <sup>2</sup>

### ***Friction modelling***

$F_N$	Normal contact force	N
$F_T$	Tangential contact force	N
$\mu$	Friction coefficient	-
$F_{fr}$	Friction force	N
$F_C$	Coulomb friction force	N
$F_S$	Static friction force	N
$\sigma$	Dahl's tangential stiffness	N/m
$\alpha$	Dahl's microslip coefficient	-
$\dot{x}$	Relative sliding velocity	m/s
$\dot{x}_s$	Stribeck velocity	m/s
$z$	Lugre's bristles deflection	m
$\sigma_0$	Lugre's bristles elastic stiffness	N/m
$\sigma_1$	Lugre's damping coefficient	N·s/m
$\sigma_2$	Lugre's viscous coefficient	N·s <sup>2</sup> /m

### ***Analytical modelling***

$P_x$	Tension force along the warp wire	N
$P_y$	Tension force along the weft wire	N
$P_{(x+y)}$	Variable sum of the tension forces	N
$u_x$	Longitudinal deformation of warp wire	mm
$u_y$	Longitudinal deformation of weft wire	mm
$\epsilon_x$	Normal strain of warp wire	mm
$\epsilon_y$	Normal strain of weft wire	mm

$w_{warp}$	Mid-span deflection of warp wire along z-axis	mm
$w_{weft}$	Mid-span deflection of weft wire along z-axis	mm
$w_C$	Displacement of contact point along z-axis	mm
$\delta_H$	Hertzian normal deformation at contact area	mm
$F_n$	Warp/weft contact force	N
$k_L$	Stiffness of a decoupled wire	N/mm
$k_C$	Contact force stiffness term	N/mm
$K_{eff}$	Effective stiffness of RUC	N/mm
$\nu_{eff}$	Effective Poisson's ratio of RUC	-
$\bar{K}$	Linearised stiffness of RUC	N/mm
$\bar{\nu}$	Linearised Poisson's ratio of RUC	-
$C_1, C_2, C_3$	Castigliano's coefficients for PWMM	mm/N
$\mathfrak{M}$	Torsional moment from in-plane shear	N·mm
$\beta$	Angle of twist between wires	rad
$\tau\{r\}$	Contact shear stress distribution	N/mm <sup>2</sup>
$a^*$	Stick region radius within contact area	mm
$k'$	Ratio between stick region and Hertz contact radius	-
$F(k', \phi)$	Incomplete elliptic integral of first kind	-
$E(k', \phi)$	Incomplete elliptic integral of second kind	-
$\phi$	Amplitude angle of the elliptic integral	rad
$A, B, \mathcal{L}$	Lubkin's function approximation coefficients	-
$F_1(e)$	Corrective factor for elliptic contact	-
$R_e$	Equivalent radius of contact	mm
$\mathcal{L}$	Torsional compliance fitting coefficient	-
$L_e$	Circumference of the ellipse of contact	mm
$\eta$	Damping loss factor	-
$\mathfrak{B}$	Out-of-plane bending coefficient	mm/N

# List of acronyms

5HS	5-Harness Satin
AAVE	Absolute Average Relative Error
APDL	ANSYS Parametric Design Language
BCC	Body-Centred Cubic
CAD	Computer-Aided Design
CLD	Constrained Layer Damper
CSV	Comma Separated Values
DIC	Digital Image Correlation
DOF	Degree Of Freedom
EAM	Element Array Model
FE	Finite Element
FEA	Finite Element Analysis
FEM	Finite Element Model
FRC	Fibre-Reinforced Composite
GPL	General Public License
GUI	Graphic User Interface
MOR	Model Order Reduction
MR	Metal Rubber
MRP	Metal Rubber Particle
NOL	Naval Ordnance Laboratory
NOMM	Non-Ordered Mesh Material
OMM	Ordered Mesh Material

PBC	Periodic Boundary Condition
PCG	Preconditioned Conjugated Gradient solver
PDE	Partial Derivative Equation
PVW	Principle of Virtual Work
PWMM	Plain-Weave Mesh Material
RUC	Repeating Unit Cell
RVE	Representative Volume Element
SAM	Slice Array Model
SFD	Squeeze Film Damper
TMW	Tangled Metal Wire





# Chapter 1

## Introduction

The presence of vibrations in mechanical systems is often undesirable. For this reason, the proper design and selection of damping element is fundamental to the correct operation and functionality of machines. Friction mesh materials have gained popularity as damping solutions especially in aerospace and defence industry, thanks to their simplicity, low cost, high amount of energy dissipated and the advantage of a large applicability to different environments. Due to their non-linear behaviour and the associated complexities, currently the relative mathematical models are limited to simplified geometries and highly reliant on test data. For this reason, a deeper understanding of the physics at the base of their behaviour is required in order to be able to fill these existing knowledge gaps.

### 1.1 Mesh materials

#### 1.1.1 Non-ordered mesh materials

With the term *non-ordered mesh materials* (NOMMs) the author refers to all the mesh materials characterised by a certain level of randomness in the structure that does not allow to identify a precise pattern for the wires.



**Figure 1.1:** Non-ordered mesh materials: example of tangled metal wire device.

Many non-ordered mesh materials used for energy dissipation are manufactured from a single metal wire that is initially coiled into an elastic spiral, then stretched and finally compressed. This material is referred to by several interchangeable names, including tangled metal wire (TMW), knitted mesh, or metal rubber (MR) for its high elasticity and mechanical characteristics that are similar to those of rubber [1]. MR can be fabricated in different shapes such as cylindrical, ring-shaped [2] or spherical [1, 3] (in this case it is referred to as metal rubber particles, MRP). In Figure 1.1 an example of a ring-shaped metal rubber is illustrated.

### 1.1.2 Ordered mesh materials

As opposed to the previous category, *ordered mesh materials* (OMMs) are organised in a precise pattern of connected wires that repeats periodically. This characteristic lends itself to a mathematical description of the repeating architecture for a subsequent development of analytical models, as will be discussed in the next chapters.

Ordered mesh materials are commercially available in a range of different shapes and dimensions for diverse applications, such as filtration, screening, acoustic attenuation (silencers), surgical mesh for tissue repairing, etc. They can be

subdivided into different categories according to their pattern and method of junction between the wires:

- i) Woven.
- ii) Knitted.
- iii) Braided.
- iv) Bonded (welded, expanded and electroformed).

In woven materials, the wires are typically interlaced following two main orthogonal directions, whereas in knitted materials the wires follow a loop path, interlacing the adjacent wires with each loop. In braided materials, three or more yarns are interlaced together so that they cross each other forming a diagonal pattern.

Excluding the case of bonded junction, where the connection does not allow a relative motion between the wires, these materials are characterised by a series of frictional contact points in every intersection between the wires, which are activated when the system is being dynamically excited resulting in energy dissipation in the form of Coulomb damping.

According to the Coulomb friction model, the quantity of dissipated energy mostly depends on the normal contact forces at the intersections and the friction coefficient between the surfaces. Moreover, increasing the number of contact points corresponds in general to an increase in the surface friction mechanics and hence results in a higher amount of energy dissipation (i.e. higher damping and loss factor). Under this perspective, ordered mesh materials offer a highly tunable solution for damping, whose response can be tailored by acting on the geometry of the mesh and on the material of the wires, for example combining different materials in order to produce a directional preference for stiffness and damping. Considering metal as constituent material for the wires, OMMs have also the advantage of being resistant to extreme temperatures, peculiarity that makes them

particularly suitable to severe environments, as aforementioned, as compared to viscoelastic materials. Additionally, while used as dampers, they can also find application as primary structural elements in withstanding potentially high intensity loads.

### 1.1.2.1 Woven and plain-weave mesh materials

A woven structure is composed of a set of longitudinal (i.e., warp) and transverse (i.e., weft or fill) wires that interlace each other according to a precise scheme. They can be subdivided into several categories based on the weaving pattern. The three basic ones are the following:

- i) Plain.
- ii) Twilled.
- iii) Satin.

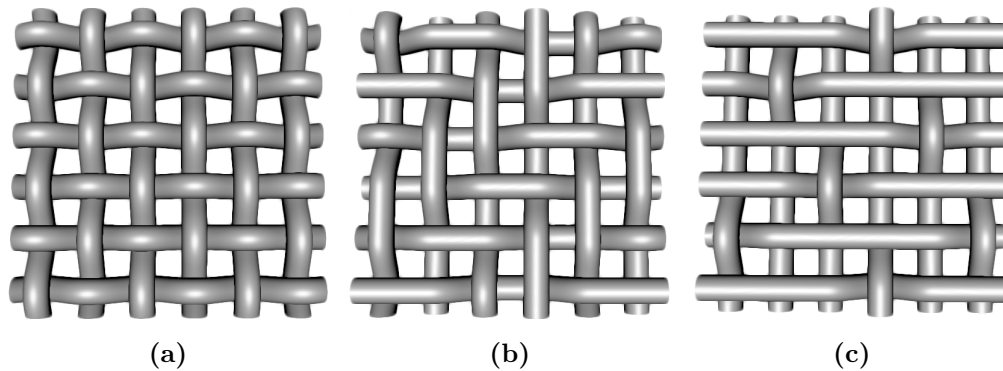


**Figure 1.2:** Basic weaving patterns: (a) plain, (b) twill and (c) satin.

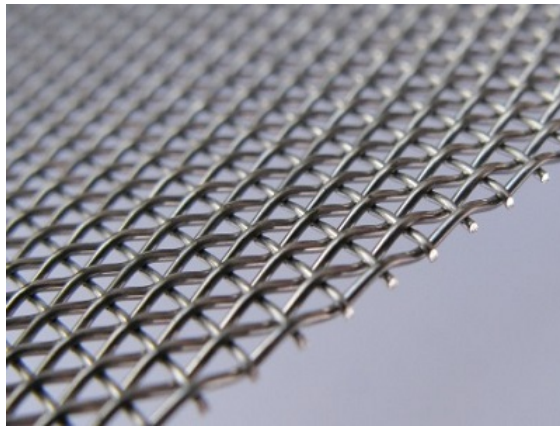


**Figure 1.3:** Woven materials: example of plain-weave mesh material.

Probably the simplest and most elementary form of woven structure is the plain-weave, where warp and weft wires interlace over and under each other in alternate order, as illustrated in Figure 1.2a. Because of its highest level of tightness among the different woven patterns [4], this type of structure is particularly stable and strong and for this reason is often employed in the manufacturing of woven technical fabrics [5]. In Figure 1.3 an example of stainless steel plain-weave mesh material is illustrated.

In the twill-weave, each weft wire floats over at least two warp wires before crossing the weave plane and interlacing under the wires again. This results into diagonal lines which are visible when observing the structure from the top, as shown in Figure 1.2b.

In the satin-weave, each weft wire floats over several (three or more) warp wires before interlacing one. The intersection points are disposed so that they are not adjacent to each other. Therefore, contrarily to the twill-weave, no diagonal lines are formed. When applied to the manufacturing of fabrics, the satin-weave pattern results in a smooth and lustrous but less durable cloth. The satin-weave pattern is usually described by the number of harnesses, representing the total number of warp wires that each weft wire floats over and under before the pattern is repeated again. For instance, in a 5-harness satin (5HS), the weft wire floats over four warp wires before interlacing under one, as represented in Figure 1.2c.

As the number of harnesses increases, this leads to a greater distance between the intersections, thus reducing the stability of the structure.

The previous discussion on woven materials is intended as a brief introduction and it is far from being exhaustive. For a thorough description of the several other existing structures the author directs the reader to [6, 7].

Because of the wide diversity of existing OMMs, the focus of this work has been narrowed to plain-weave mesh materials (PWMMs). However, the methods adopted in this research can be also applied for extending the study of ordered mesh materials to different architectures other than plain-weave.

## **1.2 Aims and main contributions**

The main aims of this research are to develop the understanding of PWMMs behaviour through a detailed investigation on their physics and to describe their non-linear frictional response by means of a set of mathematical models. Another additional purpose is to provide with an effective software tool, even if at a concept stage, that can be used for the designing of mesh material damping applications.

The present research has produced the following five main contributions:

- i) Detailed investigation on PWMMs response through numerical analysis.
- ii) Development of a set of analytical models for the characterisation of PWMMs stiffness and damping behaviour:
  - a) Tension model.
  - b) In-plane shear model.
  - c) Out-of-plane bending model.
- iii) Development of a reduced order finite element model for PWMMs, also suitable for other typologies of architectures.

- iv) Incorporation of the reduced model into a developed MATLAB-ANSYS software.
- v) Designing of four different concept dampers for industrial applications.

The finite element analysis is aimed to provide a detailed understanding of the physics of PWMMs, in particular the frictional contact mechanics responsible for the highly non-linear behaviour of these materials.

Based on the information gathered through this in-depth investigation, a set of analytical models is developed for the characterisation of PWMMs, which is capable to describe the dependence of their stiffness and damping response on the numerous parameters involved. Numerical results are then used as a validation for the mathematical models.

A novel reduced order finite element model is proposed, based on the developed analytical models, that can be implemented in a finite element commercial code. The motivation for this is achieving a considerable reduction in the computational expense when studying large mesh materials. The reduced model is incorporated in a developed MATLAB-ANSYS software that allows to study different and more complex geometries. This is validated through direct comparison with the full FE model. Finally, the novel tool is utilised for the designing of four different concept mesh friction dampers.

### **1.3 Thesis layout**

Currently the study of mesh materials is limited to simplified geometries and the available mathematical models either do not account for the actual contact mechanics occurring at their intersections, or rely on empirical data. In this thesis, a deep investigation on PWMMs is carried out, motivated by these existing research gaps. The present thesis is articulated into eight chapters and one appendix.

In Chapter 2 a detailed literature review is conducted. This includes the current state of the art of mesh materials and their application as damping devices.

The main available analytical and numerical models and experimental studies are reviewed. Particular emphasis is given to the modelling of plain-weave pattern in textiles and fabric-reinforced composites.

In Chapter 3 the geometry of PWMMs is discussed, starting from the general concept of metamaterials, which is then applied for identifying a repeating pattern that characterises their architecture. The main geometrical parameters that describe their structure are defined and some assumptions are made supported by the results of a performed image analysis.

Chapter 4 presents the analytical models developed for the characterisation of PWMMs. Initially, the most common beam theories, contact theories for elastic materials and friction models are introduced. Then, the most suitable theories for the study of PWMMs are selected. Based on these, a set of three mathematical models (tension, in-plane-shear and out-of-plane bending model) is developed for describing the mechanical response of PWMMs.

In Chapter 5 a series of finite element models is developed for the validation of the analytical solutions through direct comparison with the numerical results. After a brief introduction on the available FE commercial codes, a detailed convergence study is performed showing how parameters such as FE meshing and contact stiffness affect the accuracy of the solution. Finally, a thorough validation of each analytical model presented in Chapter 4 is reported, showing a general good agreement with the numerical results.

Chapter 6 presents a novel reduced finite element model that is obtained by the incorporation of the developed analytical models, which is aimed to reduce the computational expense of the numerical simulations. The model is implemented in an integrated MATLAB-ANSYS environment for developing a tool useful in the design of mesh material applications. A validation of the reduced model is conducted by comparing the results with the theoretical solutions, with the full FE model and with previously acquired experimental data.

In Chapter 7 the developed MATLAB-ANSYS software is exploited into the designing of friction mesh material damping applications. Four concept solutions

are presented involving different geometries, materials and loads, and the hysteretic response to cyclic loading is reported.

Chapter 8 discusses the conclusions emerging from the research conducted in this thesis, also providing with a direction for future further research. Following is a bibliography of references.

# Chapter 2

## Literature review

### 2.1 Introduction

In this chapter, a thorough literature review is reported on previous studies concerning the behaviour of mesh materials. First, the available research about ordered woven mesh materials is discussed. From this, a significant knowledge gap is identified in the field, due to the almost complete absence of specific mathematical modelling for their mechanical behaviour. The discussion is therefore extended to non-ordered metal mesh materials. Similarities and differences with ordered mesh materials are highlighted and the main experimental studies and models for their characterisation are discussed. Then the focus of the literature interrogation is moved towards plain-weave structures in general, which are typical of stand-alone textiles and woven composites, and the previous theoretical and numerical studies on this topic are discussed.

### 2.2 Behaviour of mesh materials

#### 2.2.1 Ordered mesh materials

Currently, ordered mesh materials, especially in the plain-weave pattern, are commonly used for non-structural purposes such as air and water filtration, and for

this reason in the literature there is a sensible lack of studies aimed towards their mechanical characterisation, especially regarding the damping properties of this typology of structure. Note that, with the term *ordered mesh materials* the author refers to a specific category of materials in which, not only the wires are organised into a precise pattern, but also there is an aperture between adjacent wires. Moreover, the wires in these materials are typically homogeneous. These characteristics make them differ from textiles, that will be discussed as a separate category.

Lord *et al.* [8] experimentally investigated the stiffness and damping response of a plain-weave mesh material new type of damper. A cylindrical-shaped specimen of stainless steel composed of hundreds of intersections was analysed through electrodynamic shaker vibration tests at different excitation frequencies and displacement amplitudes, showing the high non-linearity of the material. The force-displacement hysteresis loop was analysed for various amplitudes and the vibrational loss factor was shown to be in agreement with the Coulomb damping theory for a wide range of frequency ratios.

Kraft *et al.* [9] performed a study for the characterisation of a metallic woven wire mesh under uniaxial tensile loading. Several stainless-steel twill-dutch specimens, with different angles of orientation with respect to the loading direction, were tested. It was found that the mechanical properties of the structure, such as stiffness, yield and ultimate strength, toughness, and elongation to rupture are strictly dependent on fibre orientation. The authors proposed an orthotropic constitutive model to describe the material, which allows the determination of the elastic modulus for any orientation even though it relies on the mechanical properties obtained from test data in the direction of the warp and weft wires.

Glatt *et al.* [10] proposed a mathematical model for the description of the geometry of woven metal wire meshes to be subsequently employed in a series of finite element simulations. Aim of the authors was to accurately represent the 3-D structure of wire meshes for improving the numerical computation of pressure drop across these materials when used as filters. The method consists into first defining the skeleton of the mesh, represented by the wire centreline in the unit cell, which

is in general composed of the combination of straight and sinusoidal portions. The maximum amplitude of the sine function is assumed as half height of the wires along the perpendicular direction. The cross-section of the wires is assumed as ellipsoidal. The structure is then represented analytically as a series of cylinders whose axes correspond with the wire skeleton. This analytical structure is finally discretised in a series of finite cubic elements referred to as voxels (volume cells). The choice of sinusoidal functions was shown to be in good agreement with the actual shape of the structure as confirmed by 3-D images of real meshes obtained through computer tomography. However, this mathematical model only provides a geometrical description of the mesh material, and it does not characterise its mechanical response.

### **2.2.2 Non-ordered mesh materials**

Although the object of this thesis is more specifically focused on ordered mesh materials, a review on the literature concerning non-ordered mesh materials is conducted, since the two categories share many analogies and the general principles governing their behaviour are believed to be the same, first and foremost their dependency on Coulomb friction [2, 8] and the mechanism involved in their mechanical response.

Non-ordered mesh materials range from a host of different names (e.g., tangled metal wire (TMW), metal rubber, knitted mesh). Their application as dampers has been studied since the 1970s and some of the typical fields for NOMMs are turbomachinery [11], spacecraft [12, 13], cryogenics [14] and sound absorption [15]. In other researches, the usage of mesh materials as ground-borne vibration isolation for high-precision instruments [16] or as impact loading protection against hazards of explosion [17] have also been proposed. The materials used for their fabrication are usually metals such as steel [12, 14, 18], aluminium [19], copper, titanium [20], nickel based alloys [21], and shape memory alloys [22].

The damping and stiffness dynamic response of NOMMs is non-linear with respect to strain amplitude [3, 8, 23, 24]. Typically, a softening (stiffness decrease)

is observed when the dynamic amplitude is increased. General agreement among researchers is that the response of these materials is highly dependent on the contact status and performance of adjacent wires, which can be either open (no contact), sticking, or sliding [1, 25]. Applying a cyclic loading to these materials results in both the stiffness and damping being dependent on the excitation amplitude. For lower excitation amplitudes, the stiffness remains approximately constant and damping is lower [3] because the response is highly dominated by the elastic deformation of the mesh material and the frictional component is negligible. This is due to the fact that most of the contacts are either in the open status and/or the contact force is too low to significantly affect the mechanical response. Increasing the dynamic amplitude, the average stiffness of the system drops [2] and this could be explained with the fact that a larger amount of contact points are now activated and a relative motion between them now occurs.

Nevertheless, there is a certain lack of consensus about the nature of energy dissipation and how it is manifested. Some researchers have shown in their experiments that, with the presence of oil, the mechanical properties do not change noticeably [18]. This has led some to the conclusion that the damping mechanism may not be Coulomb friction. Thereby, some have proposed models that involve the combined effects of Coulombic and viscous damping [26], and in some cases also Coulombic, viscous and hysteretic damping [23] to characterise their behaviour, although there is no physical evidence to justify the employment of these mechanisms other than as a descriptive mathematical instrument.

Some justification that Coulomb friction is present has been shown in recent experimental studies on NOMMs [2, 27] where it is demonstrated that the excitation frequency does not noticeably affect the damping response and the force-displacement hysteresis loop does not change significantly. In particular, in [2] as a result of a series of dynamic testing it was witnessed that the loss factor is not dependent on frequency of excitation in a range from 1 Hz up to 400 Hz, a characteristic which is in agreement with the classical Coulomb friction damping.

### 2.2.2.1 Experimental approaches

One of the first researchers to investigate these materials was Childs [12] who, in 1978, performed a series of bench tests on a wire mesh damper as a solution to the rotordynamic instability problem of the Space Shuttle fuel turbopump. Even though the test data were not published, he highlighted good vibration damping properties from the device. Rivin [28] in 1979 and Barnes [29] in 1984 investigated the usage of wire mesh as an aircraft engine mount with the function of a vibration isolator. They both suggested a relationship between the density and the stiffness of the wire mesh and also between the damping and the material of the wires. Okayasu *et al.* [30] in 1990 studied the application of a metal mesh bearing for the liquid hydrogen turbopump of the LE-7 engine as a solution to high vibration levels. By introducing this friction damper, the device was able to operate at its third critical speed of 46,139 RPM without stability problems.

Wang and Zhu [31] in 1997 proposed a damper replacement for squeeze film dampers (SFDs) that does not require the presence of fluid, describing it as a hollow cylinder built with woven metal mesh. They also tested the same rotordynamic rig both with SFD and with the new damper for comparison, concluding that the mesh material is able to control high level of unbalance thanks to its good vibration damping properties.

Zarzour and Vance [18] in 2000 studied a stainless steel mesh damper as a substitution of SFDs concluding that it is a valid solution to reduce the amplitude of vibration in rotordynamic systems. The experiments were conducted on a test rig reproducing a power turbine that was operated up to 7000 RPM, in order to exceed its first critical speed of 3200 RPM. It was shown that the damping coefficient of the metal mesh does not change significantly in a temperature range of 54-99°C unlike SFDs, which are based on viscous materials. Moreover, other benefits were witnessed, in particular the ability of the mesh material to operate when soaked in turbine oil without affecting its properties.

Al-Katheeb [23] in 2002 studied the influence on damping and stiffness of several operational parameters such as excitation amplitude and frequency, even-

tual presence of lubrication, and axial pre-compression. In 2003 Ertas *et al.* [14], with the aim of ascertain the feasibility of applying two metal mesh damper elements into a liquid hydrogen turbopump, investigated the stiffness and damping response of mesh materials at extremely low temperatures, typical of cryogenic turbomachines.

### 2.2.2.2 Modelling

Efforts have been spent in the attempt to characterise NOMMs through mathematical models, in order to understand the relationship between performance and the several parameters involved. The biggest complexity arises from the intrinsic stochastic nature of these materials, because of which a certain level of variability in the microstructure is witnessed even for nominally identical specimens [2].

A model for stiffness and damping was proposed by Zarzour [11], where the dynamic response of NOMMs is based on a hysteretic model. An equivalent modulus of elasticity is initially determined for the material from static force-displacement measurements and then this is utilised to calculate the stiffness for mesh elements of other dimensions. However this is limited to the assumption of same type of wire mesh under the same operational conditions. Regarding the characterisation of damping, similarly to the stiffness, this also relies on experimental data, obtained either from a logarithmic decrement or from shaker tests.

A stick-slip model was proposed by Al-Katheeb [23] that is based on the combination of viscous, hysteretic and Coulomb damping, even though the viscous damping is not from a certain source. According to this model, the mesh material is described as composed of various elements, each of them represented by a combination of a spring and a damper in parallel, connected through stick-slip friction joints. When the material is subjected to external excitation, the force increases until some of the joints are freed and start slipping, resulting in a lower equivalent stiffness and damping. The mass of each wire is considered insignificant compared to the overall system, and therefore ignored. The model allows to predict how the force-displacement response changes in a cylindrical mesh damper

for different radial thicknesses. However, it is still based on empirical results and on the assumptions of a linear variation of the stiffness with radial thickness and a constant friction force at every joint.

Given the numerous parameters involved in the determination of their behaviour, a very small number of constitutive models for NOMMs exists, which are based on a theoretical study at a microscopic level. The typical approach consists in the homogenisation of the material considered as composed of several representative volume elements (RVEs) or unit cells. Three are the main theories adopted for this purpose:

- i) Pyramidal friction cells [32].
- ii) Porous material theory [33].
- iii) Helical spring microelements [1, 34, 35].

Chegodaev [32] in 2000 developed a model based on pyramidal friction elements, that characterises the mechanism of energy dissipation through friction damping in NOMMs. The model provides the damping response based on the contact status and the angle of orientation of the pyramid elements with respect to the external load. Nevertheless, the mathematical model developed is rather complicated and based on several parameters, which makes its application quite inconvenient.

Li *et al.* [33] proposed a model based on porous material theory. The NOMM is assumed as an isotropic medium composed of several unit cells. Each cell has the form of a hollow cube delimited at the edges by cantilever beams. When subjected to a compressive load, the walls of the cell deform elastically. Based on the elastic beam theory only accounting for the bending contribution, the model provides a theoretical expression for the cell wall elastic modulus as a function of the geometrical dimensions and the material properties of the wires. However, the constitutive dynamic force-displacement relationship is still based on coefficients determined through a large amount of experimental tests.

Hong *et al.* [36] established a micromechanics mathematical model for characterising the damping behaviour of NOMMs, based on a single-helix spring microelement. The stiffness of each microspring is defined for the three different contact conditions (open, sliding, sticking) as a function of the material properties of the wires, the geometry of each helix spring and the friction coefficient between the materials (for the sliding status). A contribution ratio is defined that represents the number of elements in each state with respect to the total number of elements. Finally, the overall stiffness and damping response is calculated accounting for the different status of every single unit cell. However, given the complexity of the problem of friction being non-linear, a certain approximation is required to define the contribution ratio, which is assumed to vary linearly with the deformation, from the state of open contact to the sticking condition.

## 2.3 Plain-weave pattern in textiles and composites

As introduced previously, this work is focused on ordered mesh materials (OMMs) that follow a specific repeated nominal pattern. For this reason, it is possible to find an analogy with fabrics, which are often manufactured in the form of plain-weave pattern and have been widely studied both as stand-alone textiles and as reinforcement for composite materials.

However, although a similar overall pattern, the main difference between PWMMs and woven fabrics resides in the fact that, while mesh material wires are typically homogenous solids that can be easily described mathematically through continuum mechanics, in fabrics each individual strand or yarn is actually composed of several fibres that do not follow a precise ordered structure, with many of them protruding from the surface of the yarns. This particular composition makes them differ from conventional engineering materials in many aspects, first of all they are inhomogeneous and highly anisotropic [37]. Moreover, they are characterised by a large deformability since their longitudinal stiffness is typically very low in

comparison to most structural materials.

## **2.3.1 Modelling of woven fabrics**

### **2.3.1.1 Geometry**

Since the structure of fabrics is highly irregular, for its mathematical description some assumptions are necessarily required. The threads are usually idealised into simpler geometrical forms, representing the yarn longitudinal path and yarn cross-section.

One of the first extensive studies of textile mechanics was conducted by Peirce [38], who in 1937 proposed two geometric models for the description of plain-weave fabrics, by introducing the concept of repeating unit cell (RUC). Both the models are based on the assumption of infinite flexibility of yarns, so bending is considered as negligible. In the first theory, the yarn cross-section is assumed as circular and incompressible. Their longitudinal shape is considered as uniform and composed of a straight and circular segment, the latter in correspondence of the interaction with the orthogonal yarn. In his second theory, Peirce relaxed the assumption of yarn incompressibility to extend the model for describing more tight fabrics, where the longitudinal tension, from weaving, causes flattening of the threads at the intersections, leading to an elliptic cross-section. Nevertheless, since the usage of an elliptic cross-section would have led to complex formulations, Peirce chose to retain the same equations for the circular cross-section, by only replacing the diameter of the circle with the minor diameter of the ellipse.

Peirce’s model is generally suitable for open fabrics where the assumption of circular cross-section is acceptable. To overcome this limitation and extend the model to jammed structures, in 1958 a new model was proposed by Kemp [39] where the cross-section is represented by a “racetrack” shape, consisting of a rectangle enclosed by two semicircles at the sides. This allows to account for the flattening of threads, exploiting, at the same time, the simplicity of the circular cross-section.

A more general model was developed by Hearle and Shanahan [40] in 1978, which proposes a lenticular cross-section for the yarn and employs an energy method for the description of fabric mechanics. From this model, equations for the other two models (circular and race-track cross-section) can be easily derived. Thus, the Peirce's model can be thought as a special case of the Hearle's model.

### 2.3.1.2 Tension

The characterisation of woven fabrics under tensile load was studied by Weissenberg [41] that in 1949 proposed his "trellis" model, that was able to predict strains and stresses and their relationship. However, this theory was based on an over-simplified approach, where the yarns were described as inextensible and inflexible rods that were pinned at their intersections. Moreover, they were free of rotating around their joints, therefore neglecting the resistance from contact interaction. He also stated that the Poisson's effect is manifested when fabrics are subjected to tension, even though the determination of this parameter was only based on experimental results.

In the same year, Chadwick *et al.* [42] studied the bias of woven fabrics when subjected to a simple pull, showing that warp and weft yarns not only extend under the effect of tension but also change their orientation with respect to one another and to the direction of the force. However this model was still based on the simplified trellis model proposed by Weissenberg.

In 1963 Kilby [43] proposed a new trellis model to investigate the plane stress-strain relationship in fabrics. He showed that this model yields identical results with an anisotropic elastic lamina with zero Poisson's ratio when stretched along either warp or weft directions, contrarily to what observed experimentally in fabrics. To overcome this important limitation, he therefore suggested that fabrics should be treated as an anisotropic lamina with Poisson's effect and two planes of symmetry perpendicular to each other.

In 1980, Leaf [44] proposed three different models to characterise the response of plain-weave fabrics to tensile load. The first model describes small deflections

by employing the Castigliano’s theorem, whereas the second and the third theory attempt to capture large deflections by means of a force equilibrium and an energy method. However, this model was still based on an over-simplified approach, where the actual path of the yarns was replaced by a series of zig-zag pin-jointed trusses, therefore also neglecting the contact mechanics at the intersections.

### 2.3.1.3 Bending

For the modelling of bending behaviour of woven fabrics, the first work was the one of Peirce [45] who in 1930 proposed a novel methodology to measure the flexural rigidity of fabrics based on experimental observations. A new instrumental apparatus was designed to measure the droop angle of a specimen when a specific length is held out over an edge. By considering the fabric as a Euler-Bernoulli elastic beam, this angle can be converted into the *bending length*, that represents the length of the fabric that will bend under its own weight. Although this is a simplified formulation, it is based on the same fundamental principles that are still used nowadays for measuring the static bending rigidity of fabrics.

### 2.3.1.4 Shear

The modelling of shear in woven fabrics have been largely investigated and many researchers agree that the non-linear behaviour, especially in the first region, is the result of the combination of elastic deformation and friction [46–48]. Olofsson [46] in 1967 proposed a rheological model where the fabrics are represented as an assembly of several units disposed in series, each of them composed of an elastic and a frictional element in parallel. For a series of identical elements, the overall stress-strain relationship results into  $s = Ke^{1/2}$ , where  $s$  and  $e$  represent respectively the stress and the strain, and  $K$  is a fitting coefficient that is determined through non-linear regression techniques. This model can be used to capture both the shear and the bending of fabrics. However it is still a simplified model that does not explain the mechanics involved, but it is rather based on experimental coefficients.

It is of particular interest the work of Grosberg and Park [49] who in 1966 proposed a mathematical model for the characterisation of shear in fabrics that is based on the yarn contact mechanics. In this model, the single intersection of two perpendicular yarns is represented as two crossed beams. These, for small deflections are initially imagined as welded to each other at their intersecting points like in a trellis, so the initial shear force is only given by the elastic bending of the cantilever beams. When the shear force overcomes the friction resistance, the joints start slipping resulting in a non-linear response and hysteresis. The slippage starts from the outer boundary of the contact area and progressively increases towards the centre. The friction resistance is calculated from an analysis of the contact mechanics at the intersection. The longitudinal tension of yarns generates a normal contact pressure that is thought to be distributed triangularly along the contact area, with the peak in the centre. The total contact pressure can be found through the model introduced by Peirce [38]. Therefore, the frictional moment reaction is obtained by integrating the normal pressure distribution across the slipping portion of the area multiplied by the distance from the centre and the friction coefficient. This method is conceptually very similar to the one proposed by Lubkin [50] for the problem of two elastic bodies under frictional contact, which will be discussed in detail in Chapter 4 and employed for the characterisation of PWMs. Nevertheless the main difference is the oversimplified triangular distribution of normal pressure, which might be acceptable for textile materials, whereas it is not realistic for elastic isotropic solids in contact such as in the case of mesh materials.

### **2.3.2 Modelling of fibre-reinforced composites**

In the literature there are several mathematical models for the characterisation of fibre-reinforced composites (FRCs), where an interwoven fabric (generally kevlar or carbon fibre) is embedded in another softer material referred to as matrix (e.g., epoxy resin). This kind of woven reinforcement, besides guaranteeing a superior stiffness-to-weight ratio that is particularly advantageous for structural purposes, also increases the resistance to impact and cracking with respect to unidirectional

plies, and thus one of the possible applications for these materials is building bulletproof vests [51]. The main difference with respect to mesh materials is that in composite materials the slipping between strands is restrained by the presence of the matrix, so the analytical models usually do not take into consideration frictional damping, although they are helpful in understanding the mechanics of plain-weave.

One of the most known attempts to mathematically describe woven composites is the work of Ishikawa and Chou [52]. In 1989 they proposed three novel models based on the classical lamination theory for the characterisation of the thermoelastic response of woven fabrics. These models are: the *mosaic*, the *crimp* (or also *undulation*), and the *bridging* models. Each of the models employ some geometrical idealisations to represent the plain-weave RUC. The mosaic model simplifies the plain-weave as an assemblage of cross-ply laminates neglecting the undulation of the strands, whereas the crimp model considers the actual curvature of strands in the loading direction, yet neglecting the undulation of the weft yarns. The bridging model is an extension of the previous theories obtained as a combination of the crimp model with the mosaic model. Even though it attempts to capture the three-dimensional shape of the unit cell, it is still based on a simplified approach, by using weighted averages of the effective stiffness terms.

In 1992 Naik and Ganesh [53] proposed two analytical models for plain-weave composites that account for the undulation in both warp and weft directions. These are the *Slice Array Model* (SAM) and the *Element Array Model* (EAM). Both the models are based on the same mathematical representation of the yarn cross-section and longitudinal path, the latter described by a cosine shape function. In the first model, the RUC is subdivided into a certain number of slices along the loading direction. Each slice is then idealised as a four-layered laminate to calculate its elastic coefficients. Then the slices are assembled under isostrain conditions to obtain the effective properties of the composite. In the second model, the unit cell is discretised in both the loading and its perpendicular direction, resulting in a number of elements. These are then assembled in series or in parallel to calculate the mechanical properties of the composite lamina. This approach

however does not account for the actual orientation of each slide with respect to the plane of the lamina.

On behalf of NASA, R.A. Naik in 1994 proposed an analytical model [54] for the characterisation of woven and braided composites. The longitudinal path of the yarns is assumed as composed of alternated sinusoidal and straight portions, whereas the cross-section is considered lenticular and constant along the path. The yarns within the RUC are subdivided into several slices and the novelty is that the specific orientation of each slice with respect to the lamina plane is now accounted for. The calculation of the overall stiffness matrix is therefore based on the same simplified approach as in the previously mentioned models, consisting in a weighted average of the single slice matrixes, where the weight is the volume percentage of the slice with respect to the overall RUC volume. Moreover, the dissipative mechanisms occurring at the yarn interfaces are still not accounted for.

Boubaker *et al.* [55] proposed a discrete model for the description of plain-weave dry fabrics (i.e., not embedded in a matrix material) considering also the yarn-on-yarn frictional interaction. Each yarn is subdivided into a certain number of punctual masses connected through elastic extensional and flexural springs. The deformed shape of each yarn at equilibrium is assumed as periodic and described by a Fourier series. By employing the Timoshenko's beam theory, the interaction between weft and warp yarns is introduced considering each yarn as an elastic beam subjected to an axial load and periodic lateral forces, corresponding to the normal contact forces. The normal compression of yarns at the contact point, under the effect of the normal contact force, is also included by means of the law of Kuwabata [56]. The model also accounts for the frictional force exerted between the yarns, even though by employing the simplified linear equation of the Gralen model [57], which relies on experimental coefficients, and it is also limited to the case of longitudinal tension.

Regarding the finite element analysis of woven structures, it is worth mentioning the work done by the University of Nottingham, which developed TexGen [58], an open source software under General Public Licence (GPL) for the geometric modelling of textile structures. The software allows to create a 3-D model of the

fabric that is completely tailorable by choosing between several patterns of weaving or knitting, 3-D or 2-D weave, and combining different layers. In addition, the cross-section of the yarn can be changed specifying the yarn width, height (or thickness of the textile structure in the case of 2-D weave), number of fibres, density and other mechanical properties (such as Young's modulus and Poisson's ratio). TexGen also offers the possibility to perform the meshing of the model created and export it as a CAD file for a subsequent finite element analysis. This software has been employed as a modeller for several FE analysis of woven textile structures.

Lin *et al.* [59] studied a plain-weave unit cell of 150TB E-glass fabric subjected to compressive and pure shear loading. The yarns, which in fabrics are generally composed by a bundle of fibres, in this work are considered as an orthotropic solid body with a transversely-isotropic behaviour. For the compression model, the yarns were constrained between two compression platens. The lower platen was fixed, while the upper platen was controlled by a displacement load. The simulation accounted for the yarn-yarn and yarn-platen friction contact. From the results of the pure shear simulation it was shown that, for large angles of rotation, fabric locking occurs, resulting in lateral compression of the yarns. An additional test, accounting for the combination of compression and shear, showed how the shear resistance increases with the level of compression. Analogous analysis of woven fabrics under compression has been performed by Dixit *et al.* [60]. However in both the aforementioned articles, a stiffening behaviour was shown in the numerical results, contrarily to what expected from a friction based problem, suggesting that the non-linearity was probably due mostly to the large strain theory rather than friction at the contact interfaces.

Erool and Keef [61] conducted a series of finite element studies through LS-DYNA on a Kevlar S706 plain-weave fabric under tension. The numerical results were validated by comparison with previous experimental data. First, a tensile test was simulated on a single crimped yarn, which was modelled by describing its centreline with a cosinusoidal equation. The yarn was constrained at one end and a controlled displacement was applied to the opposite end with a very low

strain rate to simulate a quasi-static test. Then, under the assumption of same geometrical dimensions for warp and weft yarns, a plain-weave model was created by replicating, rotating and translating the single yarn multiple times. This fabric model was tested under uniaxial tension along the warp direction. The model also accounted for the friction contact between the yarns. A parametric study was performed by sensibly varying the friction coefficient, showing that this value does not affect the force reaction in the case of pure tension. To investigate the response of textiles to shear, a bias extension test was also performed on a fabric model in which the yarns were oriented at 45 degrees with respect to the loading direction. The results showed how the shear of plain-weave structures leads to rotation of the yarns. However the analysis was only limited to the kinematic response of the material and the dissipative mechanisms due to friction were not investigated.

## 2.4 Conclusions

In this chapter a thorough literature review on ordered mesh materials was conducted. It was shown that there is a significant gap in the research of ordered mesh materials and therefore is the purpose of the research presented in this thesis.

Only a few works have been specifically focused on this topic, whereas the majority of the literature pertaining mesh materials is oriented towards the non-ordered type. This type was also discussed for completeness since there is a similarity with ordered materials, since their non-linear stiffness and damping response is based, to some extent (except for the plasticity which is also believed to be responsible for some of the non-linearity in NOMMs), on Coulomb friction. Nevertheless, because of their stochastic nature, NOMMs characterisation is often obtained through fitting from experimental data rather than physics-based models.

Regarding the characterisation of plain-weave structures in general, most of the available mathematical models are related to textiles and fabric-reinforced

composites. For this reason the previous research in this specific field was deeply interrogated and the main existing models were discussed. Beside a general analogy in the overall plain-weave pattern, a fundamental difference between textiles and ordered mesh materials is immediately highlighted, being the microstructure of yarns highly irregular and inhomogeneous, contrarily to typical mesh material wires. It was shown that, despite in the textile mechanics research field some important contributions have been made for the characterisation of damping of plain-weave structures, they are mostly based on either experimental data or simplified equations that do not account for the actual contact mechanics occurring at the intersections.

Therefore, the aim of the present research work is to fill this current research gap, by developing the understanding of ordered mesh materials through a detailed investigation of the physics at the base of their mechanical behaviour, paying particular attention to the investigation of the wire-to-wire frictional contact mechanics.

# Chapter 3

## Material characterisation

### 3.1 Introduction

In this chapter, the material characterisation of PWMMs is discussed, both in terms of geometrical structure and constituent media.

The definition of metamaterial is initially introduced, explaining in particular the subcategory of mechanical metamaterials and the concept of repeating unit cell that will be adopted in this research.

For the subsequent development of analytical and numerical models, the geometry of PWMMs is analysed and some parameters are identified for its characterisation, based on the assumption of highly repetitive and periodic pattern. Three different commercially available samples of PWMM are identified and compared. A digital image analysis is performed on a selected set of samples, to investigate the longitudinal shape of the wires and validate the initial assumption of highly repetitive structure.

Finally, the importance of constituent materials for the wires is discussed. Two test case materials (i.e, stainless steel and Nitinol) are presented and their mechanical properties are reported.

## 3.2 Metamaterials

A metamaterial, also referred to as architected material, is in general an artificially structured material that exhibits properties that are different from its constituent materials, as suggested by its prefix "meta" (from the Greek word  $\mu\epsilon\tau\alpha$ , meaning "beyond") [62].

Although the term metamaterial is mostly associated to electromagnetism and optics phenomena that cannot be achieved naturally (e.g. negative refractive indices and invisibility cloaking), this concept of artificially designed materials can be extended to other areas of science such as classical mechanics, thermodynamics, and also quantum physics [63].

To narrow the focus on the object of this work, *mechanical metamaterials* [64] are designed media that can exhibit unique mechanical properties. These materials are typically periodic and composed of a micro or nanoscale repeating pattern often referred to as *repeating unit cell* (RUC). Their behaviour is originated on the geometry of the RUC (rather than the constituent materials alone), which can be engineered in order to achieve specific required properties. Their topology is often optimised to achieve a higher mechanical performance as compared to the constituent materials, such as a ultra-high strength to density ratio or a tunable stiffness, as for example extremal materials, which are highly stiff for specific modes of deformation and highly compliant for other modes. Certain types of mechanical metamaterials can sometimes manifest counter-intuitive properties, as in the case of *auxetic materials*. To this category belongs any material with a negative Poisson's ratio, meaning that when stretched, it expands in the direction perpendicular to the applied tension, instead of undergoing the natural shrinkage.

Following the same basic principle of metamaterials even though in a larger scale, in this work the plain-weave pattern is intended as one of the possible architectures for ordered mesh materials that can be tailored to elicit specific desired mechanical properties, in particular the ability to absorb and dissipate large amounts of energy for damping applications.

### 3.3 Geometry of plain-weave mesh materials

For the subsequent development of a series of analytical models, it is necessary to mathematically describe the geometry of PWMMs.

Recalling from Chapter 1, the plain-weave pattern is composed of a set of longitudinal (i.e., warp) wires, which are interwoven with transverse (i.e., weft or fill) wires, so that the wires alternate between going over and under each other. This structure can be therefore represented by identifying the longitudinal shape of each wire coupled with its cross-section and its relative position with respect to the other wires and within the mesh material.

Since the plain-weave structure is periodic and highly ordered, it is possible to identify some parameters that can be considered, in the first instance, as constant across the PWMM. A first overall general description of the mesh material geometry can be provided by the aperture  $w$ , which represents the dimension of the opening between two contiguous wires, therefore indicating the relative distance between the wires. The aperture is assumed to be equal in both warp and weft directions, so that each opening is nominally squared. This parameter is of particular interest for filtration purposes, since only solid particles smaller than the opening are allowed to cross the mesh, whereas the others are retained. Another descriptive parameter is the percentage of open area, calculated as the area of the openings over the total bulk area.

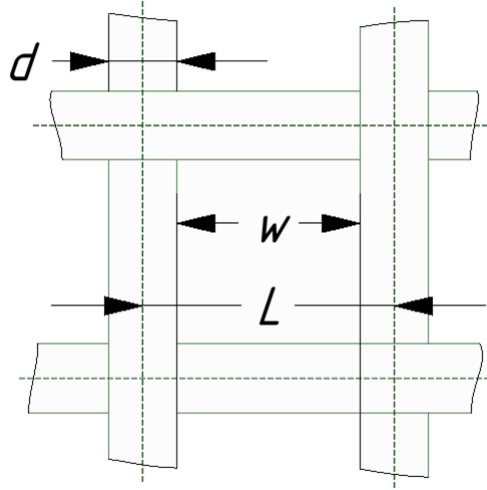


**Figure 3.1:** Geometry of plain-weave mesh materials.

The distance  $L$  between the centrelines of two adjacent wires is simply given by the sum of the wire diameter  $d$  and the mesh aperture as illustrated in Figure 3.1. This parameter also indicates the semi-wavelength of the wires as will be discussed later. The number of contact points per unit area is also an important characteristic of mesh materials, which gives information about their damping capability. In fact, the amount of dissipated energy through dry friction is strictly related to the number of intersections that are activated when the material is subjected to motion. It can be demonstrated that the number of contact points per unit area, for large meshes, tends to  $1/L^2$ . For the samples considered, the main geometrical parameters, the respective number of contact points per unit area, and the percentage of open area are reported in Table 3.1. .

Regarding the three-dimensional shape of the wires, their cross-section can be considered as circular and constant across the structure. For a plane sheet of mesh material at rest, the wires from a top view present as straight and parallel to each other, whereas from a side view they are characterised by a periodic undulation. For an exhaustive description of the geometry, an investigation on the longitudinal path of the wires is required, to find a mathematical shape function that can describe their vertical undulation. This will be performed through image analysis

Parameter	Symbol	Unit	Sample 1	Sample 2	Sample 3
Diameter of wires	$d$	mm	0.45	0.45	0.45
Aperture	$w$	mm	0.96	1.36	1.67
Semi-wavelength	$L$	mm	1.41	1.81	2.12
Contacts per unit area		$\text{cm}^{-2}$	50	30	22
Open area			46%	57%	62%

**Table 3.1:** Geometry of different PWMM samples.

and digital processing. Moreover, to validate the assumption of constant aperture, a statistical investigation is carried out by means of the same technique.

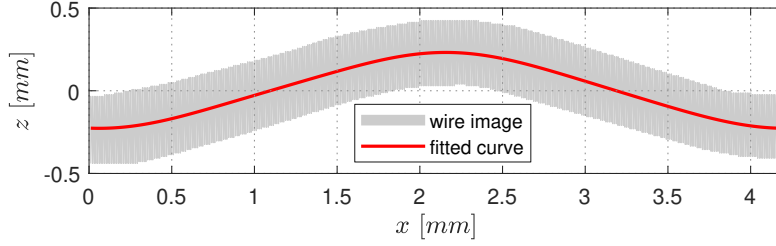
### 3.3.1 Image analysis

#### 3.3.1.1 Analysis of longitudinal path of the wires

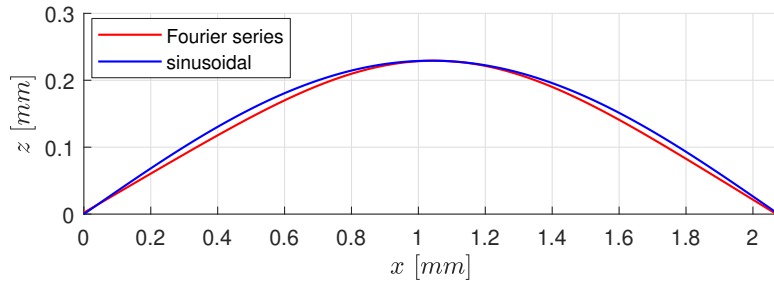
The method adopted for analysing the longitudinal shape of the wires required acquiring a side image of the mesh material, which was then analysed through digital processing. A mesh material sheet with the same dimensions of *Sample 3* from Table 3.1 has been chosen for the analysis. The sheet has been constrained between two metal plates to guarantee a flat shape of the mesh avoiding any out-of-plane bending of the material. In Figure 3.2a, a side image of the sheet is reported, which has been acquired through a Sony RX100 IV digital camera, which was oriented transversely to the plane of the mesh. The image has been subsequently digitally processed to remove the background.



(a)



(b)



(c)

**Figure 3.2:** Longitudinal undulation of the wires: (a) original image acquisition, (b) Fourier series data fitting, and (c) comparison between three-harmonic Fourier series and sinusoidal curve (the z-axis is scaled twice).

This procedure has been performed manually by means of a graphics software, since the effort to develop a dedicated algorithm in MATLAB revealed as cumbersome. Then the strand image has been converted into binary format. The procedure was performed in a single location of the mesh, under the assumption of same geometry for warp and weft wires and highly repetitive structure. The data has been fitted with a three-harmonic Fourier series through MATLAB, as shown in Figure 3.2b. From a comparison between the Fourier series and a sinusoidal function reported in Figure 3.2c, it is evident that the difference between the two curves is negligible, since the coefficient of the first harmonic (0.2216mm)

in the series is much greater than the one of the other harmonics (0.0022mm and 0.0078mm). Therefore, the longitudinal undulation of the wires can be considered as described by a monoharmonic sinusoidal function. This analysis, even though performed on a single sample, is supported by other previous experimental studies from the literature [10], also considering the high repeatability and the tolerances adopted in the mesh material manufacturing process [65].

### 3.3.1.2 Statistical investigation of mesh aperture

The previous general description of the PWMM geometry is based on the assumption of a constant aperture, which is representative of a highly repetitive and periodic structure. To validate this assumption, a statistical analysis of the aperture is performed to measure the level of uncertainty in this geometric dimension. The analysis has been performed for all the three material samples indicated in Table 3.1. Each specimen has been spray-painted in black colour in order to reduce the reflection and increase the contrast with respect to the background of the image.

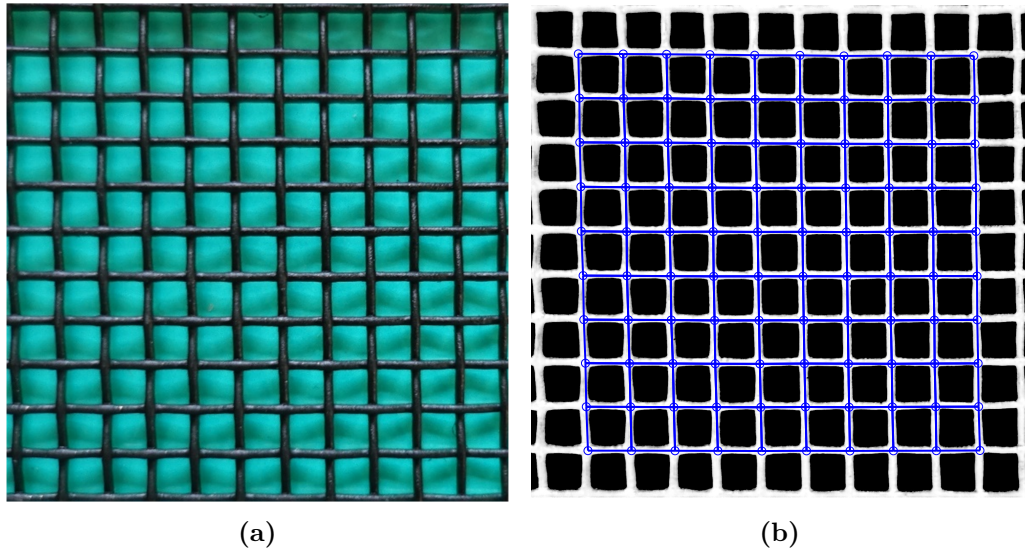
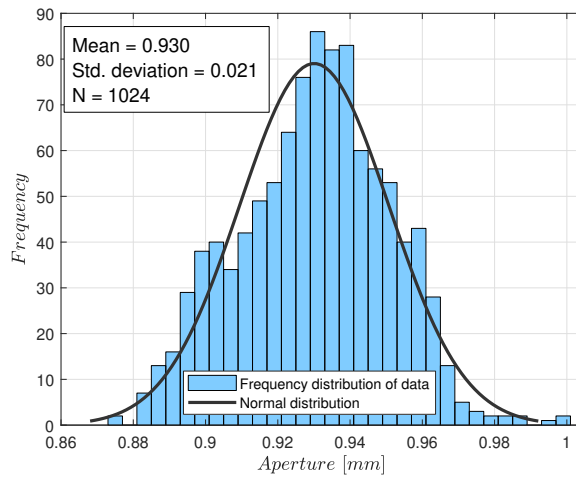


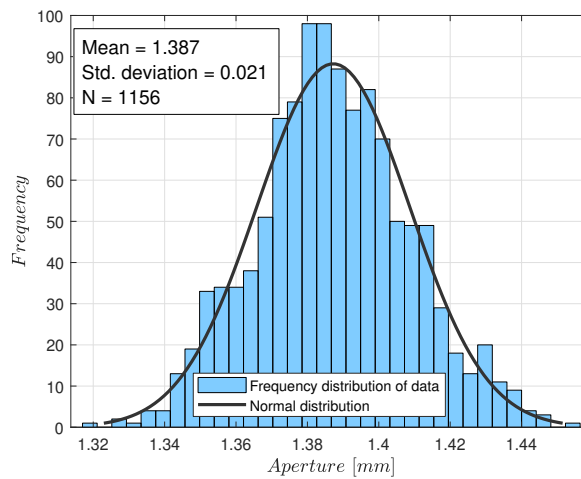
**Figure 3.3:** Aperture detection method: (a) original image and (b) processed image. In (b) the detected plain-weave pattern is represented by the blue grid.

After setting a green surface as the background, a digital image of the specimen, represented in Figure 3.3a, has been acquired by carefully positioning the camera normal to the plane of the mesh. An algorithm has been developed in MATLAB for the post-processing of the image data. The green background has been removed by adjusting the colour threshold. As in the case of the longitudinal path analysis, the image has been preliminarily converted into binary format and the colours have been inverted to obtain a complementary image. The first step of the algorithm consisted into finding the location of the mesh openings, corresponding to the black areas in the binary image. This was accomplished by employing the built-in MATLAB function *regionprops*, which is capable of performing measurements on binary images, such as detecting centroids of areas. Then, with the same method, the wire intersections are identified at the corners of each opening. The plain-weave pattern is then reconstructed by connecting all the intersection points, as represented by the blue grid in Figure 3.3b. The intersection coordinates are then used to calculate the average diagonal of each mesh cell, as the mean value of the two diagonals. From this value, the aperture is finally calculated for each opening.

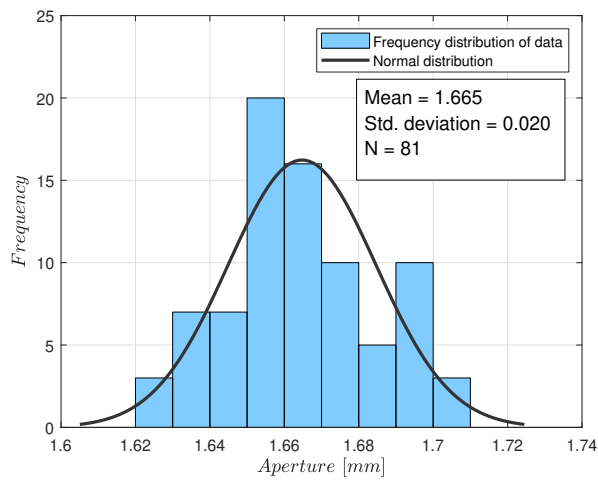
In Figure 3.4 the frequency distribution of the aperture calculated from the image data is plotted together with a fitted Gaussian function, showing a similar trend with the normal distribution for all the samples considered. For each case, the number  $N$  of openings analysed and the calculated average aperture and standard deviation are reported.



(a)



(b)



(c)

**Figure 3.4:** Frequency distribution of aperture and fitted normal distribution for *Sample 1* (a), *Sample 2* (b), and *Sample 3* (c).

For all the three samples, the calculated mean aperture is in agreement with the correspondent nominal value, with a higher relative error for *Sample 1* (Figure 3.4a) and *Sample 2* (Figure 3.4b) of respectively 3.12% and 1.99% , whereas *Sample 3* (Figure 3.4c) showed a higher accuracy with an error of 0.3% and a standard deviation of 0.020mm, corresponding to 1.2% of the average value. Moreover, the standard deviation is partially ascribable to the perspective of the original image, for which the wires appear slightly distorted in size as they are far from the centre of the picture.

The previous results indicate that the aperture can be considered as constant across the mesh material in the subsequent development of the analytical models.

## 3.4 Constituent materials

The mechanical response of mesh materials is also largely dependent on the constituent materials of the wires. This coupled with the wire geometry determine not only the overall stiffness behaviour of the mesh, but also the friction contact mechanics that is responsible for damping. Other important properties, are also strictly dependent on the wire material, such as density, hardness, plasticity, resistance to corrosion, thermal behaviour, et cetera. Although this research is based on the fundamentals for the PWMM mechanical response, where any Hookean based material can be implemented, two constituent materials are discussed and their mechanical properties are reported, which will be used throughout this research in the analytical and numerical models. At this stage, only the linear elastic properties are considered, whereas their friction behaviour will be discussed in Chapter 4.

### 3.4.1 Stainless steel

Woven mesh materials are largely commercially available in stain-steel for the high resistance to corrosion, toughness, strength and resistance to temperature variation [9], which makes them particularly suitable to water filtration, among the

other possible applications. Moreover, as discussed in Chapter 2, from numerous vibration experiments on metal mesh dampers (even though with a non-ordered structure), stainless steel was proved to be a highly reliable constituent material that guarantees almost constant damping properties for a large range of temperatures [18]. This characteristic is important when these materials are applied to extreme environments such as outer space.

Elastic modulus	$E$	GPa	200.00
Shear modulus	$G$	GPa	76.92
Poisson's ratio	$\nu$		0.30
Density	$\rho$	kg/m <sup>3</sup>	7,500

**Table 3.2:** Mechanical properties of stainless steel.

For this reason, stainless steel has been chosen as one of the possible constitutive materials for PWMs in this research. The mechanical properties for a standard stainless steel are reported in Table 3.2 and will be used in the following chapters.

### 3.4.2 Nitinol

Due to its unique mechanical properties and its frequent use in outer space application in recent years, Nitinol is also considered as a constituent material. This nickel-titanium alloy was discovered in 1959 by William J. Buehler of the U.S. Naval Ordnance Laboratory (NOL) and subsequently investigated by Buehler and Frederick E. Wang [66]. The material was named Nitinol by Buehler from its two main chemical elements and its place of discovery (**N**ickel **T**itanium **N**aval **O**rdnance **L**aboratory). One of the most notorious mechanical properties of Nitinol is undoubtedly its shape memory effect. While the material is in its martensitic phase, it can be plastically deformed and if heated above the martensite-austenite transition temperature, its shape reverts to the original one prior deformation [67]. The transition temperature varies based on the composition of the alloy. To permanently change the shape (also referred as training) of Nitinol, it is necessary to

increase its temperature to approximately 500°C while constraining the material to the desired position. In this austenitic phase, the material is restructured into ordered grains, where each nickel atom is surrounded by eight atoms of titanium, forming a body-centred cubic (BCC) lattice. Another unique property of Nitinol is its superelasticity, which permits the ability of elastically deforming to an extent that is much greater than the one of common materials. In particular, Nitinol can achieve a maximum elastic strain of more than 10%, whereas for stainless steel this value is typically around 0.3% [68].

For these unique properties together with its biocompatibility and a high resistance to corrosion, Nitinol has been employed in dental and biomedical industry, for instance in the manufacturing of stents [69]. The exploitation of Nitinol memory effect was also proposed for many aerospace applications, such as adaptive inlets and nozzles, variable geometry chevrons and variable camber fan blades, flaps, oil-lubricated bearings and gears [70]. Moreover, the engineers of NASA Glenn Research Center have recently developed a non-pneumatic shape memory tyre, composed of a Nitinol mesh of several interconnected helical coils, to be mounted on rovers [71].

Elastic modulus	$E$	GPa	95.00
Shear modulus	$G$	GPa	35.45
Poisson's ratio	$\nu$		0.34
Density	$\rho$	kg/m <sup>3</sup>	6,700

**Table 3.3:** Mechanical properties of Nitinol 60 (60NiTi).

Stiffness, hardness, density and other characteristics of Nitinol vary based on its composition and percentage of nickel with respect of titanium. The mechanical properties of 60NiTi [72], also referred to as Nitinol 60, containing 60% wt of nickel, are reported in Table 3.3. These properties will be used in the following chapters along with the ones of stainless steel. It is worth noting that, in this research, only a linear elastic behaviour of Nitinol is considered, therefore neglecting its superelasticity and shape memory effect.

## 3.5 Conclusions

In this chapter, the material characterisation of PWMMs was discussed. Starting from a general description of the plain-weave pattern, the high repetitivity of the structure was exploited to identify the aperture as a constant parameter defining the overall geometry of the material. A digital image analysis was performed to investigate the longitudinal shape of the wires. After post-processing and fitting through a Fourier series the mesh image data in a MATLAB environment, it was concluded that the undulation of the wires can be accurately described by a monoharmonic sinusoidal function. In addition, to validate the assumption of highly ordered structure, a statistical investigation on the aperture was conducted through image analysis. The results of this analysis have confirmed the validity of the assumption, with an observed average aperture in acceptable agreement with the nominal value and a low level of the aperture relative standard deviation, in particular for *Sample 3*.

The influence of the materials constituting the mesh wires was discussed and two different candidates - stainless steel and Nitinol - were presented. Their elastic mechanical properties were also reported, which will be employed in the next chapters.

# Chapter 4

## Analytical modelling

### 4.1 Introduction

In this chapter three novel analytical models are presented that describe the mechanical response of plain-weave mesh materials for in-plane (tension-compression and shear model) and for out-of-plane (bending model) loading.

Initially, the most common beam theories (Euler-Bernoulli and Timoshenko) are briefly introduced. Then, a comparison between them is performed to establish which model is the most appropriate to be employed in the subsequent development of the analytical models. The principle of virtual work and the Castigliano's theorem are then discussed as energy methods for the determination of displacements in elastic structures.

An introduction to contact mechanics is also presented, starting from the classic Hertz theory for elastic bodies. The JKR theory is also presented accounting for the contact adhesive forces. The two contact models are compared when applied to a simplified PWMMs geometry in order to perform a model selection.

The micromechanics of friction is introduced and briefly discussed, followed by discussion of the most popular macro-scale friction models (i.e., Coulomb, Dahl, LuGre), highlighting the motivation for employing the specific model in this work.

The first developed model for PWMMs to be presented is the tension-compression model. Starting from a geometrical schematisation of plain-weave mesh materials, the Castigliano's theorem and the Hertz contact theory are applied to derive the effective elastic properties of the RUC.

The shear model which describes the non-linear response of PWMMs when they are subjected to in-plane shear load. The analytical shear model is based on an in-depth study of the mesh materials frictional contact mechanics. This involves a prediction of the contact area shape and dimensions along with the distribution of normal and shear stresses over the contact area in order to calculate the friction moment reaction. This model is then applied to characterise the hysteretic response of PWMMs under an oscillating shear load and is used to calculate the relative damping factor.

The last model presented is the out-of-plane bending model, which follows the same approach adopted for the tension-compression model, and is used to predict the effect of the out-of-plane bending on the contact force at the intersecting locations.

## 4.2 Beam theories

For the development of the analytical models, in this research the PWMM wires are represented as curved elastic beams crossed at the plain-weave intersections, as will be discussed further later. For this reason, the main beam theories are introduced and compared to select the most suitable one for the characterisation of PWMMs.

Beam theories are simplified analytical models that describe the kinematics of beams, which are defined as mechanical elements in which one dimension (length) is much larger than the other two (depth and width). These models represent a simplification of the general three-dimensional solid mechanics and the beams are reduced to a one-dimensional body in which the deflection  $w(x)$  is a function of the longitudinal coordinate  $x$  only.

These theories are generally linear and based on the Hooke's law of elasticity. They allow to determine the displacements and internal forces of the beams and they are typically applicable only for small deflections. The loads are assumed to be applied transverse to the longitudinal direction.

There are different beam theories that have been developed. The most commonly adopted are:

- i) Euler-Bernoulli
- ii) Timoshenko

#### **4.2.1 Euler-Bernoulli**

The Euler-Bernoulli's is the classical beam theory and generally the simplest one. Enunciated for the first time probably around 1750 [73], it has been widely adopted in designing and used for many engineering practical applications. It is based upon three main kinematic assumptions, known as the Euler-Bernoulli hypotheses:

- i) Cross-sections do not deform significantly and can be considered as rigid.
- ii) Planar cross-sections remain planar.
- iii) Normal cross-sections remain perpendicular to the neutral axis.

As a consequence of the last assumption, the theory does not account for shear strains. The only contribution to deformation is given by the bending moment, whereas shear internal forces are neglected. Therefore, it represents a significant approximation of the real problem that is only valid for slender beams with a straight axis, where the effects of shear strains are negligible. For other engineering problems where a higher precision is required, the Timoshenko beam theory lies as an alternative model.

The equilibrium of an infinitesimal element of the beam is expressed by the following equations:

$$V = \frac{dM}{dx} \quad (4.1)$$

$$q = \frac{dV}{dx} \quad (4.2)$$

where  $M$  is the bending moment,  $V$  is the transverse shear force and  $q$  is the transverse distributed load. The Euler-Bernoulli beam theory establishes a relation between rotation, bending moment and shear transverse force, by expressing these quantities as a function of the successive spatial derivatives of the transverse deflection  $w(x)$ :

$$\theta(x) = \frac{dw}{dx} \quad (4.3)$$

$$M = -EI \frac{d^2w(x)}{dx^2} \quad (4.4)$$

$$V = -EI \frac{d^3w(x)}{dx^3} \quad (4.5)$$

where  $\theta(x)$  is the angle of rotation,  $E$  is the elastic modulus and  $I$  is the second moment of area of the beam, relative to the cross-section perpendicular to the neutral axis. The product  $EI$  is often referred to as flexural rigidity of the beam. The deflection can also be expressed directly as a function of the transverse load, by substituting Equation 4.5 into Equation 4.2:

$$\frac{d}{dx} \left( -EI \frac{d^3w(x)}{dx^3} \right) = -EI \frac{d^4w(x)}{dx^4} = q \quad (4.6)$$

For a subsequent comparison between Euler-Bernoulli and Timoshenko, consider the case of a cantilever beam subjected to a load  $P$  applied at the free end. The solution for this case can be obtained directly from 4.4. The displacement field of the beam is represented by a cubic function of the distance  $x$  from the fixed end:

$$w(x) = -\frac{Px^2(3L-x)}{6EI} \quad (4.7)$$

Which, calculated for  $x = L$ , returns the following expression for the tip deflection:

$$\delta = \frac{PL^3}{3EI} \quad (4.8)$$

### 4.2.2 Timoshenko

The Timoshenko beam theory is an extension of Euler-Bernoulli theory. In this method, the cross-sections are allowed to rotate about the neutral axis, so that shear strains are accounted for. The method is suitable for deep beams, where the shear stresses are not negligible. In Timoshenko beam theory the total deflection of the beam is given by the contributions of both bending rotation and shear deformation:

$$\frac{dw}{dx} = \varphi - \frac{1}{\tilde{K}AG} \frac{d}{dx} \left( EI \frac{d\varphi}{dx} \right) \quad (4.9)$$

where  $\varphi$  is the rotation of the cross-section about the z-axis,  $A$  is the cross-section area,  $G$  is the shear modulus of the material and  $\tilde{K}$  is a shape coefficient (whose value is usually 5/6 for prismatic sections and 9/10 for circular sections). The bending moment  $M$  and the transverse shear force  $V$  can be related to the angle of rotation  $\varphi$  and the deflection  $w$  by means of the following expressions:

$$M = -EI \frac{d\varphi}{dx} \quad (4.10)$$

$$V = -\tilde{K}AG \left( \varphi - \frac{dw}{dx} \right) \quad (4.11)$$

Consider again the case of a cantilever beam, as discussed for the Euler-Bernoulli model. Integrating Equation 4.9 and applying the proper boundary conditions, it returns the expression for the tip displacement:

$$\delta = \frac{PL^3}{3EI} + \frac{PL}{\tilde{K}AG} \quad (4.12)$$

The previous solution is equal to the one of Euler-Bernoulli (Equation 4.8) plus an additional shear displacement term that accounts for the shear rotation.

### 4.2.3 Model selection

In sight of the subsequent development of a stiffness model for PWMMs, it is necessary to perform a careful selection of the most suitable beam theory to be employed.

From a comparison between Equations 4.8 and 4.12, it is evident how the Euler-Bernoulli beam model is stiffer than Timoshenko, being the shear deformation neglected. A fundamental parameter in the selection is the *slenderness ratio*, defined as the ratio  $L/d$  of the length to the diameter of the beam. As a general rule, the usage of Timoshenko model is always recommended over Euler-Bernoulli for deep beams, conventionally those with a value of  $L/d < 10$  [74].

Parameter	Symbol	Unit	Sample 1	Sample 2	Sample 3
Diameter	$d$	mm	0.45	0.45	0.45
Semi-wavelength	$L$	mm	1.41	1.81	2.12
Slenderness ratio	$L/d$		3.13	4.02	4.71

**Table 4.1:** Slenderness ratio for different PWMM samples.

Recalling from Chapter 3, three different samples are identified and analysed as example materials. An approximation can be done considering each wire in the RUC as a cantilever beam whose longitudinal dimension is equal to the semi-wavelength of the wire. For each sample, the slenderness ratio is calculated and reported in Table 4.1. In Figure 4.1 the normalised difference in deflection between Timoshenko and Euler-Bernoulli beam theory is reported for a tip-loaded cantilever beam as a function of the slenderness ratio.

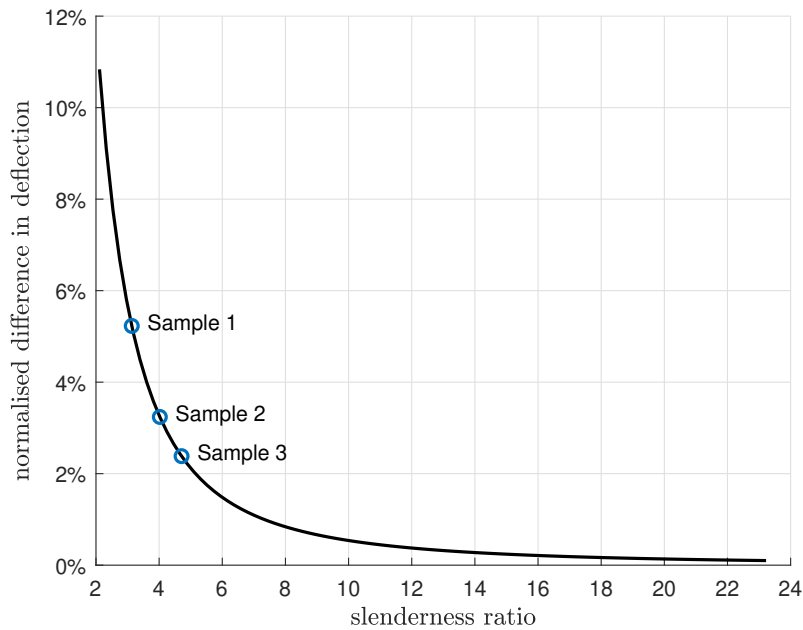


**Figure 4.1:** Normalised difference in deflection between Timoshenko and Euler-Bernoulli beam theory for a tip-loaded cantilever beam at various slenderness ratios.

From the graph it could be seen how the difference, corresponding to the shear contribution to deflection, reduces from more than 10% to almost zero as the ratio increases, meaning that the two methods tend to analogous results for slender beams. However, for the three samples considered, the results suggest that Timoshenko beam theory should be employed in the development of a stiffness model for PWMMs. Neglecting the transverse shear component, instead, would yield an overestimation of the stiffness up to more than 5%.

These preliminary considerations are only based on the assumption of a straight cantilever beam. As will be discussed further later, shear strains are introduced in the wires when subjected to tensile load because of their curved shape, leading to even higher errors if these were to be neglected.

### 4.3 Energy-based methods in structural analysis

The beam models described previously are simplified and valid for initially straight beams under lateral load only. For the structural analysis of more complex systems, the energy-based methods represent a robust approach that is suitable to many different problems. In general, they are based on the well-known principle of energy conservation, which states that energy can neither be created nor destroyed, rather converted from one form to another. In the specific case of elastic structures under static equilibrium, the work produced by the external forces acting upon the system is entirely converted to internal energy, which is stored in the body in the form of strain energy. The previous statement is only valid if the loads are applied gradually, whereas a sudden deformation of the structure would cause energy dissipation through heat generated by internal friction.

Consider a generic system subjected to an external force  $P$ , which causes a displacement  $\delta$  of its point of application. The external work done by the force is equal to:

$$W_e = \frac{1}{2}P \cdot \delta \quad (4.13)$$

Let  $\{\sigma\}$  and  $\{\epsilon\}$  be respectively the stresses and strains at any point of the system, as follows:

$$\{\sigma\}^T = \{\sigma_{xx} \ \sigma_{yy} \ \sigma_{zz} \ \tau_{xy} \ \tau_{xz} \ \tau_{yz}\} \quad (4.14)$$

$$\{\epsilon\}^T = \{\epsilon_{xx} \ \epsilon_{yy} \ \epsilon_{zz} \ \gamma_{xy} \ \gamma_{xz} \ \gamma_{yz}\}$$

The strain energy stored into the system is then:

$$U_i = \frac{1}{2} \int_V \{\sigma\}^T \{\epsilon\} dV \quad (4.15)$$

The *principle of real work* states that the work of the external force  $W_e$  is equal to internal energy  $U_i$ , and thus:

$$\frac{1}{2}P\delta = \frac{1}{2} \int_V \{\sigma\}^T \{\epsilon\} dV \quad (4.16)$$

Through this simple method, it is possible to determine the displacement  $\delta$  when a single external force is applied to a statically determinate system.

However, for the case of multiple external forces, distributed loads or statically indeterminate systems, other methods are required. In fact, considering now a structure subjected to  $n$  external forces  $\{P\}$ , associated to as many displacements  $\{\delta\}$  of their points of application, the solution of this problem would require  $n$  independent equations, which cannot be obtained by means of the principle of real work alone.

### 4.3.1 Principle of virtual work

The *principle of virtual work* (PVW) consists into observing how a system in equilibrium reacts to an infinitesimal and arbitrary virtual perturbation, which could be either a force or displacement. The virtual work is the work which is done by a real force acting through a virtual displacement (principle of virtual displacements), or by a virtual force acting through a real displacement (principle of virtual forces). The first form is useful to solve hyperstatic systems in case of redundant forces or reactions. The second form, of more interest for this work, is often used to study the deflection of complex structures.

Consider a generic system subjected to  $n$  external virtual forces  $\{P'\}$ , associated to as many real displacements  $\{\delta\}$  of their points of application. The virtual external work done by the forces is equal to:

$$W_{e,v} = \frac{1}{2} \{P'\}^T \{\delta\} \quad (4.17)$$

The associated virtual internal work or virtual strain energy of the system is:

$$U_{i,v} = \frac{1}{2} \int_V \{\sigma'\}^T \{\epsilon\} dV \quad (4.18)$$

where  $\{\sigma'\}$  and  $\{\epsilon\}$  are respectively the virtual stresses and the real strains of the system. The principle states that in a system under static equilibrium, the external virtual work is equal to the internal virtual work, and thus:

$$\frac{1}{2} \{P'\}^T \{\delta\} = \frac{1}{2} \int_V \{\sigma'\}^T \{\epsilon\} dV \quad (4.19)$$

The previous equation allows to calculate the structural displacements by means of the *unit load method*. This consists into setting a virtual unitary force in correspondence of the displacement of interest. Thus, Equation 4.19 reduces to:

$$1 \cdot \delta = \int_V \{\sigma'\}^T \{\epsilon\} dV \quad (4.20)$$

To solve the previous equation it is required to calculate the virtual stresses  $\{\sigma'\}$  and the real strains  $\{\epsilon\}$  within the system. In the following subsections, the procedure for each single internal force and finally the general solution will be presented and discussed.

#### 4.3.1.1 Normal force

Consider a rod subjected to a real normal force  $N$  and a virtual normal force  $N'$ . The virtual stress and the real strain are then:

$$\sigma'_{xx} = \frac{N'}{A} \quad (4.21a)$$

$$\epsilon_{xx} = \frac{N}{EA} \quad (4.21b)$$

where  $E$  is the elastic modulus and  $A$  is the cross-sectional area of the rod. Substituting the previous into Equation 4.18, it returns:

$$U_{i,v} = \frac{1}{2} \int_l \int \int_A \frac{NN'}{EA^2} dA dl = \frac{1}{2} \int_l \frac{NN'}{EA} dl \quad (4.22)$$

#### 4.3.1.2 Shear force

Consider a beam subjected to real shear force  $V$  and virtual shear force  $V'$  along the  $y$ -axis. The virtual stress and the real strain are then:

$$\tau'_{xy} = \frac{V'Q(y)}{I_z t(y)} \quad (4.23a)$$

$$\gamma_{xy} = \frac{\tau_{xy}}{G} = \frac{VQ(y)}{GI_z t(y)} \quad (4.23b)$$

where  $t$  is the width of the section,  $G$  is the shear modulus and  $Q(y)$  and  $I_z$  are respectively the first and second moment of area with respect to the  $z$ -axis, calculated as follows:

$$Q(y) = \int_A y dA \quad (4.24a)$$

$$I_z = \iint_A y^2 dA \quad (4.24b)$$

Substituting Equations 4.23a and 4.23b into Equation 4.18, it yields:

$$U_{i,v} = \frac{1}{2} \int_l \iiint_A \frac{VV'Q(y)^2}{GI_z^2 t(y)^2} dA dl = \frac{1}{2} \int_l \chi \frac{VV'}{GA} dl \quad (4.25)$$

where  $\chi$  is the inverse of the Timoshenko's coefficient, calculated as follows:

$$\chi = \frac{A}{I_z^2} \iint_A \frac{Q(y)^2}{t(y)^2} \quad (4.26)$$

#### 4.3.1.3 Bending moment

Consider a beam subjected to a real bending moment  $M$  and a virtual bending moment  $M'$ . The virtual stress and the real strain are then defined as:

$$\sigma'_{xx} = -\frac{M'y}{I_z} \quad (4.27a)$$

$$\epsilon_{xx} = -\frac{My}{EI_z} \quad (4.27b)$$

Substituting the previous into Equation 4.18 and recalling Equation 4.24b, it returns:

$$U_{i,v} = \frac{1}{2} \int_l \iint_A \frac{MM'y^2}{EI_z^2} dA dl = \frac{1}{2} \int_l \frac{MM'}{EI_z} dl \quad (4.28)$$

#### 4.3.1.4 Total virtual internal energy

The total virtual internal energy is finally calculated as the sum of the different components:

$$U_{i,v} = \frac{1}{2} \left[ \int_l \frac{MM'}{EI_z} dl + \int_l \frac{NN'}{EA} dl + \int_l \chi \frac{VV'}{GA} dl \right] \quad (4.29)$$

Substituting the previous into Equation 4.20, it returns:

$$\delta = \int_l \frac{MM'}{EI_z} dl + \int_l \frac{NN'}{EA} dl + \int_l \chi \frac{VV'}{GA} dl \quad (4.30)$$

Through this last expression, the deflection can be determined at any point of the structure by simply calculating the real and the virtual internal forces. This is achieved by solving separately the real system (i.e., in which the real forces are applied) and the virtual system (i.e., in which only virtual forces are applied).

### 4.3.2 Castigliano's theorem for elastic structures

The Castigliano's first theorem [75], enunciated for the first time by Carlo Alberto Castigliano in 1873 in his dissertation "*Intorno ai sistemi elastici*" (About elastic

systems), also known as the theorem of least work, states that for an elastic structure subjected to a system of external forces and under static equilibrium, the partial derivative of the strain energy (“lavoro molecolare”) considered as a function of the applied forces, with respect to one of these forces, is equal to the displacement of the point of application of the force in the direction of the force.

In mathematical terms, this is described as:

$$\delta = \frac{\partial U}{\partial P} \quad (4.31)$$

where  $\delta$  is the displacement,  $U$  is the strain energy and  $P$  is the applied force. Recalling that the strain energy of an elastic body can be expressed as the sum of the contribution of the internal forces:

$$U = \frac{1}{2} \int_V \{\sigma\}^T \{\epsilon\} dV = \int_l \frac{M^2}{2EI} dl + \int_l \frac{N^2}{2EA} dl + \int_l \chi \frac{V^2}{2GA} dl \quad (4.32)$$

Substituting the previous into Equation 4.31, it returns the expression for the displacement as a function of the internal forces:

$$\begin{aligned} \delta &= \frac{\partial}{\partial P} \left( \int_l \frac{M^2}{2EI} dl + \int_l \frac{N^2}{2EA} dl + \int_l \chi \frac{V^2}{2GA} dl \right) \\ &= \int_l \frac{M}{EI} \frac{\partial M}{\partial P} dl + \int_l \frac{N}{EA} \frac{\partial N}{\partial P} dl + \int_l \chi \frac{V}{GA} \frac{\partial V}{\partial P} dl \end{aligned} \quad (4.33)$$

To solve the integral above, it is required to express the internal forces as a function of the applied load  $P$  and calculate their derivatives.

Considering once again a cantilever beam of length  $L$  subjected to a tip load, if only the moment contribution is accounted for, the Castigliano’s theorem yields the same solution as Euler-Bernoulli (Equation 4.8):

$$\delta = \int_0^L \frac{M}{EI} \frac{\partial M}{\partial P} dx = \int_0^L \frac{Px^2}{EI} dx = \frac{PL^3}{3EI} \quad (4.34)$$

Introducing the shear contribution, the solution corresponds to the one of Timoshenko (Equation 4.12):

$$\delta = \int_0^L \frac{Px^2}{EI} dx + \int_0^L \chi \frac{P}{GA} dx = \frac{PL^3}{3EI} + \chi \frac{PL}{GA} \quad (4.35)$$

Finally, including the normal component in the equation, returns the expression for a beam-column element, which is capable of withstanding tension and compression load.

The method illustrated so far is specifically formulated to calculate a structural displacement in correspondence of an applied external force. However, its application can be easily extended for determining the displacement of a general point of the system, just by adding a dummy load with zero amplitude to the location of interest, and thus calculating the corresponding internal energy.

An analogy is evident between Castigliano's theorem and the principle of virtual work, by comparing Equation 4.33 with Equation 4.30. In fact, the virtual internal forces from the PVW, are now replaced with a derivative. However, since the internal forces are in general a linear function of the applied force, their derivatives are equivalent to the internal forces induced by a unitary load. Therefore, for the determination of displacements, the two theorems lead to the same results and Castigliano's theorem can be considered as a particular case of the PVW. For this reason, as regards the study of kinematics of mesh materials, all the conclusions found in this work can be interchangeably considered as achieved through either Castigliano or PVW, being them equivalent.

## 4.4 Contact mechanics

As previously introduced, the non-linear mechanical response of mesh materials is greatly influenced by the contact mechanics occurring at the numerous warp-weft wire intersections and currently the existing models either do not account for this aspect or employ simplified or empirical formulations. Motivated by this existing

knowledge gap, this work is aimed to develop a series of analytical models that incorporate the effect of the wire-to-wire contact interaction. For this reason in the next subsections, the main contact theories (i.e, Hertz and JKR) are discussed and compared when applied to the case of PWMs, with the purpose of selecting the most appropriate model for this research.

#### 4.4.1 Hertz theory

In 1882 Heinrich Hertz presented his theory that posed the foundations for the development of contact mechanics [76]. He provided a solution for the problem of curved elastic bodies in contact. The Hertzian theory is based on the following assumptions:

- i) Contact surfaces are continuous and non-conforming.
- ii) Strains are small.
- iii) Solids are considered as elastic-half spaces.
- iv) Surfaces are frictionless.
- v) Adhesion between surfaces can be neglected.

The surfaces are considered smooth from both a micro and a macro scale, which implies that the small surface irregularities and asperities are neglected, and the profiles of the solids are continuous up to the second derivative terms, in correspondence of the contact area. For this last assumption, the profile of each surface can be represented by a quadratic expression in proximity of the contact. Choosing the point of first contact as the origin of the coordinate system, such as the x-y plane is the common tangent to the surfaces and the z-axis is directed along the common normal, the expression for the first surface takes the following form:

$$z_1 = \frac{1}{2R'_1}x_1^2 + \frac{1}{2R''_1}y_1^2 \quad (4.36a)$$

where  $R'_1$  and  $R'_2$  are the principal radii of curvature of the first surface at the origin. A similar expression can be derived for the second surface:

$$z_2 = - \left( \frac{1}{2R'_2} x_2^2 + \frac{1}{2R''_2} y_2^2 \right) \quad (4.36b)$$

The difference between Equations 4.36a and 4.36b represents the separation between the two surfaces  $h = z_1 - z_2$ . Transposing the relation to a common coordinate system, it returns:

$$h = Ax^2 + By^2 = \frac{1}{2R'} x^2 + \frac{1}{2R''} y^2 \quad (4.37)$$

where  $R'$  and  $R''$  are the principal relative radii of curvature and  $A$  and  $B$  are positive constants. According to Equation 4.37, the regions identified by the same gap  $h$  between the undeformed surfaces are ellipses whose axes are in the ratio  $(R'/R'')^{1/2}$ . If the axes of principal curvature of each surface are inclined with respect to each other of an angle  $\theta$ , the following two equations need to be true:

$$(A + B) = \frac{1}{2} \left( \frac{1}{R'} + \frac{1}{R''} \right) = \frac{1}{2} \left( \frac{1}{R'_1} + \frac{1}{R''_1} + \frac{1}{R'_2} + \frac{1}{R''_2} \right) \quad (4.38a)$$

$$\begin{aligned} |B - A| = \frac{1}{2} \left\{ \left( \frac{1}{R'_1} - \frac{1}{R''_1} \right)^2 + \left( \frac{1}{R'_2} - \frac{1}{R''_2} \right)^2 \right. \\ \left. + 2 \left( \frac{1}{R'_1} - \frac{1}{R''_1} \right) \left( \frac{1}{R'_2} - \frac{1}{R''_2} \right) \cos 2\theta \right\}^{1/2} \end{aligned} \quad (4.38b)$$

When the two solids are pressed together by a normal compressive load  $P$ , the initial point of contact spreads into an area whose shape depends on their radii of curvature.

#### 4.4.1.1 Sphere-to-sphere contact

In the case of two solids of revolution in contact, their principal radii of curvature are the same ( $R'_1 = R''_1 = R_1$  and  $R'_2 = R''_2 = R_2$ ), so the regions of same

separation and the contact area are circles with centre at the origin of axes. This is the case of two elastic spheres in contact of radii  $R_1$  and  $R_2$ . In this case, the radius of the circular contact area is expressed as:

$$a = \left( \frac{3PR}{4E^*} \right)^{1/3} \quad (4.39)$$

where  $R$  and  $E^*$  are respectively the effective radius of curvature and the effective elastic modulus of the two spheres, calculated as follows:

$$\frac{1}{R} = \frac{1}{R_1} + \frac{1}{R_2} \quad (4.40a)$$

$$\frac{1}{E^*} = \frac{1 - \nu_1^2}{E_1} + \frac{1 - \nu_2^2}{E_2} \quad (4.40b)$$

where the subscripts 1 and 2 denote the two spheres and  $E$  and  $\nu$  are respectively their elastic modulus and Poisson's ratio. The normal pressure distribution among the contact area resulting from the load  $P$  is given by:

$$\sigma(r) = \frac{3P}{2\pi a^2} \left( 1 - \frac{r^2}{a^2} \right)^{1/2} \quad (4.41)$$

where  $r$  is the radial distance from the centre of the contact area. The pressure distribution in Equation 4.41 has the form of a semi-ellipsoid acting upon a circular area of radius  $a$ . The maximum pressure  $\sigma_0 = \frac{3P}{2\pi a^2}$  is located at the centre of the contact area. Such a pressure field generates a uniform normal displacement across the contact area and does not lead to contact outside of it.

#### 4.4.1.2 Cylinder-to-cylinder contact: parallel and perpendicular axes

If the two solids are cylindrical bodies with radii  $R_1$  and  $R_2$ , their radii of curvature are respectively  $R'_1 = R_1$ ,  $R''_1 = \infty$ ,  $R'_2 = R_2$ ,  $R''_2 = \infty$ .

For two parallel cylinders, the contours of constant gap are lines parallel to their axes. When a compressive load  $P$  is applied to the pair, a rectangular contact area is generated, whose width is calculated as [77]:

$$b = \sqrt{\frac{4PR}{\pi E^* L}} \quad (4.42)$$

where  $L$  is the axial length of the cylinders.  $R$  and  $E^*$  are again the effective radius of curvature and the effective elastic modulus from Equations 4.40a and 4.40b. The normal pressure distribution is again a semi-ellipsoid, expressed by the following equation:

$$\sigma(r) = \frac{2P}{\pi b L} \left(1 - \frac{r^2}{b^2}\right)^{1/2} \quad (4.43)$$

where the peak pressure,  $\sigma_0 = \frac{2P}{\pi b L}$ , is at the centre of the rectangular area.

If the cylinders are crossed with perpendicular axes, the lines of constant gap are circles. Under the application of a compressive load  $P$ , a circular contact area is generated, whose radius is calculated with Equation 4.39, where the effective radius of curvature is replaced by the Gaussian radius of curvature  $R = \sqrt{R_1 R_2}$ .

#### 4.4.1.3 General case and cylinder crossed with arbitrary angle

For the general case of bodies with an arbitrary profile, when the separation follows Equation 4.37, the shape of the contact area is not known in advance; however, it can be assumed as elliptical. Referring as  $a$  and  $b$  to the semi-major and semi-minor axis of the elliptic area of contact, their ratio can be found from:

$$\left(\frac{B}{A}\right) = \left(\frac{R'}{R''}\right) = \frac{(a/b)^2 E(e) - K(e)}{K(e) - E(e)} \quad (4.44)$$

where  $K(e)$  and  $E(e)$  are the complete elliptic integrals respectively of first and second kind of argument  $e = \sqrt{1 - b^2/a^2}$  (also called first eccentricity of the

ellipse), with  $a > b$ . The normal pressure distribution generated by a compressive load  $P$ , is again a semi-ellipsoid acting over the elliptic contact area:

$$\sigma(x, y) = \frac{3P}{2\pi ab} \left( 1 - \frac{x^2}{a^2} - \frac{y^2}{b^2} \right)^{1/2} \quad (4.45)$$

Once again, the maximum pressure,  $\sigma_0 = \frac{3P}{2\pi ab}$ , corresponds to the centre of the contact area.

Equations 4.44 and 4.45 apply to the case of two cylinders crossed with an arbitrary angle  $\theta$  between their axes. In the vicinity of the origin, the circular cross-section of the cylinders can be approximated by a parabola. Consider two different set of axes  $x_1y_1z_1$  and  $x_2y_2z_2$ , both sharing the same origin in the point of first contact, and such that the axes  $x_1$  and  $x_2$  are respectively aligned with the generator of the first and the second cylinder. The profile of the first cylinder of radius  $R_1$ , in the system of coordinates  $x_1y_1z_1$ , can be approximated by the following expression:

$$z_1 \approx \frac{x_1^2}{2R_1} \quad (4.46a)$$

For the second cylinder of radius  $R_2$ , in the coordinates  $x_2y_2z_2$ , the equation becomes:

$$z_2 \approx -\frac{x_2^2}{2R_2} \quad (4.46b)$$

The separation between the surfaces is then:

$$h \approx \frac{x_1^2}{2R_1} + \frac{x_2^2}{2R_2} \quad (4.47)$$

The previous equation can be transposed to a common set of axes in the coordinates  $xyz$  such that Equation 4.37 is recovered. Under these conditions, Equations 4.38a and 4.38b must be satisfied. Recalling that, for two cylindrical bodies of

radii  $R_1$  and  $R_2$ , the principal radii of curvature are  $R'_1 = R_1$ ,  $R''_1 = \infty$ ,  $R'_2 = R_2$  and  $R''_2 = \infty$ , the aforementioned equations reduce to the following:

$$(A + B) = \frac{1}{2} \left( \frac{1}{R_1} + \frac{1}{R_2} \right) \quad (4.48a)$$

$$|B - A| = \frac{1}{2} \left\{ 1/R_1^2 + 1/R_2^2 + 2/(R_1 R_2) \cos 2\theta \right\}^{1/2} \quad (4.48b)$$

The contact between cylinders with perpendicular and parallel axes are just particular solutions of the general case. In fact, for perpendicular axes,  $\theta = \pi/2$ , and thus Equation 4.48b reduces to  $A = B$ . Therefore, the contours of constant gap in Equation 4.37 are circles, as well as the contact area, for which  $a = b$ . As the angle  $\theta$  tends to zero,  $a$  increases and  $b$  reduces, so that the contact area becomes a narrower and narrower ellipse until, for  $\theta = 0$ , it degenerates into a rectangle, which can be interpreted as an ellipse of infinite major axis.

#### 4.4.2 Adhesive contact: JKR theory

In 1971, almost a century after Hertz published his contact theory, *Johnson, Kendall and Roberts* proposed a new contact solution that accounts for the always existing adhesion between elastic bodies, known as the JKR theory [78]. This complex physical phenomenon is mostly caused by the relatively weak interactive forces that are generated between atoms or molecules, referred to as Van der Waals forces. These forces rapidly decrease with the sixth power of the distance between two atoms, according to the *Lennard-Jones* potential [79]. They can be calculated theoretically for two atomically smooth surfaces, meaning that the naturally existing asperities between the surfaces are small compared to the atomic scale. In reality, the roughness of the surfaces is great enough to drastically reduce the value of surface attraction calculated theoretically. For this reason, experimental procedures have been developed to measure this quantity, for instance through the contact angle method.

The JKR theory is particularly suitable to study contact problems between soft materials or in micro- and nano-scale systems, where because of the size effect, the adhesive forces are not negligible [80].

The theory initially considers the problem of two elastic spheres of radius  $R_1$  and  $R_2$  pressed together by a normal load  $P_0$ . If the adhesive forces are initially neglected, a Hertzian contact radius  $a_0$  is established, that can be expressed for convenience as follows:

$$a_0^3 = \frac{RP_0}{K} \quad (4.49)$$

where  $K = 4/3E^*$ .  $R$  and  $E^*$  are again calculated respectively from Equations 4.40a and 4.40b.

In reality, because of the presence of attraction forces, the actual contact radius  $a_1$  is greater than the Hertzian one and it can be considered as generated by an apparent Hertz load  $P_1$ , and defined as:

$$a_1^3 = \frac{RP_1}{K} \quad (4.50)$$

The JKR theory calculates the actual contact radius  $a_1$  by calculating the condition of minimum total energy of the system. The total energy  $U_T$  of the system is given by the sum of the stored elastic energy  $U_E$ , the mechanical potential energy  $U_M$  given by the applied load and the surface energy  $U_S$ . Regarding the elastic energy, suppose to initially apply the load  $P_1$  to the system generating a contact area of radius  $a_1$ , corresponding to energy  $U_1$ . Then the load is reduced until  $P_0$  by keeping the contact radius constant and an energy  $U_2$  is released. Thus, the total elastic energy is given by the difference of these two quantities:

$$U_E = U_1 - U_2 \quad (4.51)$$

where

$$U_1 = \int_0^{P_1} \frac{2}{3} \frac{P^{2/3}}{K^{2/3}R^{1/3}} dP = \frac{2}{5} \frac{P_1^{5/3}}{K^{2/3}R^{1/3}} \quad (4.52)$$

and

$$U_2 = \int_{P_0}^{P_1} \frac{2}{3} \frac{P}{K a_1} dP = \frac{1}{3} \frac{(P_1^2 - P_0^2)}{K^{2/3} R^{1/3} P_1^{1/3}} \quad (4.53)$$

Therefore:

$$\begin{aligned} U_E &= \frac{2}{5} \frac{P_1^{5/3}}{K^{2/3} R^{1/3}} - \frac{1}{3} \frac{(P_1^2 - P_0^2)}{K^{2/3} R^{1/3} P_1^{1/3}} \\ &= \frac{1}{K^{2/3} R^{1/3}} \left( \frac{1}{15} P_1^{5/3} + \frac{1}{3} P_0^2 P_1^{-1/3} \right) \end{aligned} \quad (4.54)$$

The mechanical potential energy generated by the load  $P_0$  is calculated as:

$$\begin{aligned} U_M &= -P_0 \delta_2 = -P_0 \left( \delta_1 - \frac{2(P_1 - P_0)}{3 K a_1} \right) \\ &= -P_0 \left( \frac{P_1^{2/3}}{K^{2/3} R^{1/3}} - \frac{2}{3} \left( \frac{K}{R P_1} \right)^{1/3} \frac{(P_1 - P_0)}{K} \right) \\ &= \frac{-P_0}{K^{2/3} R^{1/3}} \left( \frac{1}{3} P_1^{2/3} + \frac{2}{3} P_0 P_1^{-1/3} \right) \end{aligned} \quad (4.55)$$

The surface energy, associated to the attractive forces, is calculated as:

$$U_S = -\gamma \pi a_1^2 = -\gamma \pi (R P_1 / K)^{2/3} \quad (4.56)$$

where  $\gamma$  represents the adhesion energy of both surfaces. Finally, the total energy is calculated as the sum of the different contributions:

$$\begin{aligned} U_T = U_E + U_M + U_S &= \frac{1}{K^{2/3} R^{1/3}} \left( \frac{1}{15} P_1^{5/3} + \frac{1}{3} P_0^2 P_1^{-1/3} \right) \\ &+ \frac{-P_0}{K^{2/3} R^{1/3}} \left( \frac{1}{3} P_1^{2/3} + \frac{2}{3} P_0 P_1^{-1/3} \right) - \gamma \pi (R P_1 / K)^{2/3} \end{aligned} \quad (4.57)$$

The condition of contact equilibrium corresponds to the minimum total energy, calculated as:

$$dU_T / dP_1 = 0 \quad (4.58)$$

By imposing the previous condition, the relation between the apparent Hertz load  $P_1$  and the actual load  $P_0$  can be found:

$$P_1 = P_0 + 3\gamma\pi R + \sqrt{6\gamma\pi RP_0 + (3\gamma\pi R)^2} \quad (4.59)$$

Combining Equations 4.50 and 4.59, finally the expression for the contact radius modified to account for the surface adhesion is obtained:

$$a^3 = \frac{R}{K} \left( P_0 + 3\gamma\pi R + \sqrt{6\gamma\pi RP_0 + (3\gamma\pi R)^2} \right) \quad (4.60)$$

It may be noted that, for a value of  $\gamma = 0$ , the previous equation reduces to the Hertzian solution.

### 4.4.3 Contact model selection

Since the mechanical response of mesh materials is highly dependent on the contact mechanics, Hertz and JKR theory are compared for the purpose of identifying which model should be employed. As already discussed, one of the major limitations of the Hertz theory with respect to the JKR theory is the neglect of adhesive forces that, in certain cases, might lead to an underestimation of the real dimensions of the contact area.

For this investigation, the contact between a pair of PWMM wires is reduced to the one of two crossed cylinders of same radius, approximation that will be recalled and adopted further in this work. Considering same diameter of the PWMM samples analysed in Chapter 3 and the mechanical properties of stainless steel in Table 3.2, the contact area is calculated for different values of contact load through Equations 4.39 and 4.60, where the effective radius is  $R = \sqrt{R_1 R_2}$ , simply equal to the radius of the cylinders (i.e.,  $R = R_1 = R_2$ ). As regards the surface energy of stainless steel, experimental values can be found in [81, 82]. A value of  $\gamma = 110mJ/m^2$ , accounting for both the surfaces involved in the contact, has been used for the calculations.

In Figure 4.2 the normalised difference in contact area between JKR and Hertz theory at various contact forces is reported. From these results, it is evident how for very small contact loads, the effect of adhesive forces is more pronounced and the JKR theory provides with a more accurate prediction of the contact area dimensions. However, this difference rapidly decreases to  $<1\%$  as the load increases, suggesting that the Hertz theory can be applied to this particular geometry and material with acceptable approximation.

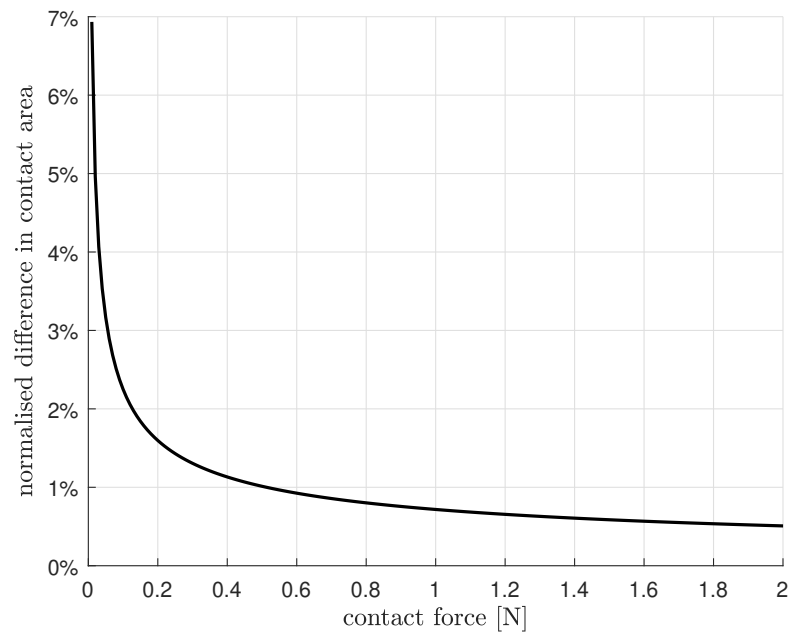


**Figure 4.2:** Normalised difference in contact area between JKR and Hertz theory for two crossed cylinders at various contact forces.

Another important assumption of the Hertz theory is that the strains are small, which implies that the size of the contact area must be much less than the radius of curvature ( $a \ll R$ ). In order to verify whether this assumption is satisfied, the ratio of the Hertzian contact radius to the effective radius of curvature is calculated as a function of the contact load for the same two crossed wires previously analysed, using the materials properties of stainless steel and Nitinol reported in Tables 3.2 and 3.3.

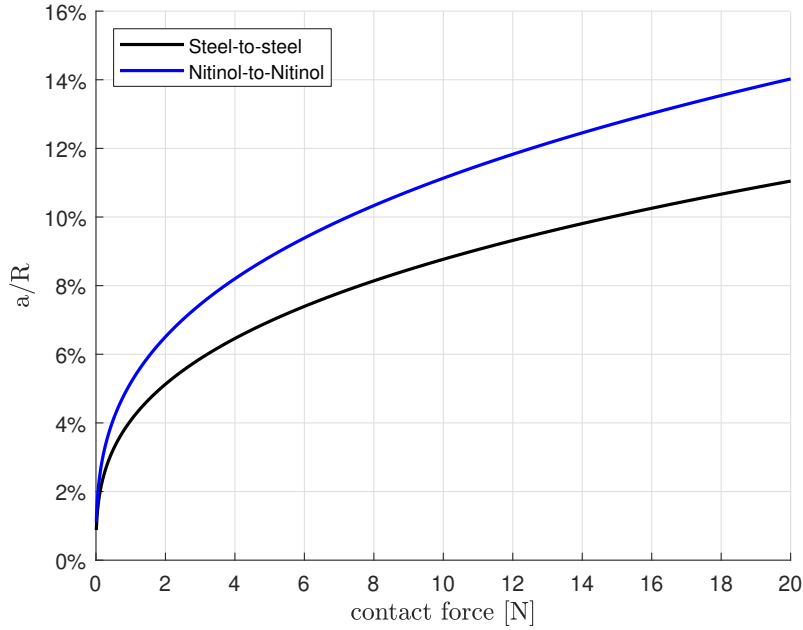


**Figure 4.3:** Ratio of Hertzian contact area to radius of curvature for two crossed cylinders at various contact forces.

From Figure 4.3, it is apparent that this condition is verified for a wide range of contact forces, being the maximum reported values of the ratio  $a/R$  roughly 11% and 14% respectively for the steel-to-steel and Nitinol-to-Nitinol contact corresponding to a normal load of 20N. As the normal load increases the percentage of  $a/R$  would continue to increase approaching asymptotically.

Finally, it is worth noting that the Hertzian theory is also based on the assumption of frictionless surfaces, which is apparently in contrast with the damping phenomena investigated in this thesis. Nevertheless, the classical Hertz theory has been successfully combined with the Coulomb friction model by several authors to solve frictional contact mechanics problems and these models are largely adopted and verified both numerically and experimentally. Based on all the aforementioned considerations, the Hertz contact theory has been employed in this work for the development of the analytical models.

## 4.5 Frictional interaction of surfaces

Friction is a complex physical phenomenon where there is a resistance to relative motion between two sliding surfaces that are in contact when they are subjected to a normal and a tangential force. It manifests as a resistive force, referred to as the frictional force, that always acts in the opposite direction of motion [83] and perpendicularly to the normal contact load, resulting in dissipation of energy in the form of heat. It can occur in multiple forms, and it is generally subdivided into internal, dry and fluid friction [84]. Dry friction, also called *Coulomb friction*, refers to the interaction between dry surfaces that move relative to one another. Only this category will be discussed, since it is the one of interest in this research.

Considering two bodies in contact initially at rest, to initiate the relative motion between them, a tangential force needs to be applied that overcomes a critical value, referred to as static friction force or sometimes as *stiction* force. The value of the force that is necessary to maintain the motion is called dynamic or kinetic friction force.

Nowadays it is commonly accepted that most of the friction problems between unlubricated solid surfaces obey to some simple principles that were discovered several centuries ago. Despite the first scientist to formulate these principles was probably Leonardo da Vinci in his Codex Madrid I [85], they are commonly attributed to Guillaume Amontons [86] and referred to as *Amontons' laws*:

- i) The frictional force is proportional to the normal load.
- ii) The frictional force is independent of the contact area.

To these two laws, a third principle is usually added, which is commonly attributed to Charles-Augustin de Coulomb [87]:

- iii) The dynamic friction force (or dynamic coefficient of friction) is independent of the sliding velocity.

Regarding the latter law, significant experimental evidence is provided to demonstrate this, such as by Bhushan [88]. As further examples in support of this theory, dynamic load tests conducted on metallic friction damping systems have shown that the vibration loss factor is independent of the excitation frequency [89,90].

The first enunciated principle can be expressed mathematically by the following linear dependency:

$$F_{fr} = \mu_{s,d}F_N \quad (4.61)$$

where  $F_{fr}$  is the frictional force,  $F_N$  is the normal contact load and  $\mu_{s,d}$  is a dimensionless number referred to as coefficient of friction. The subscripts  $s$  and  $d$  indicate that the equation refers to either static or dynamic friction. The coefficient of friction is generally dependent on materials, roughness and topology of the surfaces. It also can vary with the normal load, although for metals it remains roughly constant for a wide range of forces [79,91,92].

### 4.5.1 Micromechanics of dry friction

Dry friction between solid bodies involves a diversity of mechanisms, such as elastic and plastic deformations of the contact surfaces, chemical reactions, excitation of electrons and phonons, microfractures, material loss caused by abrasive wear and even transfer of particles from one body to the other [79]. These complex phenomena, that are strictly related to the geometry and material of the bodies in contact, occur at a microscopic level, and therefore, a deeper understanding of the nature of friction requires an inspection of the interacting surfaces at a microscopic scale.

In fact, considering for instance the contact between two flat surfaces such as the ones illustrated in Figure 4.4, although from a macroscale they appear smooth and continuous, at a microscopic level they reveal themselves as composed of a series of irregularities that are randomly distributed across the area and change in

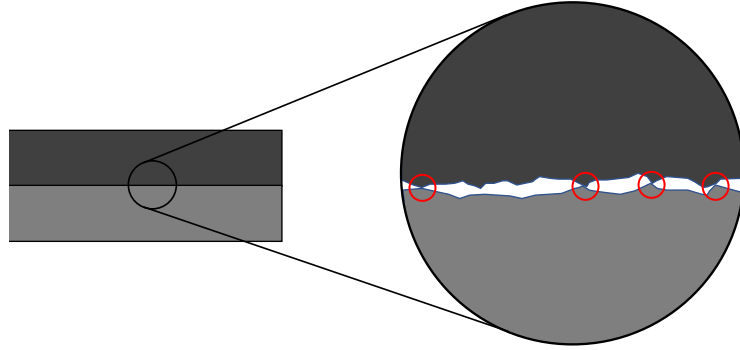


**Figure 4.4:** Representation of the contact surface on a microscopic scale: the cross-section appears as a multitude of asperities that interlock each other only in a small portion of the surface (red circles).

form and size. The surface interaction in actuality takes place only in correspondence of these peaks wherever the asperities of one body come into contact with the ones of the other generating a multitude of so-called *microcontacts*. Therefore, the true area of contact is given by the sum of all these microcontacts, and it is in general much less than the apparent flat area of contact.

The friction is generated from the interference of asperities that interlock each other so that, for the relative motion to occur, the tangential force has to be large enough to elastically or plastically deform the asperities and to overcome the adhesive forces. When fracture occurs in the asperities, it is referred to as wear.

The size of the real area is in general dependent on the normal contact load, as with this increasing, the asperities are deformed at first elastically and then plastically causing more peaks to come into contact [93]. Therefore, being the friction force proportional to the real contact area, this provides with an explanation to the first of the Amontons' laws.

One of the possible approaches for modelling the friction is through a micro-scale mathematical representation. The first micromechanical model for friction

was proposed by Coulomb and provides with a demonstration of the first two of the Amontons' laws. Consider two bodies pressed together into dry contact whose interacting surfaces are characterised by a periodic corrugated profile, as illustrated in Figure 4.5a. Initially referring to a single pair of interlocked asperities, when they are subjected to a tangential force  $F_T$ , a reaction force  $F_R$  opposes to the motion, which is directed normally to the surface at the point of contact, as represented by the free-body-diagram in Figure 4.5b. From the equilibrium condition, the following equations can be written:

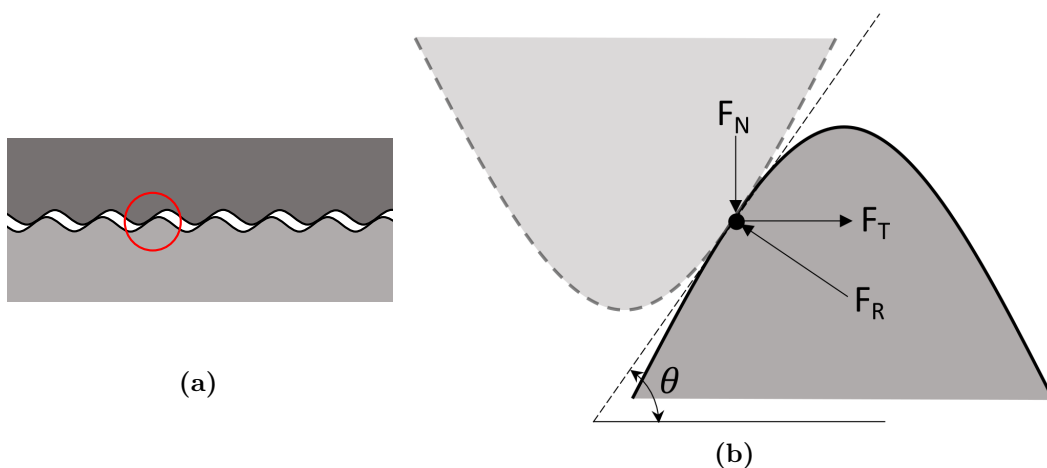


**Figure 4.5:** Coulomb's micromechanical friction model: (a) contact surfaces defined by a periodic profile and (b) free-body-diagram for a single asperity.

$$F_N = F_R \cos \theta \quad (4.62a)$$

$$F_T = F_R \sin \theta = F_N \tan \theta \quad (4.62b)$$

where  $\theta$  is the angle of the asperity surface at the point of contact. The maximum tangential force for which the relative motion is still prevented is then calculated as follows:

$$F_{T,max} = F_R \sin \theta = F_N \tan \theta_{max} \quad (4.63)$$

where  $\theta_{max}$  is the maximum slope of the asperity. Therefore,  $F_{T,max}$  represents the force of static friction and  $\mu_s$  is the coefficient of static friction:

$$\mu_s = \tan \theta_{max} \quad (4.64)$$

Despite of its simplicity, this mathematical representation demonstrates the proportion between normal load and friction force, stated by the first law of Amontons. The model can also provide with a demonstration of the Amontons' second law, by considering again the overall surface in Figure 4.5a composed of a certain number  $n$  of identical asperities. In this case, the normal load can be assumed as equally subdivided between each contact pair. The sum of the friction forces  $F_T/n$  at the multiple asperities would be equal to the case of a single asperity, meaning that the total number of asperities, and so the area of the contact surface, has no influence on the friction force.

Many other micromechanical models have been introduced, where the distribution of asperities is more complex and takes into account randomness. For instance, in 1966 Greenwood and Williamson [94] proposed a model where all the asperities have a spherical summit of same radius of curvature and their heights vary stochastically across the surface with exponential and Gaussian distribution. Andrews and Sehitoglu [95] studied the effect of roughness on fatigue life by proposing a random variation in asperity heights, radii of curvature and spatial distribution.

The high level of randomness on the surface topology and the complexities associated to friction make the employment of these micro-scale models rather inconvenient, especially to be implemented in a numerical model because of the enormous computational burden they would require for describing large systems. For this reason, macro-scale models based on experimentally determined coefficients of friction have gained more popularity and are often preferred in addressing practical engineering problems since they are particularly easy to be implemented into a dynamic numerical simulation.

## 4.5.2 Macro-scale modelling of friction

### 4.5.2.1 Coulomb model

The classic Coulomb is the most basic and probably most diffused friction model, not only because of its simplicity and straightforwardness, but mostly because it is capable of describing the response to friction with acceptable accuracy in many engineering applications [96]. In its classic form, also referred to as *pure* Coulomb solution, the friction force does not depend on the amplitude of the sliding velocity  $\dot{x}$  but only on its direction, and it is linearly proportional to the normal load  $F_N$  and to the friction coefficient  $\mu$ , in agreement with the Amontons' laws. This is expressed by the following equation:

$$F_{fr} = -\mu F_N \operatorname{sgn} \dot{x} \quad (4.65)$$

where *sgn* is the signum function, which depends on the sign of the velocity, as follows:

$$\operatorname{sgn} \dot{x} = \begin{cases} 1, & \dot{x} > 0 \\ 0, & \dot{x} = 0 \\ -1, & \dot{x} < 0 \end{cases} \quad (4.66)$$

It is worth noticing that the negative sign in Equation 4.65 indicates that the friction force is always opposite in direction with the velocity. Moreover, the variable  $\mu$  indicates that the friction coefficient is assumed as constant both under static and dynamic conditions. In fact, although typically static and dynamic friction coefficients are considered different with the first being greater than the second, in certain conditions an approximation can be done, by considering them as equal according to the pure Coulomb model. The extent of variation between static and dynamic friction coefficients depends on the materials and roughness of surfaces in contact. This has been experimentally investigated by Hwang *et al.* [97] who considered steel/steel and steel/alumina interaction both under dry

and lubricated conditions. From their experiments, a sensible disparity was measured for polished finish, whereas for ground surfaces a difference of only 9% was witnessed. For the sake of simplicity, in this work the same value of dynamic and static friction coefficient is adopted.

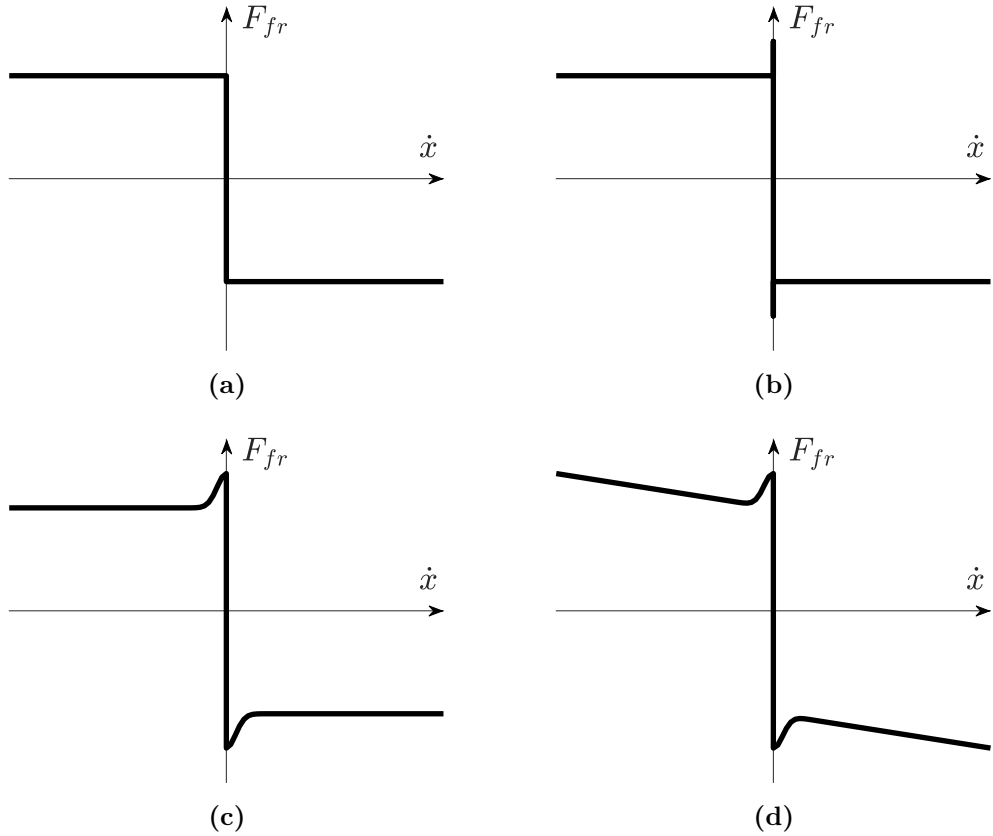


**Figure 4.6:** Coulomb model combined with different other friction models: (a) pure Coulomb, (b) Coulomb + stiction, (c) Coulomb + Stribeck, (d) Coulomb + Stribeck + viscous

Only two phases are contemplated by the Coulomb model: a stick phase, when the applied tangential force  $F_T$  is less than the static friction force, and a slip or sliding phase, when the tangential force exceeds the friction force and the motion is initiated. Mathematically, this is represented as:

$$status = \begin{cases} stick, & |F_T| \leq \mu F_N, \quad \dot{x} = 0 \\ slip, & |F_T| > \mu F_N, \quad |\dot{x}| > 0 \end{cases} \quad (4.67)$$

During the stick phase, the Coulomb model does not define the friction force, which can take any value in the interval between  $-\mu F_N$  and  $\mu F_N$ . In reality, before the relative motion is reached across the whole surface, microslip phenomena occur in a portion of the contact area, leading to a gradual increase in the friction force. The major problem with neglecting the microslip phase is that the discontinuity in the friction force at zero velocity causes a singularity in the equivalent linear damping, which tends to infinite for  $\dot{x} \rightarrow 0$ , making the computation cumbersome [98]. Since only two statuses are possible (i.e., sticking and sliding), when applied to a single DOF system, the classical Coulomb model is only able to provide with a rough approximation of its dynamic response. However, if the interacting surfaces are discretised into multiple elements (such as in the FE method), the increased number of DOFs allows to have a description of the micro-slip phase, resulting in a smoother transition from stick to slide condition.

The Coulomb model has been combined with many other friction models, to describe more complex phenomena and behaviours. Some of them are illustrated in Figure 4.6, where the friction force is plotted as a function of the velocity. For instance, the disparity in static and dynamic friction coefficient is accounted for by the stiction model in Figure 4.6b, whereas the Stribeck model [99] in Figure 4.6c provides with a smoother transition from static to dynamic phase, by introducing an exponential decay in the friction force. A linear proportion between friction and velocity is obtained by incorporating the viscous model, as in Figure 4.6d.

#### 4.5.2.2 Dahl model

The Dahl model [100] was proposed by Philip R. Dahl in 1968 and it is one of the first dynamic models for friction, together with the LuGre model that is its direct derivation [101]. It was developed with the purpose of describing the hysteresis behaviour experimentally observed in ball bearings for aerospace

industry when subjected to sinusoidal cyclic load. With respect to the Coulomb model, the Dahl model is capable of describing the microslip phenomena in dry contact of solids. In this model the friction microslip phase is related to the stress-strain curve of the materials in contact. The nonlinear response of the friction force during the pre-sliding is believed to be caused by the contribution of an elastic and a plastic component of stress. To describe this behaviour, the surface asperities are considered as a series of microsprings [102]. During the initial phase, a linear increasing can be observed in the force, when the asperities at the bonding interface are only elastically deformed. When the strain is increased further, the local stress overcomes the yield point, causing plastic deformations at the bonding interface. When the applied external force overcomes the maximum internal restoring force, macroslip occurs. After plastic deformation, if the load is released, the deformation will not return to the initial state, resulting in hysteresis loop and dissipation of energy.

The friction force is expressed as a function of the displacement by the following differential equation [103]:

$$\frac{dF(x)}{dx} = \sigma \left| 1 - \frac{F(x)}{F_C} \right| \operatorname{sgn} \dot{x} |^{\alpha} \operatorname{sgn} \left( 1 - \frac{F(x)}{F_C} \right) \quad (4.68)$$

where  $\sigma$  is the tangential stiffness of the contact surface expressed in  $[N/m]$ , that corresponds to the slope of the force-displacement curve at  $F = 0$  and it is related to the elastic stiffness of the asperities.

The term  $F_C$  represents the Coulomb friction force, equal to  $\mu F_N$ . This can be understood as a "yield force", beyond which the plastic deformation of the asperities occurs. In fact, when a tangential external force  $F_T$  is applied such that  $F_T > F_C$ , rupture of the asperities occurs leading to macroslip. Solution of Equation 4.68 is illustrated in Figure 4.7 in non-dimensional coordinates for positive values of the velocity  $\dot{x}$ . The value of  $F_C$  is approached asymptotically by the friction force as the displacement increases. For larger displacements, the Dahl model corresponds to the Coulomb model. The coefficient  $\alpha$  defines the shape of the function during the microslip phase, which is dependent according to the

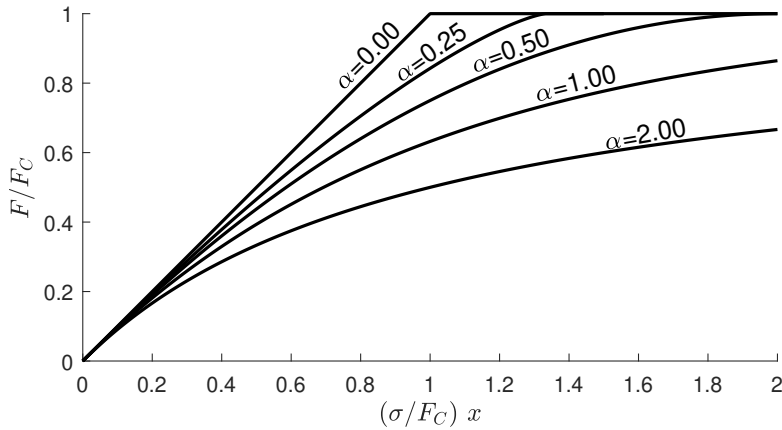


**Figure 4.7:** Dahl friction model response: friction force as a function of displacement in non-dimensional coordinates at various  $\alpha$ .

material. For brittle materials the range is  $0 < \alpha < 1$ , while for ductile materials  $\alpha \geq 1$ . The determination of the parameters  $\alpha$  and  $\sigma$  relies on experimental data and different procedures exist for their identification [104].

It may be noted that the Dahl model is only dependent on the displacement and on the sign of the velocity, therefore it is not capable of describing the Stribeck effect, which instead is a rate dependent phenomenon. Also stiction is not captured by the model, leading to inaccuracy when a great disparity between static and dynamic coefficients exists.

#### 4.5.2.3 Lund-Grenoble (LuGre) model

The Lund-Grenoble model [105], also referred to as *LuGre* model, results from a collaboration of the universities of Lund and Grenoble and it represents an extension of the Dahl model, with respect to which is also capable of capturing more complex rate dependent mechanisms that are observed experimentally such as stiction, Stribeck effect, hysteresis and varying break-away force.

In this model, the interacting surfaces are described as two rigid bodies that come into contact through a series of randomly distributed bristles, as illustrated in Figure 4.8. These represent the typical asperities that characterise contact

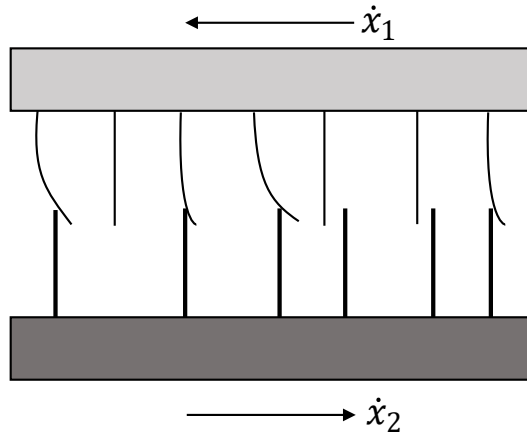


**Figure 4.8:** Lu-Gre friction model: representation of the contact surfaces as a series of bristles. For simplicity, the bristles on the lower body are represented as rigid.

surfaces and are equivalent to elastic microsprings. If a large enough tangential force is applied to the bodies, the bristles deflect until they slip.

Because of the randomness of the surfaces in contact, the model is based on the average deflection  $z$  of the bristles, defined by the following first-order differential equation:

$$\frac{dz}{dt} = \dot{x} - \frac{\sigma_0 |\dot{x}|}{g(\dot{x})} z \quad (4.69)$$

where  $\dot{x}$  is again the relative velocity between the sliding surfaces and  $\sigma_0$  is the elastic stiffness of the bristles. The term  $g(\dot{x})$  is a positive function that depends on many factors such as materials, lubrication and temperature. It represents the decay of the friction force when the velocity increases, which corresponds to the Stribeck effect. In order to achieve a good approximation of the Stribeck effect, Olsson *et al.* [106] suggest that the following form for  $g(\dot{x})$  should be chosen:

$$g(\dot{x}) = F_C + (F_S - F_C) e^{-(\dot{x}/\dot{x}_s)^2} \quad (4.70)$$

where  $F_C$  and  $F_S$  are respectively the Coulomb and the static friction force and  $\dot{x}_s$  is the Stribeck velocity.

In this model, the friction force is proportional to the deflection and the rate of deformation of the bristles and to the relative velocity of the bodies, as follows:

$$F = \sigma_0 z + \sigma_1 \frac{dz}{dt} + \sigma_2 \dot{x} \quad (4.71)$$

where  $\sigma_1$  and  $\sigma_2$  are respectively the damping and the viscous friction coefficients.

Therefore, the model is characterised in total by six parameters ( $\sigma_0$ ,  $\sigma_1$ ,  $\sigma_2$ ,  $F_C$ ,  $F_S$  and  $\dot{x}$ ), four of which are static and two dynamic. For this reason the LuGre model is highly versatile and can be adapted to be employed in describing a multitude of different friction problems [107, 108].

It is evident that the LuGre model reverts to the Dahl model for the following conditions:

$$g(\dot{x}) = \frac{F_C}{\sigma_0}, \quad \sigma_1 = \sigma_2 = 0 \quad (4.72)$$

#### 4.5.2.4 Friction model selection

In this research, the classic Coulomb friction model will be employed for both the analytical and numerical modelling. The main reason behind this choice is that the model, despite its simplicity, can capture the necessary physics to describe the mechanical response of mesh materials. As will be discussed further later in Section 4.7, several models exist that combine the Hertz contact theory with the Coulomb friction model for describing the frictional contact mechanics of elastic bodies. These models have been largely adopted in the literature and validated both through experiments and numerical analysis. In general, these models interpret the contact non-linearity as a consequence of the sliding not being achieved simultaneously in the entire interface of contact but rather progressively, with a rate that depends on the elastic properties of the materials and the friction coefficient.

The same non-linear microslip response could be represented also through the dynamic friction models discussed previously, such as for instance the Dahl model.

However in this case the non-linearity is ascribed to the plastic deformation occurring at the contact interface, instead of the elastic strain distribution accounted for by the Hertz theory. Moreover, the employment of the Dahl model relies on experimental data for the determination of its fitting parameters.

<b>Materials</b>	<b>Friction coefficient</b>
Steel-steel	0.30
Nitinol-Nitinol	0.18
Nitinol-steel	0.4

**Table 4.2:** Friction coefficient for the different material combinations.

In Table 4.2, the friction coefficients that will be utilised in the analytical and numerical models are reported for each constituent material combination. The friction coefficient for the Nitinol-Nitinol configuration was found through experimental tests by DellaCorte [109].

## 4.6 Tension-compression model

In this section, a novel analytical model is presented, which describes the mechanical response of plain-weave mesh materials to tension-compression load. As described previously, the model is based on Castigliano’s theory for elastic materials. The wires are considered as sinusoidally curved beams with the wire-to-wire interaction being achieved via Hertz’s contact theory.

Initially, the equivalent longitudinal stiffness of a wire that is decoupled from the mesh is derived. Then, the formulation is extended to account for the interaction of warp/weft wires within the RUC, by solving a set of simultaneous equations that define the kinetics of each wire.

The model defines a set of effective properties (stiffness and Poisson’s ratio) for the characterisation of PWMMs, which are calculated based on the geometrical and mechanical properties of the material and the contact between the wires. An

averaged formulation of the same properties is also provided, which will be used in the subsequent implementation of the model in a MATLAB-ANSYS environment.

### 4.6.1 Elastic stiffness of a single wire (decoupled)

As previously introduced and verified through image analysis (see Section 3.3.1.1), given the highly ordered repetitiveness of the structure, the longitudinal path of the wires can be considered periodic and described by a sinusoidal wave:

$$z(x) = Z \sin\left(\frac{\pi x}{L}\right) \quad (4.73)$$

where  $Z$  is the amplitude of the sine wave and  $L$  is the semi-wavelength which is equal to the sum of wire diameter and aperture of the mesh. The cross-sectional geometric shape is assumed as a circle of constant diameter always orthogonal to the centreline.

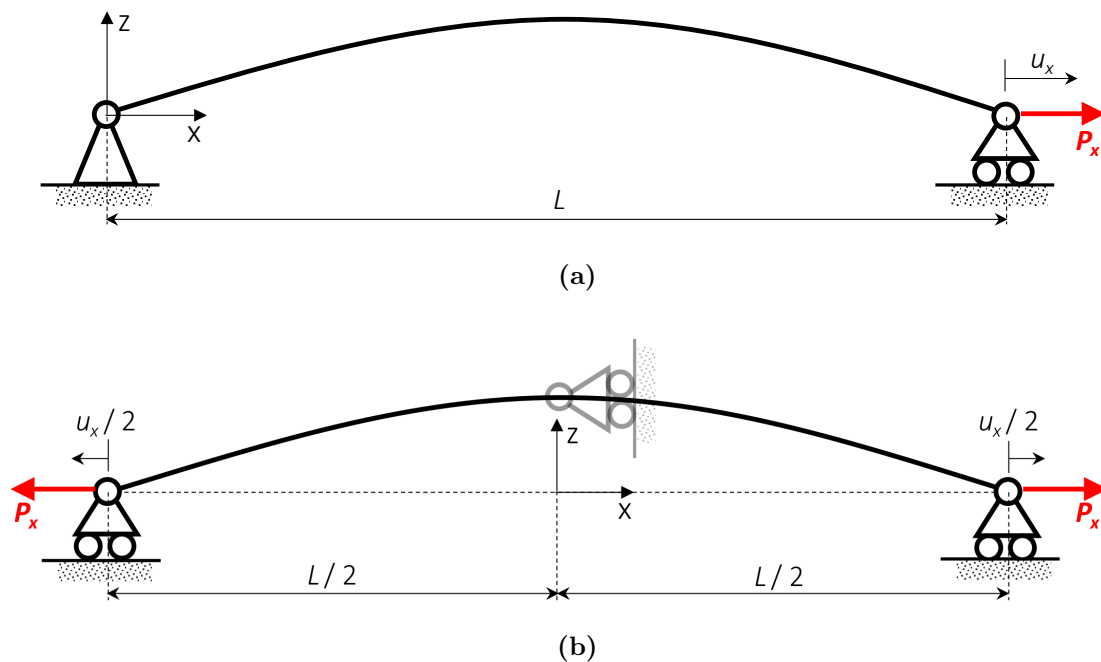


**Figure 4.9:** Boundary conditions of a single wire: (a) pin-roller supported beam and (b) roller-roller supported beam.

Consider only a portion  $L$  of a decoupled wire, constrained as in Figure 4.9a. When the wire is subjected to a uniaxial tensile load  $P_x$ , the longitudinal deformation  $u_x$  can be calculated by means of Castigliano's theorem (see Equation 4.33), returning the following expression:

$$u_x = \frac{P_x Z^2 L}{2EI} + \frac{P_x L^2}{EA\sqrt{Z^2\pi^2 + L^2}} + \chi \frac{P_x}{GA} \left( \frac{L\sqrt{Z^2\pi^2 + L^2} - L^2}{\sqrt{Z^2\pi^2 + L^2}} \right) \quad (4.74)$$

The same segment of wire can be also imagined as constrained at both extremities by a roller support, as in Figure 4.9b, with analogous kinematic results. In this case, the external load  $P_x$  is applied at both sides, and to preserve the structure stability a third roller support is included mid-span (represented with a faded line since in reality it does not produce any reaction). The overall displacement is now referred to a local coordinate frame located at mid-span and the total deformation  $u_x$  is equally subdivided between the two sides of the beam.

To deeper investigate the relationship between stiffness and curvature of the wires, a new parameter, *waviness ratio*, is now introduced, as the ratio of the wire's amplitude to the semi-wavelength:

$$\psi = \frac{Z}{L} \quad (4.75)$$

Substituting the previous into Equation 4.74 and rearranging, it yields:

$$u_x = \left( \frac{L^3\psi^2}{2EI} + \frac{L}{EA\Psi} + \chi \frac{L(\Psi - 1)}{GA\Psi} \right) P_x \quad (4.76)$$

where  $\Psi = \sqrt{1 + \psi^2\pi^2}$ . For a straight wire,  $\psi = 0$  and the previous equation reduces to only the normal force component, which corresponds to the axial deformation of a bar:

$$u_x = \frac{LP_x}{EA} \quad (4.77)$$

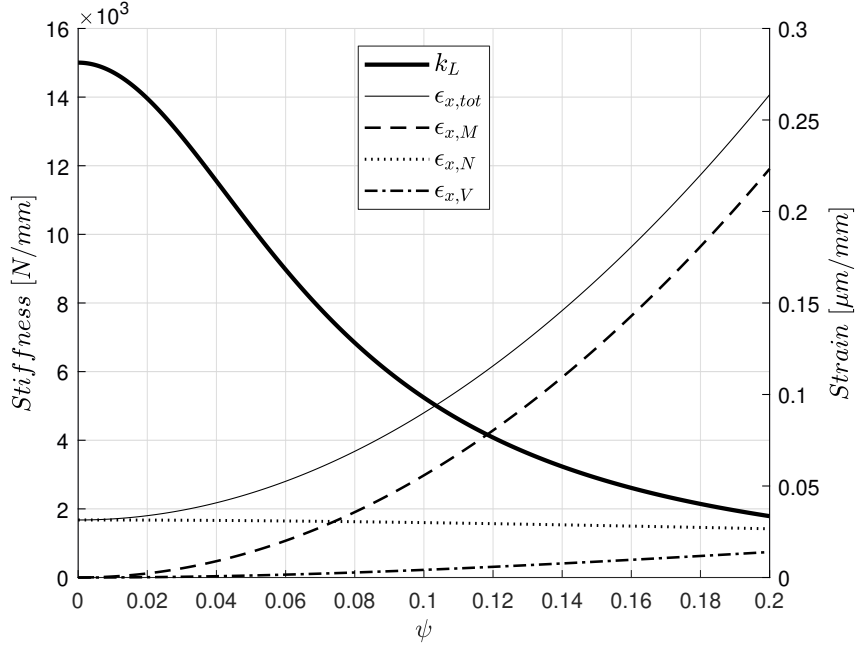


**Figure 4.10:** Stiffness and strain of a single wire at various  $\psi$ .

The static longitudinal stiffness of a single segment of wire is given by:

$$k_L = \frac{P_x}{u_x} = \frac{1}{\left( \frac{L^3 \psi^2}{2EI} + \frac{L}{EA\Psi} + \chi \frac{L(\Psi-1)}{GA\Psi} \right)} \quad (4.78)$$

where the subscript  $L$  denotes that the expression is referred to only a portion  $L$  of the wire.

The stiffness so calculated is constant with deformation and only depends on mechanical ( $E$ ,  $G$ ) and geometrical ( $L$ ,  $A$ ,  $I$ ,  $\psi$ ,  $\chi$ ) properties of the structure. It is only valid under the assumptions of small deflections and linear elasticity, according to Castigliano's theory. For this reason it does not account for non-linear behaviour due to large deflections or plasticity phenomena.

Recalling that the strain is defined as the ratio of the deformation  $\Delta L$  to the initial length  $L_0$  of a body subjected to a state of stress, the normal strain of a single wire can be approximated by the following expression:

Diameter	$d$	mm	0.45
Length	$L$	mm	2.12
Elastic modulus	$E$	GPa	200
Poisson's ratio	$\nu$		0.3

**Table 4.3:** Wire properties.

$$\epsilon_x = \frac{u_x}{L} \quad (4.79)$$

where  $L$  is again the semi-wavelength of the wire. The total strain can be subdivided into different components to analyse the influence of each internal force on the overall behaviour as  $\psi$  changes:

$$\epsilon_{x,M} = \frac{u_{x,M}}{L} = \frac{L^2 \psi^2 P_x}{2EI} \quad (4.80a)$$

$$\epsilon_{x,N} = \frac{u_{x,N}}{L} = \frac{P_x}{EA\Psi} \quad (4.80b)$$

$$\epsilon_{x,V} = \frac{u_{x,V}}{L} = \frac{\chi(\Psi - 1)P_x}{GA\Psi} \quad (4.80c)$$

where the subscripts  $M$ ,  $N$  and  $V$  denote the strain components of bending moment, normal and shear force.

In Figure 4.10, the stiffness and strain of a single wire under a tensile load of 1N are shown for different values of the waviness ratio  $\psi$ . The dimensions and material properties of the wire are described in Table 4.3. The stiffness, maximum for  $\psi = 0$  (i.e. straight bar), reduces significantly as the waviness increases. This is mostly due to the effect of bending moment that grows quadratically with  $\psi$ , and to a lesser extent to the internal shear, as is apparent from the different strain components.

## 4.6.2 Warp/weft wire interaction

The study of kinematics of mesh materials necessarily involves the understanding of the interaction between the wires associated with motion and how this affects the overall mechanical properties of the system.

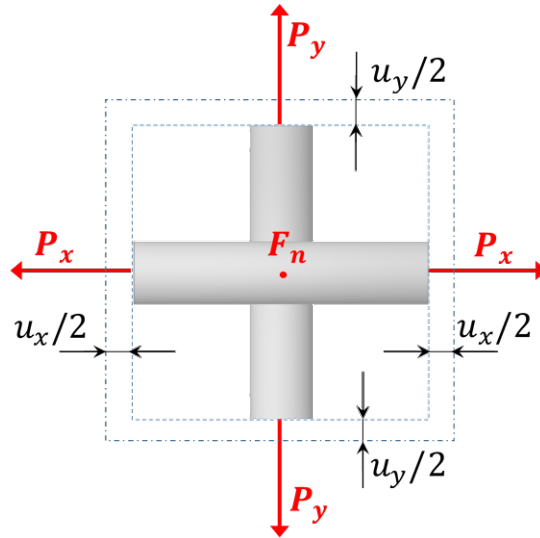


**Figure 4.11:** Schematisation of plain-weave RUC under biaxial tension.

Consider a single mesh unit cell composed of two interwoven sinusoidal wires orthogonal to each other like the one in Figure 4.11. As previously introduced, the unit cell can be thought as an infinitesimal element of an equivalent homogenous material. Therefore, its mechanical response can be characterised by a set of effective properties, such as elastic stiffness and Poisson's ratio. These properties, as will be shown below, are a function of the warp/weft contact force.

Suppose, as a first example, that an axial force  $P_x$  is only applied to the warp wire. For a wire with a waviness ratio  $>0$ , this will cause an elastic elongation of the wire along the x-axis, combined with a reduction of its amplitude. However, this vertical movement is counteracted by the presence of the weft wire that exerts a reaction through contact. If an axial force  $P_y$  is also applied to the weft wire, the reaction that this opposes to the warp wire is increased further. In both cases, the

response to tension load of the RUC depends not only on the stiffness of the wire along the load direction, but also on the stiffness of the orthogonal wire, because of the mutual reaction exerted through contact.

In general, in the presence of tension load, the contact force at the warp/weft wire intersections is responsible for increasing the overall stiffness of the structure, as compared to the stiffness of a decoupled wire discussed before. With the methodology adopted in this work, contact phenomena are incorporated in the effective properties and considered as internal forces.

#### 4.6.2.1 Contact force

For a RUC under a system of longitudinal forces  $P_x$  and  $P_y$  such as the one in Figure 4.11, in the absence of torsional rotation of the wires about their longitudinal axis, the contact force between the warp/weft pair can be assumed as:

- i) Concentrated and applied to the middle section of the wire.
- ii) Always directed normally to the mesh plane (i.e., z-axis).

Consider now the diagram of the warp wire only, reported in Figure 4.12. This is similar to the one of a decoupled wire, with the addition of the contact force  $F_n$ .

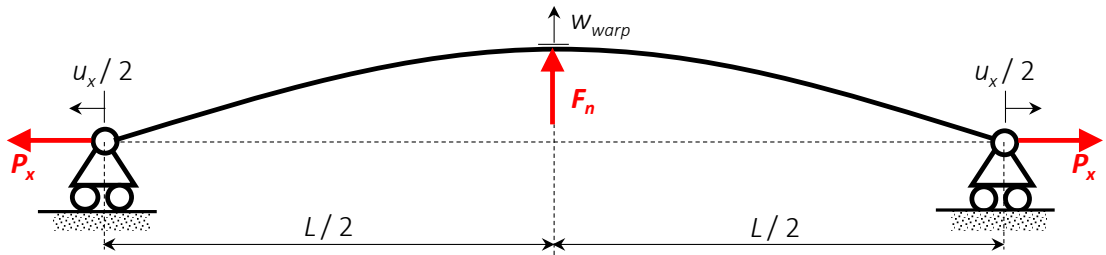


**Figure 4.12:** Diagram of warp wire with loads and boundary conditions.

The displacement  $w$  (at the mid-span) along the z-axis can be calculated by means of Castigliano's theorem (Equation 4.33), as a function of the applied forces:

$$w_{\text{warp}} = C_1 P_x + C_2 F_n \quad (4.81)$$

where:

$$C_1 = -\frac{L^3 \psi}{EI\pi^2} + \frac{L \tanh^{-1}\left(\frac{\pi\psi}{\Psi}\right)}{EA\pi\Psi} - \chi \frac{L \tanh^{-1}\left(\frac{\pi\psi}{\Psi}\right)}{GA\pi\Psi} \quad (4.82a)$$

and:

$$C_2 = \frac{L^3}{48EI} + \frac{L(\Psi - 1)}{4EA\Psi} + \frac{\chi L}{4GA\Psi} \quad (4.82b)$$

where again  $\psi = Z/L$  and  $\Psi = \sqrt{1 + \psi^2 \pi^2}$ .

The same can be done for the weft wire, remembering that the sign must be changed to preserve the consistency with the coordinate system:

$$w_{\text{weft}} = -(C_1 P_y + C_2 F_n) \quad (4.83)$$

The displacements calculated with Equations 4.81 and 4.83 are referred to a point lying on the neutral axis of the wire. However, in actuality the force is exerted through a contact area that lies on the external surface of the wire. The total force of contact can be considered as applied to a point  $C$  shared between the wires, which corresponds to the centre of the contact area. Recalling the Hertz theory, when two elastic bodies are pressed together into contact, a normal deformation  $\delta_H$  is generated on the contact area that represents the mutual approach of the bodies (also referred to as penetration depth):

$$\delta_H = \frac{a^2}{R} \quad (4.84)$$

where  $a$  is the radius of the contact area and  $R$  is the effective radius of curvature. By neglecting their longitudinal curvature, the wires can be reduced to straight cylinders initially crossed with perpendicular axes. Thus, recalling the case of

two cylinders in contact with perpendicular axes, the radius of the contact area is expressed by Equation 4.39, where the effective radius of curvature is calculated as  $R = \sqrt{R_1 R_2}$ . Considering same radius  $r$  for both warp and weft wires, the effective radius reduces to simply  $R = r$ . Combining Equation 4.39 with Equation 4.84, it returns:

$$\delta_H = \left( \frac{3}{4E^* \sqrt{r}} \right)^{2/3} F_n^{2/3} \quad (4.85)$$

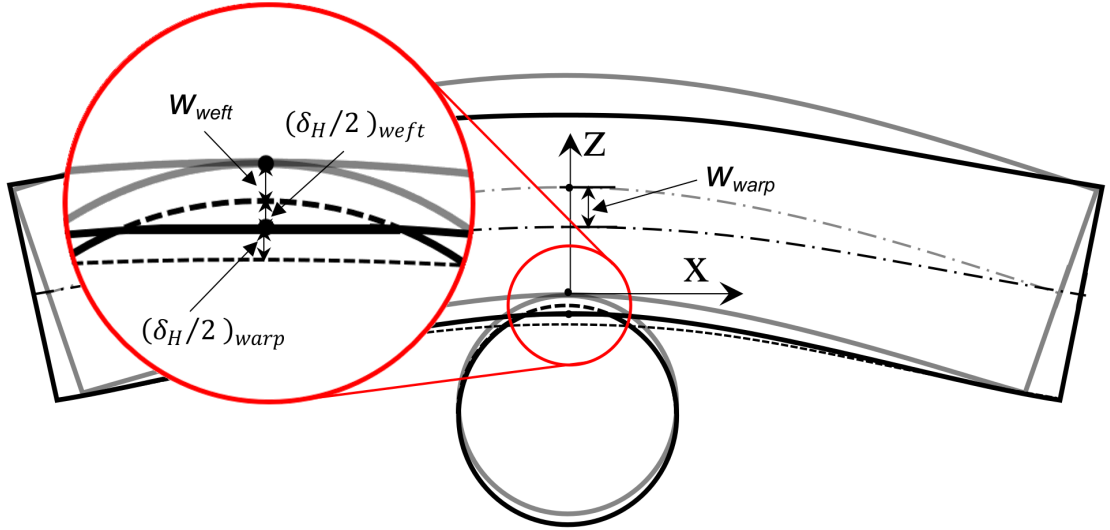


**Figure 4.13:** Kinematics of RUC under tensile load.

As represented in Figure 4.13, as regards the warp wire, the displacement magnitude of the neutral axis along the z-axis is given by the sum of the displacement magnitude of the contact point and the contact normal compression of the body (which for one wire corresponds to half the Hertzian mutual approach):

$$|w_{warp}| = |w_C| + \frac{\delta_H}{2} \quad (4.86)$$

Since the point of contact is a shared entity between the wires, the same relation must be valid also for the weft wire, now changing the sign of the contact compression:

$$|w_{weft}| = |w_C| - \frac{\delta_H}{2} \quad (4.87)$$

For the case represented in Figure 4.13,  $|w_{warp}| = -w_{warp}$ ,  $|w_{weft}| = -w_{weft}$  and  $|w_C| = -w_C$  since they are all negative in sign. Hence, replacing the absolute value and rearranging the previous two equations, it yields:

$$w_C = w_{warp} + \frac{\delta_H}{2} \quad (4.88a)$$

$$w_C = w_{weft} - \frac{\delta_H}{2} \quad (4.88b)$$

Substituting Equation 4.81 into Equation 4.88a and Equation 4.83 into Equation 4.88b, it returns the following system of two equations:

$$\begin{aligned} w_C &= C_1 P_x + C_2 F_n + \frac{\delta_H}{2} \\ -w_C &= C_1 P_y + C_2 F_n + \frac{\delta_H}{2} \end{aligned} \quad (4.89)$$

Solving the system by addition, it yields:

$$2C_2 F_n + \delta_H + C_1 (P_x + P_y) = 0 \quad (4.90)$$

Substituting Equation 4.85 into the previous, it returns:

$$2C_2 F_n + \left( \frac{3}{4E^* \sqrt{r}} \right)^{2/3} F_n^{2/3} + C_1 (P_x + P_y) = 0 \quad (4.91)$$

Let  $A$ ,  $B$  and  $D$  be the coefficients of the previous equation, as follows:

$$A = 2C_2 \quad (4.92a)$$

$$B = \left( \frac{3}{4E^* \sqrt{r}} \right)^{2/3} \quad (4.92b)$$

$$D = C_1 (P_x + P_y) \quad (4.92c)$$

The root of the cubic equation can be found by means of Cardano's formula [110]:

$$F_n = \left[ -\frac{B}{3A} + \sqrt[3]{-\frac{Q}{2} + \sqrt{\Delta}} + \sqrt[3]{-\frac{Q}{2} - \sqrt{\Delta}} \right]^3 \quad (4.93)$$

The quantity  $\Delta$  is the discriminant of the cubic equation, calculated as follows:

$$\Delta = \frac{Q^2}{4} + \frac{P^3}{27} \quad (4.94)$$

where:

$$P = -\frac{B^2}{3A^2} \quad (4.95a)$$

$$Q = \frac{D}{A} + \frac{2B^3}{27A^3} \quad (4.95b)$$

Equation 4.93 expresses the contact force  $F_n$  as a function of the tension forces  $P_x$  and  $P_y$ . This two-variable function depends on the sum of the tension forces, implying that whichever combination of tension forces that returns the same sum, would yield the same contact force. Thereby, a new variable  $P_{(x+y)} = P_x + P_y$  is introduced so that  $F_n = f(P_{(x+y)})$ . Moreover, the function is not additively separable, meaning that no functions  $g(P_x)$  and  $h(P_y)$  exist, such that  $f(P_x, P_y) = g(P_x) + h(P_y)$  (as could be verified with the rectangle theorem [111]).

It is important noticing that, for obvious physical reasons, only real solutions are of interest, and thus only real cube roots must be considered. A necessary condition is that the discriminant  $\Delta \geq 0$ . In fact, any negative value of  $\Delta$  indicates that the deformation of the unit cell is such that the wires are not in contact any more and a gap is generated between them. Such conditions occur when a state

of compression is applied to the mesh material and the contact force has become null.

It is also worth noting that the sign convention was chosen so that the contact force is positive for the configuration in Figure 4.13, meaning that it is directed upwards in the  $z$ -axis and acting upon the warp wire. An opposite reaction  $-F_n$  is acting upon the weft wire.

All the previous analysis was based on the configuration in Figure 4.13 where warp and weft wires have respectively downwards and upwards concavity with respect to the  $z$ -axis; nevertheless, it is still equally valid for the opposite configuration, just by reversing the sign of Equations 4.81 and 4.83.

In Figure 4.14, the real solutions of Equation 4.93 are plotted as a function of the sum of the tension forces  $P_{(x+y)}$ .

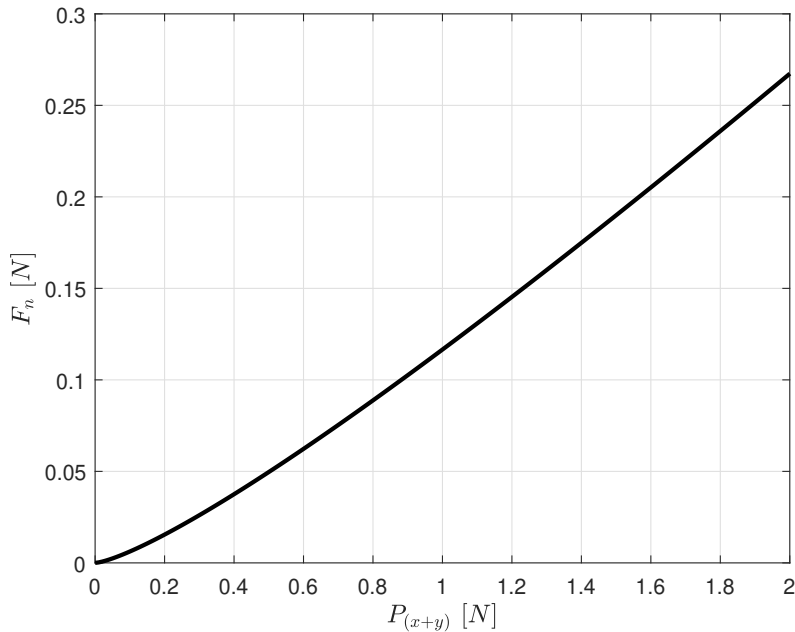


**Figure 4.14:** Contact force as a function of total tension force  $P_{(x+y)}$ .

The graph is relative to a single unit cell of mesh material and the wire properties are the same as in Table 4.3, being in this case  $Z = d/2$ . A slight non-linearity of the function is evident for lower values of tension, when the compression of

the contact area (represented by a rational exponent) produces a noticeable effect, whereas for higher values, the linear term associated to elasticity becomes dominant.

#### 4.6.2.2 Effective stiffness

Consider the case of a unit cell subjected to a tension force  $P_x$  applied to the warp wire, whilst the weft wire is free at both extremities to move along the y-axis, so that there is no external force  $P_y$  to oppose resistance to the motion. In such conditions, Equation 4.93 reduces to a function of only the variable  $P_x$ .

Considering the static equilibrium of a wire subjected to a tension force  $P_x$  and a constant contact force  $F_n$ , the longitudinal deformation of the wire can be calculated with the Castigliano's theorem as follows:

$$u_x = C_3 P_x + C_1 F_n \quad (4.96)$$

where  $C_3$  is the inverse of the stiffness  $k_L$  of a single decoupled wire (from Equation 4.78) and  $C_1$  is the coefficient from Equation 4.82a.

Since the force  $F_n$  changes with the displacement, it is possible to express the previous relation in infinitesimal terms:

$$\delta u_x = \left( C_3 + C_1 \frac{dF_n}{dP_x} \right) \delta P_x \quad (4.97)$$

The non-linear longitudinal effective stiffness of the unit cell is then calculated as the ratio of the tension force to the longitudinal displacement:

$$K_{eff} = \frac{\delta P_x}{\delta u_x} = \frac{1}{\left( C_3 + C_1 \frac{dF_n}{dP_x} \right)} \quad (4.98)$$

A new stiffness term can be introduced, which is proportional to the contact force:

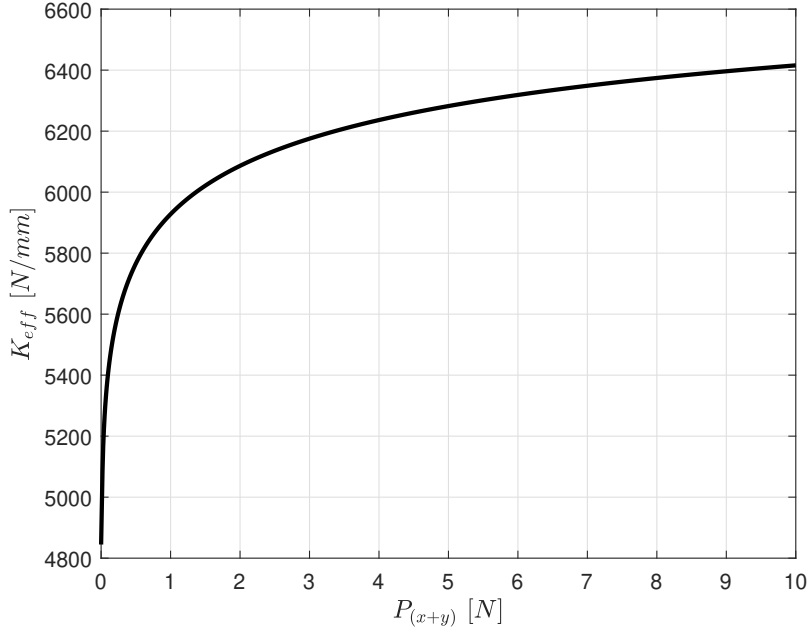


**Figure 4.15:** Effective stiffness of RUC.

$$k_c = \frac{1}{C_1 \frac{dF_n}{dP_x}} \quad (4.99)$$

Substituting the previous expression and  $C_3 = 1/k_L$  into Equation 4.98, it returns:

$$K_{eff} = \frac{1}{\left(\frac{1}{k_L} + \frac{1}{k_c}\right)} = \frac{k_L \cdot k_c}{k_L + k_c} \quad (4.100)$$

which corresponds to the equivalent stiffness of two springs in series.

In Figure 4.15, the effective stiffness from Equation 4.98 is reported. The properties from Table 4.3 are used. As introduced above, the interaction between warp and weft wires increases the stiffness of the structure, which is theoretically equal to the stiffness of a decoupled wire when no tension force is applied. This stiffening effect can be easily visualised also in Figure 4.16, where the non-linear deformation of the RUC (solid line) is compared to the linear elongation of a decoupled wire (dashed line), both subjected to uniaxial tension, the first diverging from the second as the contact force grows.

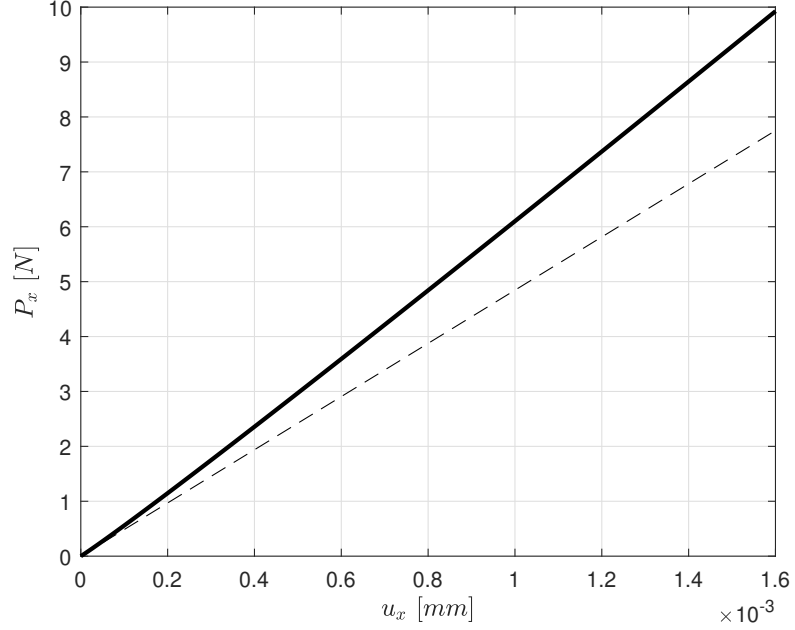


**Figure 4.16:** Force-displacement curve for the RUC (solid line) and a decoupled wire (dashed line).

#### 4.6.2.3 Effective Poisson's ratio

Consider again the general case of a mesh material unit cell subjected to a biaxial state of tension, such as the one in Figure 4.11. Recalling that the contact force can be expressed as a function of a single variable  $P_{(x+y)} = P_x + P_y$ , the infinitesimal deformation of the warp wire along the x-axis takes the following form:

$$\delta u_x = C_3 \delta P_x + C_1 \frac{dF_n}{dP_{(x+y)}} \delta P_{(x+y)} \quad (4.101)$$

Since  $\delta P_{(x+y)} = \delta P_x + \delta P_y$ , the previous equation can be reformulated as follows:

$$\delta u_x = \left( C_3 + C_1 \frac{dF_n}{dP_{(x+y)}} \right) \delta P_x + \left( C_1 \frac{dF_n}{dP_{(x+y)}} \right) \delta P_y \quad (4.102)$$

Multiplying each side by  $K_{eff}$  and substituting Eq. 4.51 into Eq. 4.54, it returns:

$$K_{eff}\delta u_x = \delta P_x + \frac{K_{eff}}{k_c}\delta P_y \quad (4.103)$$

A new quantity is now introduced that represents the effective Poisson's ratio of the mesh material:

$$\nu_{eff} = -\frac{K_{eff}}{k_c} = -\frac{k_L}{k_L + k_c} \quad (4.104)$$

It may be noted that, despite the negative sign in the previous equation, the Poisson's ratio is still a positive quantity, since the denominator is itself a negative number.

Another reasoning would lead to the same conclusions. In fact, the Poisson's ratio of a material is by definition the negative of the ratio of the transverse strain to the axial strain for a uniaxial state of stress:

$$\nu = -\frac{d\epsilon_y}{d\epsilon_x} \quad (4.105)$$

In the case of mesh materials, under the assumption of same initial length for warp and weft wires, the strain can be replaced by the elongation of the wires:

$$\nu_{eff} = -\frac{\delta u_y}{\delta u_x} \quad (4.106)$$

By means of Castigliano's theorem, an expression for the longitudinal deformation of the weft wire can be derived (analogous to Equation 4.96 for the warp wire):

$$u_y = C_3 P_y + C_1 F_n \quad (4.107)$$

Expressing the previous relation in infinitesimal terms and applying the same substitutions as in Equation 4.102, it returns:

$$\delta u_y = \left( C_3 + C_1 \frac{dF_n}{dP_{(x+y)}} \right) \delta P_y + \left( C_1 \frac{dF_n}{dP_{(x+y)}} \right) \delta P_x \quad (4.108)$$

Considering again the case of a uniaxial tension  $P_x$ , Equations 4.102 and 4.108 reduce to:

$$\delta u_x = \left( C_3 + C_1 \frac{dF_n}{dP_{(x+y)}} \right) \delta P_x \quad (4.109a)$$

$$\delta u_y = \left( C_1 \frac{dF_n}{dP_{(x+y)}} \right) \delta P_x \quad (4.109b)$$

Finally, combining Equations 4.109a and 4.109b with Equation 4.106, it yields:

$$\nu_{eff} = - \frac{\left( C_1 \frac{dF_n}{dP_{(x+y)}} \right)}{\left( C_3 + C_1 \frac{dF_n}{dP_{(x+y)}} \right)} = - \frac{K_{eff}}{k_c} \quad (4.110)$$

which corresponds to Equation 4.104.

Substituting Equation 4.104 into Equation 4.103, it returns:

$$K_{eff} \delta u_x = \delta P_x - \nu_{eff} \delta P_y \quad (4.111)$$

The previous expression is analogous to the equilibrium equation for an infinitesimal isotropic material element subjected to bi-axial tension.

With the same considerations, the expression for the weft wire deformation  $\delta u_y$  can be found:

$$K_{eff} \delta u_y = -\nu_{eff} \delta P_x + \delta P_y \quad (4.112)$$

The system of Equations 4.111 and 4.112 can be expressed in the following matrix form:

$$\begin{Bmatrix} \delta u_x \\ \delta u_y \end{Bmatrix} = \frac{1}{K_{eff}} \begin{bmatrix} 1 & -\nu_{eff} \\ -\nu_{eff} & 1 \end{bmatrix} \begin{Bmatrix} \delta P_x \\ \delta P_y \end{Bmatrix} \quad (4.113)$$

In Figure 4.17, the effective Poisson's ratio from Equation 4.104 is reported as a function of the contact force. The properties from Table 4.3 are utilised. The value is initially zero when there is no contact force between the wires. Then it increases abruptly due to the establishment of the contact interaction.

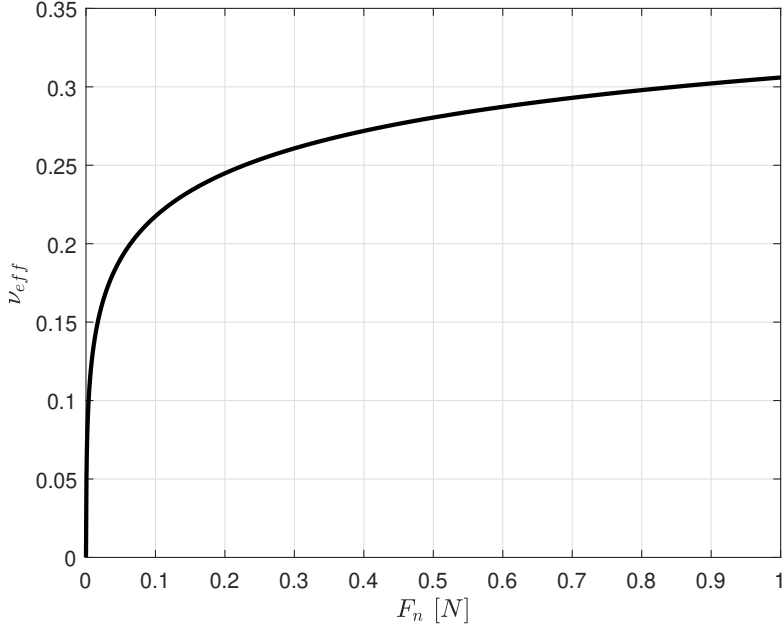


**Figure 4.17:** Effective Poisson's ratio of RUC.

#### 4.6.2.4 Linearised mechanical properties

Given a general bi-axial state of tension  $P_x$  and  $P_y$ , to find the displacements  $u_x$  and  $u_y$ , it is necessary to integrate Equation 4.113. Before, however, some manipulations are required to express the equations in terms of a common differential of integration. Assuming that, throughout the application of the forces, the ratios  $\zeta_1 = \delta P_x / \delta P_{(x+y)}$  and  $\zeta_2 = \delta P_y / \delta P_{(x+y)}$  remain constant, Equation 4.102 is reformulated as follows:

$$\delta u_x = \left( C_3 + C_1 \frac{dF_n}{dP_{(x+y)}} \right) \zeta_1 \delta P_{(x+y)} + \left( C_1 \frac{dF_n}{dP_{(x+y)}} \right) \zeta_2 \delta P_{(x+y)} \quad (4.114)$$

Integrating with respect to  $P_{(x+y)}$ , it returns:

$$u_x = (C_3 P_{(x+y)} + C_1 F_n) \zeta_1 + (C_1 F_n) \zeta_2 \quad (4.115)$$

The force ratios are also equal to  $\zeta_1 = P_x/P_{(x+y)}$  and  $\zeta_2 = P_y/P_{(x+y)}$ . Therefore, the previous equation becomes:

$$u_x = \left( C_3 + C_1 \frac{F_n}{P_{(x+y)}} \right) P_x + \left( C_1 \frac{F_n}{P_{(x+y)}} \right) P_y \quad (4.116)$$

The following two new linearised properties are now introduced:

$$\bar{K} = \frac{1}{\left( C_3 + C_1 \frac{F_n}{P_{(x+y)}} \right)} \quad (4.117a)$$

$$\bar{\nu} = -C_1 \frac{F_n}{P_{(x+y)}} \bar{K} \quad (4.117b)$$

The previous equations represent respectively a linearised effective stiffness and a linearised effective Poisson's ratio. These properties only depend on the final value of  $P_{(x+y)}$  and describe a hypothetical linear elastic deformation during which stiffness and Poisson's ratio do not vary with the force. They are not able to capture the instantaneous changing of the material properties throughout the deformation. Instead, they are only valid to calculate the final displacement, given the applied system of forces. This is represented in Figure 4.18, that shows a comparison between the non-linear and the linearised force-displacement response to tension.

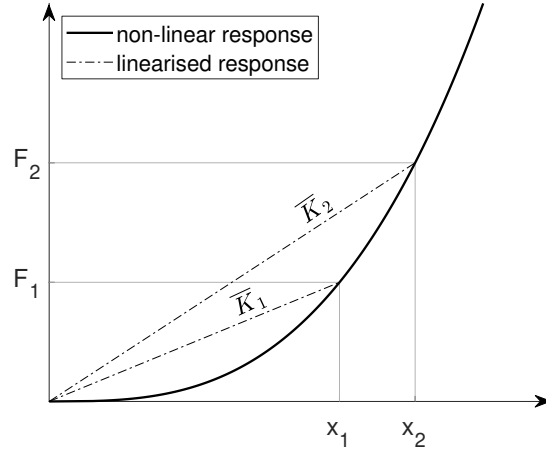


**Figure 4.18:** Comparison between non-linear and linearised response to tension (non-linearity is emphasized for better clarity).

As will be explained in more details in Chapter 6, these properties will be used for the stiffness characterisation of mesh materials in the developed reduced order finite element model. In Figure 4.19 the linearised stiffness and Poisson’s ratio are compared to the corresponding effective properties, showing a similar trend however with lower values along the whole range of tension forces.

Combining Equations 4.117a and 4.117b with Equation 4.116, it returns:

$$\bar{K}u_x = P_x - \bar{\nu}P_y \quad (4.118)$$

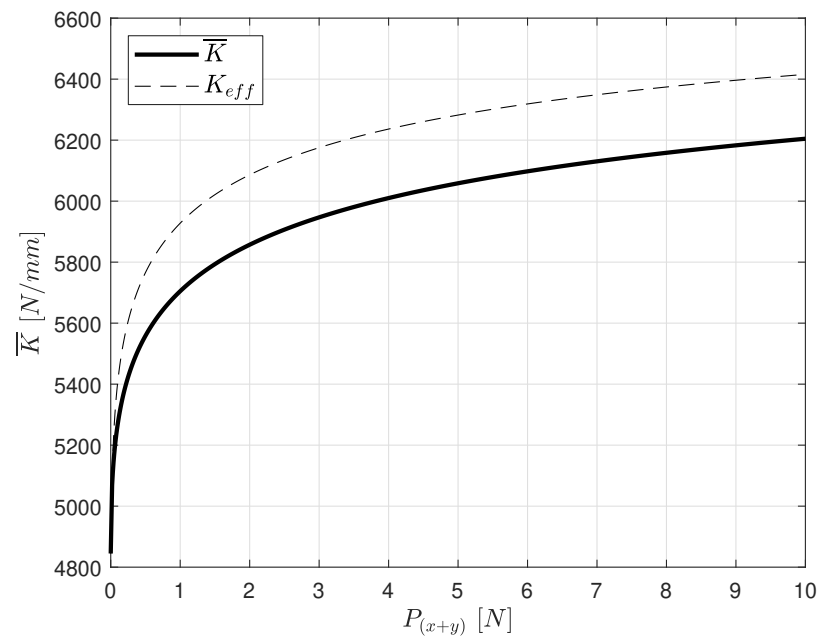
The same procedure can be applied to find the deformation of the weft wire:

$$\bar{K}u_y = -\bar{\nu}P_x + P_y \quad (4.119)$$

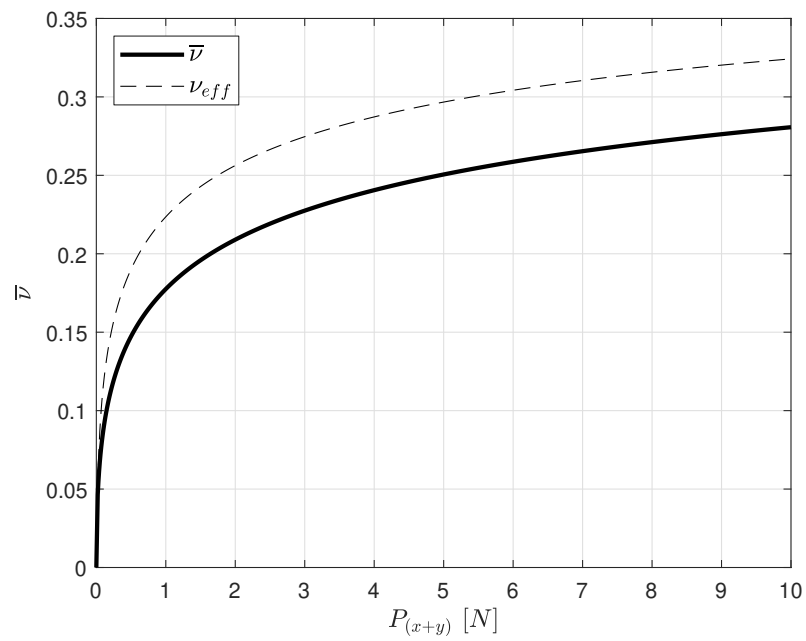
The previous equations can be expressed in a matrix form, as follows:

$$\begin{Bmatrix} u_x \\ u_y \end{Bmatrix} = \frac{1}{\bar{K}} \begin{bmatrix} 1 & -\bar{\nu} \\ -\bar{\nu} & 1 \end{bmatrix} \begin{Bmatrix} P_x \\ P_y \end{Bmatrix} \quad (4.120)$$

The previous matrix is analogous to the plane stress compliance matrix for an isotropic material.



(a)



(b)

**Figure 4.19:** Linearised effective properties: (a) stiffness and (b) Poisson's ratio.

#### 4.6.2.5 Orthotropic effective properties

All the previous equations are based on the assumption that warp and weft wires share the same mechanical properties.

For a more general case where they are built in different materials, a set of coefficients  $C_1$ ,  $C_2$  and  $C_3$  is calculated for each wire from Equations 4.82a, 4.82b and 4.78, by changing the material properties  $E$ ,  $G$  and  $\nu$  with the ones of the respective wire. As regards the contact force  $F_n$ , in Equation 4.93 the coefficients  $A$  and  $D$  are calculated as follows:

$$A = C_{2,warp} + C_{2,weft} \quad (4.121a)$$

$$D = C_{1,warp}P_x + C_{1,weft}P_y \quad (4.121b)$$

Hence, in this case the contact force cannot any longer reduce to a function of the variable sum  $P_{x+y}$ : instead, it depends separately on both the values of the tension forces  $P_x$  and  $P_y$ .

A set of effective linearised properties is calculated for each wire, as follows:

$$\bar{K}_{warp} = \frac{1}{\left(C_{3,warp} + C_{1,warp} \frac{F_n}{P_{(x+y)}}\right)} \quad (4.122a)$$

$$\bar{\nu}_{warp} = -C_{1,warp} \frac{F_n}{P_{(x+y)}} \bar{K}_{warp} \quad (4.122b)$$

$$\bar{K}_{weft} = \frac{1}{\left(C_{3,weft} + C_{1,weft} \frac{F_n}{P_{(x+y)}}\right)} \quad (4.122c)$$

$$\bar{\nu}_{weft} = -C_{1,weft} \frac{F_n}{P_{(x+y)}} \bar{K}_{weft} \quad (4.122d)$$

The relation between deformations and applied forces can be expressed by the following matrix form:

$$\begin{Bmatrix} u_x \\ u_y \end{Bmatrix} = \begin{bmatrix} \frac{1}{\bar{K}_{warp}} & \frac{-\bar{\nu}_{warp}}{\bar{K}_{warp}} \\ \frac{-\bar{\nu}_{weft}}{\bar{K}_{weft}} & \frac{1}{\bar{K}_{weft}} \end{bmatrix} \begin{Bmatrix} P_x \\ P_y \end{Bmatrix} \quad (4.123)$$

The previous matrix is analogous to the plane stress compliance matrix for an orthotropic material, where the main directions are identified by the two intersected wires.

## 4.7 Shear model

In this section, the shear model is presented, that predicts the response of plain-weave mesh materials for in-plane shear.

Recalling from the introduction, when a plain-weave mesh material is subjected to in-plane shear, this generates a relative rotation of warp and weft wires at their points of intersection. This relative motion, combined with the normal contact force exerted between the wires, dissipates energy through dry friction. As previously mentioned, the model is based on a detailed investigation on the contact mechanics of mesh materials, which involves the determination of the contact area shape and dimensions throughout the application of the load. This is achieved by employing the Hertz's contact theory and Lubkin's frictional torque formulation to the specific geometry of PWMs.

Initially, a novel approximation for the Lubkin's function is presented, which replaces the original use of elliptic integrals with a less computational expensive polynomial form.

The proposed approximation is then applied to the case of elastic spheres in contact and compared with the original formulation as a validation. Finally, the proper in-plane shear model is presented, by extending the previous formulation to the case of elastic cylinders in contact. The model is then applied to predict the hysteretic response of mesh materials to a cyclic load.

### 4.7.1 Lubkin's theory

The problem of two elastic bodies in contact subjected to relative motion was independently studied by Mindlin [112], Lubkin [50] and Cattaneo [113]. Mindlin found a solution for two spheres under tangential slipping, which was validated experimentally by Johnson [114].

In this section, the Lubkin's theory for the case of two spheres in contact under mutual torsional moment is introduced. This theory is widely adopted in the literature and large validation is available, both numerically [115, 116] and experimentally [117]. Recalling the Hertzian contact theory, if two elastic spheres are pressed together by a load  $P$ , this generates a circular and plane contact area whose radius  $a$  is defined by Equation 4.39. The normal pressure distribution acting upon the contact area is defined by Equation 4.41. When a monotonically increasing torque is applied to the sphere about their common normal, the outer annular portion of the contact area starts slipping progressively, whilst the inner zone, which is delimited by a circle of radius  $a^*$ , deforms elastically. The two regions are represented in Figure 4.20.

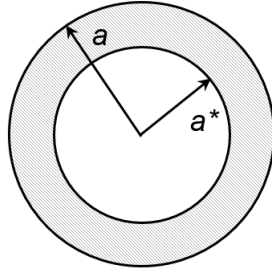


**Figure 4.20:** Sphere-to-sphere frictional torque: slipping and sticking zone of contact area.

The applied torque is calculated as a function of the sticking region radius by integrating the shear stress distribution among the contact area, as follows:

$$\mathfrak{M} = 2\pi \int_0^a \tau(r)r^2 dr \quad (4.124)$$

where  $\tau(r)$  is the shear stress at distance  $r$  from the centre of contact area. In order to solve the previous equation, it is necessary to define the distribution of tangential traction among the contact area. Within the slipping zone this is limited to the maximum compatible with the Coulomb friction law, as follows:

$$\tau(r) = \mu\sigma(r), \quad a^* \leq r \leq a \quad (4.125)$$

where  $\sigma(r)$  is the Hertzian normal pressure at distance  $r$  from the centre and  $\mu$  is the friction coefficient. In the inner stick region of the contact area, the two bodies can be reduced to elastic half-spaces in contact subjected to both normal and transverse pressure. This problem was addressed by Boussinesq (1885), Cerruti (1877) and Mitchell (1899). Lubkin, by applying these differential equations to the case of two spheres of same material in contact, provided with a formulation for the shear stresses among the sticking zone, which is based on elliptic integrals:

$$\tau(r) = \mu\sigma(r) \left\{ 1 + \frac{2}{\pi} [k^2 D(k)F(k', \phi) - K(k)E(k', \phi)] \right\}, \quad r < a^* \quad (4.126)$$

where  $K(k)$  and  $E(k)$  are respectively the complete elliptic integral of first and second kind, and  $F(k', \phi)$  and  $E(k', \phi)$  are the incomplete elliptic integral of first and second kind, as follows:

$$F(k', \phi) = \int_0^\phi \frac{dt}{\sqrt{1 - k'^2 \sin^2 t}} \quad (4.127a)$$

$$E(k', \phi) = \int_0^\phi \sqrt{1 - k'^2 \sin^2 t} dt \quad (4.127b)$$

$$K(k) = F(k, \pi/2) \quad (4.127c)$$

$$E(k) = E(k, \pi/2) \quad (4.127d)$$

$$D(k) = (K(k) - E(k))/k^2 \quad (4.127e)$$

where  $k' = a^*/a$ ,  $k = \sqrt{1 - k'^2}$  and  $\phi = \sin^{-1} \sqrt{\frac{1-r^2/a^{*2}}{1-r^2/a^2}}$ .

Finally substituting Equations 4.125 and 4.126 into Equation 4.124 and solving the integral, it yields the following expression:

$$\mathfrak{M} = \frac{\mu P a}{4\pi} \left\{ \frac{3\pi^2}{4} + k' k^2 [6K(k) + (4k'^2 - 3) D] - 3kK(k) \sin^{-1} k' \right. \\ \left. - 3k^2 \left[ K(k) \int_0^{\frac{\pi}{2}} \frac{\sin^{-1}(k' \sin \phi) d\phi}{(1-k'^2 \sin^2 \phi)^{3/2}} - D(k) \int_0^{\frac{\pi}{2}} \frac{\sin^{-1}(k' \sin \phi) d\phi}{(1-k'^2 \sin^2 \phi)^{1/2}} \right] \right\} \quad (4.128)$$

Lubkin also proposed a solution for the relative twisting angle (defined by Lubkin as half of the absolute rotation of the spheres) due to the applied moment, as a function of the radius of the stick region:

$$\beta = \frac{3\mu P}{4\pi G a^2} k^2 D(k) \quad (4.129)$$

where  $G$  is the shear modulus of the material of the two spheres.

## 4.7.2 Lubkin's function approximation

The solution proposed by Lubkin involves the usage of elliptic integrals, therefore it cannot be solved analytically as a closed-form. Deresiewicz [118] proposed a simplified solution, approximating the elliptic integrals with a power series truncated at the second term. Nevertheless, this relation is only valid for small values of the torsional moment, whilst it tends to diverge from Lubkin's solution for higher values.

In this work, a new approximation for the Lubkin's function is proposed. The main purpose behind this, is to minimise the computational demand of the model

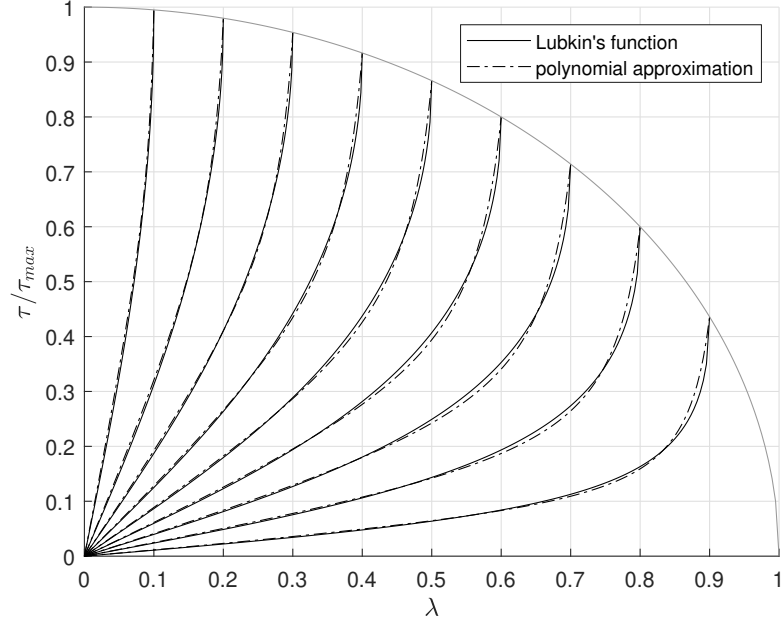


**Figure 4.21:** Lubkin's function approximation.

by replacing the elliptic integrals with a closed-form. This will allow to drastically reduce the calculation time when the model is applied to the study of mesh materials, a crucial aspect to consider, given the high number of contact points involved.

Introducing the ratio  $\lambda = r/a$ , the shear stress in the stick zone can be approximated by a polynomial form:

$$\tau(\lambda) = \frac{3\mu P}{2\pi a^2} \left( A\lambda + B \frac{\lambda^2}{\mathcal{L} - \lambda} \right), \quad \lambda < k' \quad (4.130)$$

The coefficients  $A$ ,  $B$  and  $\mathcal{L}$  of the polynomial are calculated as follows:

$$A = \left( \frac{1 - k'}{k'} \right) \left( 1 + \frac{k'}{2} \right) \frac{2\pi}{9} \quad (4.131a)$$

$$B = \left( \frac{\mathcal{L} - k'}{k'^2} \right) \left( \sqrt{1 - k'^2} - Ak' \right) \quad (4.131b)$$

$$\mathcal{L} = 1 + \alpha\sqrt{1 - k'^2} \quad (4.131c)$$

where  $\alpha$  is a fitting coefficient. High level of accuracy is obtained for  $\alpha=0.09$ .

A comparison between the Lubkin's function and the proposed approximation is presented in Figure 4.21 for different values of  $k'$ , showing good agreement between the two formulations.

### 4.7.3 Solution for elastic spheres in contact

Substituting the pressure distribution in Equation 4.124 with Equation 4.130 and Equation 4.125, it returns:

$$\mathfrak{M} = 2\pi a^3 \left\{ \frac{3\mu P}{2\pi a^2} \left( \int_0^{k'} \left( A\lambda + B \frac{\lambda^2}{\mathcal{L} - \lambda} \right) \lambda^2 d\lambda + \int_{k'}^1 (1 - \lambda^2)^{1/2} \lambda^2 d\lambda \right) \right\} \quad (4.132)$$

Solving the integral, it yields a closed-form for the torsional moment, expressed as a function of  $k'$ . In figure 4.22 the previous equation is compared to the original Lubkin's formulation (Equation 4.128) in non-dimensional form. A new formulation for the torsional angle is also proposed, as a function of  $k'$  and the torsional moment  $\mathfrak{M}$ :

$$\beta = \mathcal{Z} \frac{(k')^{-1} \mathfrak{M}}{Ga^3} \quad (4.133)$$

where  $G$  is the shear modulus of the spheres and  $\mathcal{Z} = 7/34$  is a fitting coefficient. The moment-rotation relation obtained by solving simultaneously Equations 4.132 and 4.133 is illustrated in Figure 4.23 in non-dimensional coordinates. On the same graph the novel proposed approximation is compared with Lubkin's solution, showing high agreement.

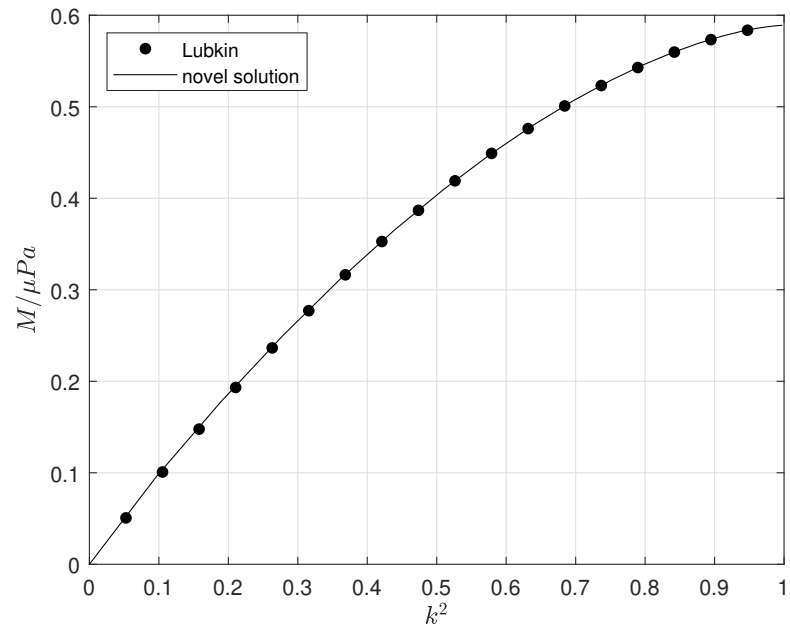


**Figure 4.22:** Non-dimensional torsional moment.

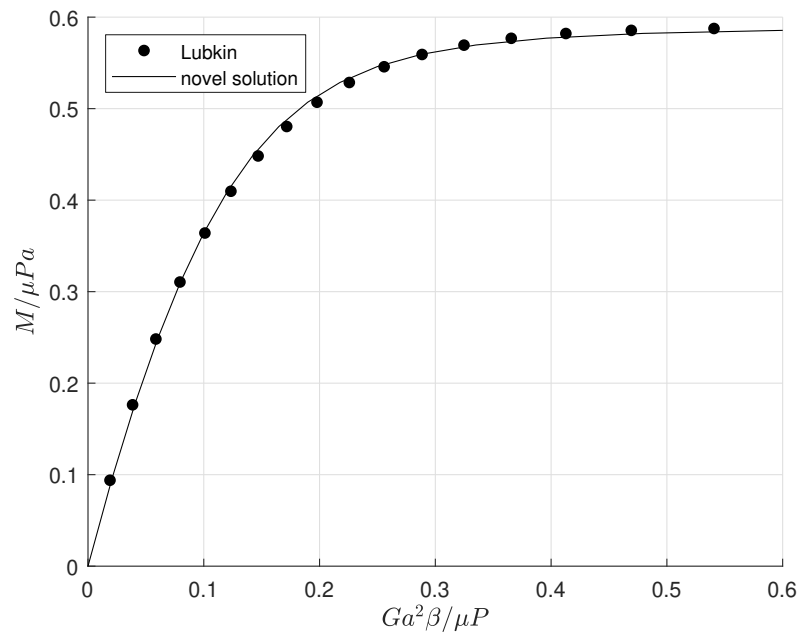


**Figure 4.23:** Solution for two spheres.

#### 4.7.4 Solution for elastic cylinders in contact

Given the small dimensions of the contact area compared to the radius of the wires, in its proximity the mating surfaces approach the shape of two straight cylinders. Therefore, the mesh warp/weft intersection can be reduced to a cylinder-to-cylinder contact problem with good approximation by just neglecting the longitudinal curvature of the wires. This is represented in Figure 4.24.

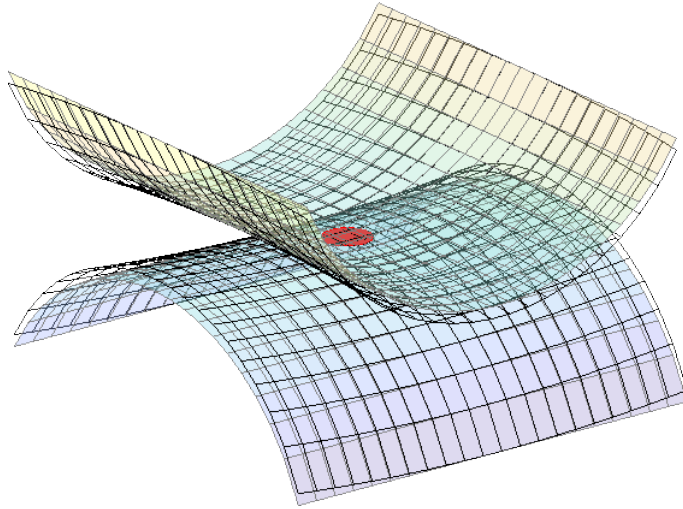


**Figure 4.24:** Warp/weft intersection: in the proximity of the contact area (red circle) the surface of the wires can be approximated to a straight cylinder.

The accuracy of this approximation is obviously related to the waviness of the wires and the size of the contact area with respect to the wires. Based on these considerations, the novel analytical solution proposed before for the case of two spheres under frictional contact can be extended to the case of cylinder-to-cylinder contact for the characterisation of mesh materials under in-plane shear load.

Recalling the Hertzian contact between two elastic cylinders, the shape of the contact area depends on the angle  $\theta$  between their longitudinal axes: for  $\theta = \pi/2$  it is circular, becoming elliptic for  $\pi/2 < \theta < 0$  and finally degenerating into a rectangle for  $\theta = 0$ . Referring to  $a$  and  $b$  as the semi-major and semi-minor axis of the elliptic area of contact, their ratio can be calculated by rearranging Equation 4.44, as follows:

$$\left(\frac{a}{b}\right) = \sqrt{\frac{(R'/R'')(K(e) - E(e)) + K(e)}{E(e)}} \quad (4.134)$$

where  $R'$  and  $R''$  are the relative radii of curvature of the cylinders and  $K(e)$  and  $E(e)$  are again the complete elliptic integrals of first and second kind of argument  $e = \sqrt{1 - b^2/a^2}$ . This last parameter represents the eccentricity of the ellipse and can be approximated as follows:

$$e \approx \sqrt{1 - \left(\frac{R'}{R''}\right)^{-4/3}} \quad (4.135)$$

In the case of PWMMs, assuming same radius  $R_c$  for both warp and weft wires, the radii of curvature become:

$$R' = \frac{R_c}{1 - \cos \theta} \quad (4.136a)$$

$$R'' = \frac{R_c}{1 + \cos \theta} \quad (4.136b)$$

The semi-major axis is then:

$$a = \left(\frac{3PR_e}{4E^*}\right)^{1/3} F_1(e) \left(\frac{a}{b}\right)^{1/2} \quad (4.137)$$

where  $R_e = (R'R'')^{1/2}$  is the equivalent radius,  $P$  is the normal contact force and  $F_1$  is a corrective factor calculated as follows:

$$F_1(e) = \left\{ \frac{4}{\pi e^2} \left(\frac{b}{a}\right)^{3/2} \left[ \left\{ \left(\frac{a}{b}\right)^2 E(e) - K(e) \right\} \{K(e) - E(e)\} \right]^{1/2} \right\}^{1/3} \quad (4.138)$$

Recalling the Hertzian pressure distribution for an elliptic contact area from Equation 4.45, this can be expressed in polar coordinates as follows:

$$\sigma(r, \theta_p) = \frac{3P}{2\pi ab} \left( 1 - \left( \frac{r \cos \theta_p}{a} \right)^2 - \left( \frac{r \sin \theta_p}{b} \right)^2 \right)^{1/2} \quad (4.139)$$

For a point along the semi-major axis, the previous equation reduces to the following:

$$\sigma(r) = \frac{3P}{2\pi ab} \left( 1 - \frac{r^2}{a^2} \right)^{1/2} \quad (4.140)$$

Analogously to the case of two spheres, if a monotonically increasing torsion is applied to the cylinders around their common normal, the outer region of the contact area starts slipping, whilst the inner portion maintains stick conditions.

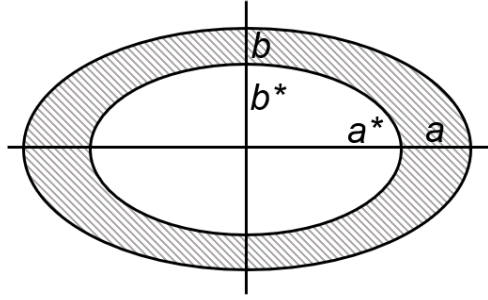


**Figure 4.25:** Elliptic contact area under frictional torsion.

As shown Figure 4.25, the two zones are delimited by two concentric, coaxial and homothetic ellipses, so that  $b/a = b^*/a^*$ , where  $a^*$  and  $b^*$  are the semi-major and semi-minor axes of the stick zone and  $a$  and  $b$  are the semi-major and semi-minor axes of the slip zone, which corresponds to the Hertzian contact area.

Once again, the torque reaction can be calculated by integrating the shear stress distribution along the contact area. Lecornu [119] provided with an expression of such integral for an elliptic contact area, as follows:

$$\mathfrak{M} = abL_e \int_0^1 \tau(\lambda) \lambda^2 d\lambda \quad (4.141)$$

where  $L_e = 4E(e)a$  is the circumference of the ellipse of semi-axes  $a$  and  $b$ , and  $\lambda = r/a$ . The previous equation also shows that the resistance to rotation is proportional to the length of the ellipse of contact. The solution found by Lecornu was limited to the value of maximum torque, which corresponds to the condition of complete slipping ( $\tau = \mu\sigma$  for  $0 < \lambda < 1$ ):

$$\mathfrak{M}_{max} = \frac{3}{32}\mu PL_e \quad (4.142)$$

To extend the solution to the partial slip condition, the tangential stresses among the contact area can be derived with analogous considerations as the case of two spheres.

Within the stick region, the approach of Lubkin for the determination of tangential traction is still valid, thus the proposed approximation from Equation 4.21 can be applied, only by changing the maximum value of the stress according to the Hertz theory, as follows:

$$\tau(\lambda) = \frac{3\mu P}{2\pi ab} \left( A\lambda + B\frac{\lambda^2}{\mathcal{L} - \lambda} \right), \quad \lambda < k' \quad (4.143)$$

where the coefficients  $A$ ,  $B$ , and  $\mathcal{L}$  are the same as Eqs. 4.131a, 4.131b, 4.131c. For the slip zone, the shear stress is again the maximum compatible with the Coulomb friction law. It is obtained by expressing Equation 4.140 as a function of  $\lambda$  and multiplying by the friction coefficient  $\mu$ , as follows:

$$\tau(\lambda) = \frac{3\mu P}{2\pi ab} (1 - \lambda^2)^{1/2}, \quad k' \leq \lambda \leq 1 \quad (4.144)$$

Finally, substituting Equations 4.143 and 4.144 into Equation 4.141, it yields the expression of the torque as a function of  $k'$ :

$$\mathfrak{M} = abL_e \left\{ \frac{3\mu P}{2\pi ab} \left( \int_0^{k'} \left( A\lambda + B\frac{\lambda^2}{\mathcal{L} - \lambda} \right) \lambda^2 d\lambda + \int_{k'}^1 (1 - \lambda^2)^{1/2} \lambda^2 d\lambda \right) \right\} \quad (4.145)$$

As regards the torsional compliance, Mindlin [120] proposed a general solution for the case of two bodies in absence of slipping, which represents a boundary for the case of partial slip:

$$\frac{\beta}{\mathfrak{M}} = \frac{3}{16b^3G} \frac{8\{BD - \nu CE\}}{\pi\{E - 4\nu(1 - k^2)\}} \quad (4.146)$$

where in this case  $k = \sqrt{1 - a^2/b^2}$ ,  $\nu$  is the Poisson's ratio and B, C, D, and E are functions of  $k^2$ . A new simplified solution is proposed for the angle of twisting, which preserves the same proportionality to shear modulus and dimensions of the contact area:

$$\beta = \mathcal{L} \frac{(k')^{-1} \mathfrak{M}}{Ga^2b} \quad (4.147)$$

where  $\mathcal{L} = 7/34$  is the same fitting coefficient as in Equation 4.133.

Comparing Equation 4.145 with Equation 4.132, a proportionality between the two expression emerges clearly: in fact, the solution for two cylinders can be written as the solution for two spheres, multiplied by the ratio of the ellipse length to the circle circumference, as follows:

$$\mathfrak{M}_{cylinders} = \frac{4E(e)a}{2\pi a} \mathfrak{M}_{spheres} = \frac{2E(e)}{\pi} \mathfrak{M}_{spheres} \quad (4.148)$$

### 4.7.5 Torque-rotation hysteresis loop and damping loss factor

In this work, alongside the importance of the mechanical response, the damping behaviour of mesh materials is of particular interest for their application as friction dampers. Therefore, an analysis of PWMMs hysteretical behaviour under the effect of cyclic loading becomes fundamental.

Lubkin developed his solution for the case of a monotonically increasing torque applied to the spheres. Deresiewicz extended the solution of Lubkin to the case

of an oscillatory couple applied to a contact pair of spheres, providing with an expression for the hysteresis loop generated and the amount of energy dissipated per cycle [118]. In this work, the original treatment of Deresiewicz is adopted to determine the changing in shear stress distribution due to the inversion of motion and then applied to the case of mesh materials. All the considerations made by Deresiewicz for an oscillatory couple are still valid for the inverse problem, when the contact pair is subjected to an oscillatory rotation, provided that the angle is governed by a monotonic function.

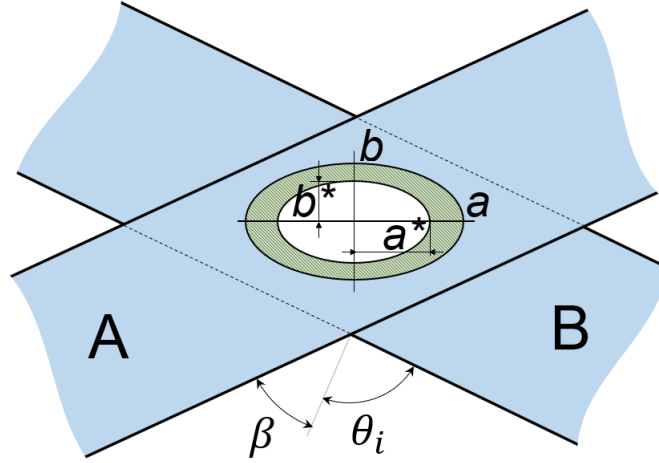


**Figure 4.26:** Rotation of the wires around their common normal: starting from an initial position  $\theta_i$  at rest, wire A is twisted by an angle  $\beta$  with respect to wire B.

Consider the warp/weft wire couple represented in Figure 4.26, initially at rest with perpendicular axes (i.e.,  $\theta_i = \pi/2$ ), and then subjected to an increasing rotation  $\beta$ . Suppose that, after the angle of twist has reached a certain value  $\beta^*$ , which corresponds to a torsional couple  $\mathfrak{M}^*$ , the motion is suddenly inverted. The slip portion  $a^*$  of the contact area that was established during the previous verse of rotation, is now ceased and restarted from  $r = a$ . Thus, an opposite shear traction is generated in the contact area that will superpose to the previous one. Let  $a^{**}$  be the boundary of the new slipping area, such that  $a^* \leq a^{**} \leq a$ . In this zone, the shear stress due to the new established slip sector is  $\tau = -\mu\sigma$ ; however, the ceasing of the previous slipping has determined a further equivalent decreasing

of the total stress, so the overall change in shear traction is actually twice (i.e.  $\tau = -2\mu\sigma$ ). Therefore, referring to the case of cylinder-to-cylinder contact, the total change in shear stress is:

$$\begin{aligned}\tau_{a^{**}} &= -\frac{3\mu P}{\pi ab} (1 - \lambda^2)^{1/2}, \quad k'' \leq \lambda \leq 1 \\ \tau_{a^{**}} &= -\frac{3\mu P}{\pi ab} \left( A\lambda + B\frac{\lambda^2}{\mathcal{L}-\lambda} \right), \quad \lambda < k''\end{aligned}\tag{4.149}$$

where  $k'' = a^{**}/a$ . The coefficients  $A$ ,  $B$  and  $\mathcal{L}$  of the polynomial are also calculated with respect to  $k''$ . The resulting shear distribution is given by the superposition of the preexisting one (Equations 4.143 and 4.144) and the change (Equation 4.149), as follows:

$$\begin{aligned}\tau &= -\frac{3\mu P}{2\pi ab} (1 - \lambda^2)^{1/2}, \quad k'' \leq \lambda \leq 1 \\ \tau &= -\frac{3\mu P}{2\pi ab} \left( 2C'' - (1 - \lambda^2)^{1/2} \right), \quad k' \leq \lambda \leq k'' \\ \tau &= -\frac{3\mu P}{2\pi ab} (2C'' - C'), \quad \lambda \leq k'\end{aligned}\tag{4.150}$$

where  $C'$  and  $C''$  are the quantities between parenthesis respectively in Equation 4.143 and 4.149. Integrating the stress distribution in Equation 4.150, it returns:

$$\mathfrak{M} = \mathfrak{M}(a^*) - 2\mathfrak{M}(a^{**}) = \mathfrak{M}^* - 2\mathfrak{M}(a^{**})\tag{4.151}$$

The rotation is found with the same process of superposition adopted for the moment: the change in twisting angle is again described by Equation 4.133, where  $\mathfrak{M}$  is now substituted by the change in moment (i.e.,  $-2\mathfrak{M}(a^{**})$ ). Thus, the resulting angle is:

$$\begin{aligned}\beta &= \mathcal{L} \frac{(k')^{-1}\mathfrak{M}(a^*)}{Ga^3} - \mathcal{L} \frac{(k'')^{-1}2\mathfrak{M}(a^{**})}{Ga^3} = \\ &= \beta^* - 2\beta(a^{**})\end{aligned}\tag{4.152}$$

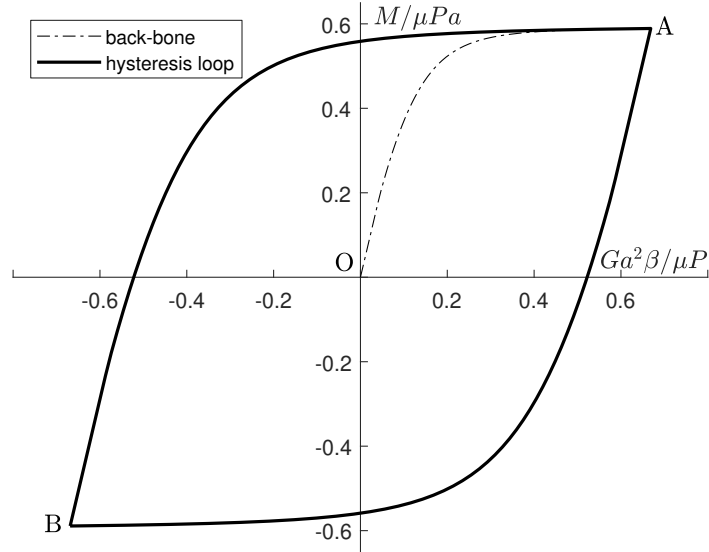


**Figure 4.27:** Torque-rotation hysteresis loop for a cylinder-to-cylinder contact in non-dimensional coordinates.

Suppose now that, once the twist angle has reached the minimum value of  $-\beta^*$ , the motion is inverted again. All the previous discussion regarding the inversion of motion is still valid, just by considering, for this case, a positive sign for the change of moment and angle.

When the reaction moment is plotted against the twisting angle, it results in a hysteresis loop, as illustrated in Figure 4.27 in non-dimensional coordinates. Referring as  $\overline{OA}$  to the initial curve (also called "back-bone" curve) ( $0 < \mathfrak{M} < \mathfrak{M}^*$ ) and as  $\overline{AB}$  to the new curve generated after the inversion of motion ( $-\mathfrak{M}^* < \mathfrak{M} < \mathfrak{M}^*$ ), from Equations 4.151 and 4.152 it is evident that the the segment  $\overline{AB}$  is simply equivalent to the segment  $\overline{OA}$  reflected both across the  $x$  and  $y$  axes and scaled two times. The same consideration applies to the segment  $\overline{BA}$ , which is again equivalent to the segment  $\overline{AB}$  reflected across the  $x$  and  $y$  axes. The curves  $\overline{AB}$  and  $\overline{BA}$  together represent the hysteresis loop for a single wire intersection of mesh material under an oscillatory rotation  $-\beta^* < \beta < \beta^*$ .

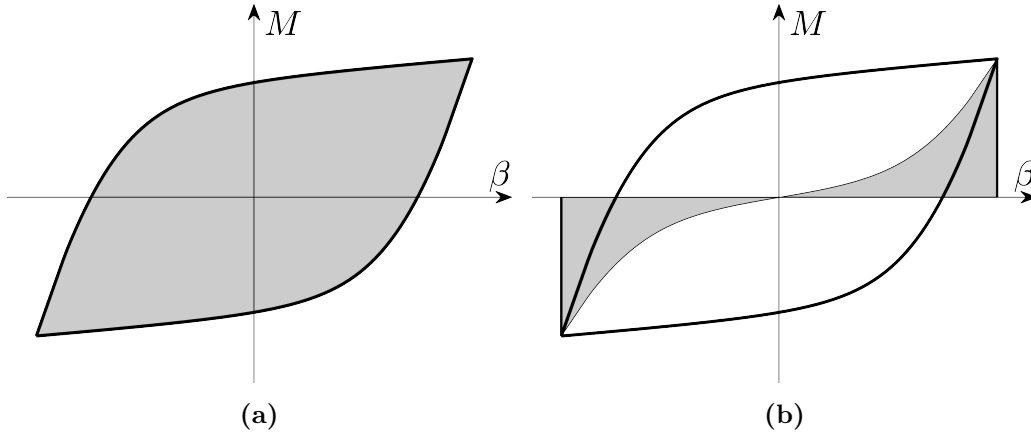


**Figure 4.28:** Calculation of the loss factor: (a) dissipated energy and (b) stored strain energy.

The hysteresis loop provides with useful information on the damping capabilities of the mesh material. The area surrounded by the loop represents the amount of dissipated energy  $W_d$  during a single cycle of displacement. The loss factor can be defined as [121]:

$$\eta = \frac{W_d}{2\pi U} \quad (4.153)$$

where  $U$  is the strain energy stored in a cycle. This is illustrated in Figure 4.28.

The periodic motion just analysed can be thought as representative of a general vibration applied to the mesh material. The simplest type of vibration is a simple harmonic motion. More complicated signals can always be represented by the sum of different harmonic motions by means of the Fourier series. Therefore, the evolution of the twist angle with time can be represented by a simple harmonic function:

$$\beta = \beta^* \sin(\omega t + \phi) \quad (4.154)$$

where  $\omega$  is the frequency,  $t$  is the time vector, and  $\phi$  is the phase shift.

## 4.8 Out-of-plane bending model

The analytical models discussed until this point allow to predict the response of mesh material to an in-plane system of forces. For a more general case, when the structure is subjected to out-of-plane loads, a further analysis is required. The method proposed in this work makes use of a combination of the Timoshenko's beam theory and the finite element method, and it is based on the same principles as for the tension model. The unit cell can be again described as two crossed beams of length  $L$ , which are in this case reduced to straight beams to simplify the calculations. By means of the finite element method, each beam is itself subdivided into two elements of length  $L/2$ , so that their central node coincides with the contact point. This is illustrated in Figure 4.29, where the nodes 1-A-2 and 3-B-4 represent respectively the warp and the weft wire.

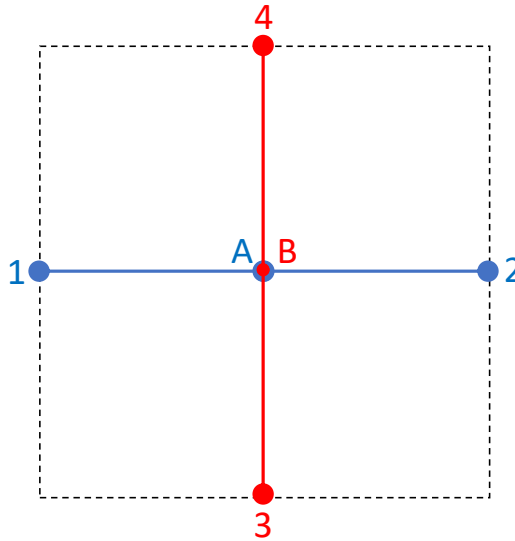


**Figure 4.29:** Schematisation of RUC as two crossed Timoshenko beams: 1-A-2 = warp wire, 3-B-4 = weft wire.

The stiffness matrix for a finite straight beam element of length  $L$  is the following [122]:

$$[\mathbf{K}_\ell] = \begin{bmatrix} \frac{AE}{L} & 0 & 0 & -\frac{AE}{L} & 0 & 0 \\ 0 & \frac{12EI}{L^3(1+\phi)} & \frac{6EI}{L^2(1+\phi)} & 0 & -\frac{12EI}{L^3(1+\phi)} & \frac{6EI}{L^2(1+\phi)} \\ 0 & \frac{6EI}{L^2(1+\phi)} & \frac{EI(4+\phi)}{L(1+\phi)} & 0 & -\frac{6EI}{L^2(1+\phi)} & \frac{EI(2-\phi)}{L(1+\phi)} \\ -\frac{AE}{L} & 0 & 0 & \frac{AE}{L} & 0 & 0 \\ 0 & -\frac{12EI}{L^3(1+\phi)} & -\frac{6EI}{L^2(1+\phi)} & 0 & \frac{12EI}{L^3(1+\phi)} & -\frac{6EI}{L^2(1+\phi)} \\ 0 & \frac{6EI}{L^2(1+\phi)} & \frac{EI(2-\phi)}{L(1+\phi)} & 0 & -\frac{6EI}{L^2(1+\phi)} & \frac{EI(4+\phi)}{L(1+\phi)} \end{bmatrix} \quad (4.155)$$

where  $E$  is the elastic modulus,  $A$  is the cross-section area,  $I$  is the second moment of area and the parameter  $\phi$  is calculated as:

$$\phi = \frac{12EI}{GA\tilde{K}L^2} \quad (4.156)$$

In the previous equation  $G$  is the shear modulus and  $\tilde{K}$  is the Timoshenko's coefficient. Referring to a portion  $L/2$  of the beam and considering only the bending and shear terms, it yields:

$$[\mathbf{K}_{\ell/2}] = \frac{8EI}{(1+4\phi)L^3} \begin{bmatrix} 12 & 3L & -12 & 3L \\ 3L & (1+\phi)L^2 & -3L & (\frac{1}{2}-\phi)L^2 \\ -12 & -3L & 12 & -3L \\ 3L & (\frac{1}{2}-\phi)L^2 & -3L & (1+\phi)L^2 \end{bmatrix} \quad (4.157)$$

Two half-beam element matrices can be assembled to form the out-of-plane bending stiffness of a wire. Referring to the warp wire, the assembled matrix takes the following form:

$$\begin{bmatrix} R_1 \\ M_1 \\ F_n \\ 0 \\ R_2 \\ M_2 \end{bmatrix} = \frac{8EI}{(1+4\phi)L^3} \begin{bmatrix} 12 & 3L & -12 & 3L & 0 & 0 \\ 3L & (1+\phi)L^2 & -3L & (\frac{1}{2}-\phi)L^2 & 0 & 0 \\ -12 & -3L & 24 & 0 & -12 & 3L \\ 3L & (\frac{1}{2}-\phi)L^2 & 0 & 2(1+\phi)L^2 & -3L & (\frac{1}{2}-\phi)L^2 \\ 0 & 0 & -12 & -3L & 12 & -3L \\ 0 & 0 & 3L & (\frac{1}{2}-\phi)L^2 & -3L & (1+\phi)L^2 \end{bmatrix} \begin{bmatrix} w_1 \\ \theta_1 \\ w_{warp} \\ \theta_{warp} \\ w_2 \\ \theta_2 \end{bmatrix} \quad (4.158)$$

The force acting at the central node of the wire corresponds to the contact force exerted by the other wire. This can be calculated from the previous matrix as follows:

$$F_n = \frac{8EI}{(1+4\phi)L^3} (-12(w_1 + w_2) - 3L(\theta_1 - \theta_2) + 24w_{warp}) \quad (4.159)$$

Rearranging the previous equation, the vertical displacement of the central node is obtained as:

$$w_{warp} = \mathfrak{B}F_n + \frac{1}{2}(w_1 + w_2) + \frac{L}{8}(\theta_1 - \theta_2) \quad (4.160)$$

where the coefficient  $\mathfrak{B}$  is calculated as:

$$\mathfrak{B} = \frac{(1+4\phi)L^3}{196EI} \quad (4.161)$$

The same procedure can be repeated for the weft wire:

$$w_{weft} = -\mathfrak{B}F_n + \frac{1}{2}(w_3 + w_4) + \frac{L}{8}(\theta_3 - \theta_4) \quad (4.162)$$

Recalling from Equations 4.88a and 4.88b the relationship between the displacement of neutral axis and contact point and the normal Hertzian compression, the following system of equations can be written:

$$\begin{aligned}
w_C &= \mathfrak{B}F_n + \frac{1}{2}(w_1 + w_2) + \frac{L}{8}(\theta_1 - \theta_2) + \frac{\delta_H}{2} \\
-w_C &= \mathfrak{B}F_n - \frac{1}{2}(w_3 + w_4) - \frac{L}{8}(\theta_3 - \theta_4) + \frac{\delta_H}{2}
\end{aligned} \tag{4.163}$$

By solving the previous system, it returns:

$$2\mathfrak{B}F_n + \delta_H + \frac{1}{2}(w_1 + w_2 - w_3 - w_4) + \frac{L}{8}(\theta_1 - \theta_2 + \theta_4 - \theta_3) = 0 \tag{4.164}$$

Substituting Equation 4.85 into the previous, it yields:

$$2\mathfrak{B}F_n + \left(\frac{3}{4E^*\sqrt{r}}\right)^{2/3} F_n^{2/3} + \frac{1}{2}(w_1 + w_2 - w_3 - w_4) + \frac{L}{8}(\theta_1 - \theta_2 + \theta_4 - \theta_3) = 0 \tag{4.165}$$

Analogously to the tension model, let A, B and D be the coefficients of the previous cubic equation:

$$A = 2\mathfrak{B} \tag{4.166a}$$

$$B = \left(\frac{3}{4E^*\sqrt{r}}\right)^{2/3} \tag{4.166b}$$

$$D = \frac{1}{2}(w_1 + w_2 - w_3 - w_4) + \frac{L}{8}(\theta_1 - \theta_2 + \theta_4 - \theta_3) \tag{4.166c}$$

Finally, the cubic equation is solved with the Cardano's formula in Equation 4.93. The solution expresses the contact force as a function of the nodal displacements of the wires along the boundaries of the RUC:

$$F_n = f(w_1, w_2, w_3, w_4, \theta_1, \theta_2, \theta_3, \theta_4) \tag{4.167}$$

The formulation can be extended to the case of warp and weft wires built in different materials, by simply changing the coefficient  $A$  in Equation 4.165 as follows:

$$A = \mathfrak{B}_{warp} + \mathfrak{B}_{weft} \tag{4.168}$$

where  $\mathfrak{B}_{warp}$  and  $\mathfrak{B}_{weft}$  are calculated from Equation 4.161 by changing the material properties with the ones of the respective wires.

## 4.9 Conclusions

In this chapter, three analytical models for the characterisation of PWMMs were presented.

The tension-compression model was based on a combination of the Castigliano's theorem and the Hertz contact theory. It provides with a set of effective properties (i.e., stiffness and Poisson's ratio) for the description of the mesh material as function of geometry of the RUC and constitutive materials of the wires. These properties are shown to be non-linear due to the Hertzian normal compression of the wires at the contact area. The model also defines the level of contact force at the warp/weft wire intersection as a function of the bi-axial state of force applied to the material and incorporates this quantity into the effective properties. A set of linearised properties is also defined that will be employed in the reduced finite element model discussed in Chapter 6.

The in-plane shear model describes the response of PWMMs to in-plane shear, which is interpreted as a rotation of the wires around their common normal. The model is capable of capturing the highly non-linear response of mesh materials during the micro-slip phase through the determination of the tangential stress distribution at the contact interface. The solution is then extended to the case of an applied cyclic load for describing the hysteretical response of the materials to vibrations.

Finally the out-of-plane bending model was presented, which was developed based on the Timoshenko beam theory and studies the effect of out-of-plane displacements on the level of contact force. Both the out-of-plane bending model and the tension-compression model, show that the contact force can be ultimately described as a function of the displacements at the RUC boundaries.

It is worth noting that the models developed in this research are based on the assumption of linear elastic constitutive materials, and therefore do not account for material non-linearities (such as plasticity, superelasticity or hyperelasticity), nor for geometrical non-linearities (i.e., large strain theory). The non-linear response

of PWMMs captured by these models is entirely due to the contact interaction at the warp/weft intersections, caused by both the normal compression of the interacting interfaces and the frictional energy dissipation associated with in-plane shear. However other potential dissipative modes besides in-plane shear (e.g., torsion, bending) are not captured by these models. Furthermore, the models are based on the geometrical characterisation discussed in Chapter 3 (constant aperture, sinusoidal longitudinal path, circular cross-section, etc.) therefore the accuracy of the analytical results is strictly related to the correctness of the related underlying assumptions.

# Chapter 5

## Numerical modelling

### 5.1 Introduction

In this chapter, the developed analytical models previously discussed in Chapter 4 are validated through numerical modelling.

The chapter opens with a general introduction on the typical process for commercial finite element codes. Some similarities and differences between the main options commercially available are listed, underlining the reasons for choosing the specific software for this research.

Since the contact mechanics plays such a significant role in the analytical and numerical models, the element formulation is presented for both the solid (wire) and contact (warp and weft wire interaction) elements. The choice of performing a three-dimensional analysis and the main advantages and disadvantages between the various available 3-D solid elements are discussed. The numerical computation of contact phenomena is presented, with a brief summary on penalty-based and Augmented Lagrangian methods for both normal and tangential contact.

A detailed description of the adopted meshing strategy is presented, with a discussion around the influence of the contact local mesh size and contact penetration and how these influence the accuracy of results.

The results of the validation compared to the analytical models from Chapter 4 are reported. For each of the analytical models (tension, in-plane shear, out-of-plane bending) a dedicated set of FE simulations are carried out and the numerical results are compared with the analytical solution for different conditions and material combinations.

## 5.2 ANSYS finite element package

Nowadays several commercial software suites for finite element analysis are available on the market. These packages are all based on the same underlying mathematical principles which constitute the finite element method (FEM), a numerical method for the solution of partial differential equations (PDE). For this reason they generally yield to similar results, provided that the physical problem is accurately reproduced by the numerical model. These software applications generally share the same organisation and their computation is divided into three main stages:

- i) Pre-processing.
- ii) Processing.
- iii) Post-processing.

For a very simplistic overview of the process, each of the stages can be defined as follows. In the pre-processing, the geometry of the model is defined and then subdivided into finite elements through the mesh generation. Materials, element formulations, boundary conditions and loads are then assigned to the model. The parameters for the subsequent solution are defined in this stage. During the processing, the finite element equations are assembled into the global stiffness matrix and the solution of the problem is carried out. Finally, in the post-processing, the numerical results produced in the previous stage are displayed.

Even though commercial finite element analysis (FEA) software programs are based on the same principles, they can differ from each other in many aspects, from the solver to the element formulations and the technology they offer for generating the geometry and meshing, applying boundary conditions and loads and for the post-processing of results. One of the most important difference is probably the contact formulations, which is of particular interest in this work.

In this work, the ANSYS Mechanical 2019R1 package [123] has been chosen for the finite element analysis, given a diffuse application of the software in the literature for similar frictional contact problems which guarantees a high reliability and repeatability of the results. Moreover, ANSYS offers several different contact formulations that can be fully adjusted mathematically. Other advantages of this software are the accessibility of the graphic user interface (GUI) and an integrated computer-aided design (CAD) tool for the generation of the geometry together with a series of flexible built-in meshing algorithms.

In this work, because of the substantially frequency-independent nature of the problem, a static structural analysis has been performed. In this type of analysis, the effects of acceleration are neglected, hence the problem is reduced to the following equation:

$$[K]\{x\} = \{f\} \quad (5.1)$$

where  $[K]$  is the stiffness matrix,  $\{x\}$  is the nodal displacement vector and  $\{f\}$  is the load vector.

As regards to the numerical processing, for a static linear problem, as in Equation 5.1, for which the stiffness matrix is independent of the displacement, a direct solver can be used that inverts the stiffness matrix to directly find the solution.

For the problem addressed in this work, the contact between the bodies introduces a boundary non-linearity and the stiffness is generally proportional to the displacement:

$$[K(x)]\{x\} = \{f\} \quad (5.2)$$

To solve this problem an iterative solver is required. In this case, the solution is broken down into several substeps and for each of them, the solver has to achieve convergence through equilibrium iterations. More specifically, the ANSYS Preconditioned Conjugate Gradient (PCG) iterative solver has been used in the following finite element analysis for its robustness and solving speed. The PCG, although requiring a higher amount of memory, is up to 10 times faster than the other available iterative solvers in ANSYS [123]. Hattori *et al.* [124] compared the performance of the ANSYS PCG solver with sparse and frontal direct solvers for the analysis of a contact between two cylindrical bodies (automotive connective rod and pin) concluding that the PCG is in most cases the fastest solver even though leading to same accuracy of the numerical results. Moreover, it handles with high performance the Augmented Lagrangian contact algorithm employed in this work, which will be discussed later.

### 5.3 Element formulation

A fundamental aspect in finite element analysis is the choice of the element formulation for the model, which is strictly related to the accuracy of the results.

From the simplest to the more complex, elements in FEM can be subdivided into 1-D, 2-D and 3-D type, according to the number of dimensions in which translation of nodes can occur. Examples are 2-node beams or trusses (1-D), triangles and quadrilaterals (2-D), tetrahedrons and hexahedrons (3-D). Therefore, the first aspect to consider is the type of analysis to perform in terms of number of dimensions to account for in the model. This mostly depends on the specific problem that has to be addressed. Although a 3-D model that reproduces the real system with high precision allows to achieve accurate results, this is not always desired because of the high computational demand required. In some cases other strategies are adopted to contain the computational cost, for instance by simplifying a general 3-D problem to a bi-dimensional one, reducing the number of degrees of freedom (DOFs) involved.

In this work, the priority was to produce a highly accurate set of numerical results as a validation for the analytical models. Moreover, the FEM was intended as a reliable method to investigate the physics of contact in a location which is, by its nature, of difficult access empirically given the small dimension. For these reasons a three-dimensional analysis has been chosen as a main strategy, despite the higher computational demand, involving the usage of solid elements for the meshing.

In contact problems such as the one object of this study, the interaction between different solids is computed by the FE software through dedicated contact elements. Particular attention should be given to their settings and how they can affect the quality of results and the performance of the simulation.

### **5.3.1 Solid elements**

Generally, in FEs two different types of 3-D solid elements are available:

- i) Tetrahedrons.
- ii) Hexahedrons (also called bricks).

Depending on the field equation (or shape function) order, they are further subdivided into linear and quadratic (higher order) elements. In linear elements, the field equation is linear, meaning that the displacement within the element varies linearly as a function of the nodal displacements. The biggest limitation is that the strains, calculated as a derivative of the displacements, are constant within the element. In high order elements, instead, the displacement field is a quadratic function, so their edges can curve and the strains vary linearly through the elements, giving them more precision at the expense of a higher computational demand. In fact, whilst linear elements are only composed of vertex nodes, higher order elements include an additional mid-side node for each edge, that corresponds to a larger number of DOFs.

Tetrahedrons are solids with four faces and four vertices, thus the correspondent linear elements are composed of four nodes only (one for each vertex), whereas the higher order tetrahedrons are 10-node elements (four corner nodes and six additional mid-side nodes). Hexahedrons, instead, are solids with six faces and eight vertices, and thus the correspondent linear elements are composed of eight nodes only, whilst quadratic hexahedrons are 20-node elements (eight corner nodes and twelve additional mid-side nodes).

Hexahedrons, as compared to tetrahedrons, have the advantage of a higher precision (due to the Gauss integration points) and a lesser number of elements is required for the same meshing. Nevertheless, for complex geometries, brick elements are of difficult application, whereas tetrahedrons can fit different shapes with less effort, also considering the wide choice of meshing algorithms available nowadays.

In this work, because of the complexity involved in meshing 3-D solids with multiple curvature (i.e., sinusoidally-curved cylinders), 10-node quadratic tetrahedral elements have been chosen for the FE meshing, which are referred to as SOLID187 in ANSYS environment. A scheme representing the node nomenclature for SOLID187 is reported in Figure 5.1.

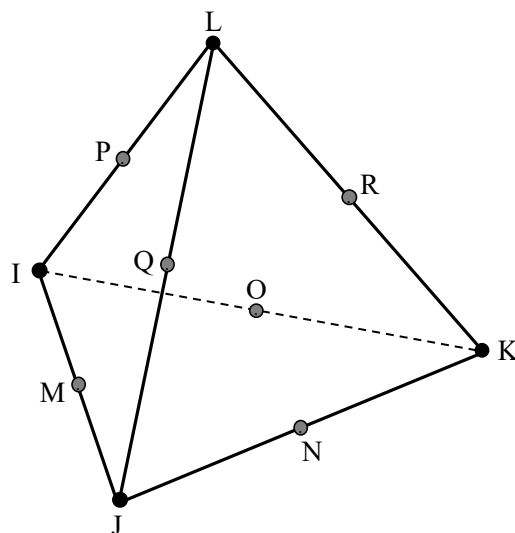


**Figure 5.1:** ANSYS SOLID187 element nodes: I through L represent the corner nodes, whereas M through R represent the mid-side nodes.

### 5.3.2 Contact elements

In FEs, the contact computation is implemented through zero-thickness interface elements that overlie the solid structural elements. These are organised into pairs of mating surfaces referred to as *Contact* and *Target element*.

In reality, two different bodies cannot occupy the same space. Hence in continuum mechanics, the contact problems are generally addressed by imposing that solids cannot interpenetrate, which is achieved by demanding a non-negative distance between their boundaries. In FEs, the contact compatibility is enforced by dedicated algorithms that establish a relationship between the solid boundaries. In general, these are penalty-based methods that allow a certain amount of penetration between the surfaces to facilitate the convergence of the model. The normal contact force is calculated as:

$$F_N = k_N \cdot x_N \quad (5.3)$$

where  $x_N$  is the amount of normal penetration allowed and  $k_N$  is a parameter referred to as normal contact stiffness. It is evident from the equation that increasing the value of  $k_N$  reduces the penetration, and the solution tends to the real one. Ideally, for an infinite value of the contact stiffness, the penetration would be zero, however numerical convergence could not be achieved. ANSYS calculates the normal contact stiffness based on the elastic modulus and the size of the underlying elements. This value can be modified by the user through a scaling factor FKN. Typically there is a trade-off between using a lower value to aid in convergence versus using a larger value to increase accuracy.

ANSYS offers two different type of behaviour for the contact pair:

- i) Symmetric: when both the contact and target element are restrained from penetrating each other.
- ii) Asymmetric: when only the contact element is restrained from penetrating the target elements.

The asymmetric contact is typically computationally less expensive, whereas the symmetric contact, although less efficient, can help achieving a lower contact penetration. In this work, the ANSYS contact elements CONTA174 and TARGE170 have been used with symmetric behaviour and a frictional type contact. High values of FKN were used and the contact stiffness was updated for each equilibrium iteration to guarantee a high accuracy and a very small penetration. An Augmented Lagrange contact formulation has been chosen in this work. In this penalty-based method the normal contact force is augmented by introducing an additional term  $\lambda$ , as follows:

$$F_N = k_N \cdot x_N + \lambda \quad (5.4)$$

Therefore, this formulation is less sensitive to the value of the normal contact stiffness. The surface interaction is determined through integration point detection rather than nodal detection, which results in a higher number of detection points per element and increases the accuracy replicating the physics of the contact.

Besides carrying compressive normal stresses, contact elements are also capable of computing the transverse interaction for friction or bonded type contact. In general, two surfaces with frictional interaction can carry transverse stresses up to a certain magnitude, beyond which they start sliding with respect to each other. The classical Coulomb friction model is the default friction model employed in ANSYS, with equal dynamic and static friction coefficients by default. Hence, recalling from Chapter 4, the transition from sticking to sliding status occurs when the tangential force  $F_T$  exceeds the product of the friction coefficient and the normal force  $F_N$ . Although theoretically for a sticking status no sliding should take place, in FEs a tangential penalty method is implemented, similar to the one for the normal contact:

$$F_T = k_T \cdot x_{sliding} \quad (5.5)$$

where  $F_T$  is the shear force carried by the contact pair,  $k_T$  is a tangential contact stiffness and  $x_{sliding}$  is the sliding distance allowed by the penalty method.

## 5.4 Meshing

As well as the afore discussed element formulation, also the level of discretisation of the numerical problem, in terms of number of elements in which the model is partitioned, has a deep influence on the accuracy of the results. Increasing the number of elements in which the problem domain is subdivided and therefore reducing their dimensions, is often referred to as h-refinement, where  $h$  indicates the characteristic length of elements, as opposed to p-refinement that consists into changing the element formulation with a higher order of interpolation. In general, the finer the mesh, the more accurately the FE model approximates the real problem, although increasing the overall DOFs and consequently the computational time. In a coarse mesh the internal stresses are interpolated within bigger elements, yielding an inaccurate distribution, especially in the presence of geometric discontinuities or concentrated loads.

Recalling the shear model from Chapter 4, the frictional moment at the warp/weft wire intersections depends on the tangential stress distribution across the contact area. Therefore, a correct computation of the stress distribution is crucial in order to accurately characterise the moment-rotation response of PWWMs to in-plane shear load. Numerically, this can be achieved only with a proper choice of the FE mesh size. Moreover, in a non-conforming contact problem, such as the one addressed in this work, where the two mating parts are initially only touching at one point, the small dimensions of the contact area cause high stress gradients requiring a finer interpolation. The strategy adopted in this work is a local refinement, restricted to a portion of the model involved in the contact, whereas in the remaining part a coarser mesh is used in order to contain the computational cost. This is illustrated in Figure 5.2 for a 3-D model of a single wire.

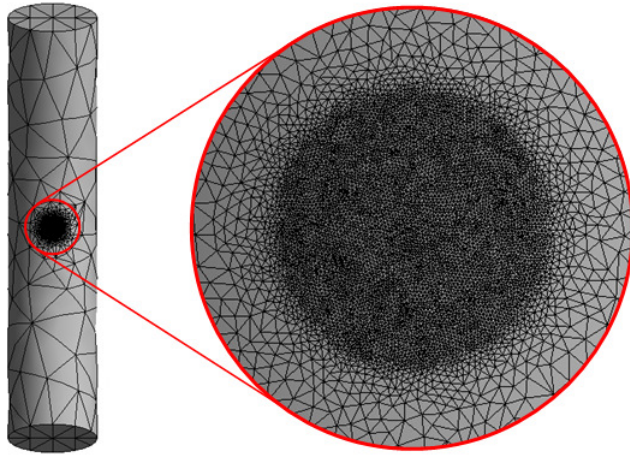


**Figure 5.2:** Local mesh refinement: in the circle a close-up image of the contact area, showing the high density of elements.

In Figure 5.3, a mesh convergence study is reported for a single RUC of mesh material under shear load (dimensions and material reported in Table 4.3), with a normal contact load of 10N and FKN=1.

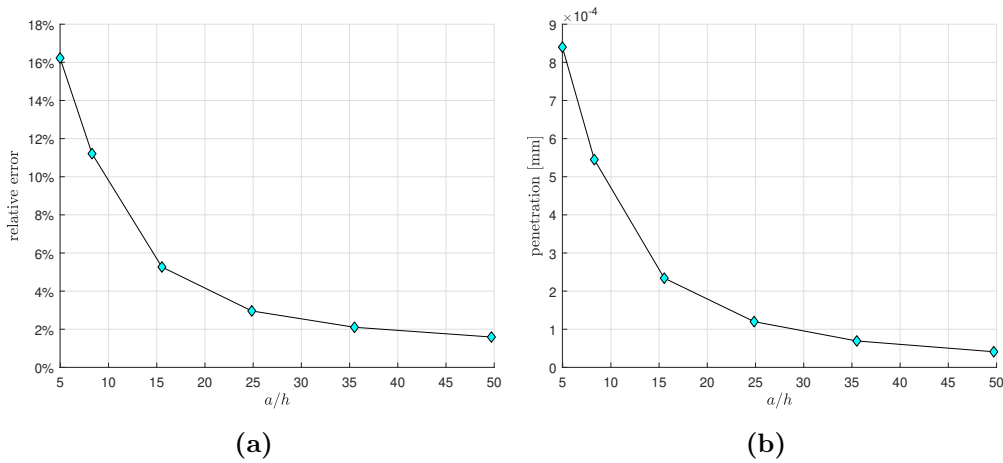


**Figure 5.3:** Contact mesh refinement demonstrating an asymptotic convergence for (a) the relative error and (b) the contact penetration.

The relative error in the reaction moment between analytical and numerical solu-

tion is reported in Figure 5.3a for different levels of mesh refinement. The error is calculated in correspondence of the peak torque at a twisting angle of 5 degrees. The quantity  $a/h$  in the x-axis is the ratio of the theoretical contact radius to the element size. Progressively increasing the number of elements in the contact area (by reducing the element size  $h$  with respect to the contact radius  $a$ ), an asymptotic behaviour of the relative error can be observed, until it reaches approximately 1.6% for 100 elements per diameter. This corresponds to an element size of  $0.5\mu m$ , being the theoretical radius of the contact area  $a=0.0249\text{mm}$  for a normal contact force of 10N. The contact penetration also follows an asymptotic trend similar to the one of the relative error, as shown in Figure 5.3b, with a progressive reduction up to 20 times the initial value.

In Table 5.1 the ratio  $a/h$ , the total number of elements and nodes in the FE mesh, and the solution time are reported for the same mesh convergence study for various element sizes.

$h$ [mm]	$a/h$	$n_{el}$	$n_{nodes}$	$t_{solution}$
0.0050	5	4169	7411	46s
0.0030	8	7889	13593	1m 12s
0.0016	16	23353	39545	4m 3s
0.0010	25	56086	94548	14m 11s
0.0007	36	111191	187338	32m 45s
0.0005	50	213823	359979	4h 25m

**Table 5.1:** Ratio  $a/h$ , number of elements and nodes, and solution time for various element sizes.

It is apparent how the solving time rapidly increases for any further refinement, from less than a minute up to more than four hours, together with the number of elements and nodes involved. Note that these values should be considered in a relative sense due to different computers yielding different solve times.

The asymptotic decreasing of relative error and contact penetration with respect to mesh size suggests a strict dependence of results on the normal contact

stiffness. Another convergence study is performed on the same model by using a constant coarse mesh size with  $h=0.003\text{mm}$  and progressively increasing the value of FKN. The relative error between numerical and analytical results is reported in Figure 5.4, calculated as in the previous convergence study.

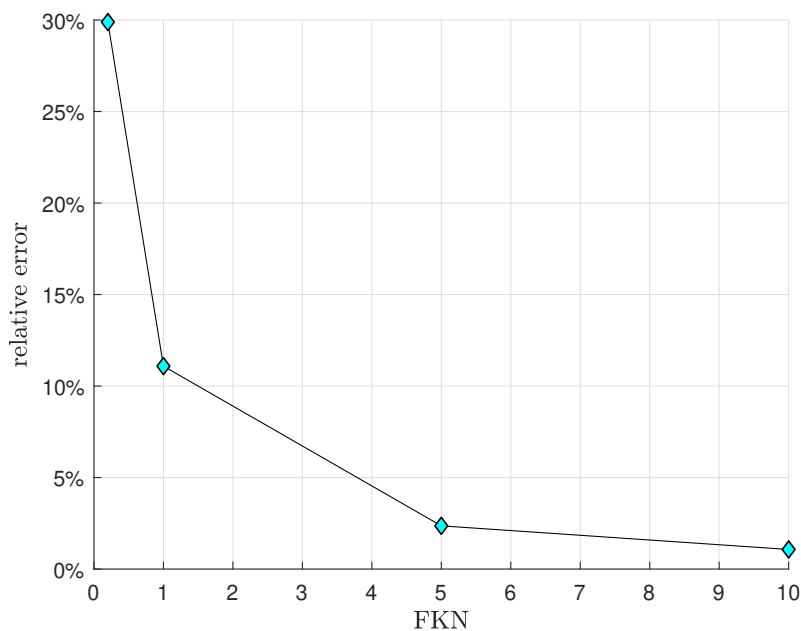


**Figure 5.4:** Effect of contact stiffness factor on numerical results.

The figure demonstrates the asymptotic convergence of the relative error as the value of FKN increases. This strategy will be exploited in this work to further increase the accuracy of the numerical validation and to decrease the computational time for large FE models. Nevertheless, for too high values of normal contact stiffness, numerical instabilities occur and one body starts oscillating, alternately penetrating and rebounding from the other, yielding incorrect results or not achieving numerical convergence.

## 5.5 Boundary conditions and loads

In reality, the numerous wires composing the mesh structure are held together by the frictional contact interaction at the multiple intersections. When the material

is not subjected to any external load, the stability of the structure is guaranteed by the elastic forces generated by bending the wires during the manufacturing process. These forces produce a very low contact force which is referred to as *pre-load* by the author. If the structure was cut in a small portion corresponding to only a single intersection, it would inevitably deconstruct into separate wires. Therefore, in order to correctly reproduce the real physics of the RUC, it is necessary to replace the surrounding mesh material with a proper set of boundary conditions that simulate the same reaction forces for when the RUC is placed within the PWMM structure.

Three different sets of boundary conditions are adopted in this work, one for each developed analytical model, that will be discussed in the next respective subsections.

The normal contact load is also generated differently for the three models. In the tension model, this is produced with a controlled longitudinal tension applied to the wire edges, whereas in the shear model the normal load is applied directly to one of the bodies, while the other body is fixed. Finally in the bending model, the contact force results from the vertical displacements applied to the wires.

## **5.6 Results**

### **5.6.1 Tension model**

Recalling from Chapter 4, both warp and weft wires are theoretically supported by a roller constraint at each extremity that allows them only to move longitudinally and rotate about the perpendicular direction.

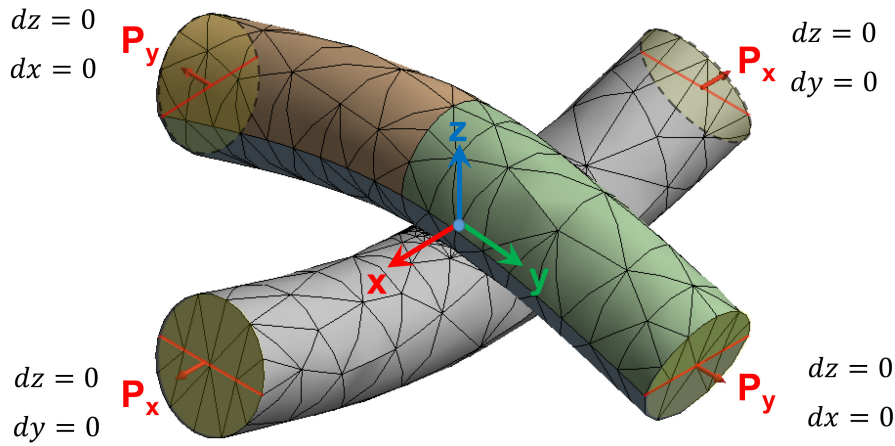


**Figure 5.5:** 3-D FE model with boundary conditions used to represent the analytical tension model.

This is implemented in the FEM by imprinting a central edge on the circular bases of the wires, to which the kinematic constraints and tension loads are then applied, as shown in Figure 5.5. Moreover, the bases are set as rigid to prevent their deformation in the vicinity of the edges during the application of the load. The wire dimensions are the same as *Sample 3* in Table 3.1. Material properties are as in Tables 3.2 and 3.3 and the friction coefficients can be found in Table 4.2. A size of 0.001mm was chosen for the FE mesh in the contact area with a value of FKN of 1000 to increase the accuracy.

Two different load configurations were carried out:

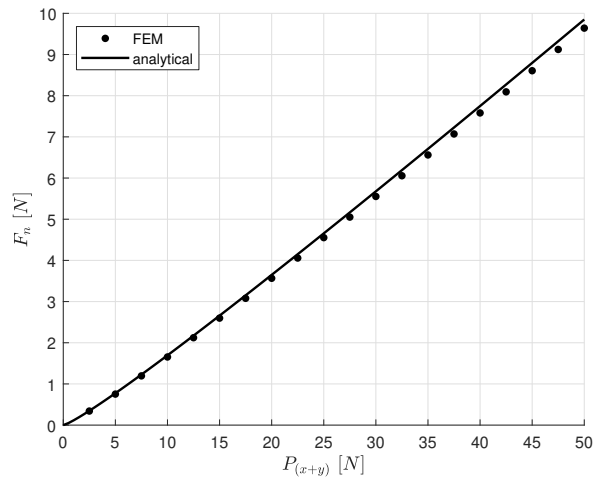
- i) S01: a biaxial system of tension forces  $P_x = P_y$  applied to warp and weft wires.
- ii) S02: only a tension force  $P_x$  applied to the warp wire, whereas the weft wire is free to deform longitudinally.

In both cases the analysis is static and divided into 20 substeps, throughout which the forces are linearly ramped from zero to a maximum value.

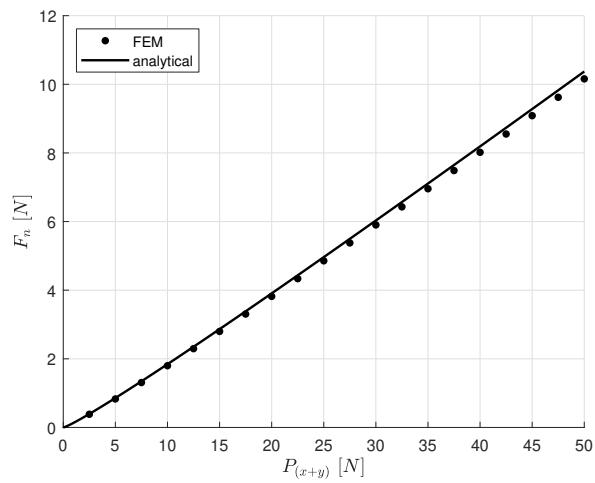
In the first load case, the normal contact force resulting from the numerical simulation is compared with the analytical solution from Equation 4.93. This is

illustrated in Figure 5.6. As regards the case of orthotropic mesh material (i.e., warp and weft wires built in two different materials), the two limit conditions of only warp ( $P_y = 0$ ) and only weft wire ( $P_x = 0$ ) under tension load are also reported in Figure 5.6c, for the case of warp wire in Nitinol and weft wire in steel.

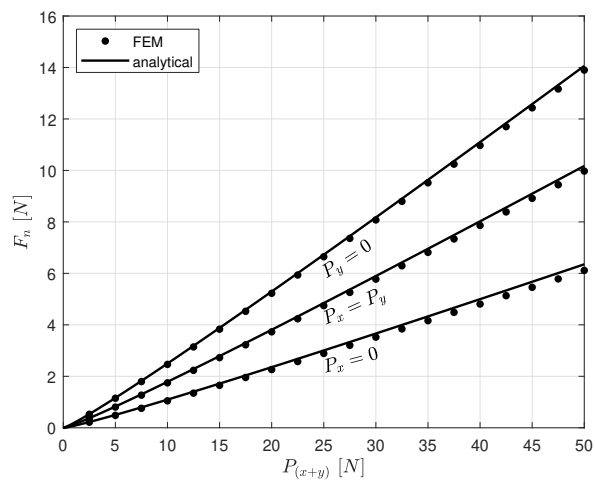
In general, a small difference between numerical and theoretical results can be observed, which remains almost constant within the range of tension load applied. An average value of approximately 2.3% for both the case of steel against steel and Nitinol against Nitinol has been calculated for the relative error, whereas for the orthotropic configuration, this value is initially higher (7.8%) and tends to approximately 2% as the loads increase. This is probably due to an error in computing the normal compression for low contact forces, for which a finer FE mesh would be required, given the small size of the contact area. For higher loads, instead, the elastic deformation of the wires becomes dominant and the error reduces, this being only limited by the accuracy of the beam theory employed in the analytical models. In fact, the absolute error, which at high loads is mostly due to a higher wire stiffness computed through the beam theory (as compared to the more accurate finite element method), was shown to grow linearly with the load. Therefore, it is believed that the range of forces applied could be extended while maintaining a similar level of relative error.



(a)



(b)



(c)

**Figure 5.6:** FEM and analytical results for S01: contact force versus total tension load for (a) steel against steel, (b) Nitinol against Nitinol and (c) Nitinol against steel.

In S02, the deformations  $u_x$  and  $u_y$  of warp and weft wires, resulting from the numerical simulation, are used for calculating the linearised stiffness and Poisson's ratio, respectively as  $\bar{K} = P_x/u_x$  and  $\bar{\nu} = -u_y/u_x$ . For the orthotropic mesh material, based on the numerical results the stiffness is calculated for warp and weft wires as follows:

$$\bar{K}_{warp} = \left. \frac{P_x}{u_x} \right|_{P_y=0} \quad (5.6a)$$

$$\bar{K}_{weft} = \left. \frac{P_y}{u_y} \right|_{P_x=0} \quad (5.6b)$$

From Equation 4.123, the following expressions for Poisson's ratio are obtained:

$$\bar{\nu}_{warp} = - \left( \frac{\bar{K}_{warp}|_{P_x=0}}{\bar{K}_{weft}} \right) \left. \frac{u_x}{u_y} \right|_{P_x=0} \quad (5.7a)$$

$$\bar{\nu}_{weft} = - \left( \frac{\bar{K}_{weft}|_{P_y=0}}{\bar{K}_{warp}} \right) \left. \frac{u_y}{u_x} \right|_{P_y=0} \quad (5.7b)$$

where  $\bar{K}_{warp}|_{P_x=0}$  and  $\bar{K}_{weft}|_{P_y=0}$  represent the stiffness of a wire when the tension is applied to the other. These are calculated analytically from the equations provided in Chapter 4, whereas the other quantities in the previous expressions are deduced from the FE simulation.

In Figure 5.7 the theoretical solution is compared with the numerical results for both isotropic and orthotropic mesh material, showing acceptable agreement. More specifically, the analytical and numerical model follow the same non-linear trend, with the FEM showing a slightly higher stiffness and lower Poisson's ratio as compared to the theoretical solution for all the materials analysed. Values of the absolute average relative error (AARE) are reported in Figure 5.7 for each material configuration.

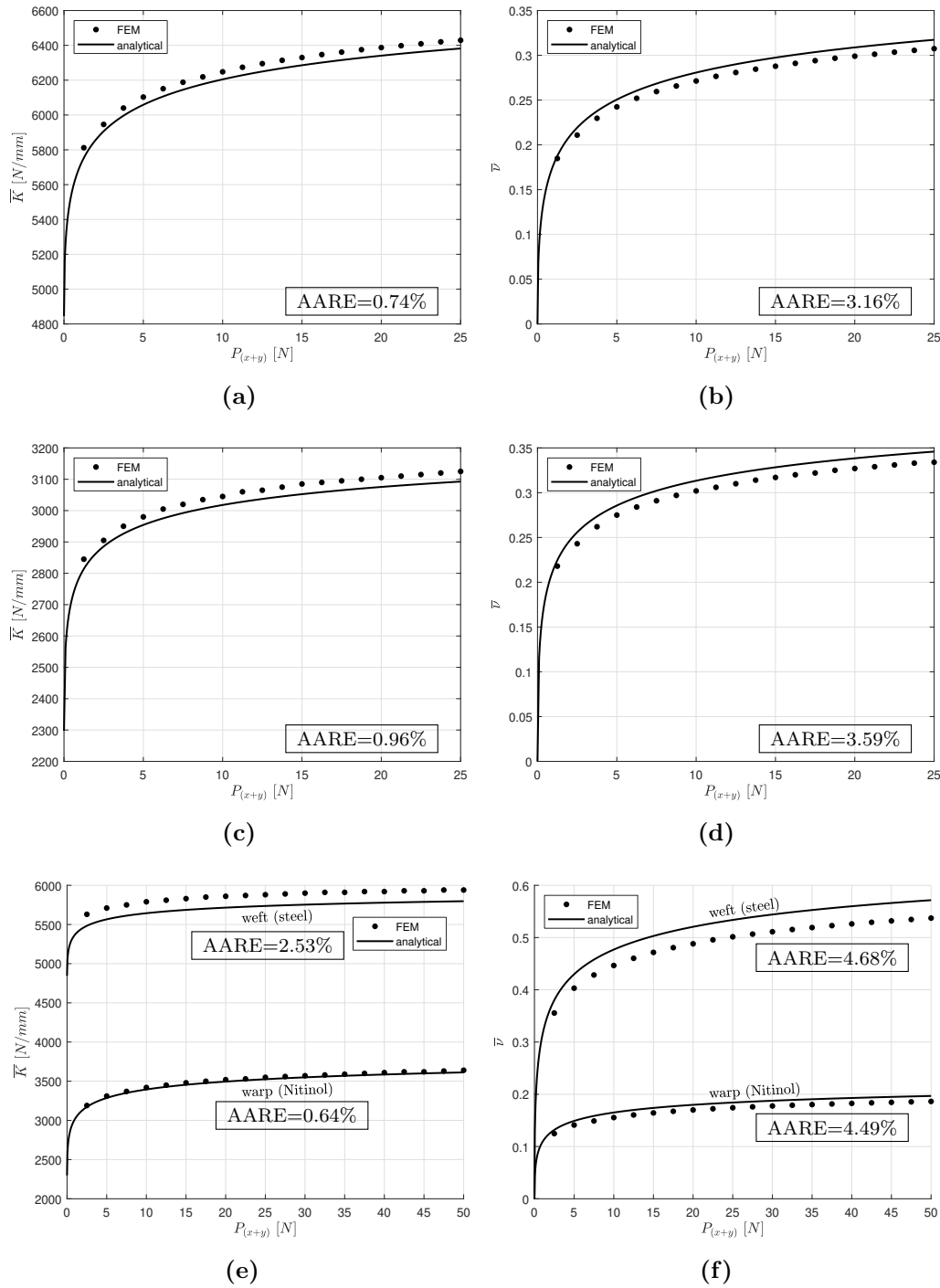


**Figure 5.7:** FEM and analytical results for S02: stiffness and Poisson's ratio for (a)-(b) steel against steel, (c)-(d) Nitinol against Nitinol and (e)-(f) Nitinol against steel.

## 5.6.2 Shear model

Recalling from Chapter 4, for the developing of the analytical model, the wires are reduced to straight cylinders, given the small dimensions of the contact area with respect to the wire radius. In order to provide with a more extensive validation of the theoretical solution and ascertain the validity of its assumptions, three different FE configurations were developed for the shear model:

- i) S03: sphere-to-sphere model, as a preliminary study.
- ii) S04: cylinder-to-cylinder model, for a direct comparison with the analytical model.
- iii) S05: wire-to-wire model, to investigate the extent of error introduced by the curvature simplification.

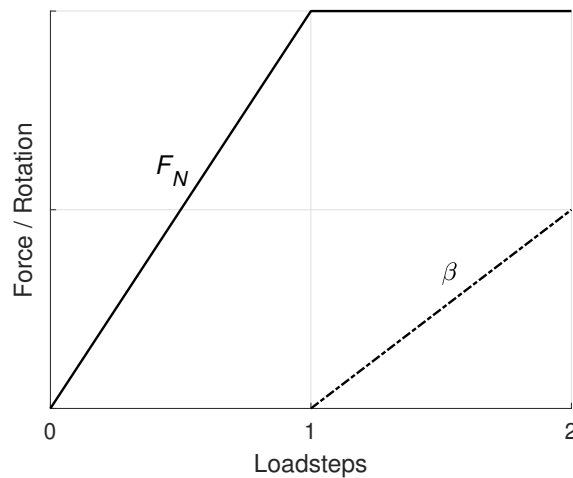


**Figure 5.8:** Load history for shear model validation.

In all the aforementioned configurations, one of the bodies is constrained with a fixed support at one face, whereas the other body is free to translate and rotate about the z-axis. The analysis is composed of two loadsteps. In the first step, to generate the contact force between the pair, a normal compressive load is applied

to the movable body, with the face where the load is applied being set as rigid to prevent it from distorting under the effect of the load. In the second step, the normal force is held constant, while a rotation is applied to the same body to generate the frictional torque. Both the normal load and rotation are linearly ramped from zero to a maximum value, as illustrated in Figure 5.8. Each step is subdivided in multiple substeps to facilitate the numerical convergence.

### 5.6.2.1 Sphere-to-sphere torsional friction

Initially, a preliminary FE analysis is conducted on the sphere-to-sphere frictional torque problem, in order to build confidence on the numerical model, by comparison with a well-established analytical solution. Since this topic has already largely studied and experimentally verified in the literature, this can be considered as a validation for the FEM itself, to ascertain the reliability of the numerical results.

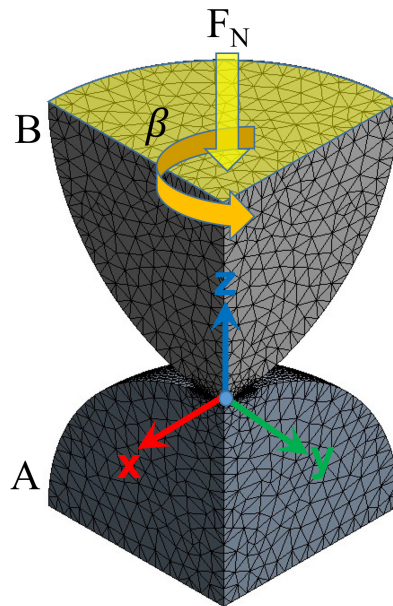


**Figure 5.9:** Boundary conditions and loads for S03.

The analysis is restricted to the case of two spheres with same diameter of 0.45mm and same material properties of steel, reported in Table 3.2. The contact

pair is represented only by two hemispheres, since, given the localised nature of the contact problem, the remaining portion of the solids does not take part in the deformation. Moreover, by exploiting the axial-symmetry of the spheres, only a sector of the hemisphere corresponding to an angle of  $\pi/2$  is represented, whilst the remaining is replaced by symmetric boundary conditions, as represented in Figure 5.9. A normal load of 5N is applied to sphere  $B$ . In Figure 5.10 a comparison between numerical results and theoretical solution from Equations 4.132 and 4.133 is illustrated. A good agreement between numerical and analytical results can be observed, with an AARE of 1.61%.

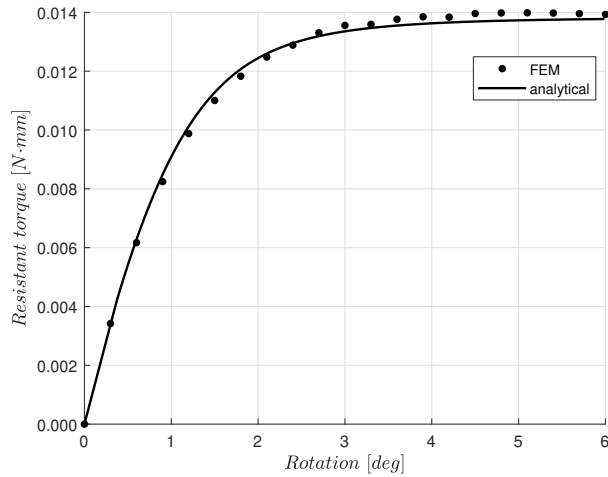


**Figure 5.10:** FEM and analytical results for S03.

### 5.6.2.2 Cylinder-to-cylinder torsional friction

The main validation of the shear analytical model is obtained by reproducing through the FEM with the same assumption of curvature neglect at the base of the theoretical formulation. The 3-D model is composed of two straight half-cylinders of the same radius as in Figure 5.11. Cylinder  $A$  is fixed at the bottom face. The load  $F_N$  and the subsequent rotation  $\beta$  are applied to the top face of cylinder  $B$ , which is set as rigid to maintain the geometric shape of the face to invoke a consistent load.

Similarly to the tension model, three different material combinations are tested,

two isotropic (i.e., steel and Nitinol) and one orthotropic (i.e. Nitinol against steel) with same material properties and friction coefficients utilised before.

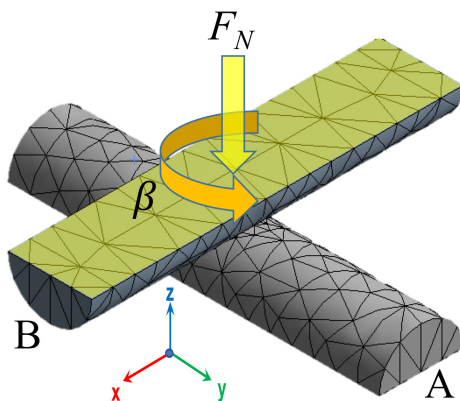


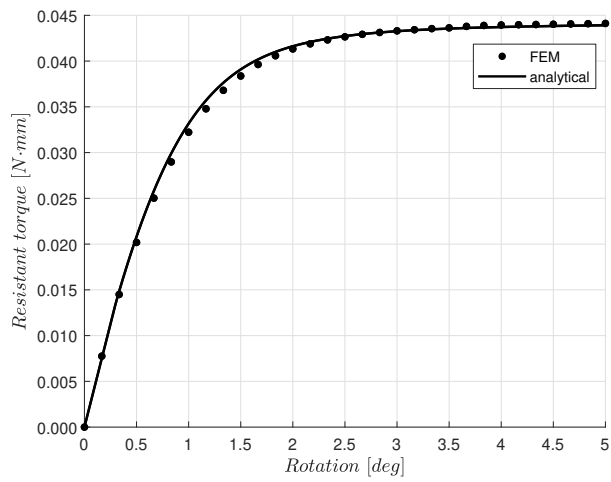
**Figure 5.11:** FEM boundary conditions and loads for S04: initially perpendicular cylinders.

The normal load for each material combination (see Table 5.2) has been scaled for each case so as to generate a similar size of contact area. For the orthotropic case, an equivalent shear modulus has been calculated for the torsional compliance as  $G_{eq} = \sqrt{G_1 G_2}$ , where  $G_1$  and  $G_2$  are the shear moduli of the constituent materials. This value has been employed in Equation 4.147 for the calculation of the twisting angle.

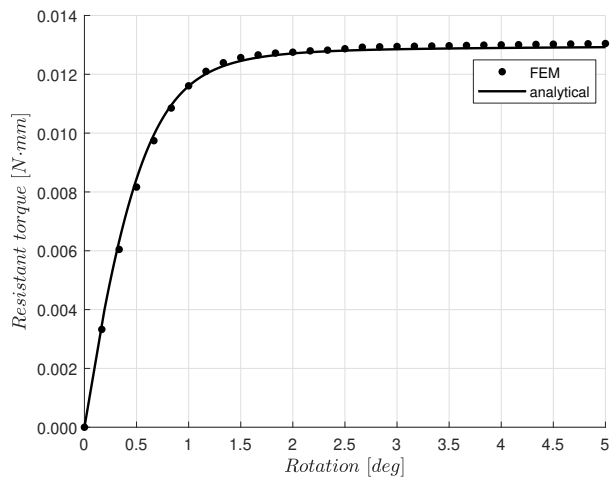
Materials	Load [N]
Steel-steel	10.00
Nitinol-Nitinol	4.89
Nitinol-steel	6.57

**Table 5.2:** Normal load for the different material combinations.

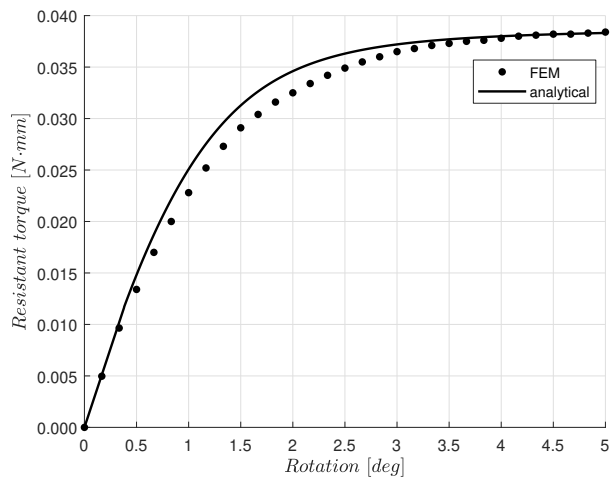
For this validation, the finest mesh from Table 5.1 is used, with a value of FKN=20 to further increase the accuracy. In Figure 5.12, the numerical results are compared with the analytical model from Equations 4.145 and 4.147, showing high accuracy over the whole range of rotation analysed.



(a)



(b)



(c)

**Figure 5.12:** FEM and analytical results for S04: (a) steel against steel, (b) Nitinol against Nitinol and (c) Nitinol against steel.

An absolute average relative error of 1.10% and 1.07% is calculated respectively for the steel-to-steel and the Nitinol-to-Nitinol isotropic cases, with a relative error at  $\beta=5\text{deg}$  of respectively 0.42% and 0.96%. With regards to the orthotropic mesh material, an increased error can be observed in the microslip (where only part of the contact area is slipping) phase as reported in Figure 5.12c, due to the simplified formulation used for the equivalent shear modulus. More specifically an AARE of 2.25% and a maximum relative error of 4.39% at  $\beta=0.33\text{deg}$  are calculated. However a high accuracy is reestablished in the macroslip phase, with an error of 0.40% at  $\beta=5\text{deg}$ .

### 5.6.2.3 Wire-to-wire torsional friction

Finally, in order to ascertain the level of error introduced in the analytical model by the curvature neglect, this assumption is relaxed and a FE model reproducing a pair of sinusoidally curved wires under frictional contact is analysed. Both the wires have been truncated with a plane parallel to the contact area, as represented in Figure 5.13.

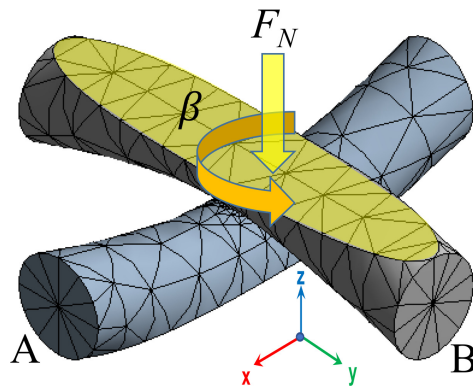


**Figure 5.13:** FEM boundary conditions and loads for S05: initially perpendicular wires.

Note that Saint-Venant’s principle applies where the stresses and deformations imparted locally at the contact do not propagate to the further field locations. The boundary condition and FE meshing are analogous to S04, with an element

size of  $h=0.0005\text{mm}$  and a value of  $\text{FKN}=10$ . Only the isotropic case of steel against steel is analysed, with a normal load of  $10\text{N}$ .

In Figure 5.14 the results of the simulation are compared with the analytical model. As it can be seen from the figure, the initial region of the micro-slip phase is almost identical with the S04 configuration.

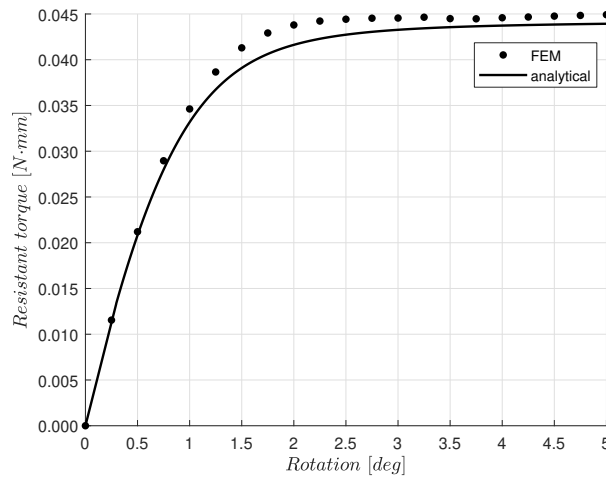


**Figure 5.14:** FEM and analytical torque-rotation response for S05.

It can be noticed that an error is introduced in correspondence of the macro-slip phase, where the torsional moment is slightly higher than the analytical model. This is most likely due to a larger contact area than the one theorised. This is due to the curvature at the contact area which is not accounted for by the Hertz contact model, but is in the FEM. An AARE of 3.31% is calculated and the highest values of the relative error are observed across the final region of the microslip phase, with a maximum of 5.65% at  $\beta=1.75\text{deg}$ . After this phase, the error decreases to a value of approximately 2.25% at  $\beta = 5^\circ$ . It is believed that the extent of this error is related to the curvature of the interacting surfaces and the dimension of the contact area.

### 5.6.3 Out-of-plane bending model

Recalling the out-of-plane bending analytical model in Section 4.8, this model predicts the contact force between the warp/weft pair as a function of the RUC boundary conditions. As a validation for the theoretical solution, the single case of mesh material under uniaxial bending is considered, meaning that the bending is only applied to one wire, whilst the other is free to extend longitudinally. As represented in Figure 5.15, bending is generated in the warp wire (i.e., parallel to x-axis) by applying a displacement along the z-axis at both of its extremities, whereas the weft wire is pinned at both ends.

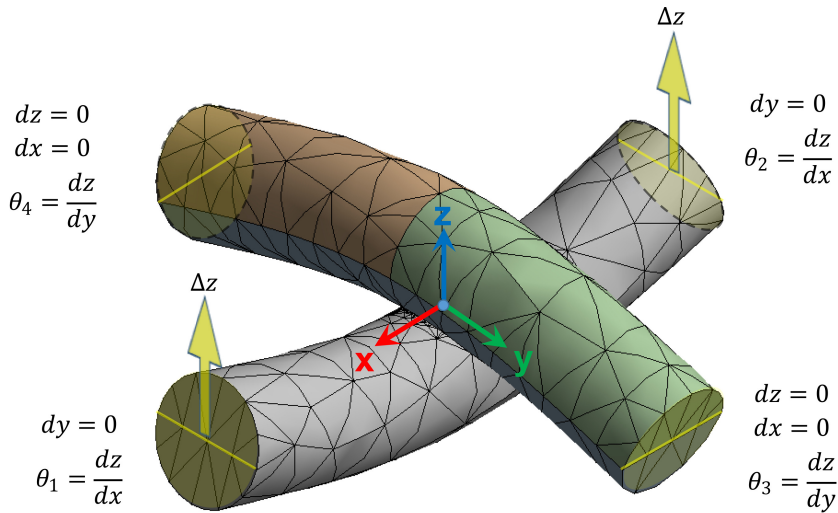
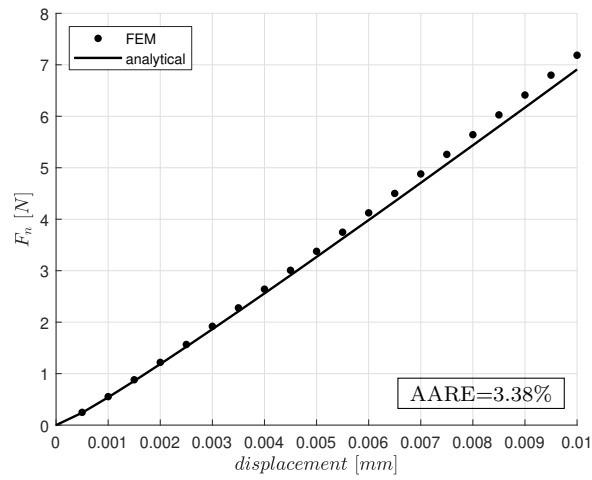


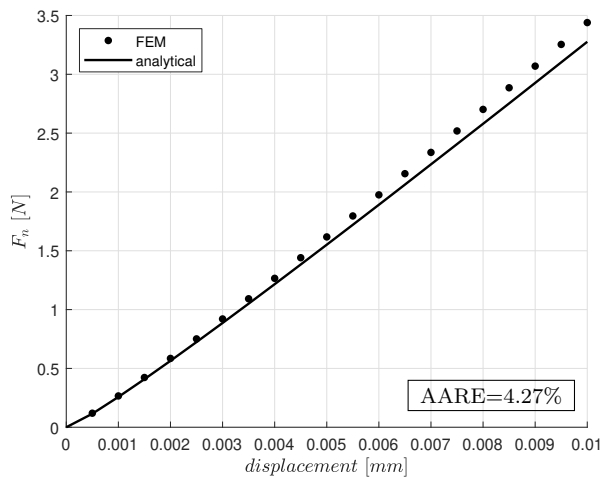
**Figure 5.15:** 3-D FE model and boundary conditions for the out-plane bending model.

Materials, wire dimensions, and friction coefficients are again the same as in the previous models. In the case of isotropic mesh material, analogous results would be achieved with the opposite configuration, by applying the displacements to the weft wire and the pinned constraints to the warp. The angle of rotation of the circular cross-section with respect to the neutral axis is scoped for each extremity of the wires and used as input for the analytical model. The simulation is composed of a single loadstep, which is divided into 20 substeps and the displacement load is ramped from zero to the maximum value of 0.01mm. Like from

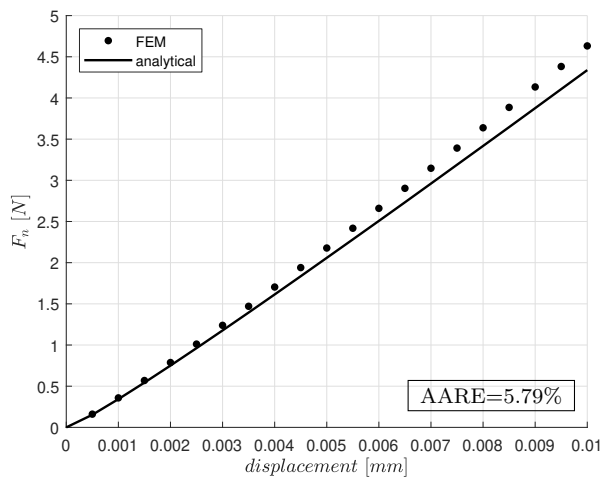
the tension model, the FE mesh element size in the contact area is increased to 0.001mm (as compared to the shear model where a smaller element of 0.0005mm was used) to facilitate the numerical convergence since, in this case, both the bodies are movable, making the convergence more difficult. Moreover, the same contact configurations and settings are used with FKN=100 to increase the accuracy. In Figure 5.16 the numerical results are compared with the theoretical solution showing a general good agreement, with a slightly higher error for the orthotropic case. This error is most likely attributed to the simplified approach of how the contact area and the out-of-plane displacements are calculated with the Hertz contact model and the Timoshenko's beam theory employed not accounting for the longitudinal curvature of the wires. Values of the AARE are reported in Figure 5.16 for each material configuration.



(a)



(b)



(c)

**Figure 5.16:** FEM and analytical results for out-of-plane bending model: (a) steel against steel, (b) Nitinol against Nitinol and (c) Nitinol against steel.

## 5.7 Conclusions

In this chapter, a thorough validation of the developed analytical models for the characterisation of PWMMs was carried out by means of the finite element method.

Due to the complexity of the frictional contact problem analysed, some critical aspects have emerged, in particular the need for a high FE mesh density in the proximity of the contact area for a correct description of the physics involved. Based on the output of a mesh convergence study, a careful choice of the parameters for the numerical model, such as mesh element size and contact stiffness, was performed in order to achieve a sufficient level of accuracy in the simulations.

A comparison between numerical results and theoretical solution has substantially confirmed a general validity of the analytical models. For all the models, three different constituent material combinations are tested, two isotropic and one orthotropic.

For the tension model, the validation shows good agreement between analytical and numerical model in both uniaxial and biaxial load. The theoretical solution is capable of predicting the contact force with a moderate relative error for a wide range of tension forces (0-50N) considered. Since for high loads the accuracy of the model is mostly limited by the simplifications of the beam theory in computing the wire stiffness and the absolute error was shown to grow linearly with the load, it is believed that the force range could be extended while maintaining the same level of relative error. Also the non-linear behaviour of stiffness and Poisson's ratio is correctly captured by the theoretical solution as confirmed by the results.

The highly non-linear response of mesh materials to in-plane shear was captured with high accuracy along a wide range of motion (0-5°) and for materials with a large difference in mechanical properties (being the stiffness of steel more than twice the one of Nitinol). It is believed that this rotation range can be extended, only limited by when the warp and weft wires come into contact in other locations other than the initial contact area. A slight error is observed in

the microslip transition for the orthotropic case, suggesting the need of a further investigation on the elastic compliance between two different materials under frictional contact.

Finally, the out-of-plane bending model was tested for the case of uniaxial bending applied to a single wire, showing acceptable agreement between numerical and theoretical results. As with the shear model, the orthotropic configuration provides a slight increase in error and is most likely due to both the longitudinal curvature of the wires and the Hertz contact model not accounting for this.

# Chapter 6

## Reduced order finite element model

### 6.1 Introduction

In this chapter a reduced order finite element model for the characterisation of mesh materials is discussed and a novel developed software that implements the reduced model into a MATLAB-ANSYS environment is presented.

A brief overview and general introduction of the techniques for model order reduction are presented and discussed. Highlighting the homogenization method adopted in this work is the primary focus.

A new equivalent reduced element is then presented, which is composed of the combination of shell and beam elements. The formulation of these two finite element types is described. A detailed discussion is reported on how these elements are assembled to form the novel beam-shell element and what their function is in replicating the mesh material mechanical response.

The MATLAB-ANSYS algorithm is then presented and its different parts are described in depth. The specific functions performed by MATLAB and ANSYS and the procedure adopted to integrate the two software applications are illustrated.

Finally, the reduced model is validated through its software implementation by analysing a single RUC under different configurations of in-plane loads and boundary conditions and comparing the results with the corresponding theoretical solution. A more complex model composed of 100 beam-shell elements (100 mesh intersections) is analysed and compared with a full FEM for further validation. A qualitative experimental validation is also performed by comparing the numerical results with previously acquired data from bias-extension tests.

## 6.2 Model order reduction techniques

The continuously increasing demand for high performances, precision and reliability of dynamic systems has pushed the numerical modelling to extremely high levels of complexity, sometimes involving several millions of DOFs. Despite the advent of supercomputers, capable of solving extreme-scale FEMs, the still valid need for an alleviation of the computational burden has incentivised the development of several different model order reduction (MOR) techniques.

For a general structural dynamics problem, the dynamic equilibrium is expressed by a set of linear second-order differential equations:

$$[M]\{\ddot{x}(t)\} + [C]\{\dot{x}(t)\} + [K]\{x(t)\} = \{f(t)\} \quad (6.1)$$

where  $[M]$ ,  $[C]$  and  $[K] \in R^{n \times n}$  are respectively the mass, damping and stiffness matrices of the *full order model*, whereas  $x(t)$ ,  $\dot{x}(t)$ , and  $\ddot{x}(t) \in R^n$  are the nodal displacement, velocity and acceleration vectors and  $f(t) \in R^n$  is the load vector. The dimension  $n$  of the vector space represents the number of total DOFs of the system, corresponding to the number of nodes multiplied by the DOFs at each node. The main aim of the reduction method is to find an equivalent system of dimension  $m$  for which  $m \ll n$ , referred to as *reduced order model* or simply *reduced model*, so as to limit the numerical expense of the full model. In general, the reduced model is defined by a new set of *reduced order coordinates*  $x_R \in$

$R^m$ , which are mathematically related to the full order coordinates through a coordinate transformation:

$$x(t) = Tx_R(t) \quad (6.2)$$

where  $T \in R^{n \times m}$  is the *coordinate transformation matrix*. Being the matrix  $T$  usually time-invariant, the same transformation can be applied to the velocity and acceleration vectors by simply differentiating the previous equation, as follows:

$$\dot{x}(t) = T\dot{x}_R(t) \quad (6.3a)$$

$$\ddot{x}(t) = T\ddot{x}_R(t) \quad (6.3b)$$

The equations of dynamic equilibrium for the reduced model are then:

$$[M_R]\{\ddot{x}_R(t)\} + [C_R]\{\dot{x}_R(t)\} + [K_R]\{x_R(t)\} = \{f_R(t)\} \quad (6.4)$$

where  $[M_R]$ ,  $[C_R]$  and  $[K_R] \in R^{m \times m}$  are respectively the mass, damping and stiffness matrices of the reduced model and  $f_R(t)$  is the equivalent load vector applied to the reduced model.

### 6.2.1 Homogenization method as a physical coordinate reduction

Depending on the type of coordinate transformation, the reduction method belongs to one of the following three categories:

- i) Physical coordinate reduction.
- ii) Generalised coordinate reduction.
- iii) Hybrid coordinate reduction.

Only the first category will be described since it is inherent to the present research. For a detailed discussion on reduction techniques, the author directs the reader's attention to [125]. In the *physical coordinate* reduction method (also called *dynamic condensation*), the reduced coordinates are obtained by removing part of the physical coordinates of the original full model. In this sense, the reduced model space represents a subset of the full model domain. The coordinate transformation matrix is represented by the following expression:

$$T = \begin{bmatrix} I \\ R \end{bmatrix} \quad (6.5)$$

where  $I$  is an identity matrix of order  $m$  and  $R$  is the condensation matrix.

The homogenization method adopted for this work can be included among the numerous existing physical coordinate reduction techniques and can be referred to as *truncated dynamic condensation* technique. Recalling from Chapter 3, the mechanical properties of mesh materials are defined based on a representative volume element (RVE) or simply repeating unit cell (RUC). The physical coordinates are reduced to only a limited subset located at the boundaries between each RUC, where a system of periodic boundary conditions (PBC) and loads is applied. At the microscopic level of the RUC, based on these reduced coordinates, homogenized stresses and strains are calculated by averaging within the RUC.

As a simplified example, the warp wire in the RUC can be considered as discretised in a number  $n$  of nodes in the full order model, as represented in Figure 6.1. The full order coordinates are the following:

$$x = \left\{ \begin{array}{c} x_1 \\ x_2 \\ x_3 \\ \vdots \\ x_{n-1} \\ x_n \end{array} \right\} \quad (6.6)$$

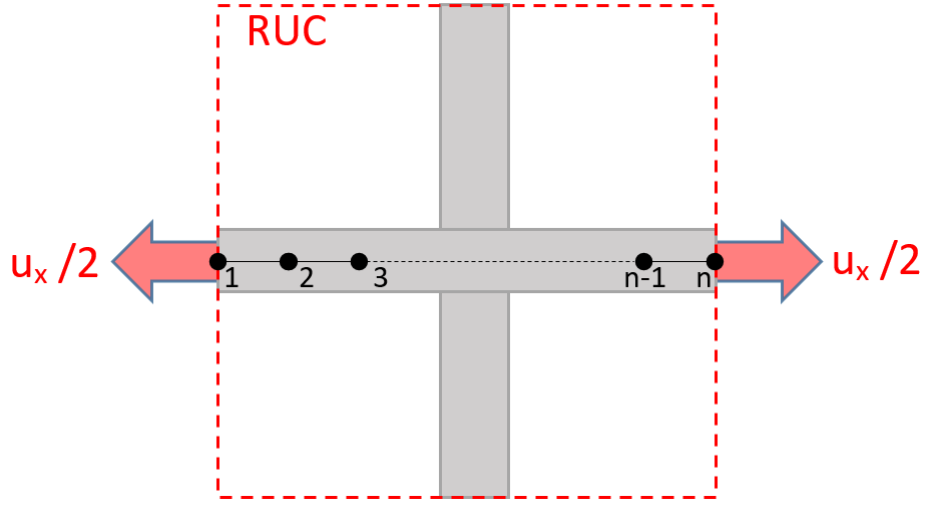


**Figure 6.1:** Example of reduction technique adopted.

The tension-compression model discussed in Chapter 4 is a function of the overall deformation  $u_x$  of the wire, which can be calculated based on the position of the initial and final nodes only (i.e., nodes 1 and  $n$ ). Therefore a proper coordinate transformation matrix  $T$  can be chosen to only retain the coordinates at the boundaries, so that the reduced order coordinates are  $x_R = \{x_1, x_n\}$ :

$$x = \begin{bmatrix} 1 & 0 \\ 0 & 0 \\ \vdots & \vdots \\ 0 & 0 \\ 0 & 1 \end{bmatrix} x_R \quad (6.7)$$

### 6.3 Reduced element formulation

To predict with high accuracy the non-linear response of mesh materials, the full numerical model must represent the contact mechanics of each wire intersection with an extremely high mesh density (recall Section 5.4). For mesh materials with

a high number of intersections involved, this would easily yield to models with millions of DOFs.

The strategy adopted in this research consists into reducing each intersection of the full model to an equivalent finite element, whose mechanical properties are defined by the developed analytical models discussed in Chapter 4. The contact force vanishes inside the RVE and can be considered as an internal force. The benefit of this method is not only the reduction of the nodes number and consequent DOFs, but also the elimination of computationally expensive contact elements and incorporation of contact non-linearities into a linear analysis. Furthermore, this reduces the issues associated with non-linear convergence of which complex non-linear contacts can often become a victim. This reduced equivalent element is representative of a single RUC and it is obtained by the combination of two basic finite element types:

- i) 3-D 8-node structural shell.
- ii) 3-D 2-node beam.

In the ANSYS environment these elements are implemented respectively under the name of SHELL281 and BEAM188. In the following sections a description of their geometry and technology is presented with the kinematic coupling and the role of the different elements within the reduced equivalent element.

### **6.3.1 SHELL281**

SHELL281 is a high-order structural shell element composed of eight nodes (four corner nodes and four mid-side nodes) with six degrees of freedom at each node: translations  $u$ ,  $v$  and  $w$  respectively along x, y and z-axes and rotations  $\theta_x$ ,  $\theta_y$  and  $\theta_z$  about the same axes. The geometry and node naming convention is illustrated in Figure 6.2.

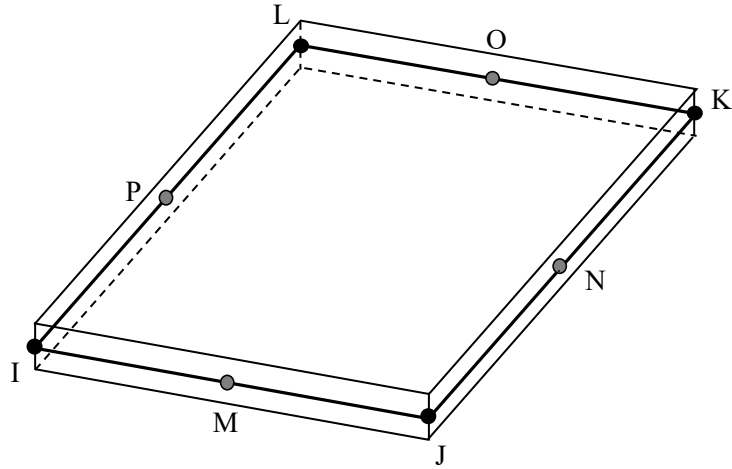


**Figure 6.2:** ANSYS SHELL281 element nodes: I through L are the corner nodes, whilst M through P are the mid-side nodes.

Since the quadratic shape functions of the element SHELL281 are analogous for all the six degrees of freedom, they can be expressed in a general form as follows:

$$\begin{aligned}
 X = & \frac{1}{4} \left( X_I (1-s)(1-t)(-s-t-1) + X_J (1-s)(1-t)(-s-t-1) \right. \\
 & \left. + X_K (1-s)(1-t)(-s-t-1) + X_L (1-s)(1-t)(-s-t-1) \right) \\
 & + \frac{1}{2} \left( X_M (1-s^2)(1-t) + X_N (1+s)(1-t^2) + X_O (1-s^2)(1+t) \right. \\
 & \left. + X_P (1-s)(1-t^2) \right) \quad (6.8)
 \end{aligned}$$

where  $X$  represents a generic displacement within the element and  $X_I, X_J, \dots, X_P$  represent the correspondent nodal displacements at the nodes I, J,  $\dots$ , P.

All the displacements  $u, v, w, \theta_x, \theta_y$  and  $\theta_z$  are defined by the previous equation, by simply replacing the generic displacement with the specific one. For example:

$$u = \frac{1}{4} \left( u_I (1-s)(1-t)(-s-t-1) + u_J \dots \right) \quad (6.9)$$

Equation 6.8 is expressed in isoparametric formulation, as a function of two natural coordinates  $s$  and  $t$ , for which  $-1 \leq s \leq 1$  and  $-1 \leq t \leq 1$ , attached to the element with the origin located at its centre.

### 6.3.2 BEAM188

BEAM188 is a 3-D 2-node beam based on Timoshenko beam theory, hence also accounting for transverse shear effects. Each node has six degrees of freedom, which include translations along x, y and z-axes and rotation about the same axes, plus an optional seventh degree of freedom for warping. The geometry and node naming convention is illustrated in Figure 6.3.

This particular element technology offers three different options for the shape functions, which can be selected by changing the value of KEYOPT(3).

- By default, KEYOPT(3)=0, which corresponds to a standard linear 2-node beam element. Since the shape functions are linear with a single point of integration, the solution quantities such as strains and stresses are constant along the beam. Hence, with this option, the element is able to correctly represent only the case of constant bending moment.
- With KEYOPT(3)=2, an internal node is added as a point of interpolation and the element is based on quadratic shape functions with two points of integration. The solution quantities vary linearly along the beam.
- With KEYOPT(3)=3, two internal nodes are added. The beam is now based on cubic shape functions and three points of integration along the length are used, resulting in quadratic variation of the solution.

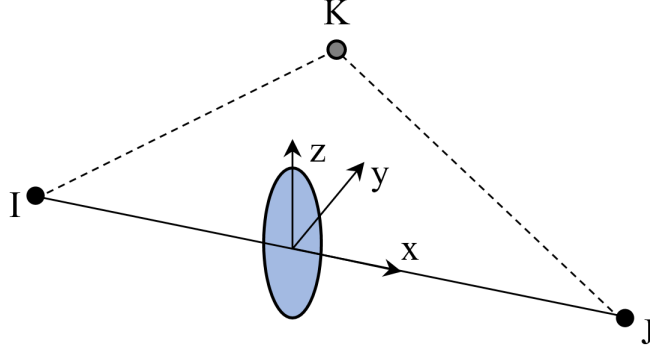


**Figure 6.3:** BEAM188: geometry and nodes.

In this work,  $\text{KEOPT}(3)=2$  has been used, with quadratic shape functions. This choice was motivated by the fact that, with this option, each beam element can be defined by only providing the coordinates of its two end nodes, thus simplifying the generation of the reduced FE mesh and at the same time maintaining a good accuracy of the results. Analogously to the SHELL181 element, the shape functions of this element can be expressed in general form, as follows:

$$X = \frac{1}{2} (X_I (-s + s^2) + X_J (s + s^2)) + X_K (1 - s^2) \quad (6.10)$$

where again  $X$  is representative of each of the six degrees of freedom. The previous equations are expressed with isoparametric formulation, with respect to a natural coordinate  $s$  with origin at the centre of the beam and oriented along the element, with  $-1 \leq s \leq 1$ .

### 6.3.3 Coupling and role of different elements

The elements previously described are combined to form a reduced equivalent element, representative of a single RUC.

A square shell element of side  $L$  is disposed so as its centre corresponds to a mesh material intersection and its mid-side nodes to a point along the warp and

weft wires. Two beams of length  $L/2$  are disposed along each side of the shell, sharing one node with each other, for a total of 8 beams and 12 nodes.

Hence, the reduced equivalent element is composed of a total of 20 nodes and 9 elements (1 shell and 8 beams). Note that where the beam elements connect to one another is a node share about those beam elements. This is represented graphically in Figure 6.4.

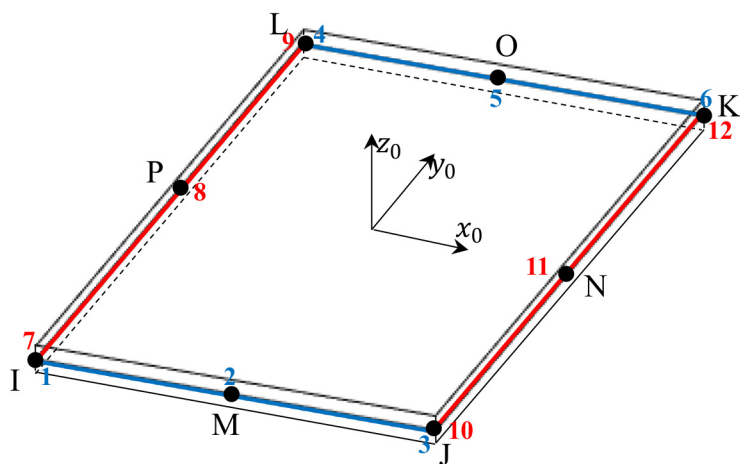


**Figure 6.4:** Reduced beam-shell element: a shell surrounded by 8 beams along the perimeter. Shell nodes are in letters (I through P) and beam nodes are in numbers (1 through 12).

Conventionally, the warp and weft directions are defined as parallel respectively to the local x-axis and y-axis. Thus, the beams in blue in the figure are representative of the warp wire, whilst the beams in red represent the weft wire. For the case of orthotropic mesh material, the mechanical properties of the beams are defined accordingly to the ones of the respective wires. Since two rows of beams are created to represent a single wire, the second moment of area of the beams must be half that of the wire.

The beam nodes are spatially coincident with the shell nodes (meaning that they share the same global coordinates), however they are mathematically independent. The coupling between these elements is guaranteed by kinematic constraint equations that impose equivalent translational displacements between

coincident nodes, allowing independence for in-plane rotation. This condition allows beams on different sides of the shell to rotate independently from each other, being only restrained by the membrane stiffness of the shell. A local coordinate system with origin in the centroid is created for each shell, where the z-axis is normal to the element and the x and y-axes are parallel respectively to the I-J and J-K sides, as represented in Figure 6.4. Vertical and horizontal beams are coupled at the corner nodes with a rotational constraint that imposes the same rotation about the local x and y-axes.

As discussed in Chapter 4 and verified numerically in Chapter 5, the mechanical response of the RUC to tension load can essentially be characterised by an effective longitudinal stiffness and an effective Poisson's ratio, whereas the non-linear frictional response for in-plane shear is represented by a torsional moment applied to the point of intersection of wires.

In the reduced model, the two element types (i.e., shell and beams) play a different role in replicating the PWMM mechanical response. Resistance to tension and in-plane bending is computed separately by the two different elements. In particular, the shell has the function of reproducing the longitudinal stiffness of the wires and the Poisson's effect, whereas the beams reproduce the in-plane bending. Thus, the shell must not offer any resistance to transverse loading, since this is already provided by the beam elements. This is achieved by using an orthotropic material formulation for the shell and setting an infinitesimally small value for the shear modulus (not zero, since it would yield to a singular stiffness matrix). With this condition, also the transverse shear and resistance to out-of-plane bending is entirely relying on beams. On the contrary, the longitudinal resistance of the beams must be reduced to nil, since already accounted for by the shell elements. This condition is achieved by setting an infinitesimally small area for the beams, being the longitudinal stiffness of a beam proportional to the cross-sectional area.

The shell longitudinal stiffness is  $K = Et$  where  $t$  is the thickness. Setting conventionally  $t = A_{wire}/L$  (being  $A_{wire}$  the cross-sectional area of the wire), the elastic modulus of the shell is calculated as follows:

$$E_x = \frac{\overline{K}L}{A_{wire}} \quad (6.11)$$

where  $\overline{K}$  is the linearised effective elastic modulus of the mesh material, calculated with Equation 4.117a. The Poisson's ratio of the shell is simply equal to the linearised effective Poisson's ratio of the mesh material (Equation 4.117b):

$$\nu_{xy} = \overline{\nu} \quad (6.12)$$

## 6.4 MATLAB-ANSYS algorithm

The finite element reduction proposed in this work requires the implementation into ANSYS of the equivalent element previously described. Moreover, to perform the numerical analysis, the mechanical properties must be constantly updated in the FEM, by solving the developed analytical models as a function of the external loads.

With this aim, a software application was developed that integrates the functionalities of MATLAB with the ANSYS finite element solver. The core of the software application is developed in MATLAB and is composed of the following parts:

- i) Main script.
- ii) Post-processing function.
  - a) Tension-compression subfunction.
  - b) In-plane shear subfunction.

### 6.4.1 Main script

In the main script, an iterative process is performed (see Appendix A). For each iteration, the ANSYS solver is called in batch mode by the MATLAB script.

The numerical solution is computed for a single substep at a time, after which the execution is returned to MATLAB for the post-processing. Throughout the whole process, data communication between the two software applications is performed by means of dedicated CSV (Comma Separated Values) archives.

In the first iteration, some initialisation values are calculated in MATLAB based on the material properties and geometry of the wires, and then passed to ANSYS. In ANSYS, after a series of preliminary actions, the solving process is carried out for the first substep. The output results are then stored in the CSV files and the execution is returned to the MATLAB main script.

The post-processing function is then called, which, based on the results of the numerical simulation, calculates the correspondent effective parameters for the materials. These are compared to the initialisation values adopted for the simulation. If some convergence criteria are met, in the next iteration the computation will proceed to the second substep, otherwise the first substep will be repeated until convergence. The whole process is repeated until completion of the simulation.

#### **6.4.2 MATLAB post-processing**

Within the MATLAB post-processing, the ANSYS output data from the previous iteration are used as input for the developed analytical models in order to calculate the effective mechanical properties of the mesh material to be used in the next iteration.

Since for a non-linear problem, such as the one investigated in this research, the properties (i.e., stiffness, Poisson's ratio and torsional moment) are proportional to the displacement, it is not possible to calculate their correct values before actually computing the displacements. For this reason, as aforementioned, an iterative procedure is required, which starts by assuming some initial values  $\overline{K}_0$ ,  $\overline{\nu}_0$  and  $\overline{\mathfrak{M}}_0$  for the mechanical properties and progressively correcting them according to the numerical output, until the convergence is met.

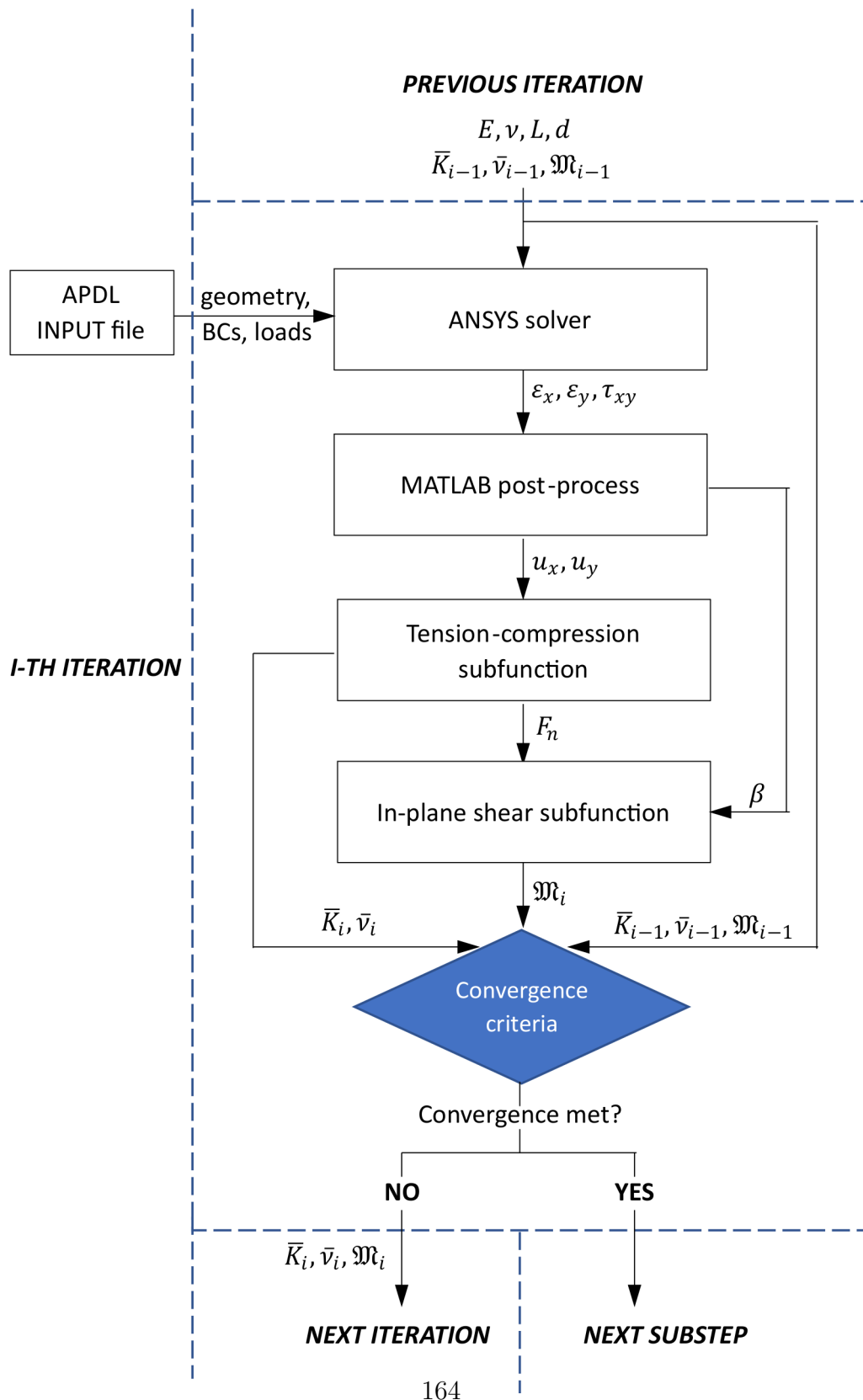


**Figure 6.5:** Logical scheme of the MATLAB-ANSYS algorithm for the  $i$ -th iteration.

At every iteration, based on the numerical results returned by ANSYS, the local deformations  $u_x$  and  $u_y$  respectively of warp and weft wires are calculated for every RUC as the product of the shell normal strains and the initial length  $L_0$  of the wires, while the twisting angle  $\beta$  between the wires is simply equal to the shell shear strain:

$$u_x = \varepsilon_x L_0 \quad (6.13a)$$

$$u_y = \varepsilon_y L_0 \quad (6.13b)$$

$$\beta = \tau_{xy} \quad (6.13c)$$

where  $\varepsilon_x$ ,  $\varepsilon_y$  and  $\tau_{xy}$  are the shell strains calculated with respect to the element coordinate system.

The calculation of the PWMM mechanical properties is then performed by the two listed subfunctions which are executed sequentially, as schematised in Figure 6.5.

The first to be called is the tension-compression subfunction that, based on the longitudinal deformations of the wires, calculates the value of the contact force  $F_n$  for each RUC, by applying the correspondent developed analytical model. The subfunction also calculates the effective longitudinal stiffness and effective Poisson's ratio of the material.

The contact force and the twisting angle are sent as input to the shear subfunction, which calculates the torsional moment generated by the frictional contact between the wires.

#### 6.4.2.1 Convergence criteria

At the end of the  $i$ -th iteration, a new set of parameters  $\overline{K}_i$ ,  $\overline{\nu}_i$  and  $\mathfrak{M}_i$  has been calculated for each RUC. These values are compared with the results of the

previous iteration by calculating a convergence parameter, which corresponds to the absolute value of the relative error, as follows:

$$X_{conv} = \left| \frac{X_i - X_{i-1}}{X_{i-1}} \right| < \textit{criterion} \quad (6.14)$$

where  $X$  is generic for each of the properties ( $\bar{K}$ ,  $\bar{v}$  and  $\mathfrak{M}$ ) and *criterion* is a parameter that specifies the maximum accepted error. A value of 1% has been used for this parameter.

If the condition in Equation 6.14 is true for all the three properties, the convergence is met for the correspondent element. If the convergence is met for all the elements in the model, the solution will proceed to the next substep.

### 6.4.3 ANSYS APDL subroutines and restart solution

All of the processes of numerical analysis are executed in ANSYS and governed through a series of subroutines developed in APDL (ANSYS Parametric Design Language) code. To allow the passage of information between ANSYS and MATLAB at each iteration, the numerical solution needs to be subdivided into different time steps and the execution of ANSYS temporarily suspended after the completion of each of them. For this purpose, a multiframe restart analysis is set in ANSYS, so that a result file is created after each substep. At the next execution of ANSYS, the result file is loaded and the solution is started from the previous converged point. If the convergence criteria in Equation 6.14 are not met during the MATLAB post-processing, the last restart file is deleted and the solving process is repeated for the unconverged substep.

At the first substep, a series of preliminary actions is performed in ANSYS:

- i) Definition of mesh material overall geometry and FE mesh generation through shell elements.
- ii) Creation of local coordinate systems for each shell element.

- iii) Automatic creation of beam elements for each shell and setting of constraint equations.
- iv) Application of boundary conditions and loads.

The steps i) and iv) are accomplished through an input file that can be edited by the user, whereas steps ii) and iii) are performed by means of dedicated APDL subroutines. At the end of the analysis, a CDB database file is generated that allows the post-processing of results in ANSYS environment.

## 6.5 Reduced model validation

A thorough validation of the reduced order finite element model is presented in the following sections. Initially, a model representing a single RUC is analysed separately under tension and shear. Then the results are validated by direct comparison with the respective analytical models. Finally, a more complex model representing a mesh material plate composed of 100 intersections is analysed and the results compared with a dedicated full FEM.

In all the performed simulations, the geometry of the wires is the same as listed in Chapters 4 and 5, corresponding to *Sample 3* from Table 3.1. The same three material combinations are tested, two isotropic and one orthotropic.

### 6.5.1 Single RUC

#### 6.5.1.1 Tension

The response to tension load is analysed by considering the case of a single RUC under uniaxial load. This corresponds to applying the tension load only to the warp wire, whereas the weft wire is left free to deform longitudinally according to the effective Poisson's ratio.

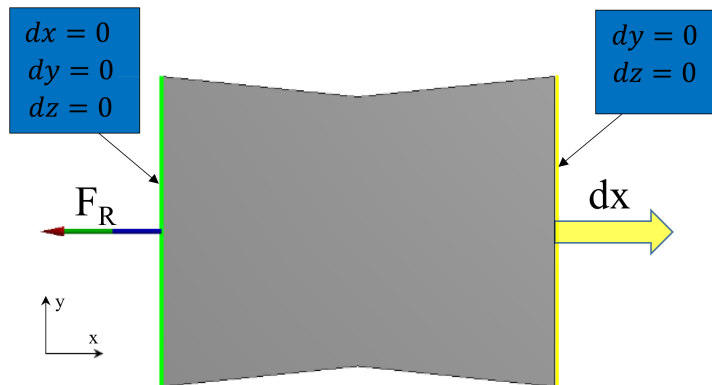


**Figure 6.6:** Deformed reduced FEM: load and BCs for uniaxial tension of a single RUC.

In Figure 6.6 the deformed shape of the element is illustrated, together with the boundary conditions and the application of the load. The nodes on the left side are restrained from translating, while a displacement load along the x-axis is applied to the nodes on the right side. The displacement load, which corresponds to the elongation  $u_x$  of the warp wire, is ramped from zero to a maximum value of 0.005mm. The simulation is divided into 20 substeps.

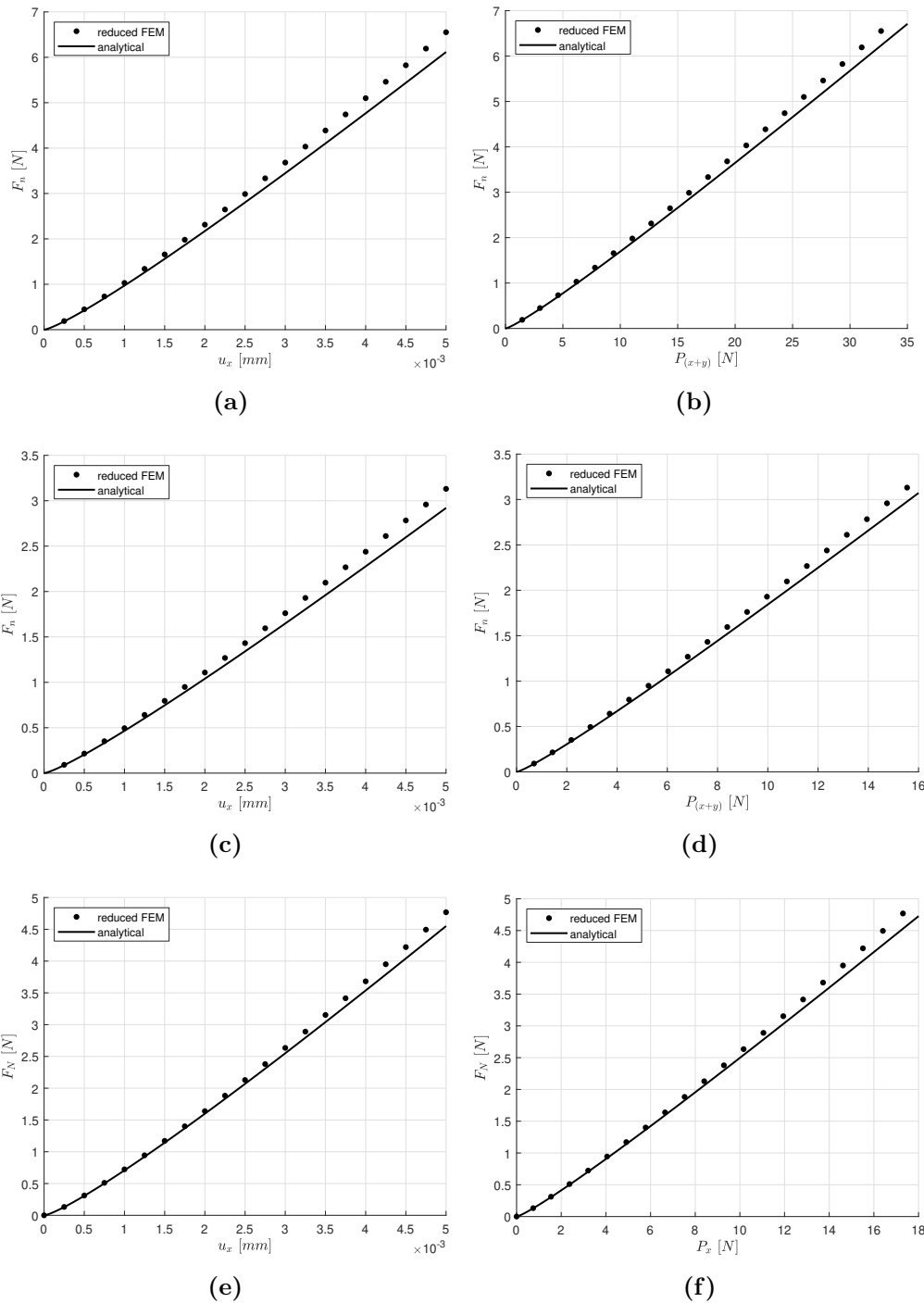


**Figure 6.7:** Reduced FEM and analytical results: contact force of a single RUC for (a)-(b) steel against steel, (c)-(d) Nitinol against Nitinol and (e)-(f) Nitinol against steel.

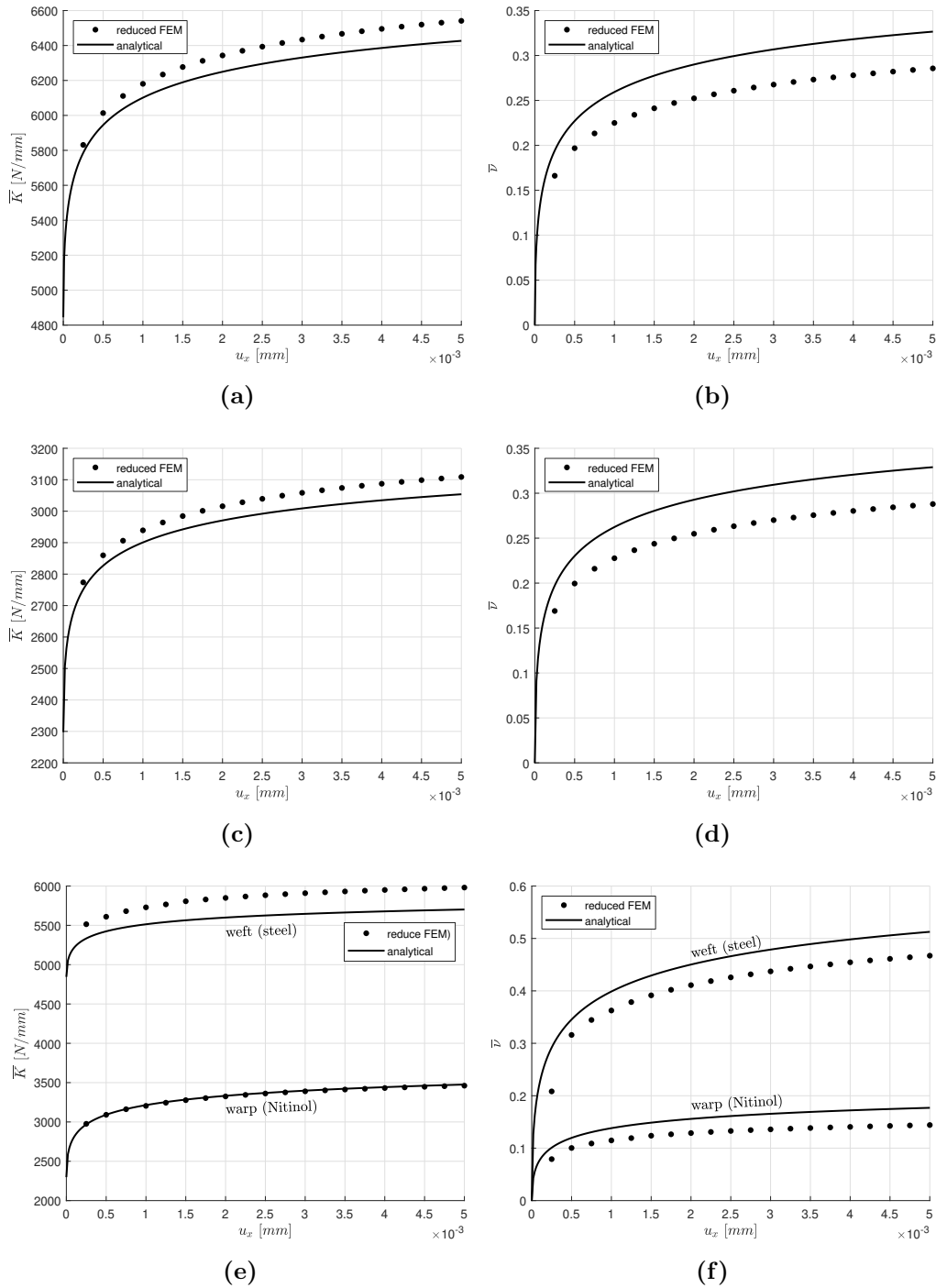


**Figure 6.8:** Reduced FEM and analytical results: linearised effective properties of a single RUC for (a)-(b) steel against steel, (c)-(d) Nitinol against Nitinol and (e)-(f) Nitinol against steel.

In Figure 6.7, the contact force resulting from the reduced model is compared with the theoretical solution. Results are plotted both against the longitudinal displacement and the tension force. An acceptable agreement is observed along the whole range of forces analysed, with the reduced model always showing higher values than the analytical model. The relative error is slightly lower when the model is controlled in force as compared to displacement, and also for the orthotropic case.

The higher response of the reduced model compared to the analytical results in terms of contact force is caused, in this configuration, by the bending stiffness of the horizontal beams representing the warp wire. The beams oppose the tendency of shell mid-side nodes to move vertically when subjected to Poisson's effect. This results in a lower Poisson's ratio and a higher stiffness of the RUC compared to the theoretical solution, as confirmed by the results reported in Figure 6.8, where the linearised effective properties obtained from the reduced model are compared to the analytical model. For the orthotropic configuration, the properties are calculated for warp and weft wires from Equations 5.6 and 5.7. Nevertheless, the choice of positioning the beams along the shell perimeter (instead of their actual physical location at the centre of the RUC) is necessary to compensate the numerical instability of the shell elements when using very low values of shear modulus.

### 6.5.1.2 In-plane shear

The pure in-plane shear load is generated in the RUC through two different configurations, illustrated in Figure 6.9.

In the first case, the left side of the element is restrained from translating, whilst a displacement along the y-axis is applied to the opposite side, as shown in Figure 6.9a. In the second case, the element is transformed with an angle of  $\pi/4$  with respect to the global coordinate system. The translational constraints are applied to the bottom vertex, whereas a displacement along the y-axis is applied to the top vertex, as displayed in Figure 6.9b. In both cases the contact force

is held constant at the value of 10N by changing the pre-load parameter in the MATLAB main script.

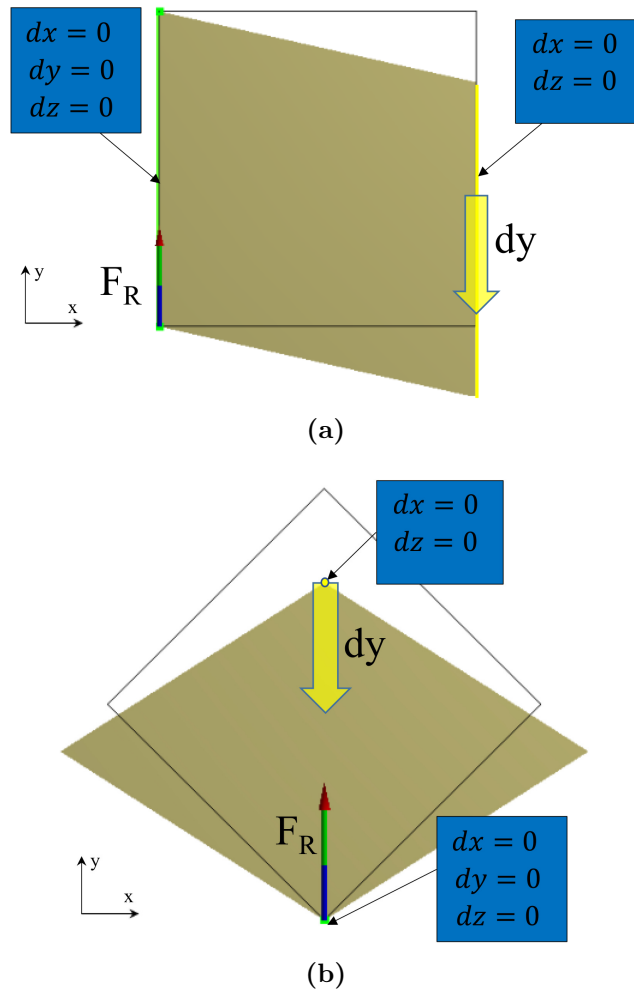
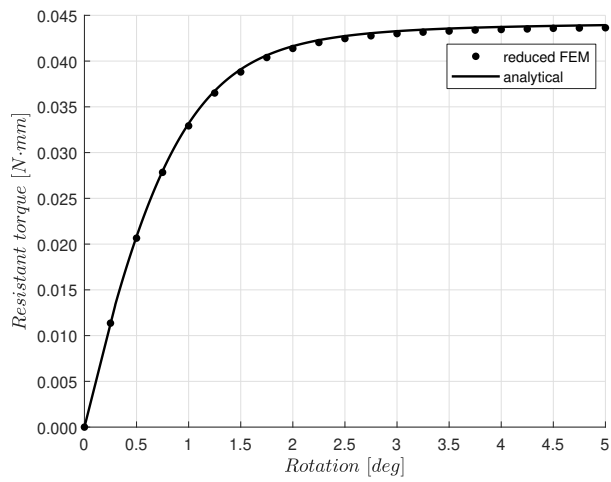
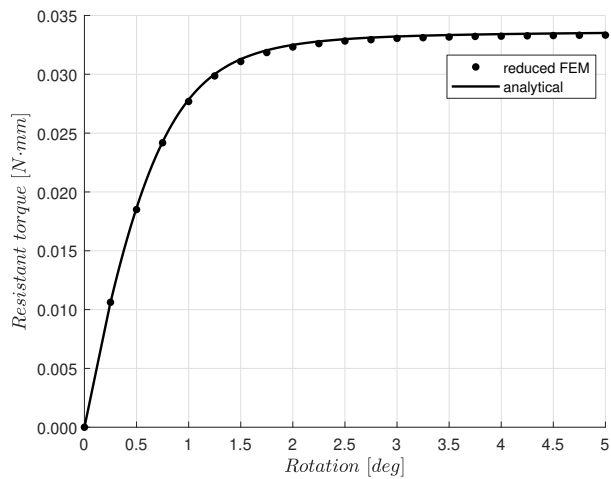


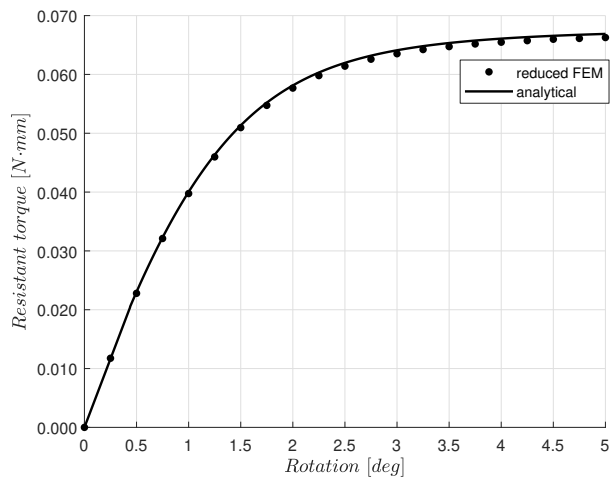
**Figure 6.9:** Deformed reduced FEM of a single RUC for (a) pure shear and (b)  $\pi/4$  transformed shear.



(a)



(b)



(c)

**Figure 6.10:** Reduced FEM validation: pure shear of a single RUC for (a) steel against steel, (b) Nitinol against Nitinol and (c) Nitinol against steel.

The previous cases are equivalent, yielding to identical results. In Figure 6.10 the numerical solution is compared with the analytical model, by converting the nodal force reaction  $F_R$  at the constrained nodes into resistant torque. It is evident how the results are nearly identical between numerical and analytical model for all the material combinations considered.

### 6.5.2 Mesh material plate

A mesh material plate composed of 10 by 10 wires for a total of 100 intersections is analysed through reduced FEM. Wire geometry is the same as for a single RUC, whereas only the isotropic case of stainless steel wires is analysed. Load and boundary conditions are represented in Figure 6.11.

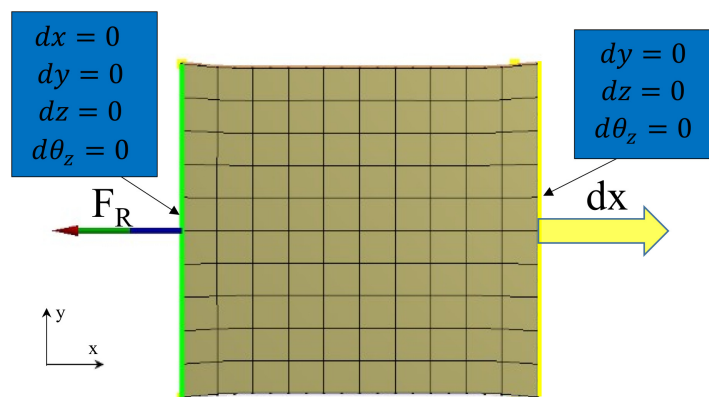


**Figure 6.11:** Reduced FEM results: load and BCs for uniaxial tension of a 10x10 mesh material plate.

The left side ( $x = 0$ ) of the plate is fixed, whereas a displacement of 0.1mm along the x-axis is applied to the opposite side ( $x = W$ ), whose nodes are also prevented from rotating around the z-axis.

A dedicated full FEM is also developed to provide results for validation. Given the high number of intersections, a coarser mesh (composed of 226,988 elements and 404,115 nodes) than the one used for a single RUC was necessary, in order to contain the computational demand. To reduce the error associated with contact

penetration, a value of FKN=300 has been used. The simulation is divided into 5 substeps to facilitate the convergence.

In Figure 6.12 the contact force computed with the reduced model (numbers in blue) is compared with the numerical results of the full model (numbers in black) for each intersection.

14.99	13.24	13.15	13.18	13.18	13.18	13.18	13.15	13.24	15.00
13.94	13.99	13.87	13.78	13.77	13.77	13.78	13.87	13.99	13.94
16.33	13.40	13.16	13.23	13.26	13.26	13.23	13.16	13.40	16.33
14.10	13.62	13.30	13.21	13.21	13.21	13.21	13.30	13.62	14.10
16.91	13.59	13.14	13.27	13.31	13.31	13.27	13.14	13.59	16.91
14.43	13.76	13.16	13.03	13.05	13.05	13.03	13.16	13.76	14.43
17.21	13.74	13.12	13.28	13.34	13.34	13.28	13.12	13.74	17.21
14.68	13.88	13.19	12.98	13.03	13.03	12.98	13.19	13.88	14.68
17.33	13.82	13.11	13.29	13.35	13.35	13.29	13.11	13.82	17.33
14.81	13.97	13.20	13.00	13.03	13.03	13.00	13.20	13.97	14.81
17.33	13.82	13.11	13.29	13.35	13.35	13.29	13.11	13.82	17.33
14.81	13.97	13.20	13.00	13.03	13.03	13.00	13.20	13.97	14.81
17.21	13.74	13.12	13.28	13.34	13.34	13.28	13.12	13.74	17.21
14.68	13.88	13.19	12.98	13.03	13.03	12.98	13.19	13.88	14.68
16.91	13.59	13.14	13.27	13.31	13.31	13.27	13.14	13.59	16.91
14.43	13.76	13.16	13.03	13.05	13.05	13.03	13.16	13.76	14.43
16.33	13.40	13.16	13.23	13.26	13.26	13.23	13.16	13.40	16.33
14.10	13.62	13.30	13.21	13.21	13.21	13.21	13.30	13.62	14.10
14.99	13.24	13.15	13.18	13.18	13.18	13.18	13.15	13.24	15.00
13.94	13.99	13.87	13.78	13.77	13.77	13.78	13.87	13.99	13.94

**Figure 6.12:** Reduced FEM contact force results: 10x10 mesh material plate under uni-axial tension. The numbers in blue are computed with the reduced model, whereas the numbers in black are computed with the full model.

Note that the decimal point is hidden by the warp wire representation and each location consists of two shown decimal places. In Figure 6.13 the contact force relative error between reduced and full model is represented graphically. The majority of the surface shows an acceptably low error (up to 4%), whilst the higher error is localised in correspondence of the boundary conditions, where the contact force is overestimated due to the stiffness of the weft wires, as already explained for the single RUC case. Note that the values between the warp and

the weft wires are linearly interpolated.

For the reduced model, only 3 iterations are required for the convergence to be met for all the elements, with a solving time of about 16 seconds, as compared to the full model that requires about an hour to complete the solution.

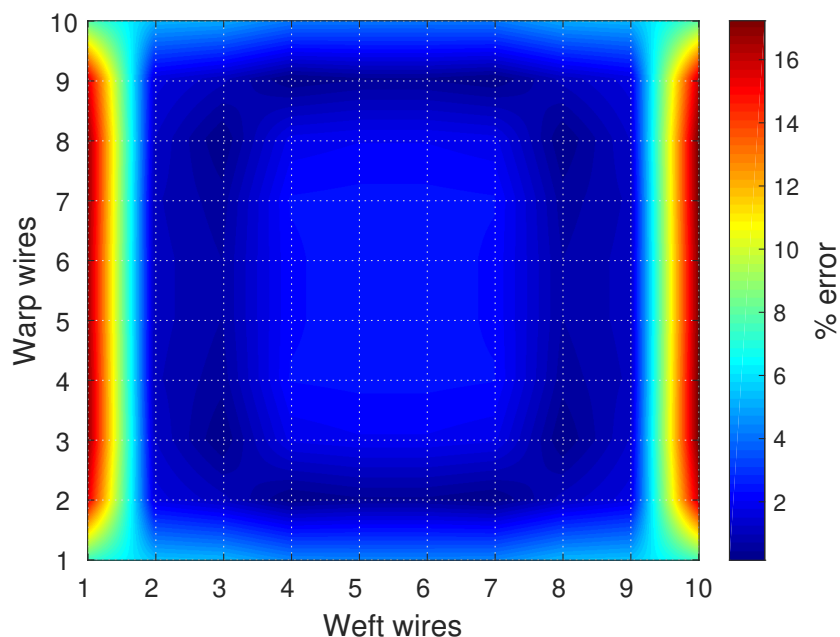


**Figure 6.13:** Contact force relative error between reduced and full model for a 10x10 mesh material plate.

### 6.5.3 Experimental validation from bias-extension test

To provide experimental validation to the reduced model, and consequently to the analytical models developed in this work, experimental results from bias-extension tests conducted by Wang *et al.* [126] are considered. This test consisted into applying a uni-axial tension to a mesh material specimen, in which the wires were oriented at  $\pm 45$  degrees with respect to the direction of the load. The test rig consisted of a hydraulic test machine to which a rectangular specimen of stainless steel PWMM was clamped by means of two grips. The lower grip was fixed whereas the top grip was controlled in displacement in order to exert

a uniaxial load. The deformation induced into the specimen by the load was recorded through a camera and the contours of shear angle were extrapolated by means of DIC (digital image correlation).

With the intent of simulating the same experiment through the reduced FE model, a 3-D model composed of a total of 233 beam-shell elements (corresponding to as many wires' intersections) was analysed through the MATLAB-ANSYS developed algorithm. This model is represented in Figure 6.14. The geometric dimensions and material properties utilised for the analysis are reported in Table 6.1.

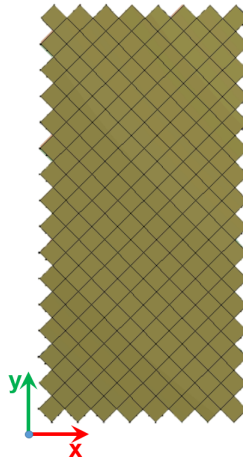


**Figure 6.14:** 3-D model of the bias-extension mesh material plate.

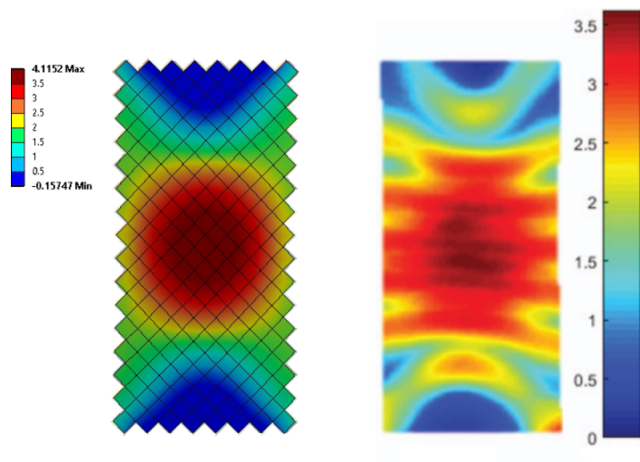
Diameter of wires	$d$	mm	0.91
Semi-wavelength	$L$	mm	2.70
Elastic modulus	$E$	GPa	200
Poisson's ratio	$\nu$		0.3
Friction coefficient	$\mu$		0.3

**Table 6.1:** Properties of mesh material employed in the experimental validation.

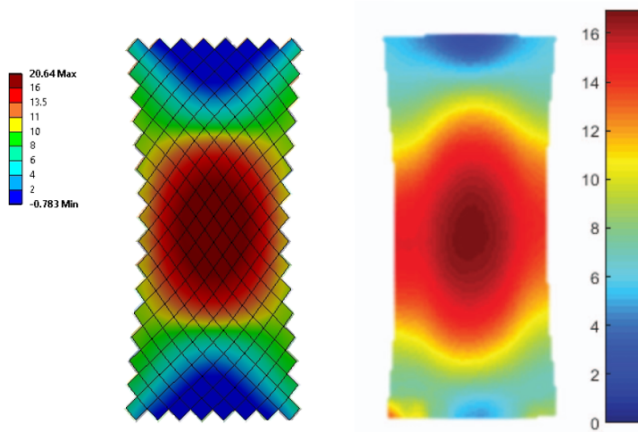
As regards the boundary conditions, the bottom nodes of the rectangular plate were fixed, whereas the top nodes were only allowed to move along the y-axis and

prevented from rotating about the z-axis. A displacement along the y-axis was applied to the top nodes and linearly ramped from zero to a maximum value of 10mm. The simulation was divided into 10 substeps. In Figure 6.15 the averaged shear strain computed through the reduced model is compared with the DIC shear angle contours from Wang *et al.* The scale colours have been adjusted according to the ones of the test results. A general agreement between numerical and experimental results can be observed, with a similar distribution of the shear across the plate and similar values of the maximum shear. As the load increases (Figures 6.15b and 6.15b), the numerical results show a slightly higher peak in shear angle and a higher stiffness in the vicinity of the boundaries (where the shear strain is lower) as compared to the test results. This suggests a decrease in stiffness at the boundaries during the experiments (as compared to the reduced model where the nodes have been fixed), possibly due to a partial slippage of the specimen within the grips, which allowed a more even distribution of the shear strains across the plate, with a correspondent decrease in the peak shear angle. This can be observed, as the value of the uniaxial displacement increases, by the almost total absence of blue contours around the edges in the experimental results, whereas in the numerical results these contours are still evident around the boundary conditions.

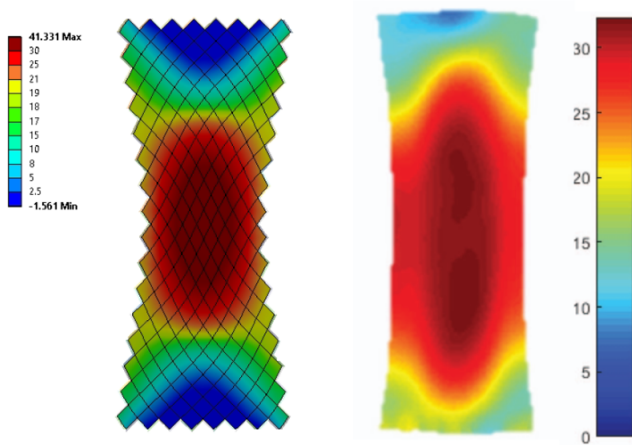
The presented results provide a qualitative validation of the analytical models and the reduced finite element model developed in this work, showing the ability of the MATLAB-ANSYS algorithm of capturing the shear behaviour of mesh materials, in agreement with what observed experimentally.



(a)



(b)



(c)

179  
**Figure 6.15:** Comparison between numerical and experimental bias-extension test results for (a) 1mm, (b) 5mm, and (c) 10mm uniaxial displacement.

## 6.6 Conclusions

In this chapter, a novel reduced finite element model was presented for the characterisation of PWMMs, which is based on the developed analytical models. This has been subsequently implemented through a newly developed software into a MATLAB-ANSYS integrated environment.

From a validation of the software, it was shown that the full FE model representing a single warp/weft wire intersection by means of hundreds of thousands of elements can be effectively reduced to a simple equivalent element, composed only by a shell and 8 beams. This allows to drastically reduce the computational demand and consequently the solving time, preserving at the same time an acceptable agreement with respect to the governing analytical models.

Nearly identical results between reduced and analytical model were achieved for pure in-plane shear load, whereas for tension load an error was observed, due to the bending stiffness of the beam elements. For a larger reduced model composed of several elements, a higher error was shown to be relegated to an area in the proximity of the boundary conditions, whilst the majority of the model showed a good agreement with the full FE results. This error is localised and confined to the boundary condition locations. If the size of the mesh was to change, this should still hold.

An experimental validation was also performed by employing data from a previous research consisting into a bias-extension test. The qualitative comparison between numerical results generated through the MATLAB-ANSYS algorithm and experimental results showed a general agreement and confirmed the validity of the developed reduced and analytical models in predicting the shear behaviour of mesh materials.

# Chapter 7

## Application: design of a damping device

### 7.1 Introduction

In this chapter, the reduced model discussed in Chapter 6 is applied to investigate the response of different PWMM geometries that, under specific boundary conditions and loads, can constitute a feasible friction damping device application. After a brief introduction on the methodology adopted for designing of these conceptual devices, some potential configurations are identified and proposed. The FE reduced model from Chapter 6 is utilised for each case and the resulting hysteretic response and correspondent damping loss factor are reported to demonstrate the system non-linearity and the energy dissipation.

### 7.2 Design concept of mesh friction dampers

The methodology adopted for designing of the following damper concepts focuses on increasing the dissipative friction force with respect to the elastic internal force, with the goal of achieving a higher damping loss factor. Although the energy dissipating modes in mesh materials are versatile and can be achieved by shear,

torsion, bending, or a combination, in the following examples the shear mode is considered. Therefore, the aim is to increase the shear strain across the material (to activate the frictional contacts) and, at the same time, generate a sufficient level of contact force at the intersections. The geometry and the boundary conditions play an important role to access the optimum damping capacity. In fact, it is required to avoid excessive limitations in motion that would prevent the device from dissipating energy effectively. An important aspect is also choosing a proper material with a low elastic modulus to reduce the internal force and a high friction coefficient to increase the energy dissipation. It should be noted that, in the following examples, the number of apertures (or wire intersections) and the wire dimensions and properties were not focused on as a point of optimising, but rather on the motion itself. For each of the examples, the load (rotation or translation) is linearly ramped from zero to a maximum value  $X$ . The resulting reaction (torque or force) is the backbone curve that is employed to generate the hysteresis loop (see Section 4.7.5), which is representative of a periodic load oscillating between  $-X$  and  $X$  for  $2.5\pi$  cycles. The geometrical dimensions of the mesh wires are the same as *Sample 3* from Table 3.1. Although the model and dampers could be applied for various materials, either stainless steel or Nitinol are employed in the examples (see Tables 3.2 and 3.3 for the mechanical properties).

## 7.2.1 Cylindrical damper

### 7.2.1.1 Torsional configuration

The first configuration analysed is a cylindrical damper with the warp wires directed along the axial direction, whereas the weft wires are wrapped radially. This particular device is intended to attenuate torsional vibrations, a common problem in all the rotational components with the function of transferring torque or mechanical power, such as shafts or drive-trains in general.

This concept can be thought as a tunable device, since the amount of damping provided can be regulated by controlling the contact force at the intersections through the axial pre-tension of the mesh material.

The model analysed is composed of 20 elements along the circumference and 8 elements along the height of the cylinder, for a total of 160 elements, resulting in a cylinder height and diameter of respectively 16.96mm and 13.50mm. The material considered is stainless steel with a friction coefficient of 0.3. The bottom end of the device is pinned, whilst the loads are applied to the top end.

The simulation is divided into two steps. In the first step, a pre-tension displacement along the z-axis is applied to the top end of the damper to generate the contact force at the intersections and is held constant throughout the rest of the simulation. In Figure 7.1a the deformation after the first step is illustrated for a pre-tension of 0.08mm and the resulting contact forces are reported for a row of elements along the axial direction.

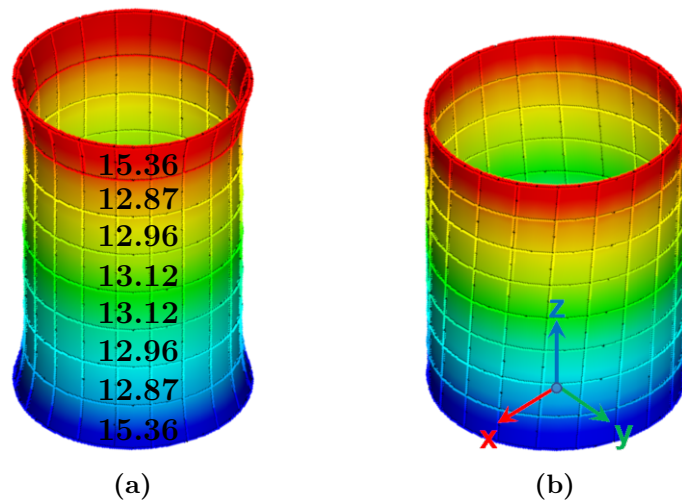


**Figure 7.1:** 3-D model of the damper under deformation. (a) Step 1: axial pre-tensioning of the device. The numbers in black represent the contact forces for the elements of the corresponding row. The deformation is scaled 50 times to enhance the radial shrinkage of the weft wires due to the effective Poisson's ratio. (b) Step 2: the twisting of the shaft causes a uniform shear strain on the elements.

In the second step, a rotation about the z-axis is applied to the top end and ramped from zero to 10 degrees. The deformed model after the rotation is shown in Figure 7.1b. The first step only comprises one substep, whereas the second

step is divided into 20 substeps to increase the resolution of results. The resulting non-linear torque reaction about the z-axis at the bottom end represents the backbone curve that is used to generate the hysteresis loop reported in Figure 7.2 for a pre-tension of 0.08mm. A parametric study was performed by varying the level of pre-tension and calculating the correspondent damping loss factor and dissipated energy per unit area (calculated with respect to the mesh bulking area), as reported in Table 7.1.

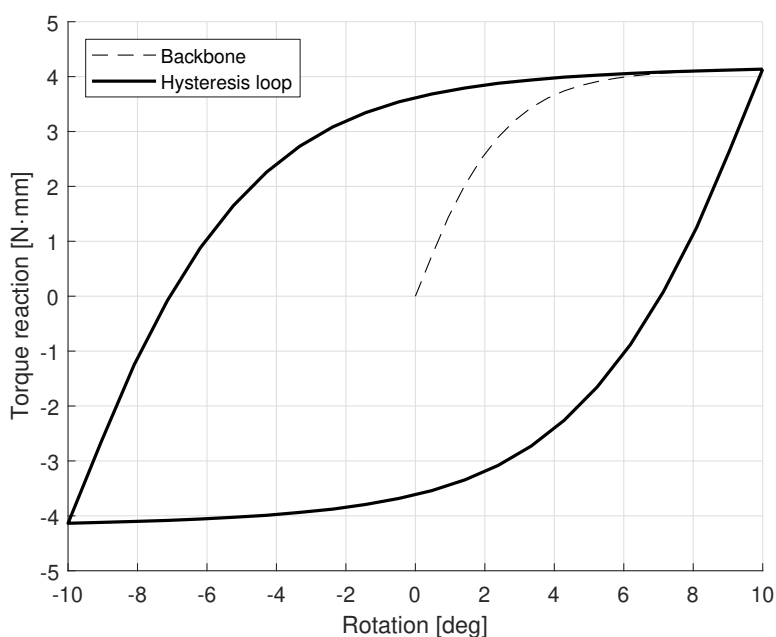


**Figure 7.2:** Torque-rotation hysteresis loop for the torsional damper with a pre-tension of 0.08mm.

Pre-tension	mm	0.03	0.05	0.08
Loss factor	-	0.8327	0.6764	0.5535
Dissipated energy per unit area	mJ/mm <sup>2</sup>	0.0011	0.0021	0.0039

**Table 7.1:** Loss factor and dissipated energy per unit area at various levels of pre-tension.

### 7.2.1.2 Linear configuration

Another configuration that has been investigated is a cylindrical linear damper, meaning that it is subjected to a linear motion directed along the axis of the cylinder.

In order to convert the axial oscillation into shear strain, which is responsible for activating the frictional contacts, the wires (and so the reduced equivalent elements in the model) are oriented at  $\pm 45$  degrees with respect to the axial direction of the damper. With this particular configuration, the contact force depends on the level of elastic pre-tension generated in the mesh material during the manufacturing process.

The reduced model analysed is composed of a total of 1600 beam-shell elements with an overall cylinder height and radius of respectively 61.46mm and 38.12mm. The 3-D model is illustrated in Figure 7.3a.

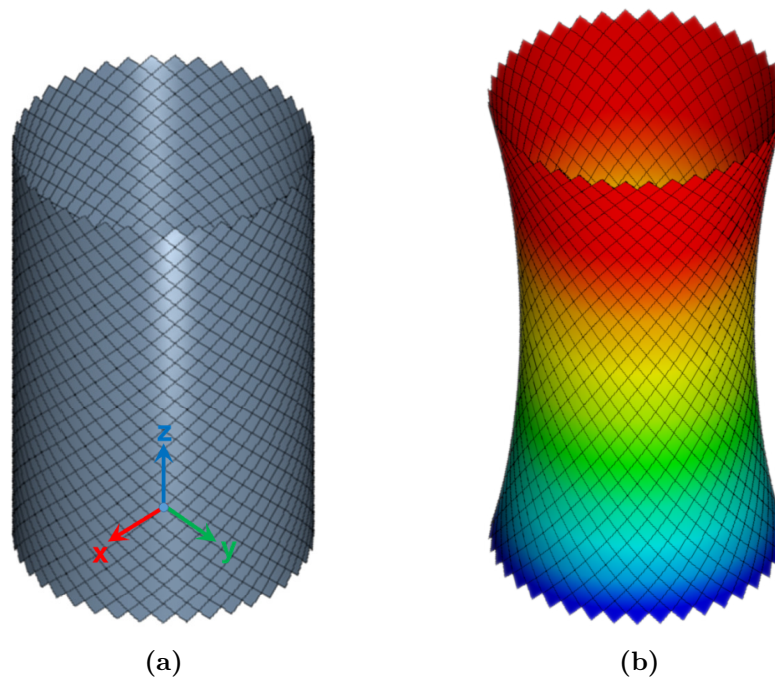


**Figure 7.3:** 3-D model of the cylindrical linear damper. (a) Underformed model. (b) Shape after deformation (results are scaled 10 times).

In this case the material used is Nitinol with a friction coefficient of 0.3. The bottom end is pinned and a vertical displacement along the z-axis is applied to the top end and linearly ramped from zero to a maximum value of 0.85mm, to represent the vibrational excitation to which the device is subjected. A level of pre-tensional contact force of 10N has been used for all the elements, by explicitly defining them into the model instead of the pre-tension discussed previously from applying a tension load to either the warp or weft wires. The simulation has been divided into 20 substeps. The resulting hysteresis loop is reported in Figure 7.4. A value of 0.1188 was calculated for the damping loss factor.

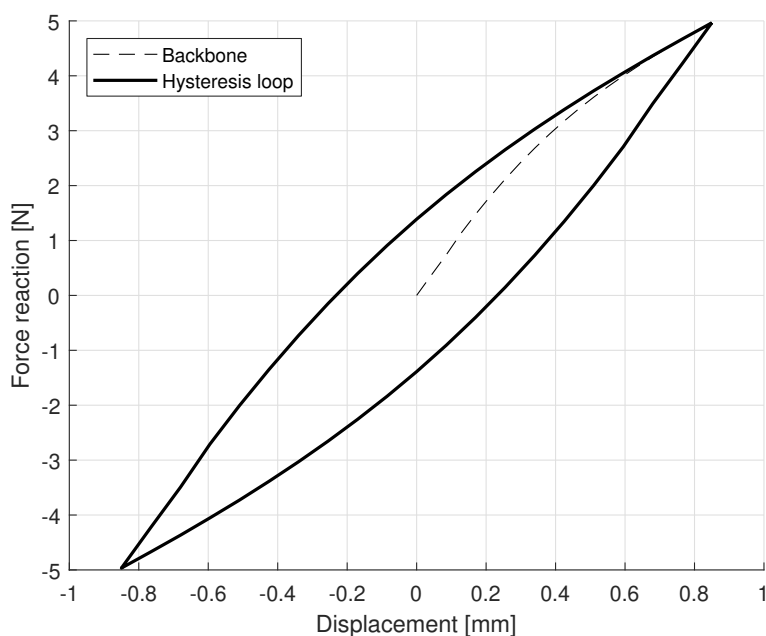


**Figure 7.4:** Hysteresis loop for the cylindrical linear damper.

The deformed shape is illustrated in Figure 7.3b. In this case, the radial shrinkage of the cylinder is caused by the shear of the elements.

In Figure 7.5 the shear strain corresponding to the maximum deformation is plotted for a generic column of elements (being the results analogous for every sector given the axial symmetry of the cylinder) as a function of the element position along the z-axis. The non-uniform distribution is minimum in correspondence of the boundary conditions and reaches a peak at mid-height, where the

radial shrinkage is also maximum. On the same figure, the frictional torque reaction corresponding to the maximum shear is also reported for the same column of elements, showing the different contribution of each wire intersection to the overall energy dissipation. Note that, because of highly distorted elements at the extremities of the cylinder, this has led to negative values of torque and strain in those locations, contrarily to what expected. Since this has not sensibly affected the overall results, it was chosen to force these values to zero in the figure.

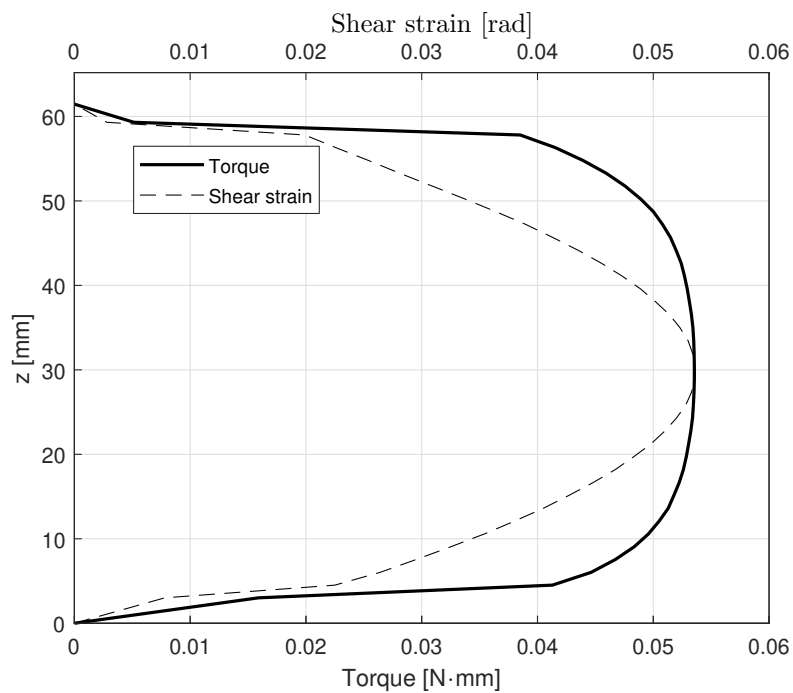


**Figure 7.5:** Variation of maximum torque reaction and shear strain for a single element along the z-axis.

## 7.2.2 Sinusoidal plate damper

Another alternative geometry is proposed as a damper concept, consisting of a sinusoidally curved plate of mesh material where the wires are oriented at  $\pm 45$  degrees with respect to the sides of the plate.

The shape of the plate can be described by the following expression:

$$z = Z_p \sin\left(\frac{\pi x}{L_p} - \frac{\pi}{2}\right) \quad (7.1)$$

where  $Z_p$  is the amplitude and  $L_p$  is the semi-wavelength of the plate sinusoid. The dimensions of the plate damper are reported in Table 7.2. The material considered is Nitinol with a friction coefficient of 0.3.

Plate amplitude	$Z_p$	mm	3.00
Plate semi-wavelength	$L_p$	mm	13.47
Plate width	$W$	mm	59.96

**Table 7.2:** Material properties and geometrical dimensions of the sinusoidal plate damper.

The model is composed of 761 intersections in total and, analogously to the cylindrical linear damper, a constant pre-tensional contact force is assigned to every element. Two potential configurations are investigated that differ from each other in terms of boundary conditions and applied loads.

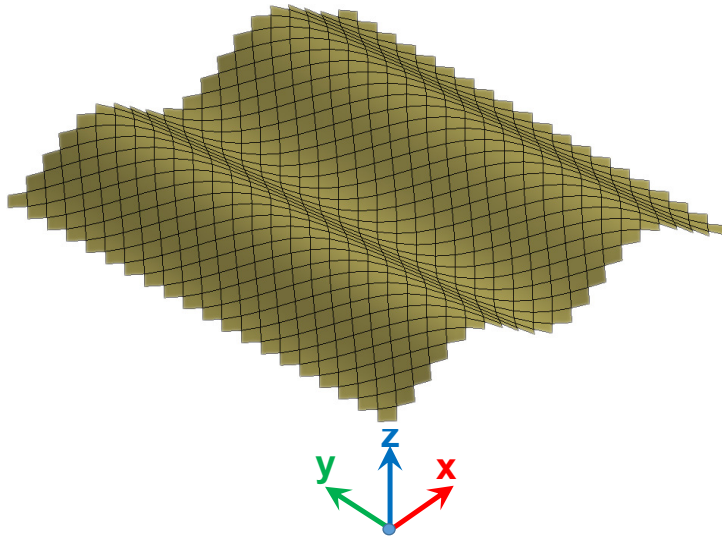


**Figure 7.6:** 3-D model of the sine plate damper.

### 7.2.2.1 Squeeze damper

In this configuration, the damper can be imagined as constrained between two frictionless rigid plates, one of which is fixed to the ground whilst the other is bonded to the source of vibration. When the top plate is subjected to an oscillation along the  $z$ -axis, this causes the squeezing of the damper, with a reduction of the plate damper sine amplitude and the elongation of the plate. The particular curved shape of the damper allows to convert the vertical compression into shear strain of the elements, which generates a corresponding non-linear frictional response.

To replicate the same conditions in the reduced model, the three bottom peaks of the plate are restrained from moving along the  $z$ -axis, while a displacement is applied to the top peaks along the  $z$ -axis, as illustrated in Figure 7.7.

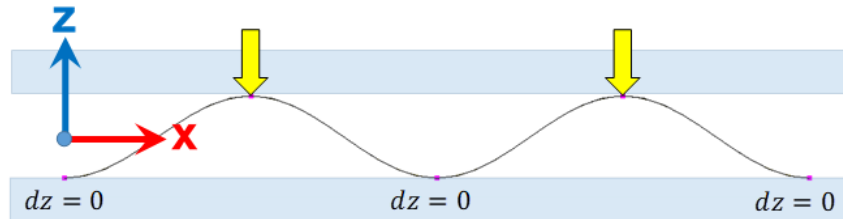


**Figure 7.7:** Boundary conditions and loads for the sine plate squeeze damper.

In Figure 7.8 the force-displacement hysteretic response of the damper is reported for a contact force of 20N. A value of 0.0597 was calculated for the correspondent damping loss factor.

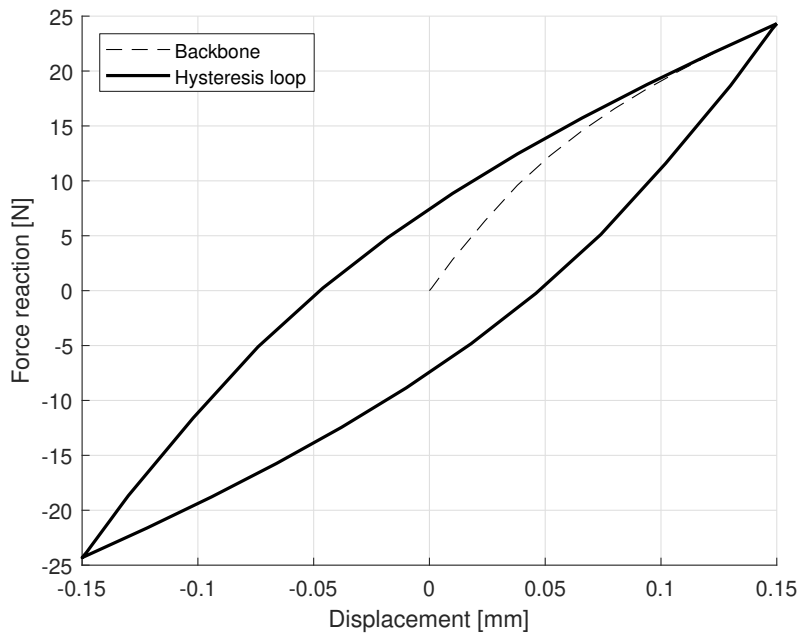


**Figure 7.8:** Force-displacement hysteresis loop for the sine plate squeeze damper.

### 7.2.2.2 Mesh material constrained layer damper

Constrained layer dampers (CLDs) are devices used for the reduction and control of vibrations that are composed of a polymeric layer that adheres to a metallic constraining layer (often either steel or aluminium). The device in operating conditions is bonded to the vibration source through the polymeric layer. When the structure undergoes vibration, the deformation of the constraining layer generates shear strain within the polymeric layer and this results in energy dissipation through viscoelastic damping. A common application of CLDs is the control of noise in vibrating panels from computer hardware components to building constructions, automotive [127] and aerospace industry.

A novel damper concept is proposed which, on the same working principle as the CLDs, replaces the viscoelastic layer with a mesh material sinusoidal sheet, pinned at its extremities to a metal plate. When the vibrating structure to which the damper is bonded undergoes bending deformation, this produces alternated tension and compression of the plate. This displacement is transferred to the mesh

and its frictional contacts are activated resulting in energy dissipation.

The sine plate model previously described is analysed under this specific load configuration, which is illustrated in Figure 7.9.

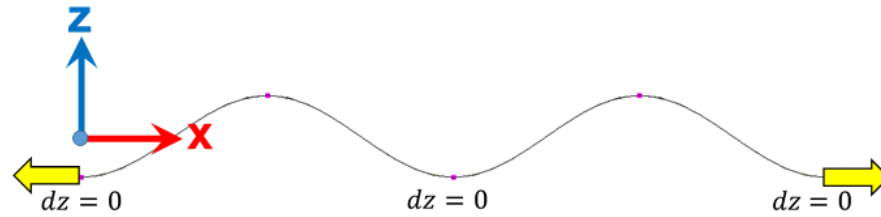


**Figure 7.9:** Boundary conditions and loads for the mesh material constrained layer damper.

The bottom peaks of the plate are restrained from moving along the z-axis, while a displacement along the x-axis is applied to both extremities in opposite directions and linearly ramped from zero to 0.5mm. To allow a sufficient freedom of motion, the displacement load is applied only to the central node (e.g.  $Y = W/2$ ) at each side.

In Figure 7.10 the shape of the model after deformation is reported. Different levels of pre-tensional contact force have been tested and the correspondent loss factor and dissipated energy per unit area are reported in Table 7.3. In Figure 7.11a the non-linear hysteretic response for a contact force of 20N is reported. In Figure 7.11b the same results are compared in normalised coordinates with the ones corresponding to 1N and 10N contact force, showing how the area of the hysteresis loop changes accordingly.

Pre-tensional contact force	N	1	10	20
Loss factor	-	0.0054	0.0506	0.0769
Dissipated energy per unit area	mJ/mm <sup>2</sup>	1.63E-05	1.92E-04	3.71E-04

**Table 7.3:** Loss factor and dissipated energy per unit area at various levels of pre-tensional contact force.

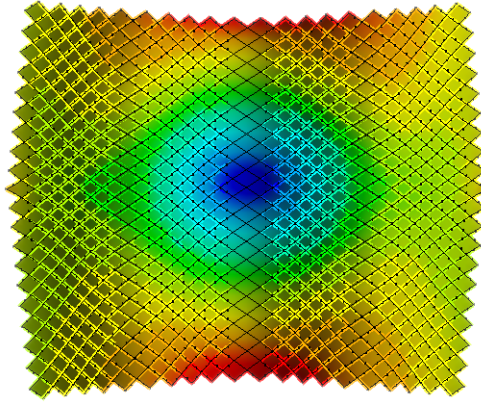


**Figure 7.10:** 3-D model of the mesh material constrained layer damper after deformation.

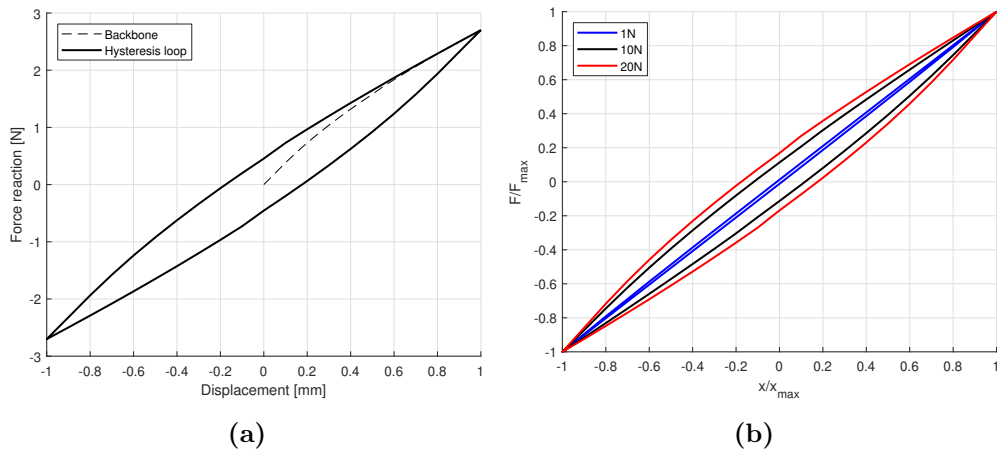


**Figure 7.11:** Force-displacement hysteresis loop for the mesh material constrained layer damper. (a) Results for a pre-tensional contact force of 20N. (b) Comparison of hysteretic response for different level of pre-tension in normalised coordinates.

## 7.3 Conclusions

In this chapter four different PWMM dampers are proposed as substitute to commonly adopted viscoelastic materials. In particular, by means of the developed reduced model, a cylinder and a sinusoidal plate are investigated as potential

damper geometries. It is found that, with the proper set of boundary conditions and with a sufficient contact force at the intersections, these damping devices show a high hysteretic response, a clear indication of their capability of energy dissipation.

These proposed solutions are intended as a concept and give an insight of the level of complexity that can be achieved with the developed MATLAB-ANSYS algorithm. By no way is this an exhaustive set of configurations. The possibilities include but are not limited to geometry, materials, and load path. The intention is to provide an illustrative example of how the reduced FEM can be used.

Although not discussed here, one of the main benefits of the model is that it can identify the damping for each contact location. It is not unimaginable to believe that this could be used as a design tool to optimise various locations depending on the loading type, especially for complex loading configurations.

# Chapter 8

## Conclusions and future work

In this research a detailed numerical and analytical investigation has been conducted on PWMMs which has brought the development of a series of analytical models for the characterisation of these materials. These models have been subsequently incorporated into a reduced finite element model for the study of different complex geometries using PWMMs and the development of a software program for the designing of mesh material damping devices. In this chapter, the main conclusions originated from the work are summarised. The most important contributions that this research has produced are highlighted and also further future research suggestions are provided, further extending this work.

### 8.1 Overall conclusions

In Chapter 2, the literature has been interrogated on the current state of the art regarding the characterisation of plain-weave structures. An evident knowledge gap was identified since the current existing mathematical models, which are mostly related to textiles and fibre-reinforced composites, typically rely on experimental data or are based on simplified equations that do not account for the frictional contact mechanics at the wire-to-wire interfaces.

In Chapter 3, the geometrical characterisation of PWMMs was conducted, by exploiting the high repetitivity of the plain-weave pattern, defined by a constant

aperture geometry and size. Through image analysis of a selected specimen, the longitudinal undulation of the wires was investigated, concluding that it can be mathematically described by a monoharmonic sinusoidal function. The initial assumption of constant aperture was validated through a further image analysis, that confirmed the high repetitiveness of the structure, with a general low value of relative standard deviation for the aperture. In addition, stainless steel and Nitinol have been identified as test case materials, only considering their linear-elastic properties.

A series of three analytical models describing the stiffness and damping mechanical response of PWMMs is presented in Chapter 4. The tension-compression model combines Castigliano's theorem and the Hertz contact theory for calculating the effective stiffness, effective Poisson's ratio, and wire-to-wire normal contact force of a single PWMM unit cell. Both the effective properties and the contact force were shown to increase non-linearly with the tension load, because of the Hertzian normal compression of the wires at the contact interface. The shear model calculates the non-linear frictional response of mesh materials for in-plane shear by employing the Lubkin model which combines the Hertz contact theory and the Coulomb friction model. The shear model was exploited to calculate the torque-rotation hysteresis loop, for characterising the vibration damping response of PWMMs for shear modes. Finally, the out-of-plane model, based on the same principles of the tension-compression model, calculates the wire-to-wire contact force resulting from out-of-plane bending of the RUC.

In Chapter 5, the three analytical models presented in Chapter 4 were validated through a comparison between numerical and theoretical results. This confirmed the validity of the mathematical models. The tension-compression model was shown as capable of capturing the non-linear effective stiffness and Poisson's ratio of PWMMs with good agreement and to compute the normal contact force at the wire-to-wire intersection with a moderate relative error. The highly non-linear frictional response of PWMMs for in-plane shear was described with high accuracy by the shear model for a wide range of wire rotations and for a large span of mechanical properties of the constituent materials. The out-of-plane bend-

ing model showed acceptable agreement between numerical and analytical results when tested for the case of uniaxial bending (only applied to a single wire).

In Chapter 6, the analytical models presented in Chapter 4 were incorporated into a reduced finite element model, where a newly developed beam-shell element was introduced as representative of a RUC. This reduced model was then implemented through a developed MATLAB-ANSYS software and validated. This was shown to achieve a drastic reduction in computation expense, maintaining, at the same time, acceptable agreement with the analytical models and the full FE model. A qualitative experimental validation was also performed by comparison with previously acquired bias-extension test data, showing a general validity of the developed models in capturing the shear behaviour of mesh materials.

The reduced finite element model and software from Chapter 6 was employed in Chapter 7 to analyse four different PWMM geometries - two cylinders and two sinusoidal plates - which are proposed as novel conceptual devices for vibration damping. It was shown that the reduced FEM is capable of analysing complex three-dimensional geometries of mesh material with different loads and boundary conditions, representing structures with a very high number of wire intersections. From the results obtained using the software, the mesh material dampers were shown to have a high hysteretic friction response, confirming their ability of dissipating energy effectively.

## 8.2 Main contributions from this work

As a result of this research, the following contributions to the knowledge were achieved, as already stated in Chapter 1:

- A detailed investigation for PWMMs through numerical analysis has been conducted and this has led to expanding the knowledge on the mechanical behaviour of these materials.
- A set of analytical models for the characterisation of PWMMs stiffness and damping behaviour was developed and discussed:

- ◇ A tension-compression model has been developed that describes the behaviour of PWMMs when subjected to tension load by capturing the non-linear effective stiffness, effective Poisson's ratio and wire-to-wire normal contact force arising from either a uniaxial or a biaxial state of tension.
- ◇ An in-plane shear model has been developed that captures the highly non-linear frictional response of PWMMs for shear mode. The model presents high precision for a wide range of motion, which encompasses the entire micro-slip phase, limited only by when the wires touch each other in a location other than the initial contact area (locking condition).
- ◇ An out-of-plane bending model has been developed that describes the effect of the out-of-plane bending of the wires on the wire-to-wire normal contact force.

This set of developed analytical models introduces a novel approach to the characterisation of mesh materials, based on the computation of the actual contact mechanics involved at the wire-to-wire intersections with the aim of capturing the nonlinear dissipative response of these materials, whereas the current state-of-the-art models either do not account for this or employ simplified mathematical models that highly rely on empirical data.

- A reduced finite element model for PWMMs was developed that employs a novel beam-shell finite element for representing a mesh material warp/weft intersection. This element is described by a set of linearised properties calculated by means of the analytical models. The major advantage of this reduced model is that the contact non-linearities are incorporated into the material properties and this permits to achieve a drastic reduction in computational demand by both reducing the number of elements in the model and the convergence issues that are often associated to non-linear problems.
- A fully operational software for the analysis of PWMMs has been devel-

oped by implementing the novel reduced FEM into a MATLAB-ANSYS integrated environment that allows to study complex three-dimensional geometries of mesh materials.

- Four different concept dampers for industrial applications have been proposed and their damping properties analysed by means of the newly developed software, to test the capabilities of the reduced FEM.

### 8.3 Suggestions for future further work

From the investigation conducted in this research, various further questions have emerged concerning the behaviour of mesh materials. Here, some of these questions are briefly listed as suggestions for future research on this topic:

- In this work, a numerical analysis has been employed as a main approach of investigation on the physics of mesh materials. A qualitative experimental validation was also performed by employing previously acquired test data. In a future work, this could be associated with an experimental study of PWMMs by means of vibration tests and digital image correlation (DIC). This can be performed both on in-plane mesh material configurations (for instance through bias-extension and picture frame tests for the characterisation of tensile and shear behaviour), and on more complex mesh material geometries, such as the cylindrical and sinusoidal plate dampers proposed in Chapter 7. An experimental validation of the frictional contact mechanics of a single wire-to-wire intersection is also suggested. This could be performed on a cylinder-to-cylinder configuration by employing a torsional friction test rig and applying a quasi-static rotation to one cylinder while fixing the counterpart and measuring the correspondent friction torque.
- In the analytical models presented, the longitudinal undulation of the wires has been neglected when computing the contact mechanics via Hertz theory. The models could be expanded to account for this aspect, to further improve the accuracy of the results.

- Throughout this research, two materials - stainless steel and Nitinol - were considered as constituents for PWMMs. As already noted previously, these only represent test case materials and the analytical models can be applied to any Hookean material. Therefore, the potential application of other materials should be explored.
- In the in-plane shear model, a simplified equation (geometric mean) has been utilised to calculate the equivalent shear modulus for the orthotropic configuration, leading to an error in the micro-slip phase. This aspect requires a further investigation to increase the accuracy when warp and weft wires are built of different materials.
- The developed analytical models are limited to a linear elastic behaviour of the wires. Effort should be spent on extending the models to account for material non-linearities such as plasticity and superelasticity. Moreover, they are based on the assumption of small deformations. This requires further work to account for geometric non-linearities.
- In the examples analysed in Chapters 6 and 7, by means of the developed software, only mesh materials with square apertures and same diameter for both warp and weft wires were considered. Plain-weave structures with different geometry (wavelength and diameter) between warp and weft wires should be considered.
- The methodology adopted in this work for the homogenisation of plain-weave materials lies itself to a description of other patterns of mesh materials with high repetitivity. This should be further investigated to extend this work to the study of other structures, such as knitted materials.



**Figure 8.1:** NASA spring tire.

As already discussed, in recent years mesh materials have been gaining considerable interest as industrial applications for harsh environments, because of their large applicability to extreme conditions, only limited by the properties of their constituent materials. The spring tire developed by NASA and mentioned in Chapter 2 (see Figure 8.1) is just an example of a potential application of these materials to aerospace industry. The analytical models and the reduced FEM developed in this work, and their subsequent software implementation, can be exploited for the designing and optimisation of mesh material friction devices. This is even more important as the popularity of mesh materials expands.

# Bibliography

- [1] J. Hong, L. Chen, Y. Ma, G. R. Tomlinson, and J. A. Rongong, “Hysteretic properties of metal rubber particles,” *Proc. Inst. Mech. Eng. C J. Mech. Eng. Sci.*, vol. 227(4), pp. 693–702, 2012.
- [2] K. Chandrasekhar, J. Rongong, and E. Cross, “Mechanical behaviour of tangled metal wire devices,” *Mechanical Systems and Signal Processing*, vol. 118, pp. 13–29, 2019.
- [3] N. Tang, J. A. Rongong, and G. R. Tomlinson, “Nonlinear behaviour of tangled metal wire particle dampers,” *International Conference on Structural Engineering Dynamics (ICEDYN2015)*, 2015.
- [4] S. Galuszynski, “Structure and tightness of woven fabrics,” *Indian Journal of textile Research*, vol. 12, pp. 71–77, 1987.
- [5] K. L. Gandhi and W. S. Sondhelm, *4 - Technical fabric structures – 1. Woven fabrics*. Woodhead Publishing Series in Textiles, Woodhead Publishing, second edition ed., 2016.
- [6] Z. J. Grosicki, ed., *Watson’s Textile Design and Colour (Seventh Edition)*. Woodhead Publishing Series in Textiles, Woodhead Publishing, seventh edition ed., 2004.
- [7] A. T. C. Robinson and R. Marks, *Woven Cloth Construction*. Plenum Press. New York., 1967.

- [8] C. Lord and J. Rongong, “Stiffness and damping of ordered frictional mesh material,” *23rd International Congress on Sound and Vibration*, 2016.
- [9] S. M. Kraft and A. P. Gordon, “Characterization of the tensile behavior of a metallic fiber woven structure,” *Textile Research Journal*, vol. 81, no. 12, pp. 1249–1272, 2011.
- [10] E. Glatt, S. Rief, A. Wiegmann, M. Knefel, and E. Wegenke, “Structure and pressure drop of real and virtual metal wire meshes,” *Berichte des Fraunhofer ITWM, Kaiserslautern, Germany*, vol. 157, 2009.
- [11] M. Zarzour, “Experimental evaluation of a metal-mesh bearing damper in a high speed test rig,” Master’s thesis, Texas A&M University, 1999.
- [12] D. W. Childs, “The space shuttle main engine high-pressure fuel turbopump rotordynamic instability problem,” *ASME J. Eng. Power*, vol. 100, p. 48–57, 1978.
- [13] H. Ao, H. Jiang, W. Wei, and A. M. Ulanov, “Study on the damping characteristics of MR damper in flexible supporting of turbo-pump rotor for engine,” *ISSCAA 2006: 1st International Symposium on Systems and Control in Aerospace and Astronautics*, pp. 5 pp. – 622, 02 2006.
- [14] B. H. Ertas, E. Al-Katheeb, and J. M. Vance, “Rotordynamic bearing dampers for cryogenic rocket engine turbopumps,” *Journal of Propulsion and Power*, vol. 19(4), pp. 674–682, 2003.
- [15] Y. Ma, H. Wang, H. Li, and J. Hong, “Study on metal rubber material’s characteristics of damping and sound absorption,” *Proceedings of ASME Turbo Expo 2008: Power for Land, Sea, and Air (GT2008)*, Berlin, Germany, 9–13 June 2008, pp. 477–486, 2008.
- [16] D. Ulgen, O. L. Ertugrul, and M. Y. Ozkan, “Measurement of ground borne vibrations for foundation design and vibration isolation of a high-precision instrument,” *Measurement*, vol. 93, pp. 385–396, 2016.

- [17] Y. Zou, C. Xiong, J. Yin, K. Cui, X. Zhu, H. Deng, and S. Song, “Research on the dynamic mechanical properties and constitutive model of metal rubber under impact loading,” *Materials Research Express*, vol. 8, no. 4, 2021.
- [18] M. Zarzour and J. M. Vance, “Experimental evaluation of a metal mesh bearing damper,” *ASME J. Eng. Gas Turbines Power*, vol. 122(2), p. 326–329, 2000.
- [19] Q. Tan, P. Liu, C. Du, L. Wu, and G. He, “Mechanical behaviors of quasi-ordered entangled aluminum alloy wire material,” *Materials Science and Engineering: A*, vol. 527, no. 1, pp. 38–44, 2009.
- [20] G. He, P. Liu, Q. Tan, and G. Jiang, “Flexural and compressive mechanical behaviors of the porous titanium materials with entangled wire structure at different sintering conditions for load-bearing biomedical applications,” *Journal of the Mechanical Behavior of Biomedical Materials*, vol. 28, pp. 309–319, 2013.
- [21] D. Zhang, F. Scarpa, Y. Ma, J. Hong, and Y. Mahadik, “Dynamic mechanical behavior of nickel-based superalloy metal rubber,” *Materials & Design (1980-2015)*, vol. 56, pp. 69–77, 2014.
- [22] Y. Ma, Q. Zhang, D. Zhang, F. Scarpa, B. Liu, and J. Hong, “The mechanics of shape memory alloy metal rubber,” *Acta Materialia*, vol. 96, pp. 89–100, 2015.
- [23] D. M. Al-Katheeb, *Design, modelling and experimental investigation of wire mesh vibration dampers*. PhD thesis, Department of Mechanical Engineering, Texas A&M University, Texas, 2002.
- [24] H. Wang, J. Rongong, G. R. Tomlinson, and J. Hong, “Nonlinear static and dynamic properties of metal rubber dampers,” *Proceedings of ISMA 2010, Leuven, Belgium*, 2010.

- [25] B. Zhu, *Theoretical and Experimental Investigation on Compressive Mechanical and Thermophysical Properties of Metal Rubber (in chinese)*. PhD thesis, School of Jet Propulsion, Beihang University, Beijing, 2012.
- [26] B. Zhang, Z. L. andand S. Billings, G. Tomlinson, and J. Rongong, “System identification methods for metal rubber devices,”
- [27] K. Zhang, Y. Zhou, and J. Jiang, “Experimental study and dynamic modeling of metal rubber isolating bearing,” *IOP Conference Series: Materials Science and Engineering, (CMSE 2015) 3–6 August 2015, Macau, China*, vol. 103, 2015.
- [28] E. Rivin, “Vibration isolation of precision machinery,” *Journal of Sound and Vibration*, vol. 13(8), pp. 18–23, 1979.
- [29] A. B. Barnes, “Improvement in machinery for woven wire mesh,” *Wire Industry*, vol. 51(605), pp. 403–404, 1984.
- [30] A. Okayasu, T. Ohta, T. Azuma, *et al.*, “Vibration problems in the LE-7 liquid hydrogen turbopump,” *26th Joint Propulsion Conference, Orlando*, 1990.
- [31] X. Wang and Z. Zhu, “Ring-like metal rubber damper,” *Journal of Aerospace Power*, vol. 12, no. 2, pp. 143–145, 1997.
- [32] D. Chegodaev, O. Mylukin, and E. Koltygin, “Design of metal rubber components,” *Publishing Company of National Defence Industry, Beijing*, p. 99–104, 2000.
- [33] Y. Li, H. Xieqing, and W. Mao, “A theoretical model and experimental investigation of a nonlinear constitutive equation for elastic porous metal rubbers,” *Mechanics of Composite Materials*, vol. 41, pp. 303–312, 2005.
- [34] W. Peng, H. Bai, J. Zheng, X. Tang, G. Li, and Z. He, “A micromechanics constitutive model of the metal rubber materials based on the radial and

- axial combined deformation of the microsprings,” *J. Exp. Mech.*, vol. 21(3), 2005.
- [35] B. Guo, Z. Zhu, and R. Cui, “Theoretical model of metal rubber,” *J. Aerosp. Power*, vol. 19, p. 314–319, 2004.
- [36] J. Hong, B. Zhu, and Y. Ma, “Theoretical and experimental investigation on nonlinear characterization of metal rubber,” *ASME 2011 Turbo Expo: Turbine Technical Conference and Exposition, June 6–10, 2011, Vancouver, British Columbia, Canada*, 2011.
- [37] J. Hu, *Structure and Mechanics of Woven Fabrics*. Woodhead Publishing, 2004.
- [38] F. T. Peirce, “The geometry of cloth structure,” *J. Text. Inst.*, vol. 28, pp. 45–96, 1937.
- [39] A. Kemp, “An extension of Peirce’s cloth geometry to the treatment of non-circular threads,” *J. Text. Inst.*, vol. 49, pp. 44–48, 1958.
- [40] J. W. S. Hearle and W. J. Shanahan, “An energy method for calculations in fabric mechanics. Part I: Principles of the method,” *J. Text. Inst.*, vol. 69, pp. 81–89, 1978.
- [41] K. Weissenberg, “The use of a trellis model in the mechanics of homogeneous materials,” *J. Text. Inst.*, vol. 40, no. 2, pp. 89–110, 1949.
- [42] G. E. Chadwick, S. A. Shorter, and K. Weissenberg, “A trellis model for the application and study of simple pulls in textile materials,” *J. Text. Inst.*, vol. 40, no. 2, pp. 111–160, 1949.
- [43] W. F. Kilby, “Planar stress-strain relationships in woven fabrics,” *J. Text. Inst.*, vol. 54, no. 1, pp. 9–27, 1963.
- [44] G. A. V. Leaf, “Woven fabrics tensile mechanics,” in *Mechanics of flexible fibre assemblies (NATO Advanced Study Institute Series; E, applied sciences*

- n. 38*), *J. W. S. Hearle, J. J. Thwaites and J Amirbayat, Nwtherlands, Alpen aan den Rijn*, pp. 143–157, 1980.
- [45] F. T. Peirce, “The handle of cloth as a measurable quantity,” *J. Text. Inst.*, vol. 21, no. 9, pp. 377–416, 1930.
- [46] B. Olofsson, “A study of inelastic deformations of fabrics,” *J. Text. Inst.*, vol. 58, no. 6, pp. 221–241, 1967.
- [47] J. Skelton, “Fundamentals of fabric shear,” *Textile Research Journal*, vol. 46, no. 12, pp. 862–869, 1976.
- [48] J. Skelton and M. M. Schoppee, “Frictional damping in multicomponent assemblies,” *Textile Research Journal*, vol. 46, no. 9, pp. 661–666, 1976.
- [49] P. Grosberg and B. J. Park, “The Mechanical Properties of Woven Fabrics - Part V: The Initial Modulus and the Frictional Restraint in shearing of Plain Weave Fabrics,” *Textile research journal*, vol. 36, no. 5, pp. 420–431, 1966.
- [50] J. L. Lubkin, “The torsion of elastic spheres in contact,” *J. Appl. Mech.*, vol. 18, pp. 183 – 187, 1951.
- [51] C. K. Chu and Y. L. Chen, “Ballistic-proof effects of various woven constructions,” *Fibres & Textiles*, vol. 18, no. 6, pp. 63–67, 2010.
- [52] T. Ishikawa and T. W. Chou, “Stiffness and strength behaviour of woven fabric composites,” *Journal of Materials Science*, vol. 17, no. 11, pp. 3211–3220, 1982.
- [53] N. K. Naik and V. K. Ganesh, “Prediction of on-axes elastic properties of plain weave fabric composites,” *Composites Science and Technology*, vol. 45, pp. 135–152, 1992.
- [54] R. A. Naik, “Analysis of woven and braided fabric reinforced composites,” *NASA Contractor Report 194930, National Aeronautics and Space Administration, Hampton, VA*, 1994.

- [55] B. B. Boubaker, B. Haussy, and J. F. Ganghoffer, “Discrete woven structure model: yarn-on-yarn friction,” *C. R. Mecanique*, vol. 335, p. 150–158, 2007.
- [56] S. Kuwabata, M. Niwa, and H. Kawai, “The finite deformation theory of plane weave fabrics,” *J. Text. Inst.*, vol. 64, no. 1-2, pp. 21–83, 1973.
- [57] J. Lindberg and N. Gralen, “Measurement of friction between single fibers. II. Frictional properties of wool fibers measured by the fiber-twist method,” *Textile Research Journal*, vol. 18, no. 5, p. 287–301, 1948.
- [58] [http://texgen.sourceforge.net/index.php/Main\\_Page/](http://texgen.sourceforge.net/index.php/Main_Page/).
- [59] H. Lin, A. C. Long, M. Sherburn, and M. J. Clifford, “Modelling of mechanical behaviour for woven fabrics under combined loading,” *International Journal of Material Forming*, vol. 1, no. 1, p. 899–902, 2008.
- [60] A. Dixit, R. K. Misra, and H. S. Mali, “Compression modeling of plain weave textile fabric using finite elements,” *Materials Science & Engineering Technology*, vol. 45, no. 7, pp. 600–610, 2014.
- [61] O. Erool and M. Keefe, “Numerical modeling techniques for woven textiles,” 2014.
- [62] W. Cai and V. Shalaev, *Optical Metamaterials: Fundamentals and Applications*. Springer New York, 2009.
- [63] K. Muamer, T. Bückmann, R. Schittny, and M. Wegener, “Metamaterials beyond electromagnetism,” *Reports on progress in physics. Physical Society (Great Britain)*, vol. 76, p. 126501, 11 2013.
- [64] X. Yu, J. Zhou, H. Liang, Z. Jiang, and L. Wu, “Mechanical metamaterials associated with stiffness, rigidity and compressibility: A brief review,” *Progress in Materials Science*, vol. 94, pp. 114–173, 2018.
- [65] “Standard Specification for Industrial Woven Wire Cloth,” *ASTM E2016-20*, 2020.

- [66] G. B. Kauffman and I. Mayo, “The Story of Nitinol: The Serendipitous Discovery of the Memory Metal and Its Applications,” *The Chemical Educator*. Springer-Verlag New York Inc., vol. 2, no. 2, pp. 1–21, 1997.
- [67] W. J. Buehler and F. E. Wang, “A summary of recent research on the nitinol alloys and their potential application in ocean engineering,” *Ocean Engineering*, vol. 1, no. 1, pp. 105–120, 1968.
- [68] T. W. Duerig and D. E. Tolomeo, “An overview of superelastic stent design,” *Proceedings of the International Conference on Shape Memory and Superelastic Technologies (SMST-2000)*, pp. 585–604, 2000.
- [69] S. W. Robertson, *On the Mechanical Properties and Microstructure of Nitinol for Biomedical Stent Applications*. PhD thesis, Engineering-Materials Science and Engineering, University of California, Berkeley, 2006.
- [70] C. DellaCorte, S. V. Pepper, R. Noebe, D. R. Hull, and G. Glennon, “Intermetallic nickel-titanium alloys for oil-lubricated bearing applications,” *NASA/TM—2009-215646*, 2009.
- [71] National Aeronautics and Space Administration, “Reinventing the Wheel”, (2017, October 26), NASA. <https://www.nasa.gov/specials/wheels/>.
- [72] C. DellaCorte, “Ni-Ti next generation bearings for space,” *Schaeffler International Bearing Conference, Herzogenaurach, Germany*, 2018.
- [73] S. P. Timoshenko, *History of strength of materials*. McGraw-Hill Book Company, Inc., N.Y., 1953.
- [74] E. Oñate, “Thick/slender plane beams. timoshenko theory,” *Structural Analysis with the Finite Element Method Linear Statics. Lecture Notes on Numerical Methods in Engineering and Sciences*. Springer, Dordrecht, vol. 37-97, 2013.
- [75] C. A. Castigliano, “Intorno ai sistemi elastici,” Master’s thesis, Polytechnic of Turin, 1873.

- [76] K. L. Johnson, *Contact Mechanics*. Cambridge University Press, 1985.
- [77] S. Timoshenko and J. N. Goodier, *Theory of elasticity*. McGraw-Hill Book Company, Inc., N.Y., 1951.
- [78] K. L. Johnson, K. Kendall, and A. D. Roberts, “Surface energy and the contact of elastic solids,” *Proceedings of the Royal Society of London. Series A, Mathematical and Physical Sciences*, vol. 324, no. 1558, pp. 301–313, 1971.
- [79] V. L. Popov, *Contact Mechanics and Friction: Physical Principles and Applications*. Springer, 2010.
- [80] G. G. Adams, *Contacts Considering Adhesion*. Boston, MA: Springer US, 2013.
- [81] R. Matjie, S. Zhang, Q. Zhao, N. Mabuza, and J. R. Bunt, “Tailored surface energy of stainless steel plate coupons to reduce the adhesion of aluminium silicate deposit,” *Fuel*, vol. 181, pp. 573–578, 2016.
- [82] R. Rosmaninho, G. Rizzo, H. Müller-Steinhagen, and L. F. Melo, “Study of the influence of bulk properties and surface tension on the deposition process of calcium phosphate on modified stainless steel,” *Proceedings of Heat Exchanger Fouling and Cleaning: Fundamentals and Applications, Santa Fe, New Mexico, USA*, 2003.
- [83] B. Bhushan, *Introduction to Tribology*. Wiley, 2013.
- [84] A. Guran, F. Pfeiffer, and K. Popp, *Dynamics With Friction: Modeling, Analysis and Experiment. Number v. 1 in Pt I*. World Scientific, 1996.
- [85] L. da Vinci, *Codex Madrid I (Ms. 8937)*. Biblioteca Nacional de España, Madrid, Spain, 1495.
- [86] G. Amontons, “De la resistance cause’e dans les machines,” *Memoires de l’Academie des Sciences*, p. 203–222, 1699.

- [87] C. A. Coulomb, “Théorie des machines simples (theory of simple machines),” *Bachelier, Paris*, vol. 18, no. 3/4, p. 203–224, 1821.
- [88] B. Bhushan, *Modern Tribology Handbook*, vol. 1. Mechanics and Materials series, CRC Press, 2001.
- [89] C. Lord, *Damping Effects of Debonded Composites*. PhD thesis, Department of Mechanical Engineering, University of Sheffield, Sheffield, UK, 2012.
- [90] H. K. Asker, J. A. Rongong, and C. E. Lord, “Dynamic properties of unbonded, multi-strand beams subjected to flexural loading,” *Mechanical Systems and Signal Processing*, vol. 101, pp. 168–181, 2018.
- [91] J. R. Whitehead, “Surface deformation and friction of metals at light loads,” *Proc. Roy. Soc. Lond. A*, vol. 201, p. 109–124, 1950.
- [92] R. J. M. Pijpers and H. M. Slot, “Friction coefficients for steel to steel contact surfaces in air and seawater,” *Journal of Physics: Conference Series*, vol. 1669, p. 012002, oct 2020.
- [93] F. P. Bowden and D. Tabor, “Friction, lubrication and wear: a survey of work during the last decade,” *British Journal of Applied Physics*, vol. 17, pp. 1521–1544, dec 1966.
- [94] J. A. Greenwood and J. B. P. Williamson, “Contact of nominally flat surfaces,” *Proceedings of the Royal Society of London. Series A, Mathematical and Physical Sciences*, vol. 295, no. 1442, pp. 300–319, 1966.
- [95] S. Andrews and H. Sehitoglu, “Computer model for fatigue crack growth from rough surfaces,” *International Journal of Fatigue*, vol. 22, no. 7, pp. 619–630, 2000.
- [96] J. Gao, W. D. Luedtke, D. Gourdon, M. Ruths, J. N. Israelachvili, and U. Landman, “Frictional forces and Amontons’ law: From the molecular to the macroscopic scale,” *The Journal of Physical Chemistry B*, vol. 108, no. 11, pp. 3410–3425, 2004.

- [97] D. H. Hwang and K. H. Zum Gahr, “Transition from static to kinetic friction of unlubricated or oil lubricated steel/steel, steel/ceramic and ceramic/ceramic pairs,” *Wear*, vol. 255, no. 1, pp. 365–375, 2003. 14th International Conference on Wear of Materials.
- [98] L. Púst, L. Pešek, and N. Yaroshevich, “Various types of dry friction characteristics for vibration damping,” *Engineering Mechanics*, vol. 18, no. 3/4, p. 203–224, 2011.
- [99] R. Stribeck, “Die wesentlichen eigenschaften der gleit- und rollenlager,” *Z. Verein. Deut. Ing.*, vol. 46, no. 38, pp. 1341–1348, 1902.
- [100] P. R. Dahl, “A solid friction model,” *Aerospace Corporation El Segundo CA*, 1968. Tech. Rep. TOR–0158(3107–18)–1.
- [101] T. Piatkowski, “Dahl and LuGre dynamic friction models — the analysis of selected properties,” *Mechanism and Machine Theory*, vol. 73, pp. 91–100, 2014.
- [102] M. Leus and P. Gutowski, “Analysis of longitudinal tangential contact vibration effect on friction force using Coulomb and Dahl models,” *Journal of Theoretical and Applied Mechanics*, vol. 46, pp. 171–184, 01 2008.
- [103] P. R. Dahl, “Solid friction damping of mechanical vibrations,” *AIAA Journal*, vol. 14, no. 12, pp. 1675–1682, 1976.
- [104] Y. Lenoir, “Identification de modèles tribologiques par pendule (identification of tribological models by pendulum),” *Comptes Rendus de l’Academie des Sciences Series IIB Mechanics Physics Astronomy*, vol. 327, no. 12, p. 1259–1264, 1999.
- [105] C. Canudas de Wit, H. Olsson, K. J. Åström, and P. Lischinsky, “A new model for control of systems with friction,” *IEEE Transactions on Automatic Control*, vol. 40, no. 3, pp. 419–425, 1995.

- [106] H. Olsson, K. J. Åström, C. Canudas de Wit, M. Gäfvert, and P. Lischinsky, “Friction models and friction compensation,” *European Journal of Control*, vol. 4, no. 3, pp. 176–195, 1998.
- [107] P. Soleimanian and H. Ahmadian, “Modeling friction effects in lubricated roller guideways using a modified LuGre model,” *Journal of Vibration and Control*, vol. 0, no. 0, pp. 1–12, 2021.
- [108] M. P. Rajapakshe, M. Gunaratne, and A. K. Kaw, “Evaluation of LuGre tire friction model with measured data on multiple pavement surfaces,” *Tire Science and Technology*, vol. 38, no. 3, p. 213–227, 2010.
- [109] C. DellaCorte and F. Thomas, “Tribological evaluation of candidate gear materials operating under light loads in highly humid conditions,” *NASA/TM—2015-218896*, 2015.
- [110] D. S. Dummit and R. M. Foote, *Abstract algebra*. Wiley, third ed., 2003.
- [111] S. F. Bellenot, “Additively separable functions.” Multivariable Calculus online handouts, Florida State University.
- [112] R. D. Mindlin and H. Deresiewicz, “Elastic spheres in contact under varying oblique forces,” *J. Appl. Mech.*, vol. 20, no. 3, pp. 327–344, 1953.
- [113] C. Cattaneo, “Compressione e torsione nel contatto tra corpi elastici di forma qualunque,” *Annali della Scuola Normale Superiore di Pisa, Serie III, vol. IX, Fasc. 1-2*, 1955.
- [114] K. L. Johnson, “Surface interaction between elastically loaded bodies under tangential forces,” *Proceedings of the Royal Society of London. Series A, Mathematical and Physical Sciences*, vol. 230, no. 1183, 1955.
- [115] S. Nadimi and J. Fonseca, “On the torsional loading of elastoplastic spheres in contact,” *EPJ Web of Conferences - Powders & Grains*, vol. 140, 2017.

- [116] D. Gradinaru and S. Spinu, “Numerical simulation of elastic torsional contact with slip and stick,” *Annals of the Oradea University: Fascicle of Management and Technological Engineering*, 2011.
- [117] E. Dintwa, M. V. Zeebroeck, E. Tijskens, and H. Ramon, “Torsion of viscoelastic spheres in contact,” *Granular Matter*, vol. 7, pp. 169–179, 2005.
- [118] H. Deresiewicz, “Contact of elastic spheres under an oscillating torsional couple,” *Journal of Applied Mechanics*, vol. 21, no. 1, pp. 52–56, 1954.
- [119] L. Lecornu, *Cours de Mécanique*. Paris, Gauthier-Villars, 1914. Tome I, Livre IV, Chap. VI.
- [120] R. D. Mindlin, “Compliance of elastic bodies in contact,” *ASME J. App. Mech.*, vol. 71, pp. 259 – 268, 1949.
- [121] S. S. Rao, *Mechanical Vibrations*. Prentice Hall, 2011.
- [122] J. S. Przemienieki, *Theory of matrix structural analysis*. Dover Publications, Inc. - New York, 1968.
- [123] “ANSYS Help Manual,” 2019.
- [124] G. Hattori and A. L. Serpa, “Influence of the main contact parameters in finite element analysis of elastic bodies in contact,” *Key Engineering Materials*, vol. 681, pp. 214–227, 2016.
- [125] Z.-Q. Qu, *Model order reduction techniques : with applications in finite element analysis*. New York: Springer, 2004.
- [126] C. Wang, K. Shankar, E. Morozov, K. R. Ramakrishnan, and A. Fien, “Characterization of shear behavior in stainless steel wire mesh using bias-extension and picture frame tests,” *J. Eng. Mech.*, vol. 146, no. 2, 2020.
- [127] B. M. Shafer, “An overview of constrained-layer damping theory and application,” *Proceedings of Meetings on Acoustics - ICA 2013 Montreal, Canada*, vol. 19, 2013.

# Appendix A

## MATLAB main script

```
clc
clear all
global G E_star L r C1a C2a C3a C1b C2b C3b K_eq_0 nu_eq_0 mu pre_FN
        n_substeps criterion FN_table orthotropic

%material properties

%warp wire
E1=200*10^9; %Young's modulus [N/m^2]
nu1=0.3; %Poisson's ratio
G1=E1/(2*(1+nu1)); %shear modulus [N/m^2]

%weft wire
E2=200*10^9; %Young's modulus [N/m^2]
nu2=0.3; %Poisson's ratio
G2=E2/(2*(1+nu2)); %shear modulus [N/m^2]

%contact properties
E_star=1/(((1-nu1^2)/E1 + (1-nu2^2)/E2)); %effective elastic modulus [N/m^2]
G=sqrt(G1*G2); %effective shear modulus
mu=0.3; %friction coefficient
```

```

%geometry
L=2.7*10^-3; %semi-period [m]
d=0.91*10^-3; %diameter [m]
r=d/2; %wire's radius [m]
Z=d/2; %wire's amplitude [m]
A=pi/4*d^2; %area [m^2]
I=pi/4*(d/2)^4; %second moment of inertia [m^4]
chi=10/9; %Timoshenko coefficient

if E1~=E2 || ni1~=ni2
    orthotropic=1; %informs functions that material is orthotropic
else
    orthotropic=0;
end

%coefficients for tension model
psi=Z/L; %waviness ratio
PSI=sqrt(1+psi^2*pi^2);

%warp wire
C1a=-(PSI*L^3)/(E1*I*pi^2) + (L*atanh(pi*psi/PSI))/(E1*A*pi*PSI)
    -(chi*L*atanh(pi*psi/PSI))/(G1*A*pi*PSI);
C2a=L^3/(48*E1*I) + (L*(PSI-1))/(4*E1*A*PSI) + chi*L/(4*G1*A*PSI);
C3a=(L^3*psi^2)/(2*E1*I) + L/(E1*A*PSI) + (chi*L*(PSI-1))/(G1*A*PSI);

%weft wire
C1b=-(PSI*L^3)/(E2*I*pi^2) + (L*atanh(pi*psi/PSI))/(E2*A*pi*PSI)
    -(chi*L*atanh(pi*psi/PSI))/(G2*A*pi*PSI);
C2b=L^3/(48*E2*I) + (L*(PSI-1))/(4*E2*A*PSI) + chi*L/(4*G2*A*PSI);
C3b=(L^3*psi^2)/(2*E2*I) + L/(E2*A*PSI) + (chi*L*(PSI-1))/(G2*A*PSI);

```

```

%initialisation values
K_eq_0=6.5; %initial effective stiffness [MPa]
nu_eq_0=0.35; %initial effective Poisson's ratio
pre_FN=0; %pre-tensional contact force [N]

n_substeps=1; %number of substeps
max_iter=3; %max. number of iterations per substep
criterion=0.005; %max. rel. err. for convergence [x100%]

%cleaning the temporary files folder
system('del/q files\*..*');

%saving initial settings (units: [MPa] and [mm])
fileID = fopen('files\settings.inp','w');
fprintf(fileID,'%5.0f,%1.3f,%5.0f,%1.3f,%2.3f,%2.3f,%5.0f,%1.3f,%1.3f,%3.3f',
E1/10^6,nu1,E2/10^6,nu2,L*10^3,d*10^3,n_substeps,K_eq_0,nu_eq_0);
fclose(fileID);

tic; %starts timer

for substep=1:n_substeps

    for n_iter=1:max_iter

        if n_iter==1
            message=sprintf('\nSUBSSTEP %d - iteration %d ',substep,n_iter);
        else
            message=sprintf('\n                iteration %d ',n_iter);
        end
    end
end

```

```

fprintf(message); %prints message on command window

if n_iter==1
    if substep==1
        system('start.bat');
        %in the first substep, starts simulation from beginning
    else
        system('restart.bat');
        %restarts simulation from last converged substep
    end
elseif n_iter>1
    if substep==1
        %if the first substep does not converge, the simulation
        %will be started again from the beginning
        system('start.bat');
    else
        %in order to re-execute the last non-converged substep,
        %it is necessary to delete the restart file
        file_name=['files\file.r',num2str(substep,'%03.f')];
        system(['del/q ',file_name]);
        system('restart.bat');
    end
end

[non_conv_num]=post_process(substep, n_iter);
%analyses results and updates material properties

if non_conv_num==0
    fprintf(2,'---> All elements converging.')
    break %exits iteration loop and starts next substep
else

```

```

        fprintf(2,'- %d non converging elements.', non_conv_num)
    end

end

%updates counter with ID of last converged substep
fileID = fopen('files\counter.csv','w');
fprintf(fileID,'%5.0f',substep);
fclose(fileID);

end

%time required for simulation
simulation_time=toc; %stops timer
simulation_time=round(simulation_time,0);
s=seconds(simulation_time);
s.Format='mm:ss';
fprintf(2,'\n\nSimulation completed. ');
fprintf(1,['\nElapsed time: ',char(s),' [mm:ss] \n']);

```